

Mathematical Modelling of the Material  
Flow and Microstructural Evolution  
During the Extrusion of AA3003  
Aluminum Alloy

by

Yahya Mahmoodkhani

A thesis  
presented to the University of Waterloo  
in fulfillment of the  
thesis requirement for the degree of  
Doctor of Philosophy  
in  
Mechanical Engineering

Waterloo, Ontario, Canada, 2013

©Yahya Mahmoodkhani 2013

## **AUTHOR'S DECLARATION**

I hereby declare that I am the sole author of this thesis. This is a true copy of the thesis, including any required final revisions, as accepted by my examiners.

I understand that my thesis may be made electronically available to the public.

Yahya Mahmoodkhani

## **Abstract**

A comprehensive mathematical model of the hot extrusion process for aluminum alloys has been developed and validated. The model is capable of predicting the material flow behaviour and microstructure evolution that occurs in aluminum alloy AA3003 during extrusion. The plasticity module was developed using a commercial finite element package, DEFORM<sup>®</sup>, a transient Lagrangian model which couples the thermal and deformation phenomena and is able to predict the temperature, strain rate and strain distribution in the billet/extrudate at any position in the container and die. Validation of the model against industrial data indicated that it gave excellent predictions of the pressure and temperature history during extrusion. Material flow effects during extrusion such as surface cladding (a transverse weld defect) as one billet is fed in after another through the die were also well predicted.

The results of the FEM model for material flow and thermomechanical history were post processed using MATLAB software to predict the grain deformation and stored energy in the extruded material as well as the thickness and extent of the transverse weld defect. Finally, the model predictions for microstructure and transverse weld were compared to microstructure observations.

The stored energy or driving pressure for Static Recrystallization (SRX) and Geometric Dynamic Recrystallization (GDRX) and how they are influenced by extrusion parameters were investigated using the mathematical model and experimental measurements. The experimental measurements for grain thickness and microstructural features made using Electron Back Scattered Diffraction (EBSD) technique and optical microscope show good agreement with model predictions. The mathematical model was then used to assess the effect a change in die design would have on the flow behaviour of the material during extrusion and on the transverse weld that forms.

## **Acknowledgements**

I have great appreciations for my supervisor, Professor Mary Wells who kindly supported me throughout my PhD program. I am very grateful for all her help and encouragement, her trust and patience and giving me this great opportunity to pursue my studies in my field of interest.

I would like to thank Professor Warren Poole (the University of British Columbia) and Dr. Nick Parson (RioTinto Alcan) for their help and guidance. I also thank Annabel Geng and Lina Grajales from The University of British Columbia for performing microscopic analyses and providing the experimental data. I appreciate our extrusion group members; Qiang Du, Payman Babghorbani, Hamid Azizi and others for their attention and comments during our group meetings. I also acknowledge Dr. Christopher Jowett for useful discussions.

Financial support from NSERC Canada and RioTinto Alcan are appreciated. I would also thank the staff in Arvida Research and Development Center (ARDC) in Jonquière QC for performing the extrusion trials and providing the extrudate samples. I am grateful to Dr. Joseph Robson and Liam Dwyer from Manchester University for helping me with the EBSD microscope examinations. I am also thankful to Professor John Humphreys for granting me permission to use the VMAP software.

Many thanks to the staff in Mechanical and Mechatronics Engineering department in University of Waterloo who helped me during my PhD program. I also thank my colleague and my friend, Amir Hadadzadeh, for his kind help and sharing his experiences with me regarding writing the thesis.

I am deeply grateful to my parents and my brothers for their prayers, support and encouragements. My greatest thanks go to my wife who did everything that she could to encourage, love, and support me during good times and hard times. And finally, my very special thank is for my lovely little girl who brought joy and happiness to our life by joining us in November 2012.

*To my wife*

## Table of Contents

AUTHOR'S DECLARATION.....	ii
Abstract.....	iii
Acknowledgements.....	iv
Dedication.....	v
Table of Contents.....	vi
List of Figures.....	x
List of Tables.....	xxii
Chapter 1 Introduction.....	1
1.1 Thermo-mechanical processing of AA3XXX aluminum alloys.....	3
1.2 Extrusion process.....	5
1.3 Challenges in extrusion of aluminum alloys.....	6
Chapter 2 Literature review.....	8
2.1 Microstructure evolution in hot extrusion of aluminum alloys.....	8
2.1.1 The deformed state.....	8
2.1.2 Restoration mechanisms during deformation.....	10
2.1.2.1 Dynamic recovery.....	10
2.1.2.2 Dynamic recrystallization.....	10
2.1.2.3 Dynamic recrystallization (DRX) during extrusion.....	13
2.1.3 Second phase particles.....	15
2.1.4 Peripheral coarse grains and control of grain structure.....	19
2.2 Modeling microstructure evolution during hot deformation of aluminum alloys.....	24
2.2.1 Empirical models.....	26
2.2.2 Physically based state variable models.....	26
2.2.3 Stored energy and driving pressure for recrystallization.....	28
2.2.4 Modeling the grain deformation during the extrusion.....	30
2.3 Simulation of the extrusion process.....	32
2.3.1 Constitutive equations for hot working.....	34
2.3.2 Thermomechanical modeling and FEM analysis of extrusion.....	34
2.4 Material flow in extrusion and internal defect formation.....	38
2.5 Summary.....	41

Chapter 3 Scope and objectives.....	42
Chapter 4 Methodology .....	44
4.1 Experimental .....	44
4.1.1 Extrusion trials.....	44
4.1.2 Characterization.....	50
4.1.2.1 Optical microscopy.....	50
4.1.2.2 Electron Back Scattered Diffraction (EBSD) microscopy and data analysis .....	51
4.1.2.3 Electrical resistivity measurement.....	53
4.2 Mathematical Model.....	53
4.2.1 Thermo-mechanical Model.....	53
4.2.1.1 Finite Element formulation.....	56
4.2.1.2 Material properties.....	58
4.2.1.3 Boundary and initial conditions.....	59
4.2.1.4 Mesh size sensitivity.....	62
4.2.2 Experimental validation of FE model.....	64
4.2.3 Post processing of FEM results .....	67
4.2.3.1 Point tracking using DEFORM post-processor .....	67
4.2.3.2 Grain shape calculation .....	68
4.2.3.3 Transverse weld boundary calculation .....	70
4.2.3.4 Stored energy calculation .....	73
Chapter 5 Results and discussion .....	75
5.1 Round bar extrusion .....	75
5.1.1 Material flow .....	75
5.1.2 Thermomechanical history .....	76
5.1.2.1 Temperature history – Parametric study.....	81
5.1.2.2 Summary .....	83
5.1.3 Microstructure evolution .....	83
5.1.3.1 Microstructure characterization.....	83

5.1.3.2 Geometric Dynamic Recrystallization (GDRX) .....	91
5.1.3.3 Stored energy and driving pressure for recrystallization .....	100
5.1.3.4 Effect of ram speed on as-extruded microstructure .....	106
5.1.3.5 Summary .....	109
5.2 I-Beam extrusion.....	111
5.2.1 Material flow.....	111
5.2.2 Thermomechanical history.....	112
5.2.3 Microstructure evolution.....	116
5.2.3.1 Grain thickness.....	116
5.2.3.2 Stored energy .....	117
5.2.4 Summary .....	118
Chapter 6 Transverse weld formation.....	119
6.1 Dead metal zone.....	120
6.2 Evaluation of transverse weld thickness .....	121
6.3 Effect of billet material [103].....	124
6.4 Effect of feeder geometry .....	127
6.5 Effect of feeder geometry on extrusion load, temperature and accumulated strain – Model predictions.....	128
6.6 Effect of extrusion ratio on transverse weld length – Model predictions for regular feeder ...	130
6.7 Summary .....	131
Chapter 7 Summary, conclusions and future work.....	133
7.1 Summary .....	133
7.2 Conclusions.....	134
7.2.1 Mathematical modelling and its effectiveness: .....	134
7.2.2 Microstructure evolution and effect of process parameters: .....	135
7.2.3 Transverse weld formation: .....	136
7.3 Future work.....	137
7.3.1 Microstructure characterization .....	137
7.3.2 Modelling the microstructure evolution.....	137
7.3.3 Modelling the defect formation.....	137



Appendix A Stored energy for different extrusion conditions (round bar extrusion) .....	139
Appendix B Optical microscope observations after extrusion (round bar extrusion) .....	140
Appendix C Resistivity changes after extrusion (round bar extrusion).....	144
References .....	145

## List of Figures

Figure 1-1 Aluminum application in European Cars (CAGR stands for “Compound Annual Growth Rate”) [3]. .....	1
Figure 1-2 Percentage distribution of semi-finished products by product type in 2005 [6]. .....	2
Figure 1-3 Schematic illustrating the process used for AA3XXX alloys to make automobile radiators (Billets with a diameter of around 30 cm are extruded to profiles with wall thickness of down to 0.2 mm). .....	3
Figure 1-4 Typical microstructure for AA3003 billets: (a) as-cast and (b) Homogenized at 550°C for 8 hrs [12]. .....	4
Figure 1-5 Typical thermo-mechanical history experienced during the extrusion process for AA3XXX aluminum alloys when making heat exchangers. ....	4
Figure 1-6 Components of a typical direct extrusion press. ....	5
Figure 1-7 Typical examples of complex aluminum extrusions [15]. .....	6
Figure 1-8 Microstructure inhomogeneity through the cross-section of extruded AA3003 (Macrograph is showing a quarter of cross-section of a bar extrudate), Reproduced with the permission from Grajales [17]. .....	7
Figure 2-1 Experimental results for microscopic flow during extrusion of AA6061 [20]. ....	9
Figure 2-2 (left) Schematic indicating the mechanism of GDRX. By increasing the strain, serrated high angle grain boundaries (HAGBs - bold lines) become closer while the subgrain size (lighter lines) remains approximately constant. Eventually HAGBs contact each other and elongated grains pinch off form small grains [21], (Right) Schematic, illustrating the steps (d) to (e) showing that during large deformation opposite serrations of elongated and thinned grains contact and in three dimensions they perforate and a new grain appears. As deformation continues perforation becomes bigger and produces a group of new grains [22]. ....	11
Figure 2-3 Polarized light micrograph from tangential section of Al at torsional strains of $\epsilon=60$ , 400°C and strain rate of $0.2 \text{ s}^{-1}$ for initial grain sizes of: (a) 100 $\mu\text{m}$ and (b) 2000 $\mu\text{m}$ [25]. .....	12

Figure 2-4 Measured subgrain size compared to calculated grain thickness for Al torsionally deformed to strains of up to $\epsilon=60$ at 400°C and strain rate of 0.5 s <sup>-1</sup> for two different initial grain sizes [26].	13
Figure 2-5 OIM micrograph from surface of AA6061 extrudate (black lines represent high angle boundaries) [34].	14
Figure 2-6 Measured Electron Back Scattered Diffraction (EBSD) maps showing High-angle (15°) grains in the undeformed material (P0) and other positions in the billet moving closer to the die and in the extrudate [36].	14
Figure 2-7 Curve fitting for grain dimensions for various effective strains for AA7020 (a and c) and AA6082 (b and d) [39].	15
Figure 2-8 Optical micrographs of AA3003 showing second phase particles for different homogenization conditions: a) as-cast; b) 500°C for eight hours; c) 550°C for eight hours; and d) 600°C for 24 hours. Micrographs reproduced with permission from Geng [43].	16
Figure 2-9 TEM images from AA3003 showing how the morphology of the dispersoids changes during heating (a) 350°C, (b) 400°C, (c) 500°C and (d) 580°C [42].	17
Figure 2-10 Temperature dependent solubility of Mn in Al-1.25Mn-0.5Fe-0.1Si (graph produced using FactSage 6.03 software).	17
Figure 2-11 Macrostructure of 25mm bar AA6005A extrusion for different ram speeds (mm/sec) on the x-axis and billet temperatures (°C) on the y-axis showing: (a) as extruded and (b) after solution heat treatment [50]. The thickness of PCG is indicated on the picture.	20
Figure 2-12 Effect of billet temperature and ram speed on grain structure of AA6005A 25mm bars with extrusion ratio of 17.5 [50].	21
Figure 2-13 Schematic drawing of different die configurations and simulation results for fraction recrystallized [57].	22
Figure 2-14 Proposed theory for PCG structure formation: (a) through (c) microstructure evolution during the deformation, (d) through (f) traditional theory of PCG formation and (g) through (j) proposed theory of PCG formation based on experimental results. Dark lines represent HAGBs and light gray lines represent LAGBs [53].	23

Figure 2-15 Grain structure at the die exit for indirect extrusion of 6061 Aluminum alloy. The billet was quenched 1 min after the ram stopped [34]. .....	23
Figure 2-16 Connectivity of sub-models for microstructural modeling at (a) the ‘macro’ level, and (b) the ‘micro’ level [61]. .....	25
Figure 2-17 Calculated change in the grain boundary area (S) as compared to the original grain boundary area ( $S_0$ ) assuming spherical initial grains as a function of the total strain [70]. S = the grain boundary area of the deformed structure and $S_0$ = the grain boundary area of the undeformed structure. ....	29
Figure 2-18 Representation of grain deformation and GDRX for (a) Cubic grain and (b) Truncated octahedral grain [51]. .....	31
Figure 2-19 Comparison of numerical predictions (a, b) and experimental results (c, d) during extrusion at different starting temperatures [81] (Billet diameter = 75mm, ER = 30).....	33
Figure 2-20 Predicted distribution of strain (left) [96] and strain rate (right) [81] during the extrusion process for 6XXX aluminum alloys.....	35
Figure 2-21 Heat balance in the extrusion process [73]. .....	36
Figure 2-22 Temperature distribution (a) with the feeder plate and (b) without the feeder plate [69].	36
Figure 2-23 Validation of modeling results with experimental measurements. (left) Load-stroke curve [79], (right) Temperature change before die for AA7XXX aluminum alloys [89].....	37
Figure 2-24 (a) Schematic of back-end defect formation [18], (b) cross section of extrudate containing back-end defect [101]. ....	39
Figure 2-25 (a) Schematic of the transverse weld formation [86], (b) Longitudinal section of extrusion showing the front of the transverse weld [101].....	39
Figure 2-26 (left) Thickness of transverse weld along the extrusion, different colored lines show the clad thickness at different sides of the profile [103], (right) profile x-section.....	40
Figure 3-1 Microstructural changes and parameters of interest during each step of extrusion.....	43
Figure 4-1 Temperature profiles for homogenization treatments. ....	45

Figure 4-2 Microstructure of billets for different homogenization conditions: (a) as-cast, (b) 500°C for 8 hrs, (c) 550°C for 8 hrs and (d) 600°C for 24 hrs. Reproduced with permission from Geng [43]. ... 45

Figure 4-3 Rio Tinto Alcan’s state of the art extrusion press (1- extruded strip exits here, 2- billet position for extrusion, 3- mechanical billet loading system, 4- ram, 5- Water quench unit). ..... 46

Figure 4-4 Location of thermocouples at the middle of bearing length to record the exit temperature at the surface of extrudate. .... 47

Figure 4-5 Picture of the final extrudate shape from the two extrusion dies used in the trial: (a) I-beam extrudate [43] and , (b) round bar extrudate. .... 48

Figure 4-6 Schematic of two different feeder geometries. .... 48

Figure 4-7 Schematic of the extrusion press at RioTinto Alcan’s Research and Development Center and quench tank layout along with sampling length. .... 50

Figure 4-8 Polarized light micrograph showing the starting grain structure of the as-cast billet [17]. 51

Figure 4-9 Locations on longitudinal section of extrusion sample chosen for EBSD analyses. .... 53

Figure 4-10 Schematic showing the billet being extruded into an I-beam section showing: Solid model of the billet and I-beam (left) and mesh used in the container, billet and I-beam (right). .... 54

Figure 4-11 Schematic showing the billet being extruded into a round bar: sectioned solid model (right), and FEM mesh used in the billet and tooling (left). .... 55

Figure 4-12 Typical mesh resolution distribution at the die corner for (a) I-beam and (b) Rod extrusion with extrusion ratio of 70. .... 56

Figure 4-13 Volumetric heat capacity changes over the temperature for the billet (AA3003) and tooling material (H13) [108]. .... 59

Figure 4-14 Boundary numbering and directions of heat transfer inside tooling. .... 60

Figure 4-15 Predicted temperature change at the surface of the extrudate during the water quench and subsequent air cooling with different HTC values, compared to experimental measurement (ram speed = 32 mm/sec). .... 62

Figure 4-16 Effect of minimum element size on distribution of accumulated plastic strain. .... 63

Figure 4-17 Effect of mesh size at the die corner on (a) the predicted extrusion load (at 50% extruded), and (b) computation time for simulation of extrusion of the whole billet. ....	64
Figure 4-18 Round bar extrusion (2D model) - comparison between model predictions (lines) and measurements (symbols) for extrusion load and temperature (a) billet temperature = 400°C and ram speed=2mm/s, (b) billet temperature = 500°C and ram speed=32mm/s, (for both cases extrusion ratio= 70, billets homogenized at 550°C for 8 hours and minimum mesh size=0.25mm. ....	65
Figure 4-19 I-beam extrusion (3D model) - validation of simulation results for: (a) Extrusion load and (b) Temperature (Homogenization treatment prior to extrusion: 550°C for 8h, Extrusion temperature = 550°C). ....	66
Figure 4-20 Graphical comparison of predicted and measured extrusion load for different conditions listed in Table 4-2, at a ram stroke where 50% of billet is extruded. ....	67
Figure 4-21 Flow pattern for different points that all go to the same section in the extrudate and blow-ups showing the schematic of original shape and arrangement of initially spherical grains before and after the deformation. ....	69
Figure 4-22 FE model-predicted velocity field showing (a) the direction and (b) the magnitude of velocity through the deforming material (extrusion ratio = 70, arrows show the direction of velocity for each node). ....	70
Figure 4-23 Finite element discretization of extruding material at the die corner showing the mesh size at different positions. ....	71
Figure 4-24 Schematic showing the point tracking procedure during one time step (dotted lines represent the exact flow lines, B is the exact position of point A after time increment $\Delta t$ , B' and B'' are numerically estimated position after time increment $\Delta t$ ). ....	72
Figure 4-25 Determining the transverse weld shape using point tracking method for an extrusion ration of 17, (a) position of points before extrusion starts, (b) position of tracked points right after the breakthrough. ....	73
Figure 5-1 Model-predicted deformation of initial network of circular cells in the billet during the extrusion, (extrusion ratio = 70, billet temperature = 500°C and ram speed = 8 mm/sec). ....	75

Figure 5-2 Model-predicted flow pattern through the rod thickness at the mid-length section of the extrudate (numbers on curves represent time after the extrusion starts in seconds, extrusion ratio = 70, billet temperature = 500°C and ram speed = 8 mm/sec). ..... 76

Figure 5-3 Temperature histories for center and surface of mid-length section of extrudate for: (a) whole extrusion cycle and (b) die region (ram speeds = 8 mm/sec, billet temperatures = 500°C and extrusion ratio = 70) ..... 77

Figure 5-4 Histories of strain rate, Zener-Hollomon parameter and strain for center and surface of mid-length section of extrudate; (left) the whole extrusion cycle, (right) die region (ram speeds = 8 mm/sec, billet temperatures = 500°C and extrusion ratio = 70)..... 78

Figure 5-5 Average Zener-Hollomon parameter distribution from center to the surface of mid-length section of extrudate (ram speeds = 8 mm/sec, billet temperatures = 500°C and extrusion ratio = 70).79

Figure 5-6 Strain rate changes versus accumulative plastic strain (ram speeds = 8 mm/sec, billet temperatures = 500°C and extrusion ratio = 70). ..... 80

Figure 5-7 Model predicted (a) Spatial distribution of the accumulated effective plastic strain across the rod radius after extrusion, (b) strain history during the extrusion at the center and surface of the extrudate (for an extrusion ratio of 70, billet temperature of 500°C and ram speed of 8 mm/sec), the highlighted area represents the time period that the center is not gaining considerable strain..... 80

Figure 5-8 Model predictions for the effect of extrusion conditions on the temperature of the extrudate center at the mid-length section after it exits the die; (a) effect of extrusion ratio for ram speed of 8 mm/s, billet temperature of 500°C and homogenization of 8 hours at 550°C, (b) effect of ram speed for different homogenization conditions, billet temperature of 500°C, and extrusion ratio of 70. .... 81

Figure 5-9 Model-predicted temperature histories for the center and surface of the mid-length section of extrudates for three different ram speeds; 2 mm/sec, 8 mm/sec and 32 mm/sec (homogenization = 8H550, extrusion ratio = 70 and billet temperature = 400°C and 500°C)..... 82

Figure 5-10 Optical macrographs showing the quarter section of as-extruded macrostructure across the radius of extrudates with ER = 70; (a) homogenization of 8H500, billet temperature = 400°C, ram speed = 32 mm/sec, (b) homogenization of 24H600, billet temperature = 350°C, ram speed = 8 mm/sec (with permission from Grajales [17])..... 84

Figure 5-11 Optical macrographs showing the as-extruded transverse macrostructure across the radius of extrudates with three different extrusion ratios of 17, 70 and 280 (extrudate diameters of 1", ½" and ¼" or in millimeters; 25.4, 12.7 and 6.35 mm, respectively), for all three cases the billet temperature is 400°C and homogenization condition is 8 hours at 550°C. Ram speed for ER = 17 is 8 mm/sec and that of ER = 70 and 280 is 2 mm/sec, Macrographs reproduced with permission from Grajales [17]..... 84

Figure 5-12 Optical micrograph showing the longitudinal structure of extrudate from center to surface for an extrusion ratio of 70, homogenization treatment prior to extrusion: 550°C for 8h, billet with preheat of 400°C and ram speed of 2 mm/s, magnified graphs clearly show the fibrous structure at the center (upper left) and granular fine structure at the surface (upper right) [35]. ..... 85

Figure 5-13 Locations on longitudinal section of extrusion sample chosen for EBSD analyses. The maps are for sample #4 in Table 4-4..... 86

Figure 5-14 “1 mm long” EBSD map shown in Figure 5-13 split into two parts for magnification (sample #4 in Table 4-4). ..... 87

Figure 5-15 EBSD maps from center and subsurface of extrusions with different extrusion ratios. Left sides of subsurface maps are at 0.8, 0.5 and 0.3 mm from the surface respectively for extrusion ratios of 17, 70 and 280 (for detailed extrusion conditions for each case refer to Table 4-4). ..... 88

Figure 5-16 Cumulative misorientation line scans from selected locations at subsurface of extrudate showing the split grains in extrusion direction and random mis-orientation in the transverse direction (a) sample #4 and (b) sample #2 in Table 4-4..... 89

Figure 5-17 EBSD maps from longitudinal section at the center of the extrudate, possible microstructural mechanisms for some features indicated on the figure, (a) sample #2 and (b) sample #4 in Table 4-4 (ER = 70). ..... 90

Figure 5-18 “1 mm long” EBSD maps from longitudinal sections at a location between the center and surface of the extrudates (refer to Figure 5-13 for exact location), (a) sample #2 and (b) sample #4 in Table 4-4. .... 91

Figure 5-19 Comparison of model predicted (dashed lines) changes in the grain thickness along the length of the extrudate at the center-line relative to the mass balance approach (solid line) and



experimental measurements (symbols for two different extrusion ratios of 17 and 70 (experimental results taken from [17])).	92
Figure 5-20 Model-predicted spatial grain thickness across the radius of the extrudate for three different locations along the extrudate using an extrusion ratio of 70, ram speed = 2 mm/sec and temperature = 500°C.	93
Figure 5-21 Grain thickness across the radius of extrudate at a mid-length section for (a) different extrusion ratios with extrusion temperature of 500°C and ram speed of 8 mm/s, (b) different temperatures and ram speeds with extrusion ratio of 70.	94
Figure 5-22 Schematic showing the stages that a grain undergoes during large strain deformation: (a) undeformed state, (b) dislocation jungle formation during the deformation, (c) dislocations reorder and develop cell structure or subgrains (DRV), (d) and (e) with more deformation the thickness of grain decreases until it reaches a critical value (i.e. subgrain size) under which the grain starts to split up to several grains.	95
Figure 5-23 Model-predicted grain thickness for different extrusion ratios across the diameter of the extrudate as well as measured subgrain size at different positions along the extrudate diameter for different extrudates listed in Table 4-4.	96
Figure 5-24 (a) Model predictions for grain thickness and subgrain size measured by EBSD, (b) Optical micrograph for the surface of the extrudate, (for both a and b: Extrusion ratio=17, Billet preheat temperature=500°C and ram speed = 8 mm/s, position along the extrudate = 53%) [35].	97
Figure 5-25 Predicted grain thickness versus measured subgrain size for extrusion ratio of 70, ram speed of 2 mm/s, billet temperature of 500°C, homogenization of 8 hours at 500°C and the position of 52% along the extrudate (EBSD maps on sides of the graph correspond to locations of subgrain size measurements at center and surface and the “1 mm long” map corresponds to highlighted region on the graph).	98
Figure 5-26 Estimation of GDRX layer thickness using the average subgrain size at the surface of the extrudate.	99
Figure 5-27 Effect of extrusion ratio on the thickness of the GDRX layer, (a) thickness in mm, (b) normalized based on extrudate diameter.	100

Figure 5-28 Predicted effect of homogenization on Zener drag. ....	101
Figure 5-29 Calculated stored energy and estimated Zener drag compared to microstructure at the same section for homogenization of 8 hours at 550°C, extrusion ratio of 70, ram speed of 8 mm/s and billet temperature of 500°C, (micrographs reproduced with permission from Grajales [114])......	102
Figure 5-30 Model-predicted effect of extrusion ratio on stored energy at the center of mid-length section of the extrudate, extrusion temperature of 500°C, homogenization of 8 h at 550°C and ram speed 8 mm/s.....	103
Figure 5-31 Macrographs from x-section of extrudates with the same conditions as extrudates in Figure 5-30, (Annealing treatment: 10 minutes at 550°C), Reproduced with the permission from Grajales [17]......	103
Figure 5-32 Effect of temperature (a) and ram speed (b) on calculated total stored energy at the center of mid-length section of the extrudate with extrusion ratio of 70, (different homogenization treatments; 500°C for 8 hrs, 550°C for 8 hrs and 600°C for 24 hrs). ....	104
Figure 5-33 Effect of extrusion conditions and homogenization treatment on total stored energy at the center of mid-length section of the extrudate with an extrusion ratio of 70. ....	105
Figure 5-34 Effect of extrusion conditions and homogenization treatment on recrystallization driving pressure at the center of the extrudate with an extrusion ratio of 70. ....	106
Figure 5-35 Micrographs of longitudinal section from center to the surface of as-extruded samples from extrudates with billet preheat temperature of 400°C, extrusion ratio of 70, homogenization of 8 hours at 550°C and different ram speeds of 2, 8 and 32 mm/sec (Reproduced with the permission from Grajales [17]) .....	107
Figure 5-36 Micrographs of transverse section from center to the surface of the extrudate with billet preheat temperature of 400°C, extrusion ratio of 70, homogenization of 8 hours at 550°C, ram speed of 2 mm/sec and different post extrusion annealing conditions; as-extruded, 1minute at 525°C and 10 minutes at 525°C, (Reproduced with the permission from Grajales [17])......	107
Figure 5-37 Model predictions for effect of ram speed on temperature history at the center line during the extrusion and subsequent water quench and air cooling; (a) billet temperature = 400°C, (b) billet	

temperature = 500°C (micrographs shows the longitudinal section grain structure of extrudate for different conditions), Micrographs reproduced with the permission from Grajales [17].	109
Figure 5-38 Model-predicted velocity distribution for material extruded at 400°C (left) and 550°C (right).	111
Figure 5-39 Model predicted flow pattern of different points through the half thickness of the mid-length section of I-beam extrudate at two different extrusion temperatures (from ‘center’ to the ‘surface’ shown in Figure 4-10).	112
Figure 5-40 Model-predicted strain and temperature distribution through x-section at mid-length of the I-beam extrudate, (billet temperature = 550°C).	113
Figure 5-41 Model-predicted strain distribution at the mid-length section through the thickness of the I-beam extrudate, (‘center’ and ‘surface’ refer to center and surface points mid-width across the I-beam as shown in Figure 4-10).	114
Figure 5-42 Thermomechanical history for ‘center’ and ‘surface’ on mid-width of I-beam mid-length section.	115
Figure 5-43 Average Zener-Hollomon parameter and micrographs of different areas of extrudate (Center and surface refer to center and surface points mid-width across the I-beam as shown in Figure 4-10, homogenization treatment before extrusion: 550°C for 8h) [12].	116
Figure 5-44 Model-predicted grain thickness and subgrain size from the ‘center’ to ‘surface’ at mid-length section of I-beam extrudate.	117
Figure 5-45 Calculated stored energy from the ‘center’ to ‘surface’ at mid-length section of I-beam extrudate; (a) stored energy from dislocations, (b) total stored energy (including energy from grain boundaries).	118
Figure 6-1 Schematic of transverse weld formation showing: (a) end of the extrusion of the first billet, (b) shearing the 10% billet butt off the first billet, (c) loading the second billet into the container, and (d) beginning extrusion of the second billet, showing the development of the transverse weld, (e) the length of the transverse weld ( $l_{TW}$ ) with minimum clad thickness of $t_m$ divided into $l_1$ and $l_2$ .	119

Figure 6-2 – Optical macrograph showing the cross section of transverse weld at 0.2 m (a) and 1 m (b) from stop mark for an extrusion ratio of 70 (first billet AA6063 and second billet AA3003) Trial #3 in Table 4-3, TW shown in the figure is the thickness of the transverse weld or clad layer, Macrographs reproduced with permission from Parson [117]...... 120

Figure 6-3 Model-predicted boundary between the first and second billet inside the feeder at the end of extrusion stroke (extrusion ratio = 70, billet temperature=500°C, ram speed = 2 mm/sec). ..... 121

Figure 6-4 (a) Model predicted shape of the transverse weld between the first and second billet for the first 2m of the extrudate, (b) micrograph of extrudate x-section at 1300 mm from the stop mark showing the experimental measurement of the first billet layer clad onto the surface of the second billet (extrusion ratio = 70, billet temperature=500°C, ram speed = 2 mm/sec) first billet is AA6063 alloy and the second billet is AA3003. .... 122

Figure 6-5 Graphical comparison of predicted and measured clad layer thickness on extrudate. .... 123

Figure 6-6 (a) Model predictions and experimental measurements for transverse weld thickness in logarithmic scale, (b) power law trendline fitted on model predictions, (first and second billet AA3003 with homogenization of 24H600 and 8H550, respectively), Experimental data from [117]. ..... 124

Figure 6-7 Effect of different billet material combination on the thickness of transverse weld along the extrudate (legends represent the codes for aluminum alloy used for first and second billets for each test, 3003A stand for 3003 aluminum alloy homogenized at 600°C for 24 hours and 3003B stands for the same alloy homogenized at 550°C for 8 hours), Experimental data from [117]. ..... 126

Figure 6-8 Comparison of transverse weld contrast for marker materials (a) and regular AA6063 (b) at 1000 mm position, Macrographs reproduced with permission from Parson [117]...... 126

Figure 6-9 Model-predicted effect of feeder geometry on the shape of the transverse weld at different ram strokes, (Model predictions were done for an extrusion ratio of 70, billet temperature = 500°C, ram speed = 2 mm/sec). ..... 127

Figure 6-10 Comparison of model predictions (lines) to measurements (symbols) showing the effect of feeder shape on transverse weld geometry for extrusion ratio of 70, (model predictions for AA3003

billet with the homogenization of 8H550, extruded at 500°C and ram speed of 2 mm/sec, experimental data for trials #4 and #7 in Table 4-3), Experimental data from [117]..... 128

Figure 6-11 Model predictions for effect of feeder geometry on: (a) extrusion load, and (b) exit temperature at the surface of extrudate (extrusion ratio = 70, billet temperature = 500°C, ram speed = 2 mm/sec). ..... 129

Figure 6-12 Model-predicted effect of feeder geometry on (a) effect of feeder geometry on accumulative plastic strain distribution along the extrudate x-section and (b) flow pattern in deformation zone (both figures are for mid-length x-section of extrudate). ..... 130

Figure 6-13 Predicted effect of extrusion ratio on transverse weld length for the regular feeder geometry (refer to Figure 6-1e for description of  $l_{TW}$ ,  $l_2$  and  $t_m$ ). ..... 131

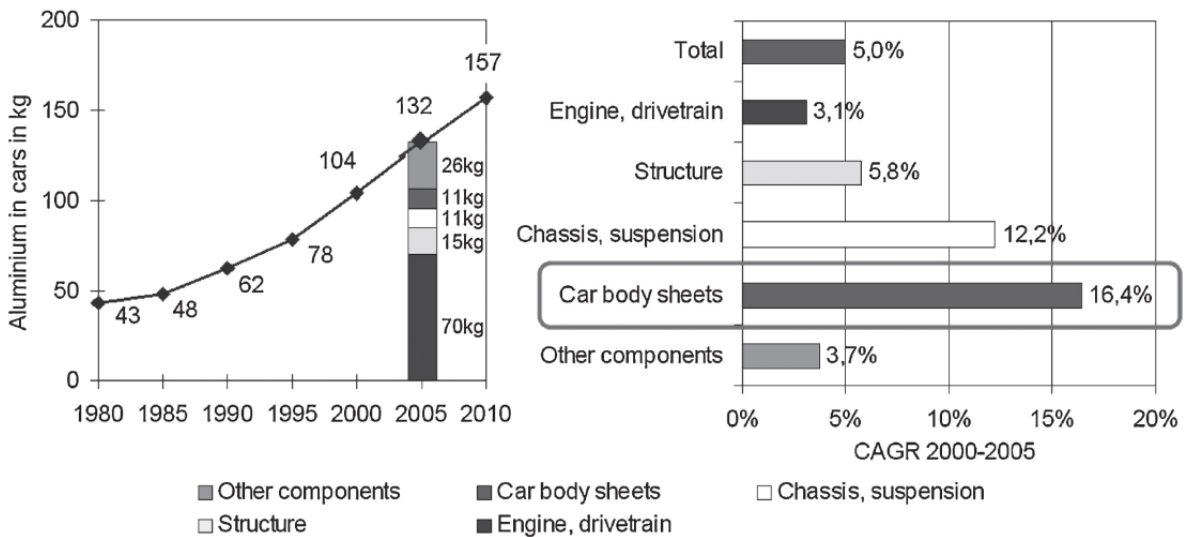
## **List of Tables**

Table 2-1 Parameters in empirical equations of recrystallization for commercial purity aluminum and Al-1Mg alloy [63].....	26
Table 4-1 Chemical composition of the AA3003 alloy used for the billet material .....	44
Table 4-2 Range of extrusion conditions studied during extrusion trials. ....	49
Table 4-3 Extrusion trials performed for evaluation of transverse weld.....	49
Table 4-4 Samples selected for EBSD analysis. ....	51
Table 4-5 Values and units of parameters used in Equation 4-5 [11]. ....	58
Table 4-6 Thermophysical properties used in the model [108]. ....	59
Table 4-7 Microstructure model constants and tuning parameters. ....	74
Table 5-1 Grain thickness comparison at the center of the extrudate (experimental results taken from [17]) .....	91
Table 5-2 Constituent particle and dispersoid data for various homogenization treatments [43, 113] and calculated Zener drag. ....	100
Table 6-1 Thickness of surface weld layer (clad layer) for various extrusion conditions, regular feeder. ....	122

# Chapter 1

## Introduction

Rapidly increasing fuel prices over the past few years and the focus on low emission vehicles are causing consumers to move away from large trucks and sport utility vehicles toward more efficient cars. This consumer trend, coupled with proposed CAFÉ regulations reaching 36.7 mpg by 2017 and 51.3 mpg by 2025 [1] have motivated North American car companies to re-examine the use of lightweight materials, in particular aluminum, in their vehicles. By 2020, the average aluminum content of vehicles produced in North America is projected to rise to 171 kg, up from about 148 kg in 2008, as automakers choose lighter engine blocks, hoods and other components [2]. Figure 1-1 shows the historical growth of aluminum in European cars.



**Figure 1-1 Aluminum application in European Cars (CAGR stands for “Compound Annual Growth Rate”) [3].**

In 2012, Canada produced 2.78 million metric tons of aluminum which was about 6.3% of the total global aluminum production of 45.2 million metric tons [4, 5]. RioTinto Alcan is one of the major aluminum producers in Canada who makes and casts aluminum rolling slab for sheet fabrication and also aluminum billet for aluminum extrusion production. Of the total aluminum production, aluminum extrusions are extensively used for manufacturing of industrial products especially in the transportation area. Figure 1-2 shows the fraction distribution of major aluminum

products in 2005 when the world total aluminum production was 31.9 million metric tons per year [5].

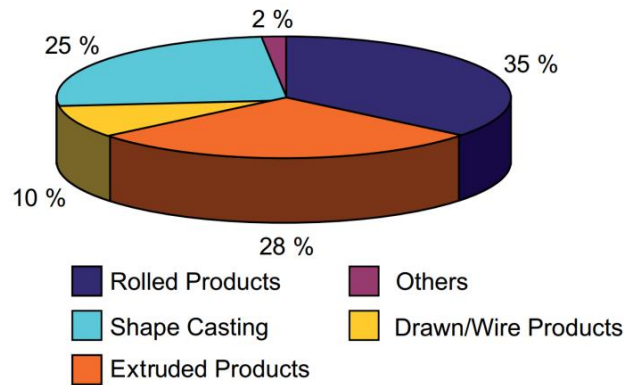


Figure 1-2 Percentage distribution of semi-finished products by product type in 2005 [6].

Central to the competitiveness of Rio Tinto Alcan and other aluminum manufacturers, is the quantitative linkage between products and the processes by which they are made. This type of activity has gained attention internationally and there are significant programs underway to develop through process models for various metallurgical fabrication processes. Inherently, the need for these types of models is that the properties of the metal products depend on the microstructure of the material which in turn is a complex function of composition, grain size and orientation, distribution of phases and precipitates and its thermo-mechanical history. The development of a particular microstructure and the desired properties in an industrial process however is less than straightforward because the latter usually involves a complex deformation and temperature path which can be very different through the thickness of the material depending on its location.

This research is part of a larger research program being done in conjunction with the University of British Columbia in Vancouver, BC and RioTinto Alcan in Jonquiere, Quebec. The overall objective of the project is to develop a through process model for the extrusion and manufacturing of aluminum heat exchangers which are typically made from aluminum alloy AA3XXX and used in automotive applications. The manufacturing of aluminum heat exchangers involves a complicated thermal mechanical history over a number of processing steps including: Direct Chill (DC) casting to produce the billet, homogenization, hot extrusion, cold deformation and annealing. The microstructure changes in the material, and hence the final properties of the product, are dependent to a large extent on the linkage between the starting microstructure, the thermo-mechanical history experienced during these processing steps and the chemistry of the alloy. The research I have

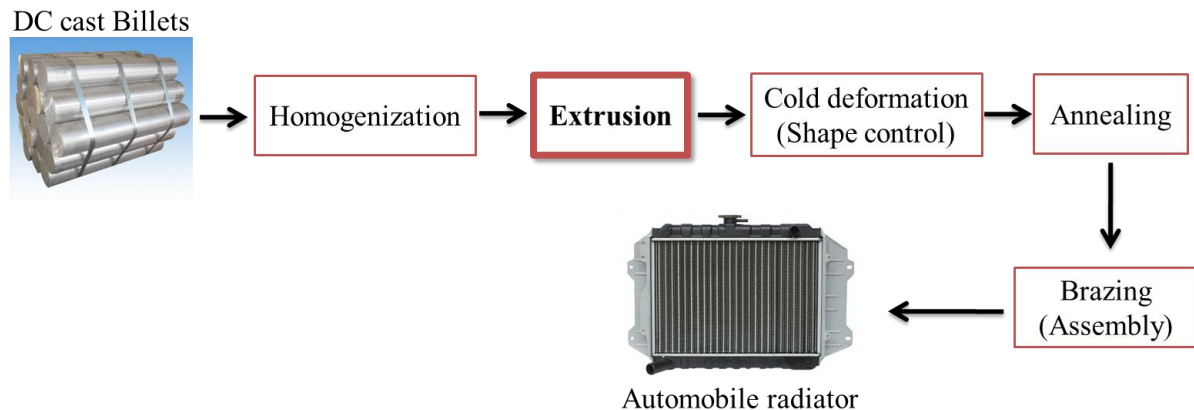


undertaken as part of the research program was to develop a model of the microstructure changes during extrusion of AA3XXX aluminum alloys with a focus on AA3003.

The AA3XXX alloys are non-heat treatable aluminum alloys in which manganese (Mn) is the major alloying element. These alloys typically also contain iron (Fe) and silicon (Si). Commercial AA3XXX aluminum alloys have a good combination of strength, workability, conductivity, weldability and corrosion resistance, hence they have found wide application in the packaging, architecture and transportation industry [7, 8, 9, 10]. Generally, after the AA1XXX series, the AA3XXX series are the most extrudable aluminum alloys compared to other commercial aluminum alloys [7].

## 1.1 Thermo-mechanical processing of AA3XXX aluminum alloys

The typical manufacturing history to produce a heat exchanger is shown in Figure 1-3. This process usually includes: Direct Chill (DC) casting to produce a billet, followed by homogenization, hot extrusion, cold deformation, annealing and brazing [11].



**Figure 1-3 Schematic illustrating the process used for AA3XXX alloys to make automobile radiators (Billets with a diameter of around 30 cm are extruded to profiles with wall thickness of down to 0.2 mm).**

As-cast AA3XXX billets typically consist of interdendritic phase e.g. Fe/Mn ( $Al_6$ ) and alpha phase ( $\alpha-Al_{15}(Mn)_3Si_2$ ) and the aluminum matrix is typically supersaturated in solute atoms (Figure 1-4a). During homogenization of the as-cast billets, the continuous brittle network of interdendritic phase breaks up to small particles, so called constituent particles, and some precipitation of dispersoids may also occur from supersaturated regions inside the grains. Once

precipitation has occurred, the dispersoids can start to grow if enough thermal energy is available. These dispersoids can pin the grain boundaries and prevent recrystallization nucleation during subsequent extrusion. Figure 1-4 shows typical as-cast and homogenized microstructures for AA3XXX alloy.

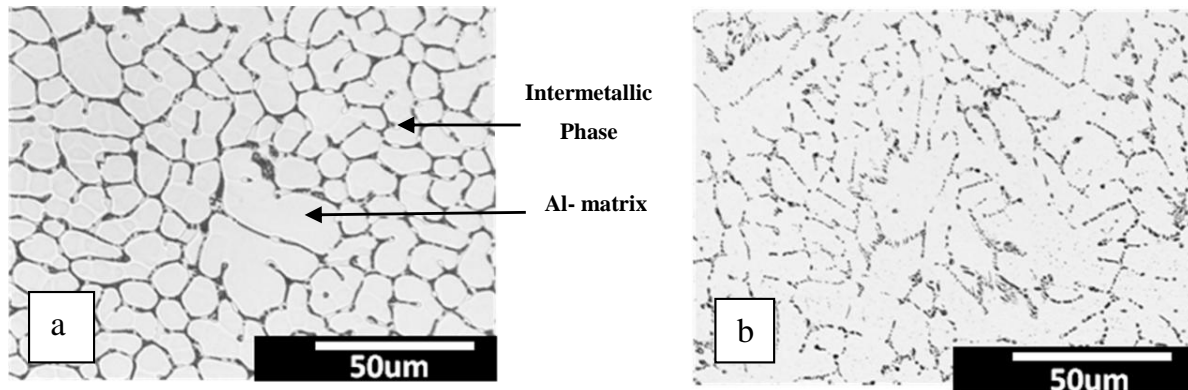


Figure 1-4 Typical microstructure for AA3003 billets: (a) as-cast and (b) Homogenized at 550°C for 8 hrs [12].

Hot extrusion of homogenized billets includes preheating of the billets, extrusion and a water quench after extrusion to retain the as-extruded microstructure and minimize surface recrystallization and grain growth. Figure 1-5 represents a typical temperature and strain history during the thermo-mechanical processing of AA3XXX alloys.

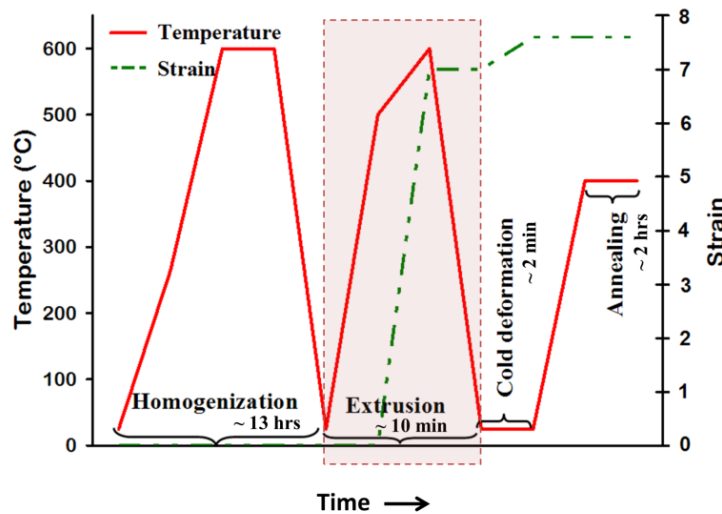


Figure 1-5 Typical thermo-mechanical history experienced during the extrusion process for AA3XXX aluminum alloys when making heat exchangers.

In order to optimize the final product properties, there must be a good understanding of the effect of process parameters on microstructure evolution. Different methods have been widely used to study the microstructure evolution during production of aluminum alloy products. One way is to run a series of experiments in which variables are changed and the response to this is observed and measured. This approach is time consuming and models developed using these techniques can only be used under a limited range of process conditions. An effective and economic method is to develop fundamentally based mathematical models that are experimentally validated. As shown in Figure 1-5, during the thermo-mechanical processing of AA3XXX alloys, the majority of deformation takes place during the extrusion step. So modeling of the extrusion process as an intermediate step between homogenization and cold deformation is of high importance for predicting the final properties.

## 1.2 Extrusion process

Direct extrusion is a hot metal forming process that involves pushing a pre-heated billet (with standard dimensions of 660-1830 mm in length and a 76-838 mm diameter [13]) with a ram through a die which determines the cross sectional geometry of the extruded product (Figure 1-6). The metal is thus shaped along its entire length according to the die profile. Extrusion processes have been in use for more than 100 years as manufacturing processes to produce long length products with constant cross sections [9].

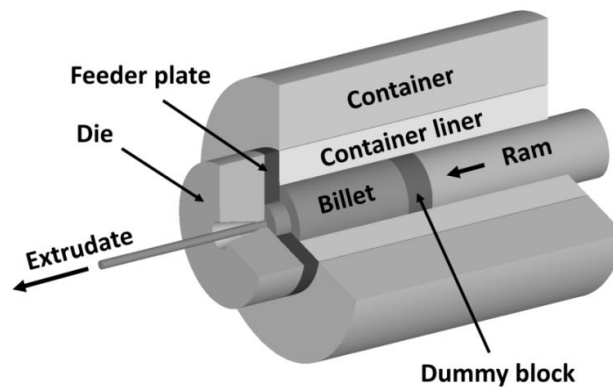


Figure 1-6 Components of a typical direct extrusion press.

A wide range of cross-section shapes can be produced by hot extrusion, including complex thin-walled open and hollow sections (Figure 1-7). As-extruded material usually has accurate dimensions

over the whole length of the profile [14]. The main concern in terms of dimensional inaccuracy is the loss of straightness which usually occurs during the cooling stage and can easily be restored by cold stretching.

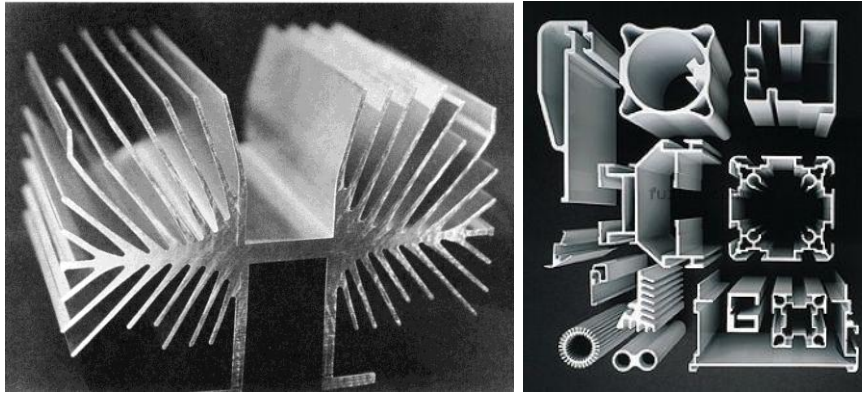


Figure 1-7 Typical examples of complex aluminum extrusions [15].

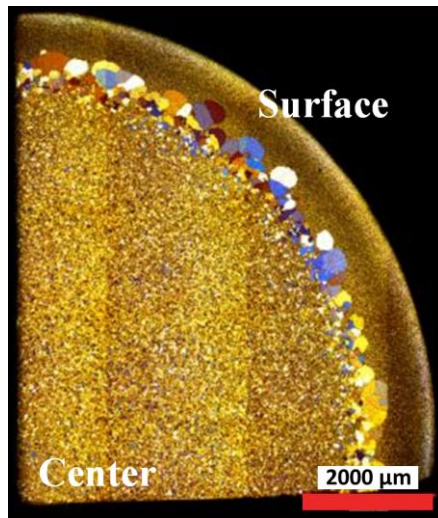
### 1.3 Challenges in extrusion of aluminum alloys

Extrusion of aluminum alloys takes place under large strains and significant friction at the interface between the billet and tooling causes intensive heat production especially near the surface. As a result, great care must be taken to optimize the process parameters to avoid reaching the melting point of the material (in this case  $\sim 650^{\circ}\text{C}$  for AA3003 [7]). The important processing parameters during extrusion include: the ram speed, extrusion ratio, the incoming billet temperature and starting microstructure.

In comparison with other bulk deformation processes such as rolling in which the material (sheet or plate) moves with the tooling (rolls), in extrusion the tooling (die and container) do not move with the material (billet). Friction (usually sticking friction) between the billet and container, in conjunction with typical inhomogeneous metal flow during extrusion results in inevitable internal extrusion defects such as the back-end defect and transverse weld formation during billet-on-billet extrusion. The back-end defect occurs at the last portion of the extrusion and a transverse weld occurs in the first portion of the extrusion during billet-on-billet extrusion where billets are extruded one right after the other. Both of these defects can be affected by the tooling geometry (i.e. extrusion ratio) but are not as sensitive to process conditions such as temperature and ram speed.

On the other hand, due to deformation inhomogeneity through the thickness of the extrusion and along its length, different recrystallization mechanisms can be activated at different spatial positions

which can result in changes in extrudate grain structure both through its thickness and along its length. The ability to produce a fine grained equiaxed structure throughout the extrudate has been the most important challenge for the industry as it provides good mechanical properties which are uniform throughout the extrudate [16]. Figure 1-8 shows typical microstructure inhomogeneity across the section of extruded AA3003 with small recrystallized grains at the center, large recrystallized grains at the subsurface and an unrecrystallized fine structure at the surface.



**Figure 1-8** Microstructure inhomogeneity through the cross-section of extruded AA3003 (Macrograph is showing a quarter of cross-section of a bar extrudate), Reproduced with the permission from Grajales [17].

## **Chapter 2**

### **Literature review**

This chapter will summarize the relevant literature in terms of the mathematical models that have been developed for the aluminum extrusion process and more specifically the models that have been used to quantify the microstructure changes that occur during extrusion of AA3XXX aluminum alloys.

#### **2.1 Microstructure evolution in hot extrusion of aluminum alloys**

During extrusion of aluminum alloys significant microstructure changes take place and these changes are very dependent on the starting microstructure prior to extrusion as well as the specific thermomechanical history experienced by the material during and after the extrusion process. The microstructure changes may include: precipitation and/or dissolution of precipitates, constituent particle fracture, dynamic recovery (DRV), dynamic and static recrystallization (DRX and SRX), and grain growth. The ability to model these changes is imperative as it can provide a knowledge based processing tool that can be used to optimize and understand how the microstructure changes are influenced by the extrusion process.

The majority of the research on extrusion of aluminum alloys has focused on the 6XXX alloys and to lesser extent the 7XXX alloys. In comparison, relatively little modelling work has been done on extrusion of 3XXX aluminum alloys in terms of macroscopic models capable of predicting the thermomechanical history and material flow behavior as well as some of the microstructure changes that occur.

Recovery and recrystallization processes can occur both during and after extrusion and are influenced by the precipitate state and stored energy in the matrix. During extrusion, the inhomogeneity of deformation through the thickness of the billet and the effects of friction at the interface can lead to through profile effects such that different recrystallized grain structures occur both through the thickness of the extrudate and along its length.

##### **2.1.1 The deformed state**

Figure 2-1 shows the flow of the material during an extrusion operation. As shown in Figure 2-1, a region of high shear is apparent as the billet flows towards the die such that a sub-surface region of

the billet becomes the surface of the extrudate. After extrusion, the structure typically consists of severely elongated grains that are called “fibres”. Deformation at the surface of the extrudate can be up to 60 times more than in the center and is reflective of the material flow experienced in both the billet and the die [18]. Microscopic observations confirm this and show that the grains in the dead metal zone (in the corners of the container where the metal does not flow) remain equiaxed whereas grains in the shear zone (transition zone on the dead metal zone boundary, typically at a 45° angle to the dead metal zone) become very elongated providing some evidence on the flow pattern and deformation experienced by the metal as shown in Figure 2-1. Micrographs taken from three directions show that the grains become more and more deformed “like spaghetti” as they traverse through the deformation zone [19].

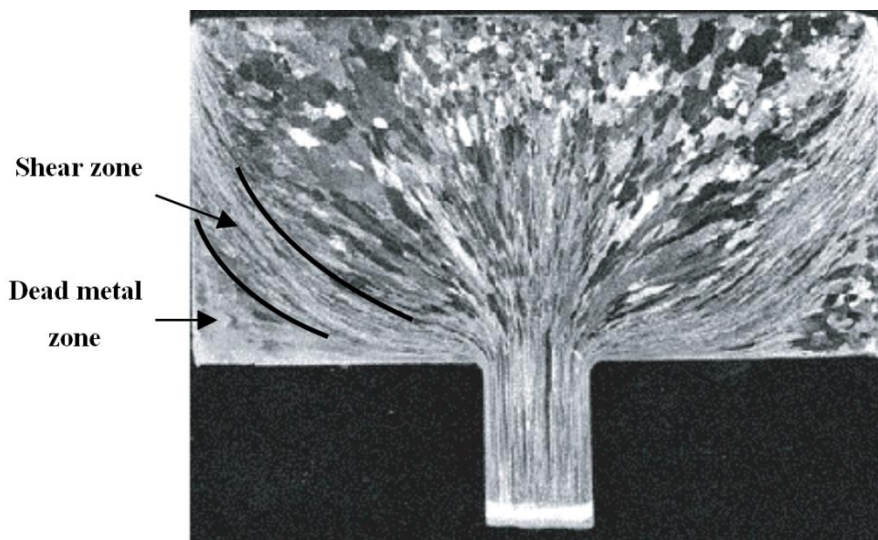


Figure 2-1 Experimental results for microscopic flow during extrusion of AA6061 [20].

During deformation, two major microstructure changes occur that increase the internal stored energy of the material. The first one is the increasing grain boundary area due to the change of the grain shape or increase of the grain aspect ratio and the second relates to the accumulation of dislocations in the material. Creation of new boundaries is achieved via two mechanisms. The first is related to the incorporation of dislocations into the grain boundary wall which are being produced continuously during the deformation. The second one is the formation of a smaller scale internal structure (sub-grains) inside the deformed grains that result from dislocation accumulation [21]. This mechanism takes place in the aluminum with a very high rate and consumes the majority of dislocations that accumulate inside the grains.

## **2.1.2 Restoration mechanisms during deformation**

### **2.1.2.1 Dynamic recovery**

In aluminum alloys dynamic recovery (DRV) is the primary softening mechanism during hot deformation because the dislocations can move easily (glide, cross-slip and climb). The reason aluminum recovers so readily is due to its high stacking fault energy (SFE) [21, 22]. During recovery, dislocations rearrange themselves into subgrains within the deformed grains. This phenomenon starts from the yield point and continues up to a plateau where the annihilation and generation rates of dislocations balance each other and the macroscopic flow stress appears to plateau [22]. Studies show that in dilute aluminum alloys, DRV continues even to very large strains (torsional strains larger than 100) [22].

### **2.1.2.2 Dynamic recrystallization**

Dynamic Recrystallization (DRX) includes nucleation and growth of new grains during the deformation operation and this is rarely observed in aluminum alloys. The occurrence of DRX is usually associated with a peak in the stress-strain curve of the material [21] followed by a decrease, but generally aluminum alloys do not show this behavior during deformation as evidenced by their flow stress curves. However, there is some experimental evidence that some aluminum alloys do experience some variations of classical DRX and include: Continuous Dynamic Recrystallization (CDRX) and Geometric Dynamic Recrystallization (GDRX) [21, 23]. Both of these variations in DRX mechanisms will not cause a sudden decrease in the flow curve.

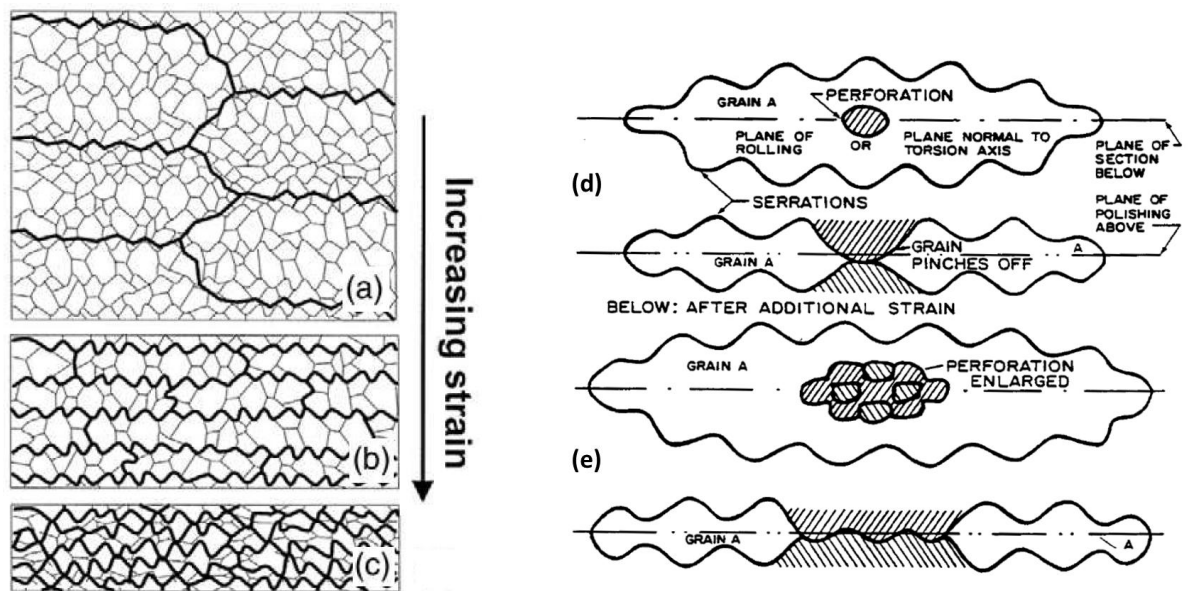
During CDRX, subgrains inside the deformed grains transform to grains by continuous accumulation of dislocations on their boundaries [21]. Dislocations produced during the deformation accumulate progressively on Low Angle Grain Boundaries (LAGBs) causing an increase of misorientation of subgrain boundaries until they reach a critical value and then formation of High Angle Grain Boundaries (HAGBs). Perdrix et. al. [24] reported this phenomenon in aluminum alloys for the first time.

GDRX is a form of dynamics recrystallization that was first identified in heavily deformed aluminum alloys that had been torsion tested [25]. It is thought that in situations where high amounts of strain are experienced and the deformed grain thickness approaches the subgrain diameter size GDRX can occur. During GDRX, grain boundary serrations contact each other and the grains can



pinch off to form fine recrystallized grains [22, 25, 21, 26, 27, 28]. Figure 2-2 shows a simplified schematic of GDRX in which impingement of serrated grain boundaries is the main mechanism. McQueen [25] was one of the first researchers to propose this mechanism and confirm it experimentally for aluminum alloys [27, 22].

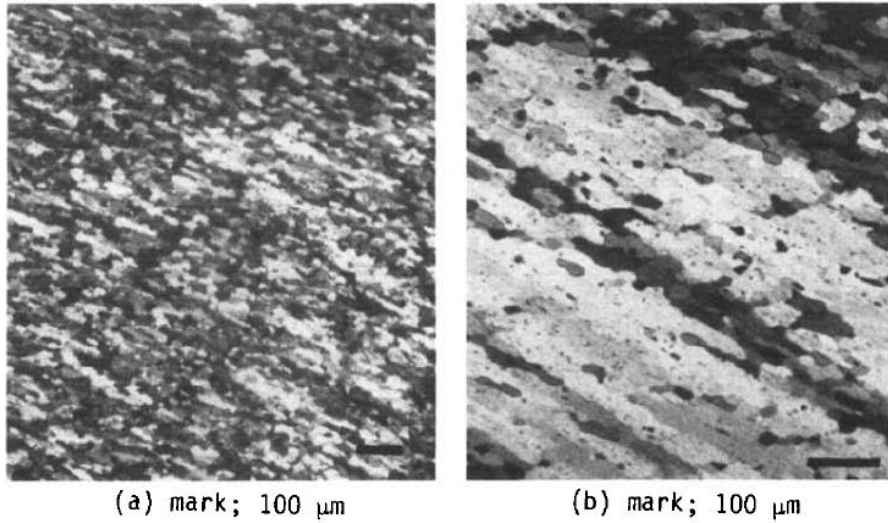
During industrial extrusion of aluminum alloys, the large strains of extrusion together with severe shear deformation arising from friction at the surface can cause the thickness of the original grains to decrease to that of subgrain size and as a result Geometric Dynamic Recrystallization (GDRX) may occur.



**Figure 2-2 (left) Schematic indicating the mechanism of GDRX. By increasing the strain, serrated high angle grain boundaries (HAGBs - bold lines) become closer while the subgrain size (lighter lines) remains approximately constant. Eventually HAGBs contact each other and elongated grains pinch off form small grains [21], (Right) Schematic, illustrating the steps (d) to (e) showing that during large deformation opposite serrations of elongated and thinned grains contact and in three dimensions they perforate and a new grain appears. As deformation continues perforation becomes bigger and produces a group of new grains [22].**

GDRX has been reported in several studies during hot deformation of aluminum and aluminum alloys tested in both torsion and plane strain to strains of 5-60 (aluminum [25, 26], Al-1Mn [29], AA5XXX [30, 28, 31]). GDRX was observed at strains of 3 in plain strain compression [31] and 5.7 in torsion [29]. However to date no one has conclusively shown that it does occur during industrial extrusion operations.

McQueen et al [25, 26] studied the torsional deformation of Al at 400°C over a large range of strains, from 0.5 to 60, for two different initial grain sizes of 100  $\mu\text{m}$  and 2000  $\mu\text{m}$  using POM (Polarized Optical Microscope), SEM, TEM and STEM techniques. For starting grain sizes of 100  $\mu\text{m}$  they observed a structure of equiaxed crystallites (or grains) with a diameter of the measured steady-state subgrain size but the original grain boundaries were not distinguishable in the structure. For the alloy with a starting grain size of 2000  $\mu\text{m}$  after deformation to the strain of 60, the structure consisted of elongated grains with 4-6 subgrains across each. The measured steady-state subgrain size was similar for both initial grain sizes. Figure 2-3 [25] shows the final structure for the aluminum alloys with the two different starting grain sizes. Figure 2-4 [26] shows a graph of the predicted change in grain thickness during torsion testing as a function of strain as well as the measured subgrain sizes for the experiments conducted and the boundary below which GDRX would be expected to occur.



**Figure 2-3 Polarized light micrograph from tangential section of Al at torsional strains of  $\epsilon=60$ , 400°C and strain rate of  $0.2 \text{ s}^{-1}$  for initial grain sizes of: (a) 100  $\mu\text{m}$  and (b) 2000  $\mu\text{m}$  [25].**

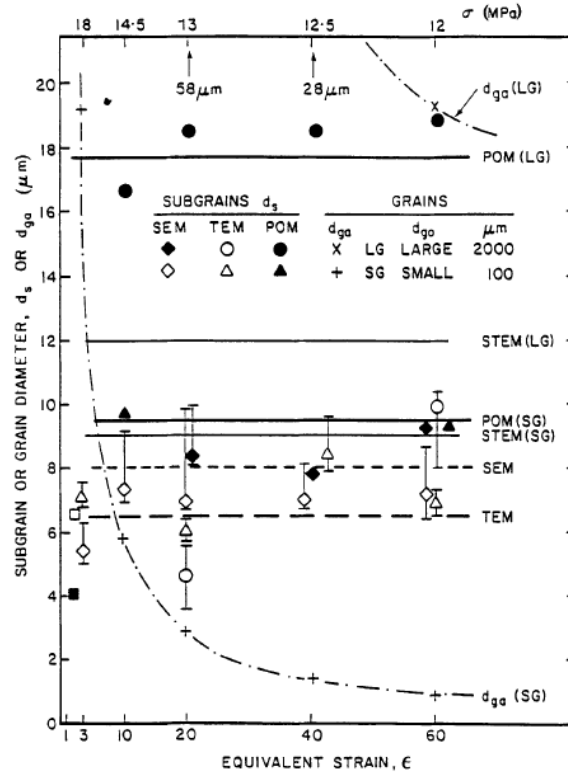


Figure 2-4 Measured subgrain size compared to calculated grain thickness for Al torsionally deformed to strains of up to  $\epsilon=60$  at  $400^\circ\text{C}$  and strain rate of  $0.5 \text{ s}^{-1}$  for two different initial grain sizes [26].

Jazaeri and Humphreys [32] studied the restoration mechanism after large amounts of deformation (rolled up to 98%, strain up to 3.9) for aluminum alloys with different starting grain sizes. The fine grain ( $<5\mu\text{m}$ ) aluminum alloys they studied only exhibited recovery and no dynamic recrystallization was observed. However they did observe grain fragmentation in coarse grain aluminum alloys ( $>50\mu\text{m}$ ) due to formation of deformation bands and micro-shear bands. They concluded that in large scale deformation (high strain) of finer-grained alloys, fragmentation of extremely thinned grains does not play a major role, but a process of dynamic recovery takes place and removes a significant amount of high angle boundaries. This may suggest that other than strain, the minimum initial grain size is another factor that affects the restoration mechanisms during the deformation.

### 2.1.2.3 Dynamic recrystallization (DRX) during extrusion

Although some researchers have suggested DRX can occur during extrusion of aluminum alloys [33, 34, 35] this has not been shown conclusively. A challenge has been separating this dynamic recrystallization mechanism from what may occur statically if the alloy is not quenched fast enough.

Van Geertruyden et. al. [34] observed the equiaxed fine grain structure at the surface of an AA6061 extrusion (Figure 2-5) and mentioned the possibility of GDRX, but there was no experimental evidence to prove conclusively that this was the recrystallization mechanism that had occurred.

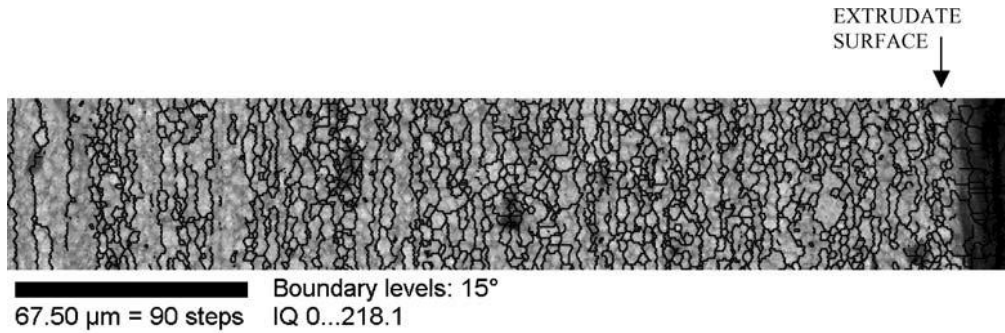


Figure 2-5 OIM micrograph from surface of AA6061 extrudate (black lines represent high angle boundaries) [34].

Parvizian et. al. [36, 37] observed an initial increase and final decrease in grain size in the direction of material flow during the extrusion of 6082 aluminum alloy as shown through EBSD micrographs (Figure 2-6). They explained this phenomena by suggesting the GDRX occurrence. They studied the evolution of High Angle Grain Boundaries (HAGBs) and Low Angle Grain Boundaries (LAGBs) which form the boundaries of subgrains on a partially extruded and quenched billet but there was no definitive experimental evidence that GDRX had occurred.

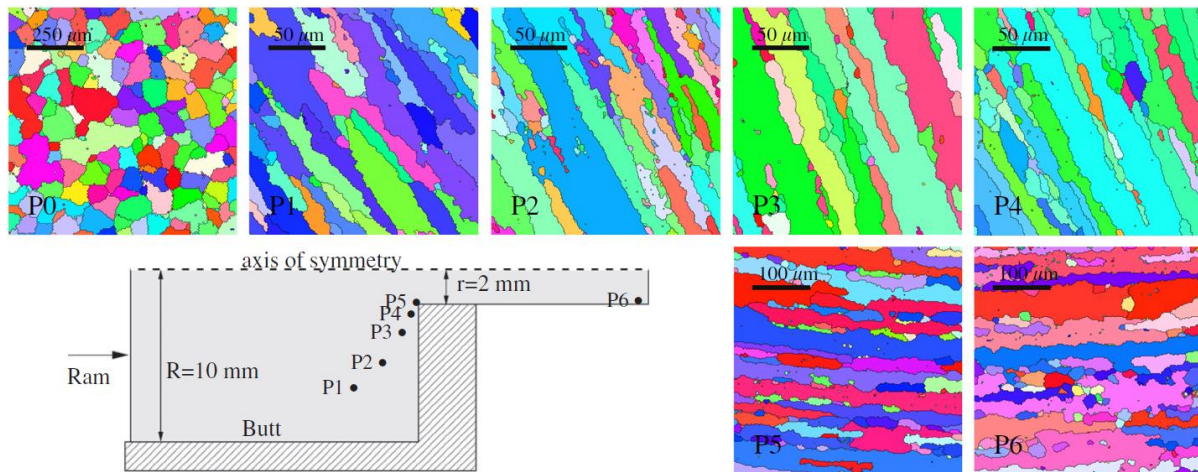
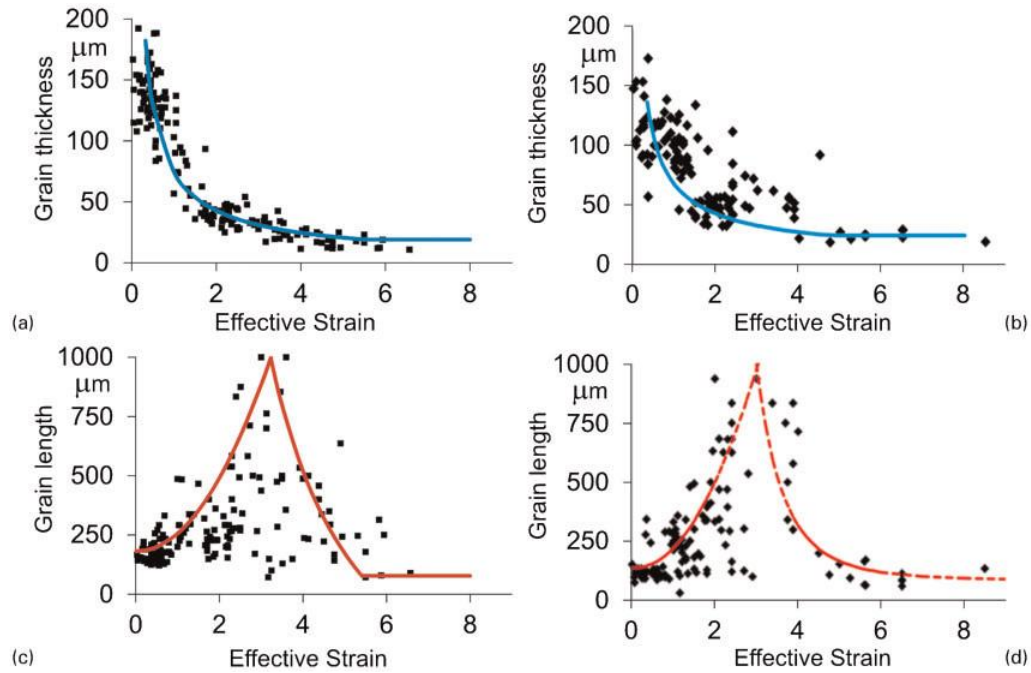


Figure 2-6 Measured Electron Back Scattered Diffraction (EBSD) maps showing High-angle ( $15^\circ$ ) grains in the undeformed material (P0) and other positions in the billet moving closer to the die and in the extrudate [36].

Donati et al. [38, 39] studied the grain shape evolution during the extrusion of 6XXX and 7XXX aluminum alloys by combining FEM simulations with experimental measurements. They defined an analytical model for calculation of grain thickness and length by fitting exponential functions onto curves of measured grain thickness versus model predicted strain (Figure 2-7). Their measurements of the grain thickness showed that after a strain of 3.5-4, the grain thickness reached a size which was 1 to 2x the subgrain size. At this point, the average length of the grains started to decrease rapidly as the strain increased but the average thickness of the grains remained constant. This provides some physical evidence for GDRX. Although their model appears to be able to predict the strain at which the grain pinch-off or GDRX happens, the data points show large deviations from the curves fit with the exponential functions suggesting that changes in the grain shape during deformation are not only related to effective plastic strain but also other parameters need to be considered.



**Figure 2-7** Curve fitting for grain dimensions for various effective strains for AA7020 (a and c) and AA6082 (b and d) [39].

### 2.1.3 Second phase particles

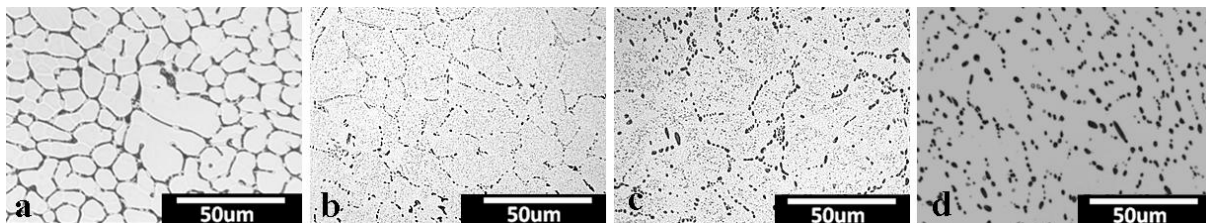
In AA3003 aluminum alloy as-cast material consists of primary aluminum matrix with a network of interdendritic eutectic second phase particles called “constituent particles” with shapes in the as-cast state of rods or plates [40, 41]. These particles have been known to be a mixture of two intermetallic

compounds of  $Al_6(Mn, Fe)$  and  $\alpha - Al(Mn, Fe)Si$  [40]. During the homogenization some  $Al_6(Mn, Fe)$  transforms to  $\alpha - Al(Mn, Fe)Si$  and spheroidization and break-up of rod particles and the eutectic network take place [41]. During the extrusion process, the constituent particles can break-up or experience shape changes due to the deformation conditions experienced.

Due to rapid cooling during the casting process the matrix is super saturated with solute atoms (mainly Mn). So that during the homogenization treatment small precipitates (mostly  $\alpha - Al(Mn, Fe)Si$ ) with the size of  $<100\text{nm}$  nucleate and grow in the matrix [42]. These fine precipitates are called “dispersoids” and have a strong effect on the subsequent microstructural evolution of the material.

The microstructure that evolves during extrusion is very sensitive to the as-homogenized or starting microstructure as well as the extrusion process variables and subsequent cooling history after extrusion to room temperature. The homogenization treatment will dictate the starting microstructure which can be characterized by its average grain size, the volume fraction and average size of the constituent particles and dispersoids and the supersaturation of the aluminum matrix.

Figure 2-8 [43] shows the effect of homogenization conditions on the second phase particle evolution in an AA3003 aluminum alloy. In Figure 2-8b and c the small precipitates are present in the matrix but in Figure 2-8d no dispersoids are distinguishable in the matrix due to a long homogenization time at high temperature; because of the high temperature and long times, the atoms can diffuse over long distances and join the larger constituent particles. As shown in Figure 2-8c there are some particle free zones (PFZ) around the constituent particles that are due to long range diffusion of atoms in the vicinity of constituent particles. Figure 2-9 [42] shows high magnification TEM images of dispersoids in AA3003 aluminum alloy quenched from different temperatures while heating from room temperature to  $600^\circ\text{C}$  with a rate of  $50^\circ\text{C}/\text{h}$ .



**Figure 2-8 Optical micrographs of AA3003 showing second phase particles for different homogenization conditions: a) as-cast; b)  $500^\circ\text{C}$  for eight hours; c)  $550^\circ\text{C}$  for eight hours; and d)  $600^\circ\text{C}$  for 24 hours. Micrographs reproduced with permission from Geng [43].**

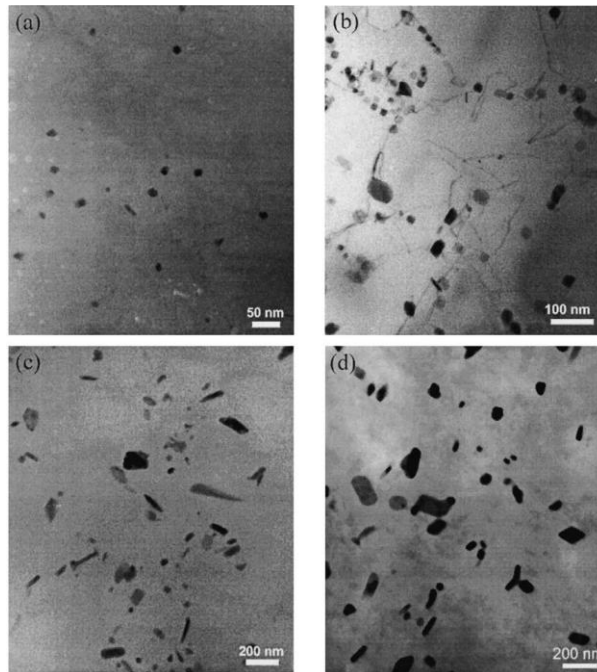


Figure 2-9 TEM images from AA3003 showing how the morphology of the dispersoids changes during heating (a) 350°C, (b) 400°C, (c) 500°C and (d) 580°C [42].

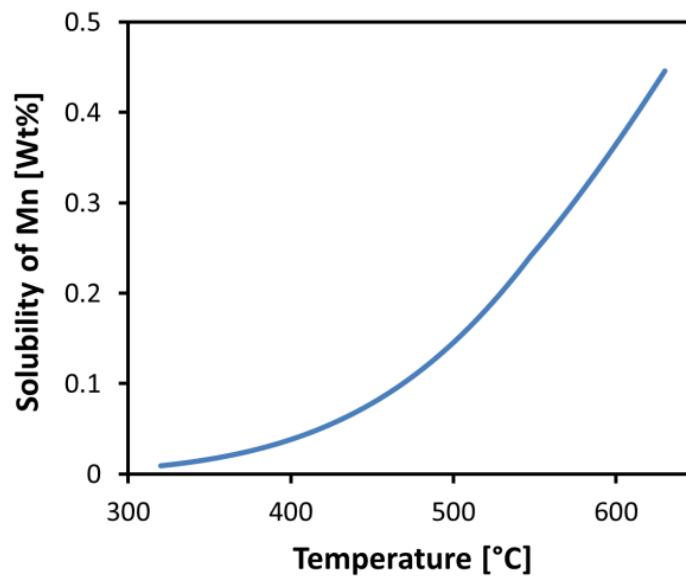


Figure 2-10 Temperature dependent solubility of Mn in Al-1.25Mn-0.5Fe-0.1Si (graph produced using FactSage 6.03 software).

In 3XXX aluminum alloys the Mn solute content varies significantly with temperature (Figure 2-10) so that precipitation and dissolution of second phase particles may occur during each

step of the processing sequence and have a big effect on the microstructure evolution during subsequent steps. For example post homogenization slow cooling rates may result in the growth of large particles (constituent particles) and less solute content in the matrix compared to high cooling rates that can result in a supersaturated matrix in which the dispersoids can precipitate during subsequent pre-deformation heating [44]. The former case is more likely to recrystallize after subsequent deformation as large particles can stimulate nucleation of new grains. On the other hand, fine dispersoids can prevent the nuclei from growing due to Zener drag. The drag pressure for growth of recrystallization nuclei is found to be proportional to  $F/r$ , where  $F$  is the volumetric fraction of the second phase particles and  $r$  is the average radius of the particles [45].

During deformation of two-phase alloys (matrix and particles), the particles affect the overall dislocation density and also the inhomogeneity of deformation in the matrix. However the density and arrangement of dislocations depends on the deformability of the particles during the deformation [21].

McQueen studied the hot working behaviour of different aluminum alloys and found out that the peaks in the stress-strain curve which occur during the deformation are not due to DRX but are attributed to dynamic precipitation and coarsening of precipitates along with DRV [46].

Miroux and coworkers [47] measured the evolution of solute and second phase during industrial processing (hot rolling) of AA3103 alloy. They concluded that during preheating (9 hours at 430°C), the Mn solute content decrease and dispersoids grow and during subsequent break down rolling, the number-density of dispersoids increases significantly. During hot deformation of supersaturated AA3XXX alloys, significant precipitation may occur during recovery which strongly retards the kinetics of recrystallization [48].

Huang et al. [49] investigated the effect of homogenization on recrystallization and precipitation during the thermo-mechanical processing of AA3003 alloy for manufacturing automobile heat exchangers including homogenization, extrusion and brazing. They performed the homogenization at two different temperatures (460°C and 600°C) and found that homogenization at lower temperatures produces finer precipitates which prevents recrystallization after extrusion (at 450°C) but during brazing at high temperature (600°C) a very coarse grain structure would appear due to a low number of recrystallization nuclei.



#### **2.1.4 Peripheral coarse grains and control of grain structure**

A common defect in hot extruded aluminum alloy products is the formation of recrystallized grains at the surface or sub-surface of the extrusion [50, 51, 52, 53]. This is usually called Peripheral Coarse Grains (PCG). An extrudate having this defect includes a layer of coarse recrystallized grains at the surface and unrecrystallized fibrous grains in the core that makes the surface softer than the core. These coarse surface grains degrade the properties of the extrusion such as surface quality, strength, fracture toughness, stress corrosion resistance, fatigue resistance and machinability [50, 51, 54]. So generally an unrecrystallized or fibrous structure is desirable after extrusion and sometimes even after subsequent forming and heat treatment [50].

In cases where uniform mechanical property is of importance, the recrystallized layer must be machined away [51, 55]. So the larger the recrystallized layer, the more material needs to be removed, resulting in a higher yield loss.

Generally several methods can be applied to avoid PCG formation in aluminum alloys: controlling the exit temperature (as low as possible to avoid recrystallization), adding some recrystallization-inhibiting elements such as manganese, sound billet casting with appropriate homogenization and applying the maximum possible extrusion ratio to get the critical strain value for recrystallization [9].

Parson and coworkers [50] studied the effect of ram speed, billet temperature, extrusion ratio and quenching method on grain structure and recrystallization of AA6XXX (Al-Mg-Si) extrusions (Figure 2-11). They concluded that the depth of PCG decreases with higher billet temperature, lower ram speed, higher cooling rate and lower extrusion ratio. Figure 2-12 shows the effect of billet temperature and ram speed on recrystallization and the grain structure of the extrudate.

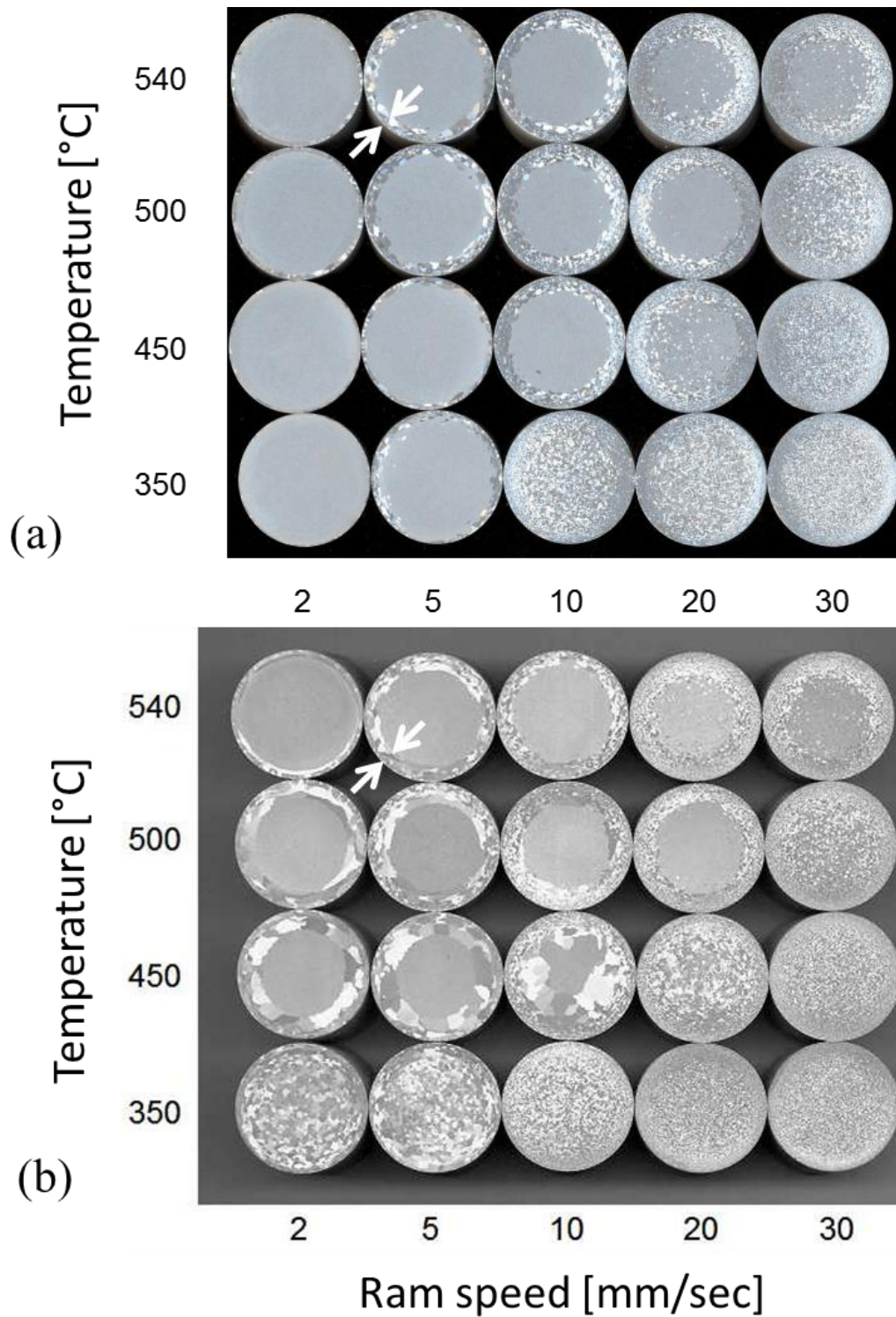


Figure 2-11 Macrostructure of 25mm bar AA6005A extrusion for different ram speeds (mm/sec) on the x-axis and billet temperatures (°C) on the y-axis showing: (a) as extruded and (b) after solution heat treatment [50]. The thickness of PCG is indicated on the picture.

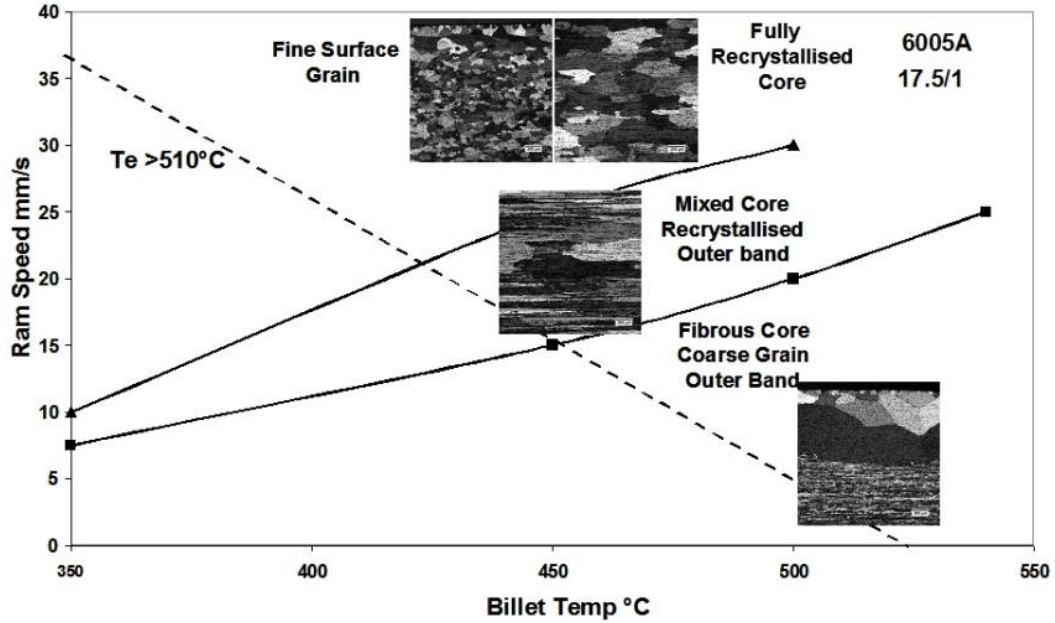


Figure 2-12 Effect of billet temperature and ram speed on grain structure of AA6005A 25mm bars with extrusion ratio of 17.5 [50].

It has been demonstrated that proper die configuration (e.g. choked die aperture) can prevent PCG formation and allow for higher ram speeds [56]. Figure 2-13 shows different die configurations that Duan and Sheppard [57] used in their simulations. Their results showed that during extrusion of a 75mm billet diameter, with an extrusion ratio of 20 and a die land length of  $H=5\text{mm}$ , the best configuration between three cases shown in Figure 2-13 is the one with  $h=3.5\text{mm}$  and  $\theta=10^\circ$  (die c) which results the lowest recrystallization at the surface.

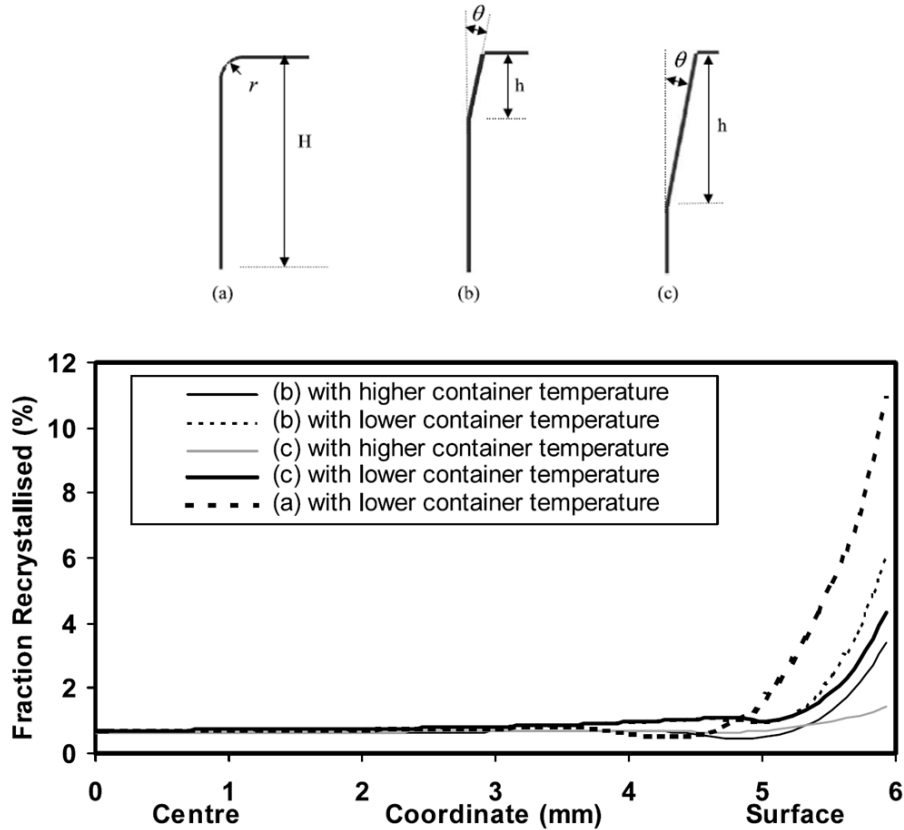


Figure 2-13 Schematic drawing of different die configurations and simulation results for fraction recrystallized [57].

Although, several studies have been made to understand the formation of PCG [50, 52, 53, 58] the mechanism of this phenomenon is still unclear [52].

Van Geertruyden, Misiolek and coworkers [34, 52, 53, 59] have done research on the formation of surface recrystallization in extrusion of aluminum alloys. They believe that abnormal grain growth after the die exit is responsible for PCG formation [52, 53, 34]. Their suggested mechanism includes grain fragmentation (known as GDRX) at the DMZ<sup>1</sup>/shear zone interface followed by very quick grain growth after the material exits the die (Figure 2-14). Figure 2-15 shows the grain structure at the die exit for indirect extrusion of an AA6061 alloy.

Eivani et al. [60] investigated the effect of process conditions on formation of PCG. By combining hot compression and heat treatment they applied thermo-mechanical histories resembling that of peripheral parts of the extrudate. Based on their experiments, high temperature plays the main role in formation of PCG. They found that increasing strain rate would result in finer and more

<sup>1</sup> Dead Metal Zone

homogeneous recrystallized grain structure but very large strain rates result in a significant temperature rise and consequently increase the recrystallized grain size.

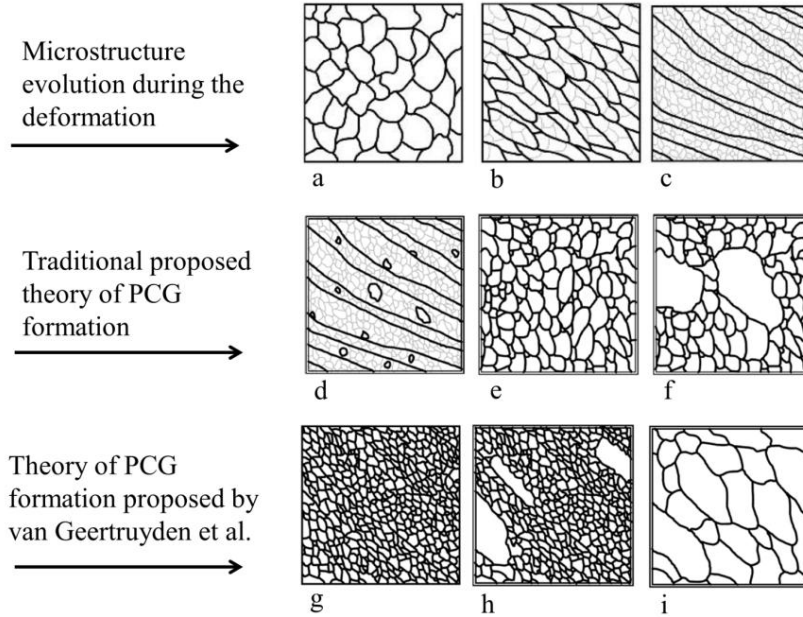


Figure 2-14 Proposed theory for PCG structure formation: (a) through (c) microstructure evolution during the deformation, (d) through (f) traditional theory of PCG formation and (g) through (j) proposed theory of PCG formation based on experimental results. Dark lines represent HAGBs and light gray lines represent LAGBs [53].

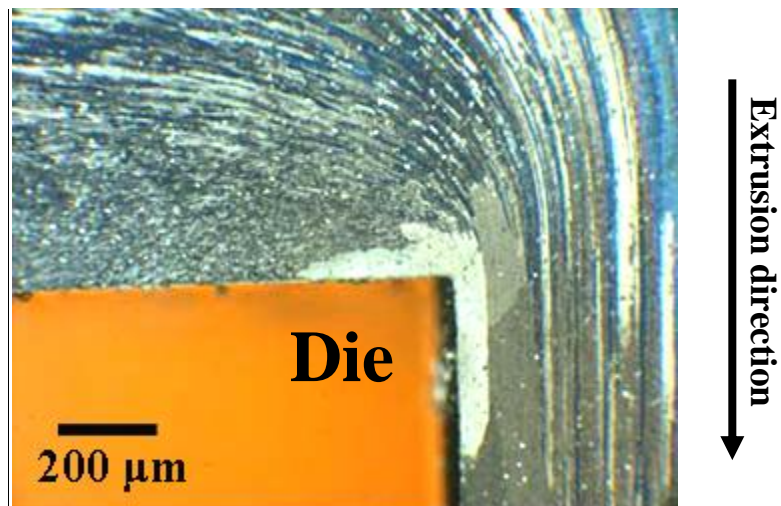


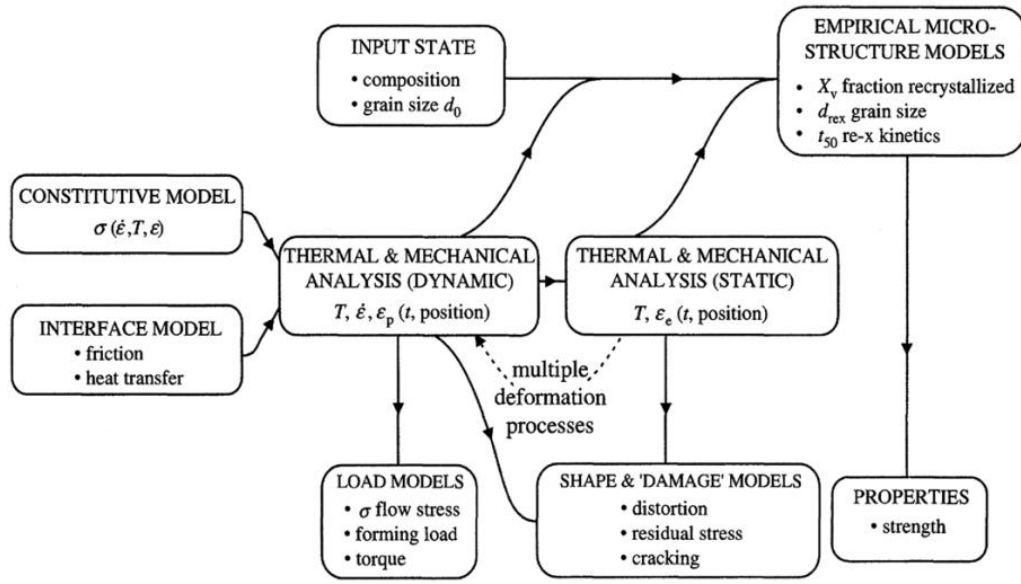
Figure 2-15 Grain structure at the die exit for indirect extrusion of 6061 Aluminum alloy. The billet was quenched 1 min after the ram stopped [34].

## **2.2 Modeling microstructure evolution during hot deformation of aluminum alloys**

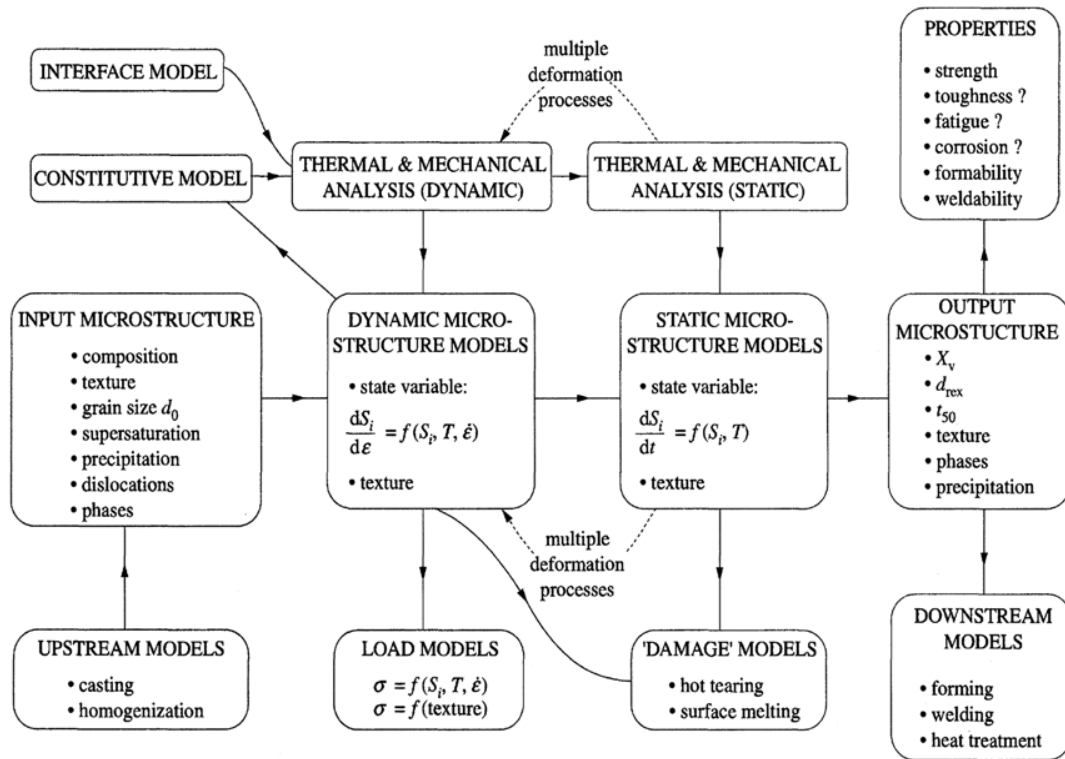
Control of the microstructure, texture and properties of a material during a thermo-mechanical process can be done by the use of quantitative models which are capable of accurately predicting the effect of process parameters on the product [21]. Many different approaches have been presented for modeling of microstructure evolution during and after hot deformation. These include; empirical, state variable, statistical approaches, Monte Carlo methods and Cellular automata methods.

Modeling of microstructure during hot deformation can be done at two levels: At the ‘macro’ level where microstructure models are used for post-processing of thermo-mechanical history, and at ‘micro’ level where microstructure predictions are coupled into the FEM model such that they are used to determine the constitutive behavior of the material during the next time step [61]. Figure 2-16 illustrates the connectivity of sub-models at the ‘macro’ level and the ‘micro’ level for microstructure modeling of thermomechanical processing.

The majority of microstructure models developed for hot deformation of aluminum alloys consider only the dynamic recovery during the hot deformation and static recrystallization after deformation. Preliminary attempts have been made to model recrystallization after extrusion of 2XXX, 6XXX and 7XXX aluminum alloys [51, 57, 54, 52, 55, 58, 53] but, to date, no microstructure models have been developed and validated for extrusion of AA3XXX alloys. However, some research has been done on modeling the microstructure evolution during the rolling of AA3XXX aluminum alloys such as AA3004 [62].



(a) 'macro' level sub-models connectivity



(b) 'micro' level sub-models connectivity

Figure 2-16 Connectivity of sub-models for microstructural modeling at (a) the 'macro' level, and (b) the 'micro' level [61].

### 2.2.1 Empirical models

The empirical models involve using empirical equations (many fitting parameters with no physical basis) to predict the microstructure evolution. In these models, recrystallized grain size and recrystallization kinetics are typically modeled as functions of the Zener-Holloman parameter,  $Z = \dot{\epsilon} \exp(Q_{\text{def}}/RT)$ , as following [63, 64]:

$$d_{\text{rex}} = \alpha d_0^a \epsilon^{-b} Z^c \quad 2-1$$

$$t_{50} = \beta d_0^p \epsilon^{-q} Z^{-r} \exp(Q_{\text{def}}/RT) \quad 2-2$$

Where  $\alpha$ ,  $\beta$ ,  $a$ ,  $b$ ,  $c$ ,  $p$ ,  $q$  and  $r$  are constants and  $d_0$  is initial grain size.

**Table 2-1 Parameters in empirical equations of recrystallization for commercial purity aluminum and Al-1Mg alloy [63]**

Parameter	Commercial purity aluminum (initial grain size 37 $\mu\text{m}$ )	Al-1Mg
$\alpha$	311	435
$\beta$	$4.1 \times 10^{-6}$	$9.8 \times 10^{-6}$
$a$	1	1.3
$b$	0.5	0.39
$c$	-0.33	-0.24
$p$	1	1.35
$q$	1.5	2.7
$r$	0.75	1.1
$Q_{\text{def}}$	220000	230000

### 2.2.2 Physically based state variable models

Physically based state variable models mostly involve explicit incremental calculation of state variables of which the initial values can be measured experimentally [61]. These models quantify parameters such as dislocation density, subgrain size and misorientation to predict flow stress and subsequent recrystallization. The general form of the differential state variable equation for hot deformation is:



$$\frac{dS_i}{dt} = f_1(S_1, S_2, \dots, T, \dot{\epsilon}) \quad 2-3$$

Where  $S_i$  represents the state variables. The flow stress can also be described as a function of the state variables:

$$\sigma = g_1(S_1, S_2, \dots) \quad 2-4$$

Sellars and Zhu [65] developed a model to predict the internal state variable evolution during hot working and subsequent recrystallization parameters of a 5XXX aluminum alloy in both the transient and steady state hot deformation conditions and applied this to rolling.

$$d\rho_r = d\rho_r^+ + d\rho_r^- = \left( C_1 \rho_r^{1/2} - C_2 \frac{\sigma_f}{Z} \rho_r \right) d\epsilon \quad 2-5$$

$$d\delta = \frac{\delta}{\epsilon_\delta \delta_{ss}} (\delta_{ss} - \delta) d\epsilon \quad 2-6$$

$$d\theta = \frac{1}{\epsilon_\theta} (\theta_{ss} - \theta) d\epsilon \quad 2-7$$

Where  $\rho_r$ ,  $\delta$  and  $\theta$  are the density of random dislocations, subgrain size and misorientation, respectively.  $\epsilon_\delta$  and  $\epsilon_\theta$  are characteristic strains that may be related to deformation conditions such as the Zener-Holloman parameter ( $Z = \dot{\epsilon} \exp(\frac{Q_d}{RT})$ ),  $\sigma_f$  is frictional stress and “ss” stands for steady-state. Steady-state subgrain size may be a function of Zener-Holloman parameter [62]:

$$\delta_{ss} = A + B \ln Z \quad 2-8$$

Where A and B are constants. They assumed site saturated nucleation of recrystallization after hot deformation and used Vatne’s [62] model for recrystallization kinetics to calculate the fraction recrystallized and recrystallized grain size:

$$X(t) = 1 - \exp(-X_{\text{ext}}(t)) \quad 2-9$$

$$X_{\text{ext}}(t) = \frac{3}{4} \pi N_V (G \cdot t)^3 \quad 2-10$$

$$t_{50} = C_3 P_D^{-1} N_V^{-1/3} \quad 2-11$$

$$d_{\text{rex}} = A N_V^{-1/3} \quad 2-12$$

$X$  is instantaneous recrystallized volume fraction,  $N_V$  is number density of nuclei,  $G$  is growth rate, and  $P_D$  is driving pressure for recrystallization.

Some research have been done to couple state variable models to FEM predictions to capture dynamic changes in microstructural parameters such as subgrain size and dislocation density [57, 66, 67, 68, 36].

Velay [69] applied a combination of empirical and physical models to a FEM code to study the effect of the feeder plate on the evolution of subgrain size during the extrusion of 2XXX and 6XXX aluminum alloys. He predicted a more uniform substructure in extrusion with feeder plate rather than without feeder plate (refer to Figure 2-22 for the effect of feeder on temperature distribution).

Vatne et. al. [62] developed a physically based state variable model to model the recrystallization of AA3004 aluminum alloy after hot deformation. They observed a good quantitative agreement between their model predictions and experimental measurements for recrystallized grain size and fraction recrystallized.

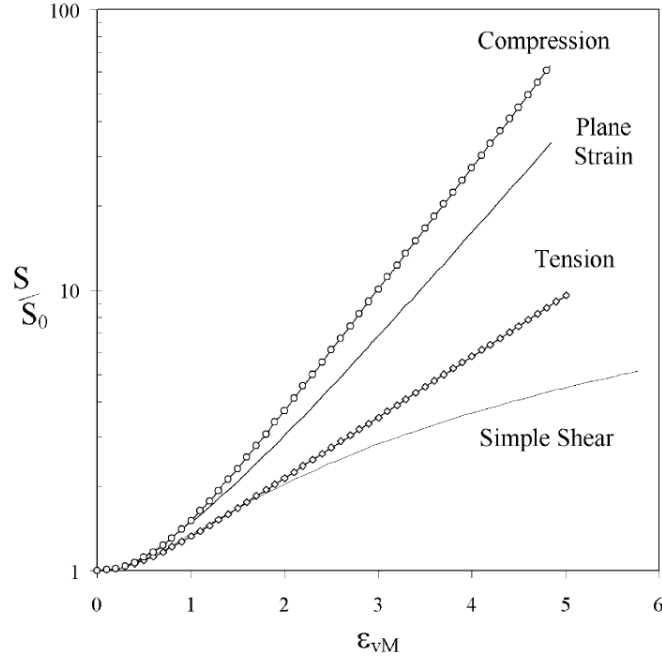
### 2.2.3 Stored energy and driving pressure for recrystallization

During bulk deformation operations such as extrusion, a very small amount of deformation work is stored in the material (<5%) whereas the rest of it is given out as heat [21]. This energy is stored in the material in the form of dislocations and point defects. A significant part of the stored energy is due to the increase in grain boundary area. During deformation, the shape of the grains change and to keep the continuity of material, new boundaries are created. This is done by incorporation of dislocations generated during the deformation into the grain boundaries [21]. The increase of the grain boundary area depends on the mode of deformation (Figure 2-17) [70, 21]. The energy associated with High Angle Grain Boundaries (HAGB) has been measured for different materials and for aluminum was measured to be 324 mJm<sup>-2</sup> [21], a good estimation for dilute aluminum alloys.

The dislocation density can be estimated from mechanical properties such as the flow stress. A rough estimation of dislocation energy ( $E_{\perp}$ ) can be calculated using Equations 2-13 and 2-14. Usually to simplify the calculations, dislocation energy ( $E_{\perp}$ ) is taken to be equal to stored energy ( $E_{\perp}$ ) in most deformation cases:

$$\sigma = C_4 G b \sqrt{\rho} \quad 2-13$$

$$E_{\perp} = C_5 \rho G b^2 \quad 2-14$$



**Figure 2-17** Calculated change in the grain boundary area ( $S$ ) as compared to the original grain boundary area ( $S_0$ ) assuming spherical initial grains as a function of the total strain [70].  $S$  = the grain boundary area of the deformed structure and  $S_0$  = the grain boundary area of the undeformed structure.

Where  $C_4$  and  $C_5$  are constants of the order of 0.5 for a wide range of materials [21]. There are other equations in the literature for estimation of stored energy in dislocations. In the state variable approach, the stored energy ( $E_{\perp}$ ) is usually a function of dislocation density, subgrain size and misorientation as shown in Equations 2-15 [65] and 2-16 [62]:

$$E_{\perp} = \frac{Gb^2}{10} \left[ \rho_i \left( 1 - \ln(10b\rho_i^{1/2}) \right) + \frac{2\theta}{b\delta} \left( 1 + \ln\left(\frac{\theta_c}{\theta}\right) \right) \right] \quad 2-15$$

$$E_{\perp} = \frac{Gb}{\delta} \left[ \frac{\alpha\theta}{4\pi(1-\nu)} \left( 1 + \ln \left( \frac{\theta_c}{\theta} \right) \right) + 0.5C_p^2 \frac{b}{\delta} \right] \quad 2-16$$

Where  $\rho_i$  is the internal dislocation density which consists of two parts, ‘random’ dislocations and ‘geometrically necessary’ dislocations ( $\rho_i = \rho_r + \rho_g$ ).  $\theta_c$  is the critical value of the misorientation angle that distinguish LAGB from HAGB (approximately 15°),  $C_p$  and  $\alpha$  are constants of the order 5 and 3 respectively and  $\nu$  is Poisson’s coefficient  $\sim 0.33$ . Nucleation of recrystallization is affected by the inhomogeneity of stored energy and at a larger scale, the magnitude of stored energy influences the growth rate of the new recrystallized grain. When second phase particles (e.g. dispersoids) are present in the matrix, they can pin the nucleated grain and prevent growth from occurring. This drag pressure from the dispersoids is called “Zener Drag” and is estimated using the following equation [21]:

$$P_z = \frac{3\gamma_{gb}F_v}{2r} \quad 2-17$$

Where  $\gamma_{gb}$  is the energy per unit area of grain boundary,  $F_v$  is the particle volume fraction and  $r$  is average radius of the particle. The growth rate of the recrystallized grain is a function of grain boundary mobility and effective driving pressure [62]:

$$G = M(E - P_z) \quad 2-18$$

Where  $M$  is the mobility of the grain boundary which is strongly affected by temperature.

## 2.2.4 Modeling the grain deformation during the extrusion

Modeling the grain deformation will benefit the microstructure model from two points of view:

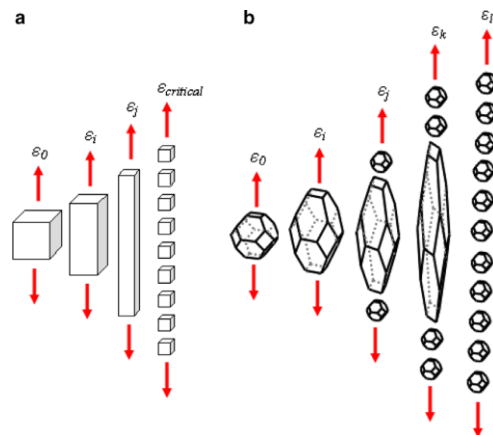
- Calculation of stored energy from grain boundaries: to calculate the stored energy from grain boundaries in deformed material there needs to be the grain boundary area which is calculated using the dimensions of the deformed grain.
- Prediction of geometric microstructural evolutions: tracing the thickness of deforming grain one can predict when the grain thickness reaches that of subgrain and grain starts to split to smaller grains (Geometric Dynamic Recrystallization).

Previously, little work has been done on modelling the grain shape evolution during complex deformation processes such as extrusion however some publications are available on modeling the grain deformation during simple deformation conditions, such as compression, plain strain compression, tension and simple shear.

Bate and Hutchinson [70] calculated the grain boundary area changes of a spherical initial grain for simple deformations including compression, plain strain compression, tension and simple shear. Based on their calculations for all deformation conditions, the grain area increase in spherical grains is more than that of cubic grains. Gil Sevillano et. al. [71] studied the deformation of a cubic grain under different strain states. Singh and Bhadeshia [72] assumed an initial grain shape of truncated octahedron which is more realistic shape for the grains as it is one of the best 3D shapes to approximate a sphere and it fills the space.

De Pari and Misiolek [51] studied the occurrence of GDRX during the hot rolling of AA6061 alloy by modeling the truncated octahedral grain deformation during rolling. Figure 2-18 [51] shows a schematic of grain deformation and GDRX in large strain deformation for two different initial grain shapes.

Donati et al. [38, 39] used regression methods to find the relation between the grain dimensions and equivalent strain that the material experiences during extrusion. They used an FEM simulation to estimate the equivalent strain at the locations that grain size measurements were performed. By embedding their equations into the FEM commercial code DEFORM-2D they captured the history of grain shape evolution during the extrusion. Refer to Figure 2-7 and descriptions for more information on this work.



**Figure 2-18 Representation of grain deformation and GDRX for (a) Cubic grain and (b) Truncated octahedral grain [51].**

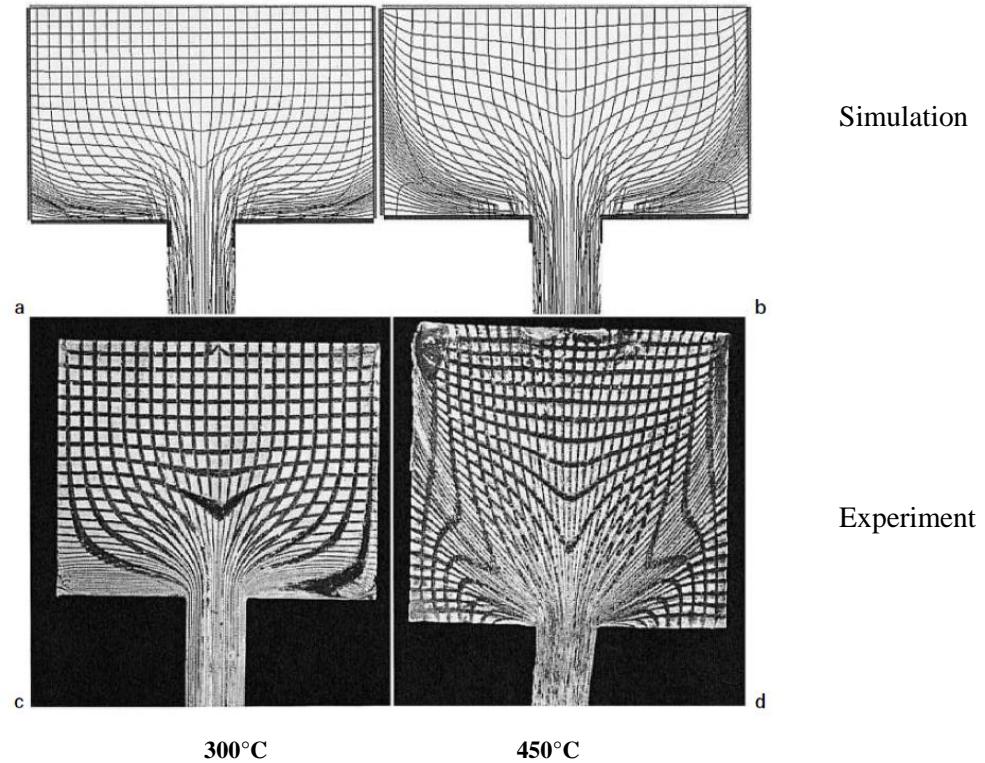
## 2.3 Simulation of the extrusion process

In order to understand the microstructure evolution both during and after extrusion it is necessary to develop mathematical models capable of accurately modelling the thermo-mechanical history experienced at different locations in the billet during extrusion and couple this to microstructure evolution equations.

Modelling of the thermo-mechanical aspects of extrusion are typically based on thermal-mechanical finite element method models [57, 73, 74, 20]. The models require input on the constitutive behaviour of the alloy and the appropriate boundary conditions, in particular the friction and heat transfer at the interface between the working metal and the extrusion press. These techniques are useful for predicting macroscopic process variables such as loads and measured temperatures and also details of the thermo-mechanical history experienced by the material at any position in the extrusion [75].

During the extrusion process, inhomogeneity of deformation can result from redundant deformation and the effects of friction at the interfaces. This can lead to through profile effects such as different recrystallized grain structures at the surface as compared to the center [76, 20, 55, 54, 53, 12, 77, 78, 79, 57]. In addition, the propensity for the material to recrystallize can vary through the profile and is dependent both on the starting microstructure as well as the thermo-mechanical history experienced by the material during extrusion. In order to understand the microstructure evolution both during and after extrusion, it is necessary to develop mathematical models capable of accurately modelling the thermo-mechanical history experienced at different locations in the billet during extrusion and couple this to microstructure evolution equations. Among the mathematical methods, Finite Element Method (FEM) analysis is accepted to be a powerful numerical tool for simulation of metal forming and especially the extrusion process which experiences high levels of plastic strain [75, 80].

In Figure 2-19 [81] the predicted deformation pattern using numerical modeling is compared to experimental results for extrusion of an aluminum alloy (AA2024) at two different temperatures. As observed temperature has a large effect on the deformation pattern and hence on inhomogeneity of deformation. For experimental observations, billets were sectioned along the meridian plane prior to the extrusion and square gridlines were engraved.



**Figure 2-19 Comparison of numerical predictions (a, b) and experimental results (c, d) during extrusion at different starting temperatures [81] (Billet diameter = 75mm, ER = 30)**

Physical modelling methods have been used to either validate the numerical models and/or to better understand the material flow pattern and boundary conditions of the problem. Several techniques have been used to determine the material flow pattern during the extrusion. Some researchers used cheaper and easier to extrude model materials such as plasticine and wax [82, 83] while some others used the real material [81, 84, 85]. Mostly two techniques were used: layers of different colors in case of plasticine and grid-pattern techniques.

Using grid-pattern technique, Valberg [85] could accurately model the flow pattern over the whole volume of the billet and extrudate for the extrusion of AlMgSi1 alloy. He put indicator pins of different material (AlCu2.5) in horizontal and vertical holes which were drilled into the billet and traced them in the extruded material. Based on his results he suggested that a very thin layer of the material at the surface of the extrudate (in his case 50  $\mu\text{m}$  for an extrusion ratio of 40 with billet diameter of  $\sim 100$  mm) comes from a region in the dead metal zone where he called it co-extrusion zone in his later publications [86].

Schikorra et. al. [84] also used the grid-pattern technique similar to that of Valberg [85] and they found that the surface of the billet completely sticks to the container during the whole extrusion until the ram sweeps it off the container.

### 2.3.1 Constitutive equations for hot working

One of the main challenges in thermomechanical modeling of the extrusion process is determining the constitutive relationship for the material. A common expression used is based on the hyperbolic sine relationship as shown in Equation 2-19 [87].

$$A(\sinh \alpha\sigma)^n = \dot{\epsilon} \exp(Q_{HW}/RT) \quad 2-19$$

Where  $n$ ,  $\alpha$  and  $A$  are constants and  $Q_{HW}$  is the activation energy for hot working or activation energy for thermally activated creep. Kocks and Chen [88] developed a physically based constitutive equation for cubic metals that is based on the effect of solute atoms on the stress required for moving dislocations as shown in Equation 2-20:

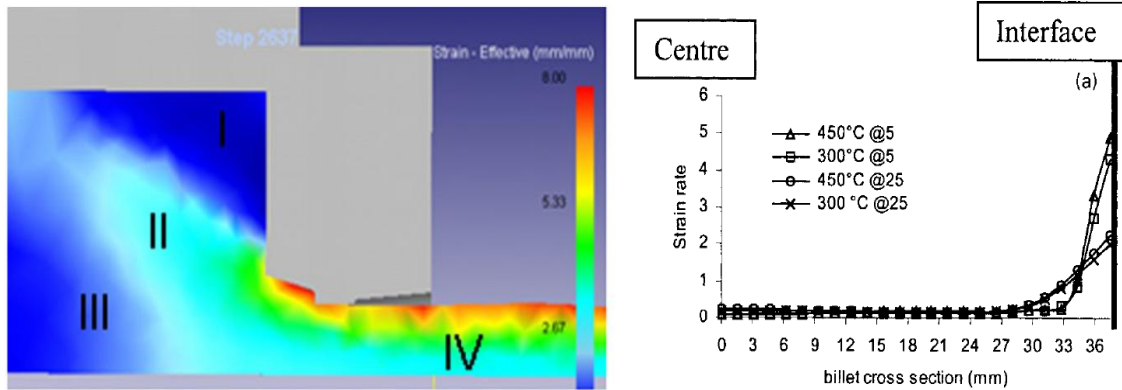
$$\dot{\epsilon} = A \left( \frac{\sigma}{\mu} \right)^n \frac{\mu b^3}{kT} \exp\left(-\frac{Q_d}{RT}\right) \quad 2-20$$

Where  $\mu$  is the shear modulus,  $b$  is Burger's vector,  $k$  is Boltzmann constant and  $Q_d$  is activation energy for self-diffusion of diffusing species.

### 2.3.2 Thermomechanical modeling and FEM analysis of extrusion

Much work has been done on thermomechanical modeling of extrusion of aluminum alloys (including 1XXX, 2XXX, 5XXX, 6XXX and 7XXX alloys) and the most work has been done on AA6XXX [89, 82, 73, 74, 90, 91, 92, 93, 94, 79]. The main purpose of the majority of thermomechanical models was to determine the spatial and temporal distribution of temperature, strain and strain rate. In Figure 2-20 model predictions of strain and strain rate during extrusion of some aluminum alloys are shown.





**Figure 2-20 Predicted distribution of strain (left) [95] and strain rate (right) [81] during the extrusion process for 6XXX aluminum alloys.**

Temperature is one of the most important parameters in extrusion [73]. Temperature changes during extrusion determine the surface quality and properties [89] and also temperature has a large effect on friction, heat transfer, flow stress and the extrusion load [73]. Heat transfer is affected by the temperature difference between billet and tooling and also the material thermophysical properties change with temperature.

Sheppard [89] compared various methods for calculation of temperature in extrusion of aluminum alloys and studied the effect of extrusion parameters such as extrusion ratio and velocity on this variable. To get a realistic distribution of temperature, heat generation by deformation and friction and heat transfer between billet, tooling and atmosphere must be considered (Figure 2-21).

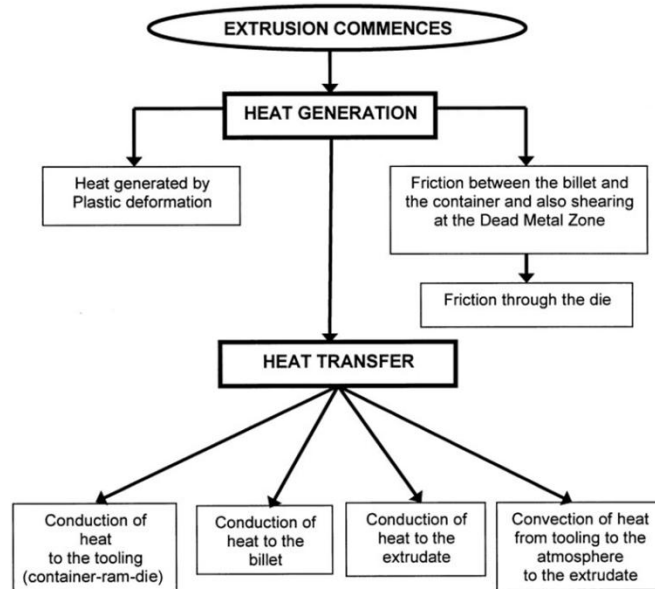


Figure 2-21 Heat balance in the extrusion process [73].

By thermomechanical modeling of hot extrusion of aluminum alloys, Velay [69] showed that temperature distribution would be more uniform with a feeder (Figure 2-22).

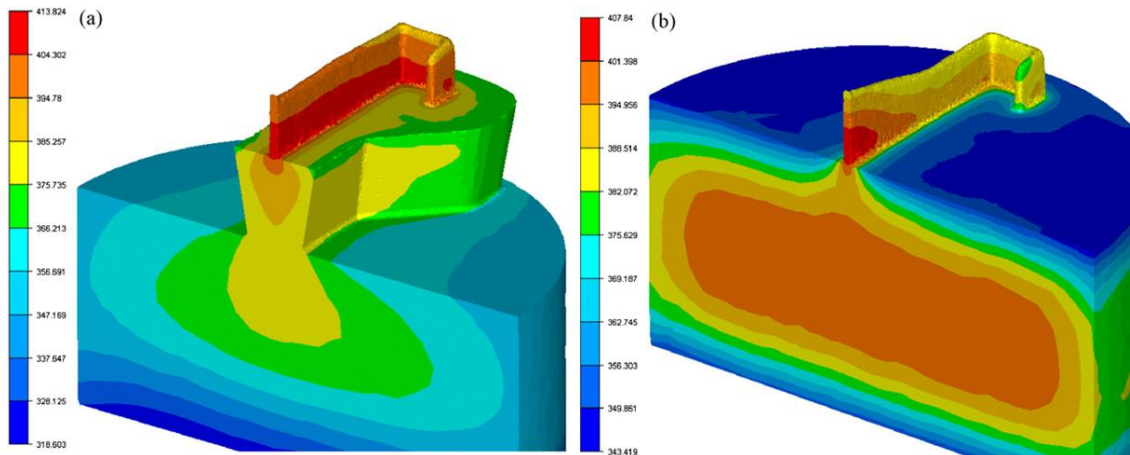
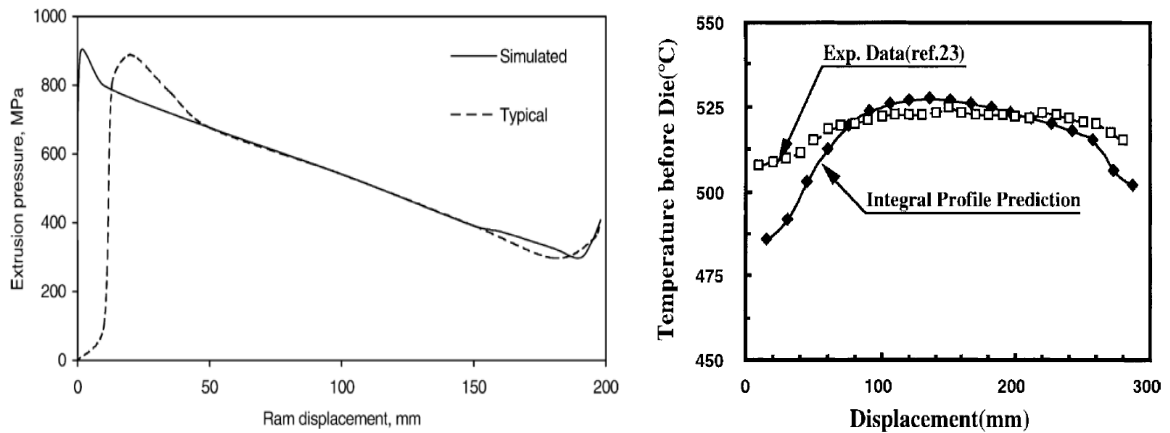


Figure 2-22 Temperature distribution (a) with the feeder plate and (b) without the feeder plate [69].

Two important parameters in modeling of hot extrusion include: the heat transfer coefficient (HTC) and friction factor. Different values have been chosen by different researchers [57, 74]. The value of HTC has usually been considered to be in the range of 11-25 kW/m<sup>2</sup>°C. In hot extrusion of aluminum alloys, the friction between the billet and container is usually modeled using an interface shear factor ( $m$ ) with values ranging from 0.6~1 [57, 92, 81, 74]. Friction between the billet and ram,

is usually modeled using  $m=0.3\sim 0.7$  [74, 57], as a lubricant is usually applied on the bottom of billets (such as graphite).

Experimental validation of thermomechanical models for extrusion has been done primarily on three aspects: load-stroke curve, temperature changes and deformation pattern. Figure 2-23 shows some experimental validation of extrusion load and temperature change. An example of experimental validation for deformation pattern is shown in Figure 2-19.



**Figure 2-23 Validation of modeling results with experimental measurements. (left) Load-stroke curve [79], (right) Temperature change before die for AA7XXX aluminum alloys [89]**

There has been much research done on modeling the extrusion of aluminum alloys using commercial FEM packages [92, 90, 54, 73, 77, 79]. There are several commercial FEM codes such as DEFORM<sup>TM</sup>, FORGE<sup>TM</sup> and Q-FORM<sup>TM</sup> that have been developed for modeling of metal forming processes [75]. Among them, the DEFORM code is relatively popular and has been used by numerous researchers for simulation of extrusion of aluminum alloys [54, 12, 80, 75, 52].

Important issues in a FEM code are: deformation description, solution procedure, selection of the type of flow formulation, application of material models, and re-meshing [75]. Deformation can be described in three formulation methods; Lagrangian Formulation in which FEM mesh is attached to the deforming body, Eulerian formulation where the mesh is fixed in space and the material flows through the mesh, and Arbitrary Lagrangian-Eulerian (ALE) that is somewhere between the above two methods [80, 75]. Normally the Lagrangian approach is suitable for transient-state problems like the break-through in extrusion and the Eulerian and ALE method is better for analyzing steady-state problems such as the rolling process. Due to the transient state of the extrusion process, the Eulerian

method is not an appropriate approach so that the Lagrangian method must be used in which the elements move and deform with the material. Due to the large amount of deformation accompanied with the extrusion, elements in the deformation zone undergo huge deformation and remeshing is needed frequently depending on the mesh and step size.

Sheppard et. al. [90, 57, 96, 91] have applied the finite element method to study the interactions between die design, forming parameters (i.e. ram speed, container temperature, billet temperature and extrusion ratio) and the product quality (extrudate shape, surface condition and microstructure) by the use of commercial FEM codes FORGE2<sup>®</sup> and FORGE3<sup>®</sup>.

Boncheva et. al. [92] used the finite element code MARC to simulate extrusion of a 2XXX aluminum alloy. They linked the thermomechanical model with a microstructure model to predict the microstructure evolutions during the cooling. They determined optimum preheat temperature, extrusion velocity and cooling rate to get favorable product quality but they did not experimentally validated their microstructural predictions such as fraction recrystallized and grain size evolution.

## **2.4 Material flow in extrusion and internal defect formation**

Prior to extrusion, billets are typically Direct Chill (DC) cast, cooled to room temperature and then reheated so that a homogenization heat treatment can be performed. The as-cast billet microstructure is typically not uniform and the surface of the billet (its skin) often contains coarse intermetallic precipitates and oxide particles [97]. During the extrusion process, sticking friction usually occurs between the billet and container which results in inhomogeneous flow of material towards the die, such that the center of the billet flows towards the die faster than the billet surface [98, 12]. This causes the surface of the billet to accumulate in front of the dummy block and eventually flow towards the center and finally this original billet surface material flows into the central parts of the extrudate. This is called the “back-end” defect and usually happens in the last third of the extrusion stroke [99, 100]. Figure 2-24 shows a schematic view of the back-end defect formation during extrusion as well as an image showing the cross section of a round bar extrusion which contains back-end defect. When extruding more than one billet, the extrusion is stopped before the back-end defect can occur, the remaining part of the billet is sheared off and a new billet is loaded into the container. The two billets then butt up against each and they essentially become “welded” together as the extrusion continues and the billet surfaces are forced together. In this billet-on-billet extrusion process, which is often used in modern aluminum extrusion plants as a means to maintain continuous production, transverse welding of the two billets can occur; the billet surfaces are forced together

under high pressure as the ram pushes them towards the feeder and into the die. Due to the material flow pattern, as the billet enters the feeder and die, the interface (transverse weld) between the billets does not remain flat and can manifest itself on the extrudate as a clad surface layer [97]. Figure 2-25a shows the schematic of formation of transverse weld and Figure 2-25b is an image from a longitudinal section of a round bar extrudate showing the shape of front portion of transverse weld.

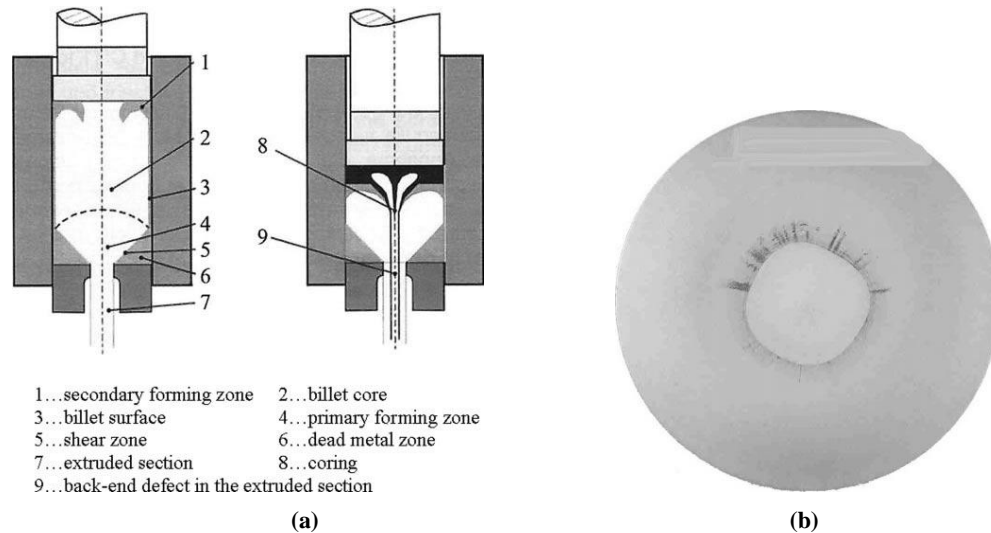


Figure 2-24 (a) Schematic of back-end defect formation [18], (b) cross section of extrudate containing back-end defect [100].

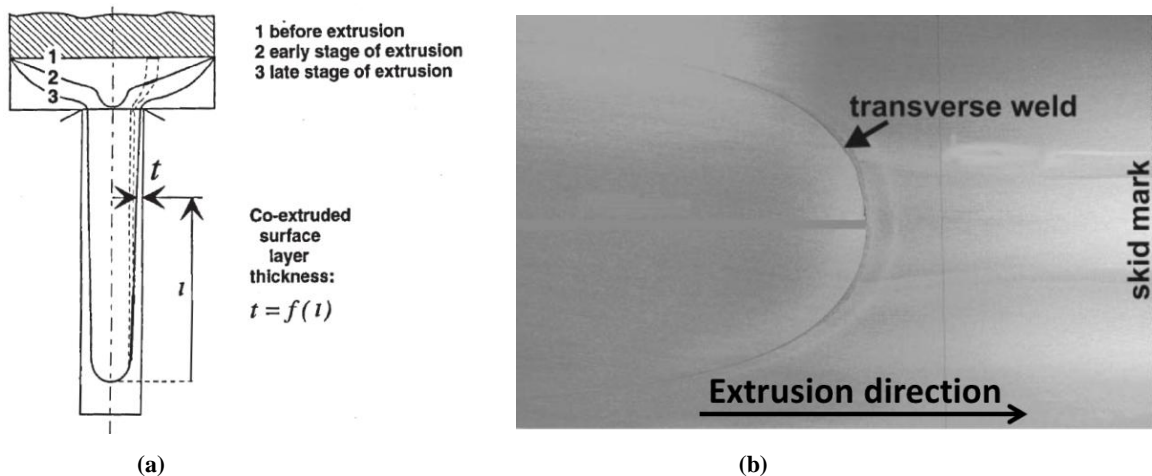


Figure 2-25 (a) Schematic of the transverse weld formation [86], (b) Longitudinal section of extrusion showing the front of the transverse weld [100].

One of the main objectives in continuous billet-on-billet extrusion is to minimize the transverse weld interface length while at the same time providing a weld strong enough to withstand the stretching process. It has been shown that the transverse weld length depends on how fast the material from the old billet flows out at the die corners [101]. Consequently, the geometry of the feeder and die can significantly affect the length and thickness of the transverse weld in the extrudate [100, 102].

Hatzenbichler and Buchmayr [100] used the commercial code DEFORM to study the effect of process parameters on the length of the transverse weld defect and the back-end defect. Based on their simulations, the friction between the billet and the pad has the most effect on the length of the back end defect but the effect of the friction conditions on the length of transverse weld is not significant. They defined the length of the transverse weld to be the distance from skid mark (stop mark) to the section at which the clad thickness is 0.5mm, but experimental results by Jowett et al. [102] confirms that the transverse weld continues to much longer distances (refer to Figure 2-26).

Jowett et al. [102] measured the thickness of the transverse weld along the extrudate for different feeder geometries and they found that the thickness of the clad layer is proportional to (extruded length)<sup>-1.5</sup>. Figure 2-26 [102] shows the measured clad thickness along the extrudate in a log-log scale graph. The extruded profile is a stepped flat shape with wall thicknesses of 1.5, 3 and 4.5 mm from one side to the other side of the cross-section. The different colours correspond to the clad thickness along different sides of the profile.

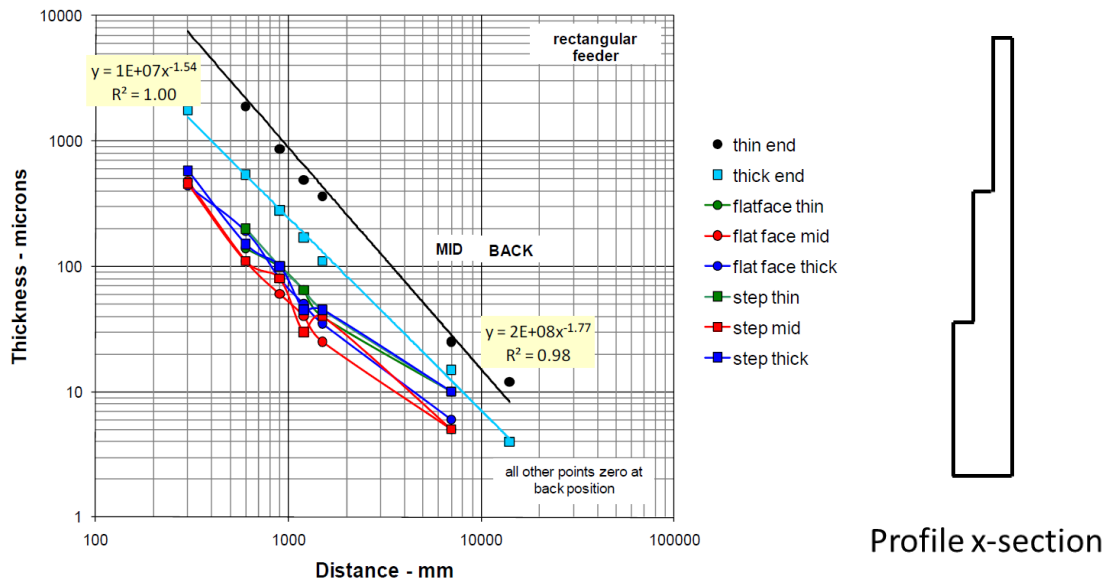


Figure 2-26 (left) Thickness of transverse weld along the extrusion, different colored lines show the clad thickness at different sides of the profile [102], (right) profile x-section.

## **2.5 Summary**

Although much research has been done to model the microstructure evolution during extrusion of aluminum alloys for AA2XXX, AA6XXX and AA7XXX, there is a lack of literature data and research on the microstructural evolution and modeling for extrusion of AA3XXX. A key aspect in predicting the microstructure evolution is accurate representation of the deformed microstructure including the stored energy in the material as well as the shape and distribution of the deformed grains and precipitates in the matrix.

Although the deformed grain shape and how it evolves during the extrusion process and hence the propensity for GDRX to occur has been studied by a few researchers, there is a need for more accurate models and more conclusive validation in this area.

Comparing recent works on simulation of transverse weld formation in billet-on-billet extrusion with experimental results indicates that simulations are underestimating the length of transverse weld. So that there need to be more accurate models to get better estimations of the length and thickness of the transverse weld.

## **Chapter 3**

### **Scope and objectives**

Rio Tinto Alcan, one of the world's largest aluminum billet suppliers produces value added products for the automotive industry, such as heat exchangers made from AA3XXX aluminum alloys. In order to satisfy the customers with their requests for specific properties and microstructure, there needs to be a good understanding of the effects of process parameters and alloy composition on the final product. A collaborative research and development project was initiated between Rio Tinto Alcan, the University of Waterloo and the University of British Columbia to develop a through-process model for the manufacturing of AA3XXX heat exchangers. This process route includes: casting, homogenization, extrusion, cold deformation, annealing and brazing. This research has focused on the extrusion process and I have simulated what occurs during extrusion of AA3XXX aluminum alloys including the microstructure changes that occur in the deformed state and how they vary spatially in the product (extrudate). In this work the main objective is to develop, validate and apply a quantitative model to study the effects of initial microstructure and process parameters on the microstructure evolution during and after the extrusion process for AA3XXX aluminum alloys. The initial microstructure is mainly affected by alloy composition and homogenization conditions. During extrusion, the process parameters of interest are extrusion temperature, ram speed and extrusion ratio as well as the die geometry.

The modeling has been done by using a commercial FEM code DEFORM in conjunction with calculations for the stored energy and grain shape evolution to predict the evolution of the microstructure of the deformed state during extrusion. The main contribution of this work is to develop an understanding of the inter-relationship between the starting microstructure, extrusion process variables and final microstructure in the extrudate. Figure 3-1 shows a schematic presentation of the extrusion process and the list of microstructural changes and parameters of interest in this work.

In addition, the validated model was also used to understand and quantitatively predict the formation of the transverse weld defect during billet-on-billet extrusion and how it is influenced by the extrusion conditions as well as die geometry.

Validation of model predictions was performed at two levels: thermo-mechanical validation using experimental data measured during extrusion trials that were performed at Rio Tinto Alcan's



Jonquiere facility and microstructure characterization of the extruded samples produced via the extrusion trials.

Although some research has been done to model the microstructure during extrusion of aluminum alloys AA2XXX and AA6XXX, no work has been published on the microstructure evolution during extrusion of AA3XXX alloys.

The detailed objectives of this work are summarized below:

- Develop and validate a FEM model of the extrusion process for AA3XXX aluminum alloys.
- Development and validation of microstructure models for AA3XXX alloys that can be used to predict microstructure evolution of the deformed state during extrusion.
- Investigate the effects of extrusion parameters (billet temperature, extrusion ratio and ram speed) and starting microstructure on microstructure evolution in the extrudate.
- Model the material flow pattern and the formation of the transverse weld and the effect extrusion process parameters and die geometry have on its length and thickness.

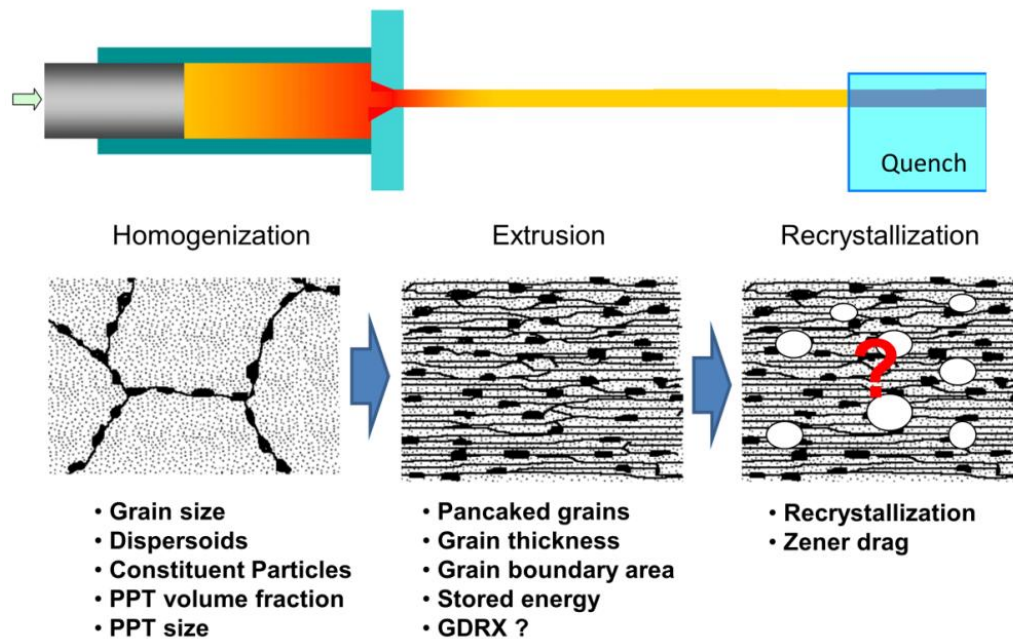


Figure 3-1 Microstructural changes and parameters of interest during each step of extrusion.

# Chapter 4

## Methodology

In this research, a mathematical model of the deformation and microstructure evolution was developed and validated for AA3003 aluminum alloy during hot extrusion.

To support the mathematical modelling work, a series of extrusion trials were done using the instrumented extrusion press at Rio Tinto Alcan's Arvida Research and Development Center (ARDC) in Jonquiere, Quebec.

### 4.1 Experimental

#### 4.1.1 Extrusion trials

Extrusion trials were carried out using cylindrical billets with 101.6 mm diameter and 200-400 mm length, DC cast at Rio Tinto Alcan and homogenized using a Carbolite™ (HRF) circulating air furnace at ARDC. Table 4-1 shows the chemical composition of the AA3003 alloy used for billets.

**Table 4-1 Chemical composition of the AA3003 alloy used for the billet material**

<b>Element</b>	<b>Mn</b>	<b>Fe</b>	<b>Si</b>	<b>Ti</b>
<b>Wt%</b>	1.27	0.54	0.10	0.02

Different homogenization treatments were given to the as-cast AA3003 billets so that the effect of starting microstructure on the microstructure evolution during extrusion could be assessed. In total, three different homogenization treatments were used to provide a large variation in starting structure: 500°C for 8 hours (8H500), 550°C for 8 hours (8H500) and 600°C for 24 hours (24H600), as shown in Figure 4-1. In all cases the heat up rate was 150°C/h up to 50°C below the soaking temperature. For the last 50°C a heating rate of 50°C/h was employed and the billets were water quenched after the hold period.

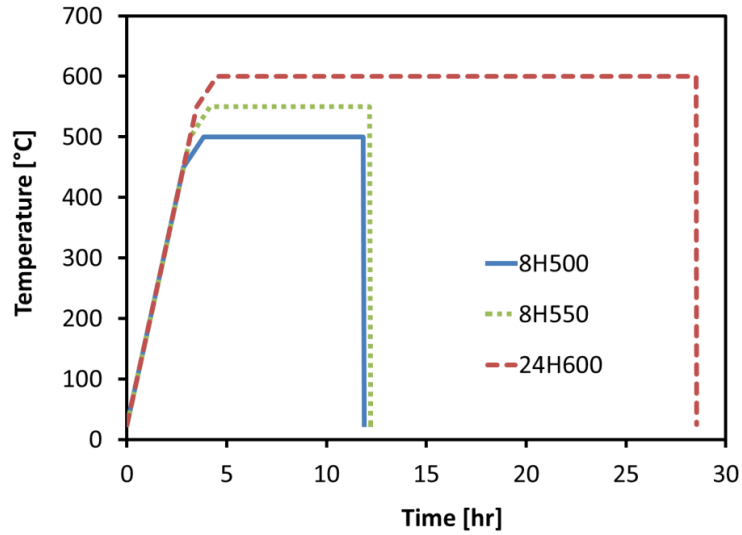


Figure 4-1 Temperature profiles for homogenization treatments.

Figure 4-2 [43] shows the optical micrographs for the starting microstructure of the as-cast billet as well as the homogenized billets exposed to different soak conditions. The as-cast microstructure shows a cellular dendritic structure with a eutectic containing constituent particles, while the homogenized billets show breakup of the eutectic constituent particles and some precipitation of dispersoids. Figure 4-2d shows that after 24 hours at 600°C there are almost no dispersoids remaining in the matrix [43].

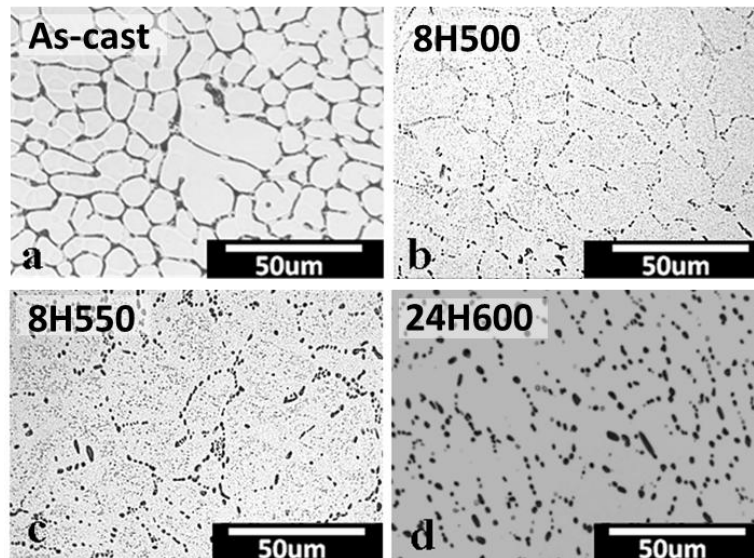
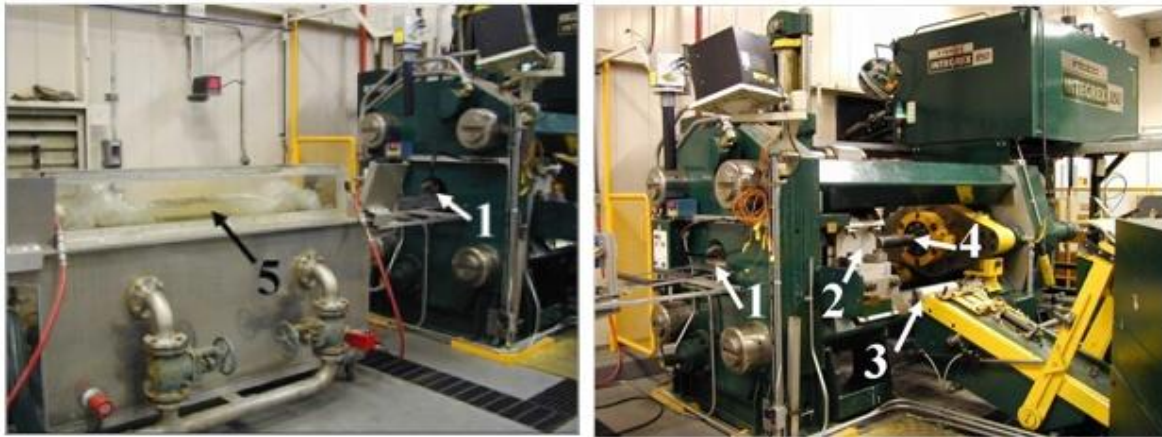
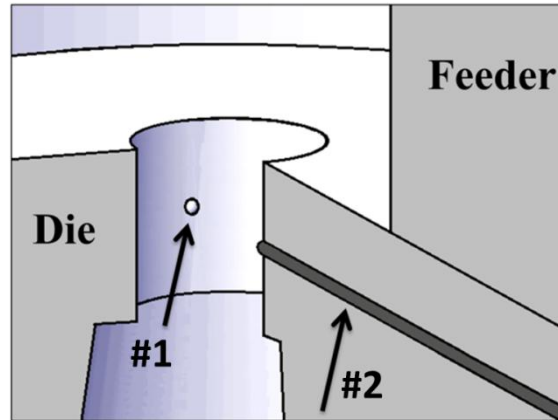


Figure 4-2 Microstructure of billets for different homogenization conditions: (a) as-cast, (b) 500°C for 8 hrs, (c) 550°C for 8 hrs and (d) 600°C for 24 hrs. Reproduced with permission from Geng [43].

Figure 4-3 shows Rio Tinto Alcan's state-of-the-art research extrusion press that was used for extrusion trials. This is a 780 tonne direct extrusion press with a 106 mm diameter container. The press is fully instrumented such that most parameters can be measured and recorded during the extrusion process. The main ram position is measured using a Baluff digital position transducer and this information is used to calculate extrusion speed. Extrusion force is determined by the hydraulic pressure acting on the main and side cylinders. Billet temperature is accurately measured by three contact thermocouples located on the billet loading clamp. The container liner contains 12 thermocouples in holes drilled through the container liner such that they touch the liner surface. For the experimental trials two stainless steel sheathed thermocouples were positioned inside tight fitting holes spark eroded laterally through the sides of the die plate and emerging at the mid length position on the bearing. Figure 4-4 shows the location of these thermocouples in the die bearing.



**Figure 4-3 Rio Tinto Alcan's state of the art extrusion press (1- extruded strip exits here, 2- billet position for extrusion, 3- mechanical billet loading system, 4- ram, 5- Water quench unit).**



**Figure 4-4** Location of thermocouples at the middle of bearing length to record the exit temperature at the surface of extrudate.

At the end of the extrusion of each billet, the final temperature of the extrudate was manually measured at two locations using a two prong contact thermocouple; (1) immediately after the die exit and (2) after the quench unit (The locations of these measurements are indicated in Figure 4-7 as “Manual TC”). These measurements were then used to estimate the heat transfer rate in the standing wave quench.

Homogenized billets were rapidly preheated to extrusion temperature in an induction furnace with a heating rate of  $\sim 30^{\circ}\text{C}/\text{sec}$  and then moved by the mechanical loading system to the billet position in the press. To compensate the temperature drop during the loading, the billets were preheated up to  $10^{\circ}\text{C}$  above the extrusion temperature and each billet spent 2 to 6 minutes in the preheat furnace, based on the billet length and ram speed used for the previous billets. Then the billets were pushed into the container by the ram and extruded through the die. After exiting the die, the extrudate enters the water circulated quench bath to retain the as-extruded microstructure.

Three series of extrusion trials were carried out using two different die geometries; I-beam and round bar extrusions (Figure 4-5). In the first two series of trials the objective was to study the effect of extrusion conditions and starting microstructure on microstructure evolution during extrusion. The last trial was done to measure the transverse weld defect on round bar extrudate and how it was affected by the die geometry. For the first two trials, the range of extrusion conditions studied included the extrusion temperature ( $350\text{-}550^{\circ}\text{C}$ ), extrusion ratio (17-280), ram speed (2-32 mm/sec). In total 29 billets were run under a number of different extrusion conditions. Table 4-2 shows the range of conditions tested during the extrusion trials with these billets.

Table 4-3 show the trials conducted to measure the transverse weld. All these trials were performed with billet temperature of 450°C, ram speed of 20 mm/sec and extrusion ratio of 70. Different alloys were used for alternative billets to get better contrast between the transverse weld and the extrudate after etching. Extrusion trials with tapered feeder were performed to investigate the effect of feeder geometry on the length of the transverse weld. While this type of geometry is not commonly used for aluminum extrusion, it was selected to impose a major change in the material flow during extrusion. The maximum inner diameter of the tapered feeder was 60 mm (equal to the diameter of regular feeder) and its exit diameter was 12.7 mm (the same as the die diameter). In both cases, the feeder depth was 25.4 mm. Figure 4-6 provides a schematic of the two feeder geometries used.

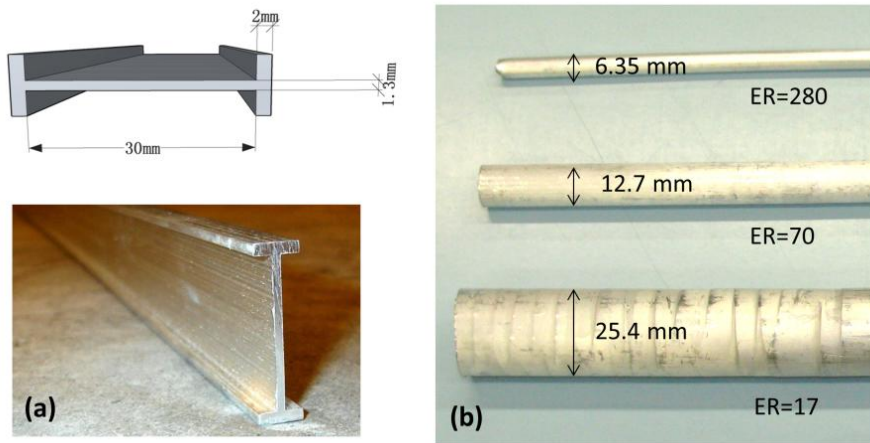


Figure 4-5 Picture of the final extrudate shape from the two extrusion dies used in the trial: (a) I-beam extrudate [43] and (b) round bar extrudate.

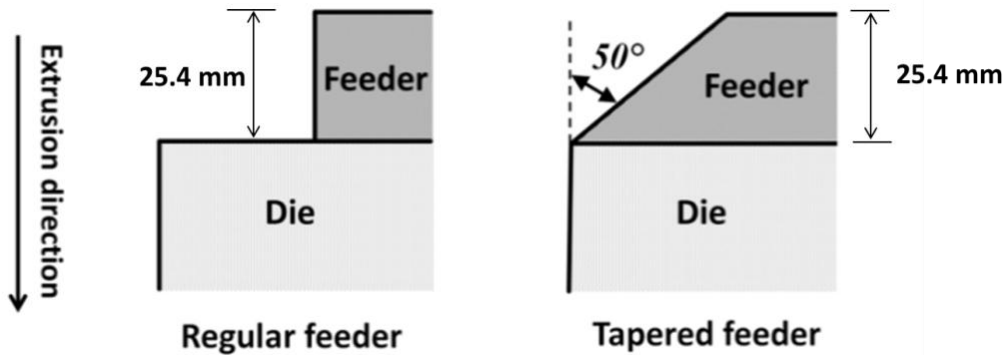


Figure 4-6 Schematic of two different feeder geometries.

**Table 4-2 Range of extrusion conditions studied during extrusion trials.**

Extrusion Parameter	Round bar			
	I-Beam			
Extrusion ratio	130	17	70	280
Temperature (°C)	400, 550	400, 500	350, 400, 500	400, 500
Ram speed (mm/s)	14	8	2, 8, 32	2,8
Billet length (mm)	200	400	200	200
Homogenization	550°C for 8 hours	550°C for 8 hours	500°C for 8 hours 550°C for 8 hours 600°C for 24 hours	550°C for 8 hours

**Table 4-3 Extrusion trials performed for evaluation of transverse weld.**

Test #	Trial	Billet material	Homogenization
<b>Test #1</b> <b>(Normal feeder plate)</b>	#1	AA6063	---
	#2	AA6063	---
	#3	AA3003	600°C for 24 hours
	#4	AA3003	500°C for 8 hours
	#5	AA6063	---
<b>Test #2</b> <b>(Tapered feeder)</b>	#6	AA6063	---
	#7	Al-1.3%Cu	---

After extrusion, the extrudate was water quenched two meters away from the extrusion die, and hence some changes in the microstructure may have occurred after extrusion, based on the time that the deformed material spent at high temperature prior to and after the quench.

Figure 4-7 shows a schematic illustration of the extrusion press and quench unit as well as typical sampling points on the extrudate for subsequent microstructure analysis. The sampling length position is shown in Figure 4-7 from which the front, middle and back samples were cut. During the extrusion of each billet, the ram was stopped when 10% of the billet length remained in the container. The ram

and container then moved back to make it possible to cut off the butt scrap. Typically the butt or discard length is set as a % of the original billet length. In our case with a starting billet length of 200 mm about 20 mm of butt scrap was left. The extrusion process then continues once the container is repositioned and the next billet loaded. During the press stop when the butt is sheared and the next billet loads, a visible stop mark forms where the die bearing contacts the profile. This mark, known as the stop mark, can be distinguished on the surface after extrusion.

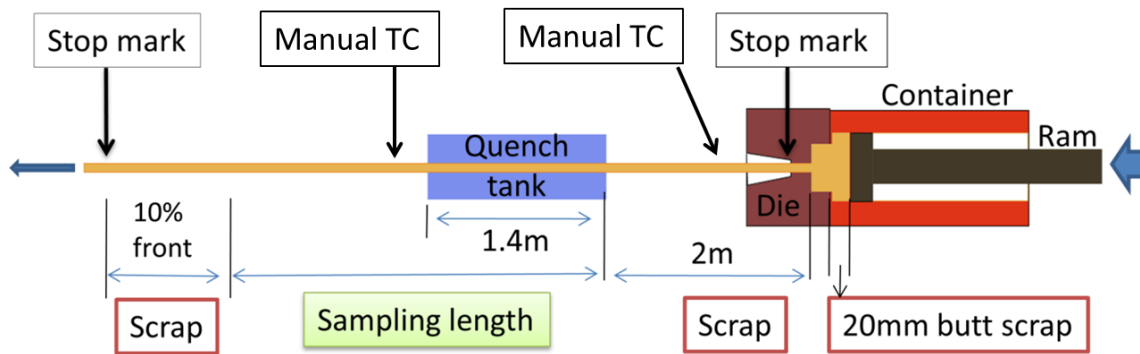


Figure 4-7 Schematic of the extrusion press at RioTinto Alcan’s Research and Development Center and quench tank layout along with sampling length.

## 4.1.2 Characterization

### 4.1.2.1 Optical microscopy

Optical metallography samples were taken from the front, mid-length and end locations along the sampling length of each extrudate (Figure 4-7), prepared with standard metallographic techniques, anodized with Barker’s reagent and then observed under polarized light in an optical microscope. Optical microstructure characterization of the homogenized billets and extrudates was done by co-workers at UBC [43, 17]. Figure 4-8 shows the starting grain structure of the as-cast billet. Average grain size of  $73\mu\text{m}$  was measured by Grajales [17]. It was observed that the homogenization does not affect the grain structure so that the homogenized structure would have the same grain size that as-cast structure has.

To measure the thickness of the transverse weld the extrudate was sectioned at different positions, polished and etched for 60 seconds using Poulton’s reagent (2 mL HF, 3 mL HCl, 20 mL HNO<sub>3</sub>, 175 mL water) and digital images were taken using the optical microscope with variable lightning filter to see the contrast between the clad layer and the extrudate. Measurements of transverse weld thickness



for the third series of trials (Table 4-3) was performed by co-workers at ARDC [103] using the same procedure but the etchant of HF 0.5% solution.

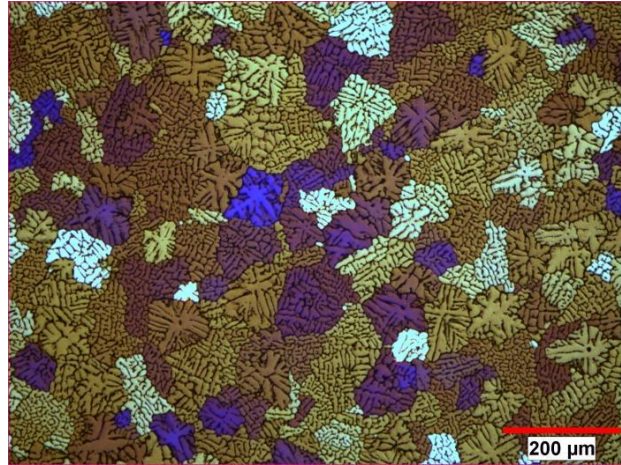


Figure 4-8 Polarized light micrograph showing the starting grain structure of the as-cast billet [17].

#### 4.1.2.2 Electron Back Scattered Diffraction (EBSD) microscopy and data analysis

To better investigate the deformed microstructure in terms of grain dimensions and subgrain size, Electron Back Scattered Diffraction (EBSD) microscopy was performed on as-extruded samples that were distinguished to be unrecrystallized by optical microscope. Table 4-4 shows the list of samples selected for EBSD analysis. EBSD microscopy was performed at different positions from center to the surface of each sample to investigate the possible microstructural transitions through the extrudate radius. This work was done using the FEG-SEM system available at Manchester University in the UK. Some other EBSD work was also completed by co-workers at UBC [17].

Table 4-4 Samples selected for EBSD analysis.

Sample number	Extrusion ratio	Homogenization condition	Billet temperature (°C)	Ram speed (mm/sec)
#1	17	550°C for 8 hours	400	8
#2	70	550°C for 8 hours	400	2
#3	280	550°C for 8 hours	400	2
#4	70	500°C for 8 hours	500	2
#5	17	550°C for 8 hours	500	8

The EBSD scans were done in a CAMSCAN Maxim FEG-SEM instrument that was equipped with HKL Channel 5<sup>2</sup> EBSD acquisition system. The step sizes of 0.2 and 0.4  $\mu\text{m}$  were used to observe the subgrain and grain structures, respectively. EBSD maps consisting of 250,000-1,250,000 pixels were then analyzed by VMAP, an in-house software package [104]. To avoid fake boundaries from “orientation noise” in heavily deformed structure, boundaries with misorientation below 2° were ignored. In this work boundaries with misorientation between 2° and 15° were defined as Low Angle Grain Boundaries (LAGB) and those with misorientation greater than 15° were defined as High Angle Grain Boundaries (HAGB).

The sampling plane was parallel to extrusion direction and passing through the center of extrudate to cover the whole radius. Figure 4-9 shows a schematic of sectioned extrusion sample and the locations of EBSD scans. EBSD sample preparation was performed using a Struers automatic polishing machine and included:

- Grinding on standard silicon carbide (SiC) paper from grade #600 to #1200.
- Polishing on 3  $\mu\text{m}$  diamond cloth to remove scratches from the grinding.
- Polishing with OPS colloidal silica suspension to get a high quality finish.

Additional EBSD at UBC was performed using Zeiss Sigma FE-SEM equipped with the GEMINI column and EDAX DigiView IV EBSD Camera. Data was collected using EDAX TSL Orientation Imaging Microscopy (OIMTM) Data Collection software and processed using EDAX TSL OIMTM Analysis 6 [17].

---

<sup>2</sup> HKL Channel 5 is a trademark of Oxford Instruments plc.

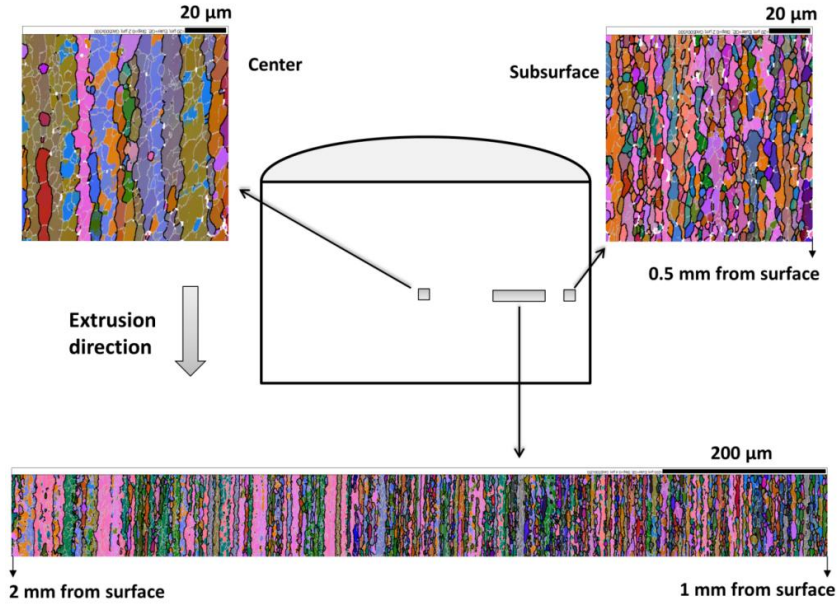


Figure 4-9 Locations on longitudinal section of extrusion sample chosen for EBSD analyses.

#### 4.1.2.3 Electrical resistivity measurement

Conductivity measurements were performed on samples before and after extrusion and converted to resistivity. This was done to assess how much precipitation occurred during the extrusion process. The measurements were performed using a Sigmatest<sup>®</sup> 2.069 made by Foerster Instruments Inc.<sup>™</sup> with absolute accuracy of +/-0.5% and resolution of +/-0.1 at the frequency of 60 kHz [105]. The device was calibrated prior to each set of measurements and the measured electrical conductivity was converted to electrical resistivity using the Equation shown below:

$$\rho = \frac{10^3}{\gamma_c} \quad 4-1$$

Where  $\rho$  is electrical resistivity in nΩm and  $\gamma_c$  is electrical conductivity in MS/m.

## 4.2 Mathematical Model

### 4.2.1 Thermo-mechanical Model

The commercial finite element (FE) packages DEFORM-2D and DEFORM-3D were used to mathematically model the extrusion process. DEFORM-2D was used to model the extrusion of the

round bar extrudate which has an axisymmetric geometry and DEFORM-3D was used to model the extrusion of the I-beam profile. The codes are based on the flow formulation approach using an updated Lagrangian procedure. The choice of FE package to use was dictated by two factors: 1) the requirement that it could model the large-scale plastic deformation associated with extrusion (with the ability to remesh), and 2) the need to predict loads over the entire range of the extrusion process (i.e., under both the transient start-up phase, followed by steady-state).

Figure 4-10 shows a schematic of the billet extruded into an I-beam section and the mesh used in the billet, extrudate and tooling. Due to existence of two symmetric planes in the geometry of the model, only one quarter of the extrusion geometry (shaded region in Figure 4-10 on the left) was simulated to save computational time. Figure 4-11 shows the schematic of the 2D round bar extrusion model and the mesh used. In this study, the model consisted of five objects to be simulated and included: the billet, ram, container, feeder plate, and die. Figure 4-10 also shows the location of the thermocouple at the midpoint of the die bearing length, which was used to measure the surface temperature of the extrudate during the extrusion trials.

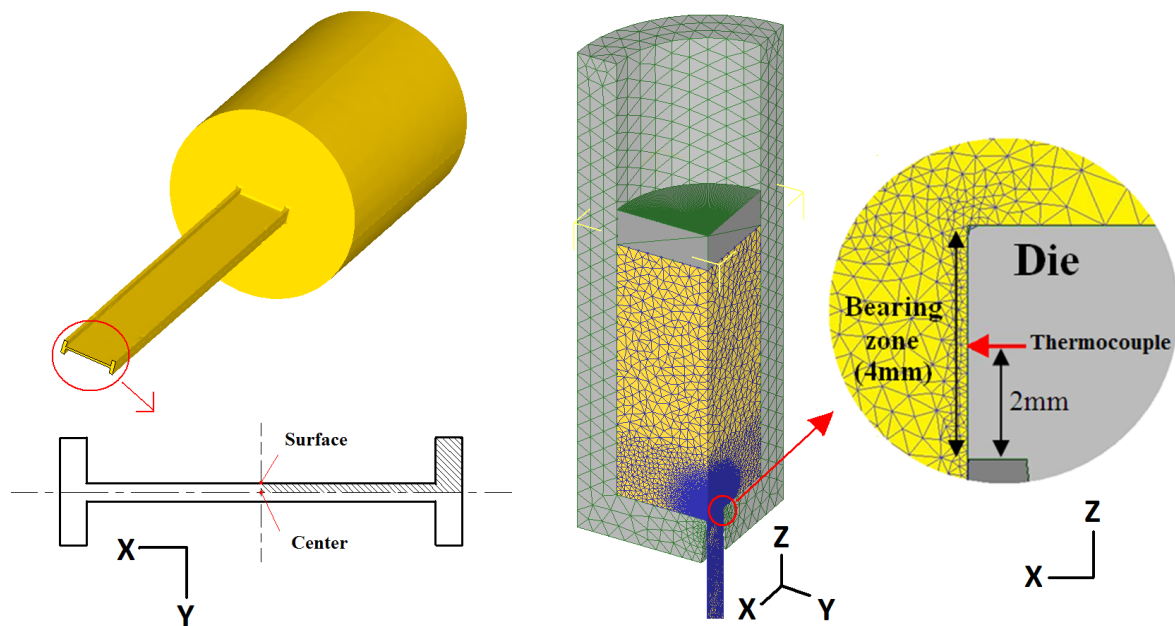


Figure 4-10 Schematic showing the billet being extruded into an I-beam section showing: Solid model of the billet and I-beam (left) and mesh used in the container, billet and I-beam (right).

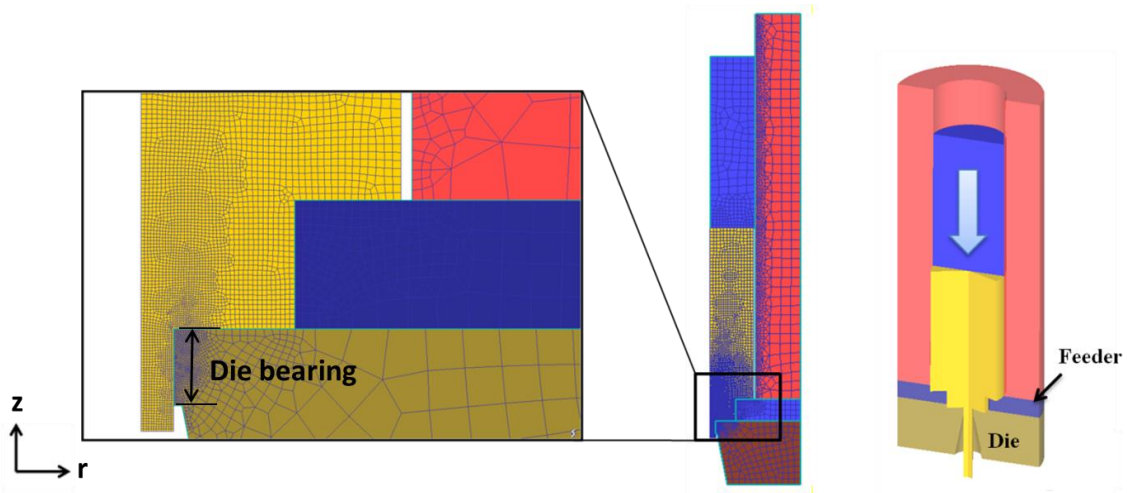


Figure 4-11 Schematic showing the billet being extruded into a round bar: sectioned solid model (right), and FEM mesh used in the billet and tooling (left).

Since there is large plastic deformation associated with the process, the billet material was assumed to behave as a rigid-viscoplastic material. Whereas the other objects were defined as being rigid during deformation; only the billet was involved in deformation to which the flow formulation applies. In order to get a reasonable combination of accuracy and speed, the mesh density was optimized spatially (finer near the die, and coarser away from the die) and dynamically during the extrusion simulation based on the gradient of the strain rate and strain being experienced so that the mesh density would be higher in regions with localized deformation. Consequently, there were three criteria to determine relative mesh density for a given location; relative mesh size which is applied by defining windows with specific mesh size, strain rate gradient and strain gradient. A weighting factor was specified to each criterion that shows the priority and effectiveness of that criterion in determination of mesh density. In this work weighting factors of 0.7, 0.2 and 0.1 were used for mesh windows, strain rate distribution and strain distribution, respectively. Figure 4-12 shows typical mesh size distribution for 2D and 3D extrusion models near the die corner.

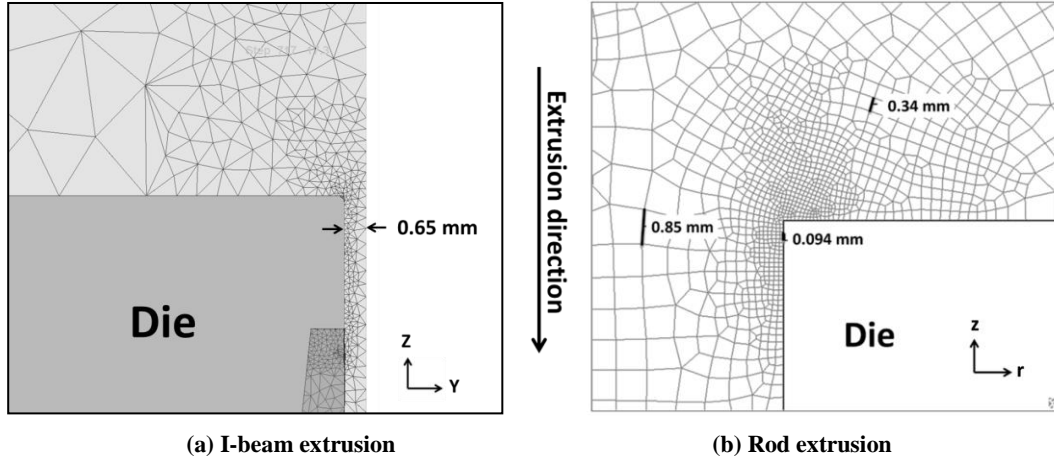


Figure 4-12 Typical mesh resolution distribution at the die corner for (a) I-beam and (b) Rod extrusion with extrusion ratio of 70.

#### 4.2.1.1 Finite Element formulation

For the I-beam extrusion the 3D geometry of the model was discretized into a series of four-node tetrahedral elements and for the round bar extrusion the geometry was modeled as a 2D axisymmetric extrusion set-up with a series of four-node, quadrilateral elements (Figure 4-10 and Figure 4-11). For both 2D and 3D models linear and isoparametric elements were used.

The FEM formulation in DEFORM is based on minimum work rate principle that can be shown by Equation 4-2. This equation is determined using the variational method for solving the work rate equation. To remove the incompressibility constraint, the penalty method is used [97, 79].

$$\delta\pi = \int_V \bar{\sigma} \delta \dot{\epsilon} dV + K \int_V \dot{\epsilon}_v \delta \dot{\epsilon}_v dV - \int_S \mathbf{F}_i \delta \mathbf{u}_i dS = 0 \quad 4-2$$

Where  $\int_V \bar{\sigma} \delta \dot{\epsilon} dV$  is the variational form of the work done by body forces or the plastic work,  $\int_S \mathbf{F}_i \delta \mathbf{u}_i dS$  is the term for surface traction work and  $K \int_V \dot{\epsilon}_v \delta \dot{\epsilon}_v dV$  represents the change in volume that is multiplied with a very large positive constant,  $K$ , which is called the penalty constant [97]. This number is usually chosen to be larger than  $10^6$  to ensure that the volume change or volumetric strain rate,  $\dot{\epsilon}_v$ , remains negligible. Using a very large number for  $K$  will cause convergence problems and hence increase the numerical calculation time [79]. In this work  $K$  was chosen to be  $10^9$ .

Because of non-linearity of the plastic deformation formulations, Equation 4-2 which is formulated in terms of nodal velocity, can be integrated using the Newton-Raphson numerical

integration method. Convergence criteria were based on both velocity and force convergence with a velocity error limit of 0.001 and force error limit of 0.01.

For the thermal part of the problem, the thermal energy balance equation is used. It is assumed that the only heat source inside the body is heat generated from plastic deformation. Using the divergence theorem and finite element formulation the energy balance equation can be written in following form [97]:

$$\mathbf{C}\dot{\mathbf{T}} + \mathbf{K}_c\mathbf{T} = \mathbf{Q} \quad 4-3$$

Where  $\mathbf{C}$  is the heat capacity matrix,  $\mathbf{K}_c$  is the heat conduction matrix,  $\mathbf{Q}$  is the heat flux vector,  $\mathbf{T}$  is the vector of nodal point temperatures, and  $\dot{\mathbf{T}}$  is the vector of nodal point temperature rates. The heat flux has several components and can be written as below in which  $\mathbf{N}$  is interpolation function:

$$\begin{aligned} \mathbf{Q} = & \int_V \eta(\bar{\sigma}\dot{\bar{\epsilon}})\mathbf{N}dV + \int_{S_r} \sigma\varepsilon(T_e^4 - T_s^4)\mathbf{N}ds + \int_{S_t} h(T_e - T_s)\mathbf{N}ds \\ & + \int_{S_c} h_{lub}(T_d - T_w)\mathbf{N}ds + \int_{S_c} q_f\mathbf{N}ds \end{aligned} \quad 4-4$$

The first term in right hand side is the heat generated by plastic deformation and  $\eta$  is the heat generation efficiency and represents the fraction of the mechanical work that is converted to heat. Only a small part of the plastic work is stored in the material and the rest of it generally converted into heat. After some level of strain the material can no longer store the plastic work and  $\eta$  remains close to 1.0 for the rest of deformation [106]. The critical strain at which this occurs for some aluminum alloys (AA2024) is reported to be in order of 0.5 [106]. Because of the very large amount of deformation taking place in the material, it was assumed that all of the mechanical work done during deformation was converted to heat. The second and third terms are the heat transferred from the environment through radiation and convection, the subscripts  $e$  and  $s$  (in  $T_e$  and  $T_s$ ) stand for environment and surface. The fourth term is the heat transferred from the die to the workpiece,  $T_d$  and  $T_w$  are temperatures of the die and workpiece surface, respectively, and the last term is the heat generated by friction at the die-workpiece interface.

The thermal equation is also non-linear which was also solved numerically using the Newton-Raphson iteration method with an error limit of 0.00001.

Deformation and thermal equations are solved for each time step and the new values for nodal coordinates, velocities and temperatures are initial values for the next step.

#### 4.2.1.2 Material properties

In this work the physically-based constitutive model developed by Kocks and Chen [88] shown in Equation 4-5 was used to capture the temperature and strain rate dependency of the material as it is being deformed as well as the influence the chemistry and homogenization treatment had on the flow stress of the material:

$$\dot{\varepsilon} = A \left( \frac{\sigma}{\mu} \right)^n \frac{Gb^3}{kT} \exp\left(-\frac{Q_d}{RT}\right) \quad 4-5$$

Where,  $\sigma$  is the stress,  $G$  is the temperature dependent shear modulus,  $n$  is the stress exponent,  $\dot{\varepsilon}$  is the strain rate,  $k$  is the Boltzman constant,  $T$  is the deformation temperature,  $b$  is the temperature dependent magnitude of the Burgers vector,  $Q_d$  is the activation energy for diffusion of the diffusing species,  $R$  is the gas constant,  $A$  and  $n$  are material constants that were calculated based on the starting chemistry and homogenization treatment [11]. Values and units of parameters used in Equation 4-5 are listed in Table 4-5 [11].

**Table 4-5 Values and units of parameters used in Equation 4-5 [11].**

Parameter	Value				Unit
	8H500	8H550	24H600		
A	$4.87 \times 10^{41}$	$1.04 \times 10^{40}$	$5.51 \times 10^{35}$ [17]		---
n	10.5	9.7	8.1		---
$Q_d$	211.4				$\text{kJ} \cdot \text{mol}^{-1}$
G	$G = G_0 \left( 1 + \left( \frac{T - 300}{T_m} \right) \frac{T_m}{G_0} \frac{dG}{dT} \right)$ $T_m = 933^\circ\text{K}, G_0 = 25.4 \text{ GPa}, \frac{T_m}{G_0} \frac{dG}{dT} = -0.5$				GPa
b	@300°C 0.291	@400°C 0.292	@500°C 0.293	@600°C 0.295	nm
k	$1.38065 \times 10^{-23}$				$\text{Pa} \cdot \text{m}^3 \cdot \text{K}^{-1}$
R	8.314				$\text{J} \cdot \text{K}^{-1} \cdot \text{mol}^{-1}$



Thermophysical properties used for the billet (AA3003) and container, die and dummy block (H13 tool steel) used in the model are shown in Table 4-6 for thermal conductivity and emissivity and in Figure 4-13 for volumetric heat capacity.

Table 4-6 Thermophysical properties used in the model [107].

Material	Thermal conductivity ( $\text{W}\cdot\text{m}^{-1}\cdot\text{K}^{-1}$ )	Emissivity
AA3003	180.2	0.5
H13	24.5	0.7

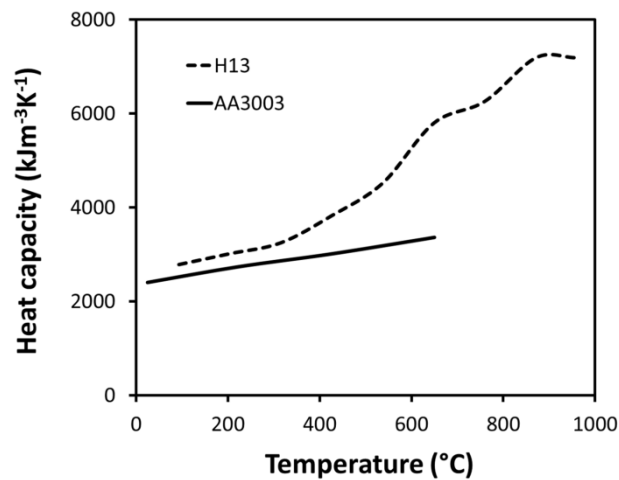


Figure 4-13 Volumetric heat capacity changes over the temperature for the billet (AA3003) and tooling material (H13) [107].

#### 4.2.1.3 Boundary and initial conditions

Friction conditions and the heat transfer coefficient between the billet and tooling are two important boundary conditions that play major roles in extrusion both from a modeling and also from an industrial point of view. Because of high temperature and inevitable large hydrostatic pressure inside the container as well as no lubricant usage, there is almost no control on the friction conditions between the billet and container, and the billet and the feeder. The friction condition at these interfaces (boundaries #1 and #3 in Figure 4-14) is considered to be sticking with almost no relative movement of billet on the container surface [98].

To model the friction between the dummy block and the billet (boundary #2) and also between the extrusion and the bearing part of die (boundary #4), an interface shear factor approach was used as shown in the Equation shown below:

$$f_s = m k$$

4-6

Where  $f_s$  is the frictional stress,  $k$  is the shear flow stress of the material and  $m$  is the interface shear factor which was considered to be 1.0 in this work.

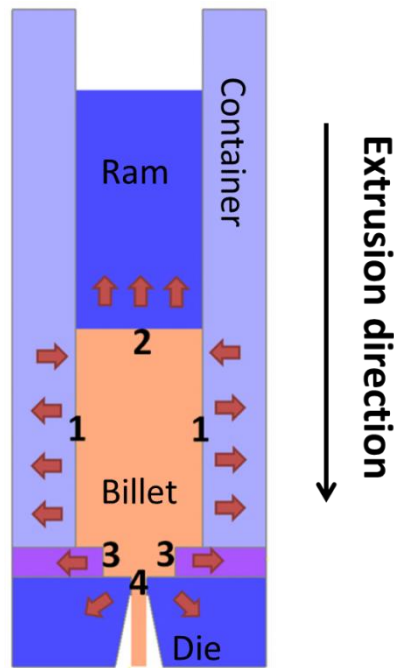


Figure 4-14 Boundary numbering and directions of heat transfer inside tooling.

The heat transfer coefficient (HTC) between the billet and tooling was assumed to be  $25 \text{ kWm}^{-2}\text{K}^{-1}$  [57] and the convection coefficient of air to have an average value of  $0.02 \text{ kWm}^{-2}\text{K}^{-1}$  [107, 108]. In Equation 4-4, HTC and convection coefficient of air is shown by  $h_{lub}$  and  $h$  respectively. The initial model parameters were set to follow those of the experimental extrusion trials. For rod extrusion, the initial temperature of the ram was set to  $250^\circ\text{C}$  for all conditions and the initial temperature of the container, die and feeder were set to  $350^\circ\text{C}$ ,  $400^\circ\text{C}$  and  $480^\circ\text{C}$  for billet temperatures of  $350^\circ\text{C}$ ,  $400^\circ\text{C}$  and  $500^\circ\text{C}$ , respectively. For I-beam extrusion the initial temperature of tooling (container, die and

feeder) was set to 450°C for all conditions and the temperature of the ram was set to 250°C for all simulations.

#### **4.2.1.3.1 Post-extrusion quench: evaluation of HTC in the quench bath**

Evaluation of the post extrusion cooling rate is an important issue in modeling the thermal history of the material. As mentioned earlier, there is a water quench bath placed after the die to quench the extrudate. In this work, it is assumed that a constant average surface heat transfer coefficient (HTC) could be used to quantify the heat transfer between the water quench and the extrudate. This is obviously a simplification since boiling water heat transfer will occur however during the quench but will provide us with an overall average rate of heat transfer in the bath. To evaluate the HTC in the quench bath the temperature change was calculated for different values of HTC and the value which gives the best fit with experimental measurement was chosen.

Figure 4-15 shows the predicted temperature changes at the surface of the extrudate during the water quench followed by air cooling after the quench. Different HTC values of 6, 7 and 8 kW/m<sup>2</sup>°C were used in the thermal model and the results were compared to experimental measurements. As shown in Figure 4-15 an HTC of 8 kW/m<sup>2</sup>°C shows the best fit with experiment so that this value was taken for calculation of temperature change of extrusion inside the quench bath. The convection coefficient during the air cool portion of the quench was assumed to have an average value of 0.02 kWm<sup>-2</sup>K<sup>-1</sup> [107, 108].

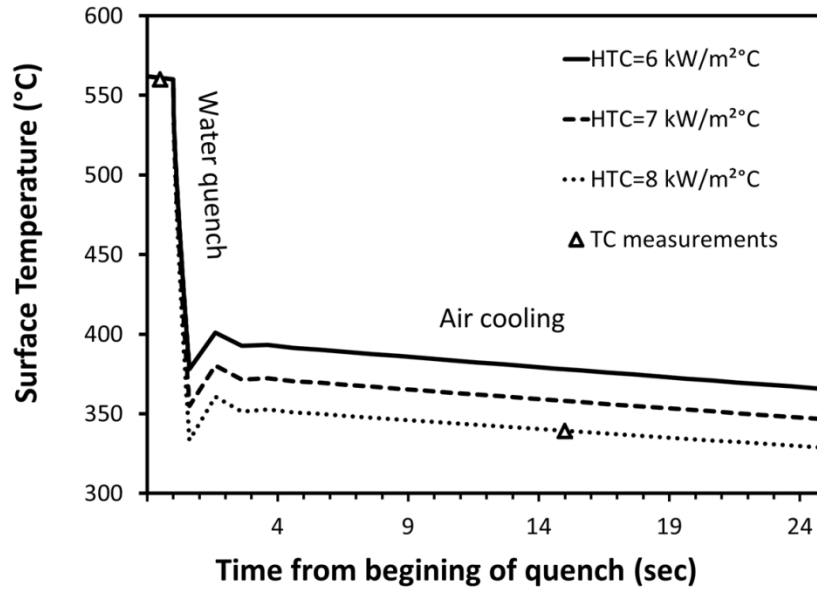
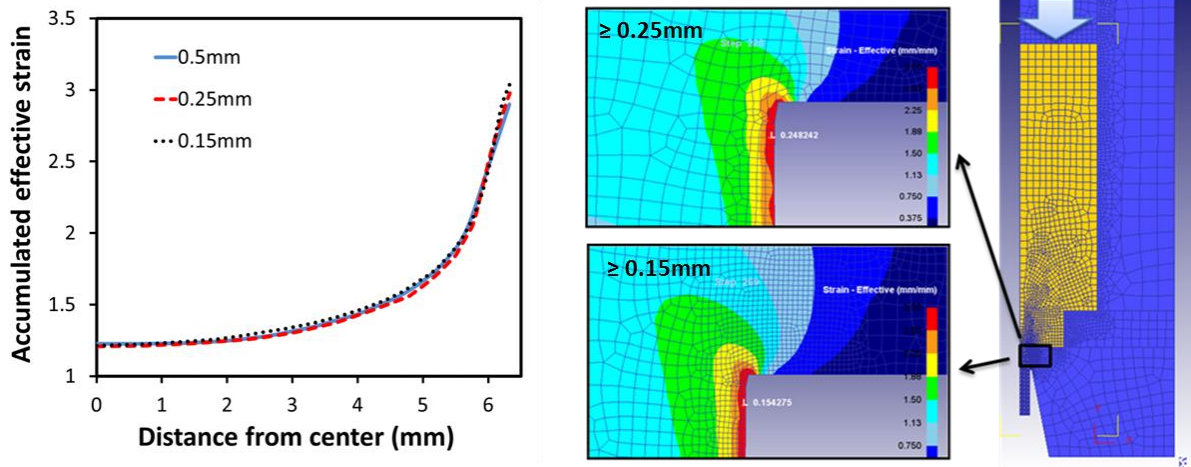


Figure 4-15 Predicted temperature change at the surface of the extrudate during the water quench and subsequent air cooling with different HTC values, compared to experimental measurement (ram speed = 32 mm/sec).

#### 4.2.1.4 Mesh size sensitivity

All FEM models are sensitive to mesh size, but as long as the element size is appropriate with respect to the time step size, spatial effects you want to resolve, the magnitude of the velocity and distribution of the strain rate, accurate results can be obtained. Figure 4-16 shows the effect of the minimum element size in the deformation zone (near the die corner) on the distribution of strain. The mesh sizes of 0.15, 0.25 and 0.5 mm (mentioned in Figure 4-16) corresponds to element size at the die corner and at the center parts of the die the mesh size is about 5 times larger. As shown in the diagram, the effect of mesh size has a minimal effect on the accumulated effective strain predictions except close to the surface. These results are from the early stages of the simulation for an extrusion ratio of 70 extruded at 500°C.



**Figure 4-16 Effect of minimum element size on distribution of accumulated plastic strain.**

To determine the mesh sensitivity of the model close to the surface, a number of simulations were carried out with different mesh sizes (0.5, 0.25, 0.15, 0.1 and 0.07mm) at the die corner where the smallest element size was defined due to highest gradient of velocity and strain rate. Figure 4-17a shows the effect of mesh size at the die corner on the extrusion load. The secondary vertical axis shows the normalized values that are calculated by dividing the predicted load by 3.32 MN - the calculated load for the smallest mesh size (0.07 mm). As observed when using small enough elements at the die corner the model error due to mesh size can be reduced to less than 1%. As shown in Figure 4-17b, a decreasing mesh size causes the computation time to simulation the whole extrusion cycle for one billet to increase dramatically from a couple of days using a mesh size of 0.5mm (near the die corner) to more than a year using a mesh size of 0.07mm. The time for small mesh sizes (0.15, 0.1 and 0.07 mm) was estimated by determining the time needed for a given ram stroke and calculation of the time needed for the complete ram stroke assuming linear relation between the ram stroke and time. Hence a compromise is needed that reflects the need for accurate results that can be produced in a timely manner. For our simulations we used a minimum mesh size of 0.25mm near the die corner and a maximum size of 6mm near the center of the billet. For the I-beam extrusion, due to low thickness of extrudate, smaller mesh size was used at the die corner (<0.1 mm).

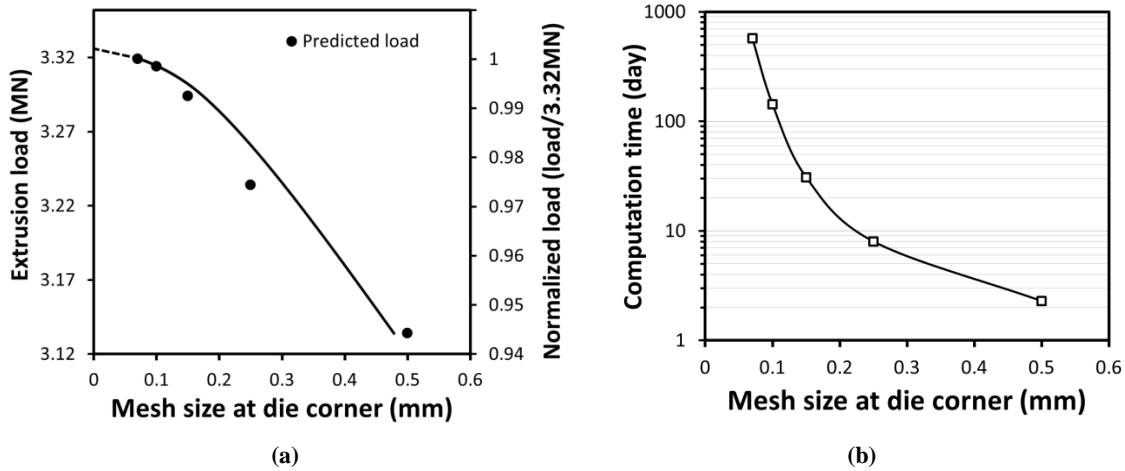
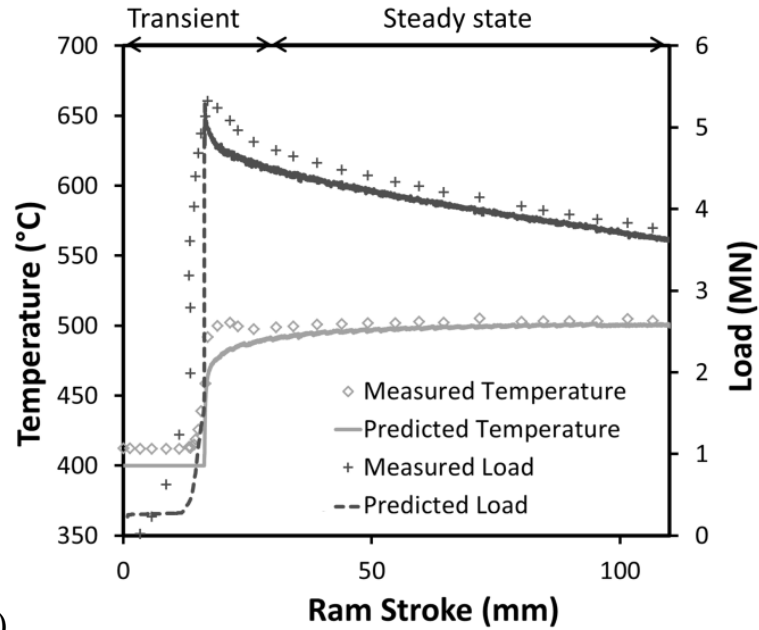


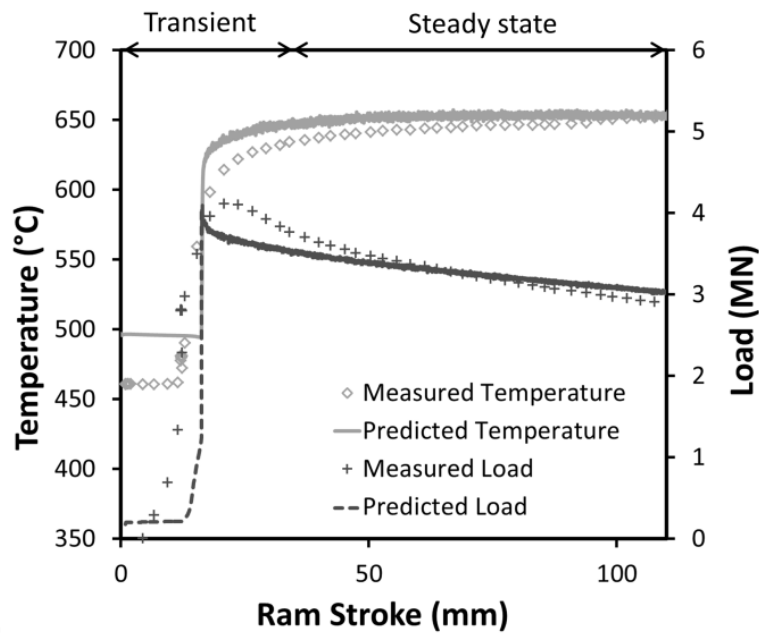
Figure 4-17 Effect of mesh size at the die corner on (a) the predicted extrusion load (at 50% extruded), and (b) computation time for simulation of extrusion of the whole billet.

#### 4.2.2 Experimental validation of FE model

To validate the model, load/temperature predictions during extrusion were compared to measured data acquired during the extrusion trials. In Figure 4-18 and Figure 4-19, it can be seen that the model is able to capture both the transient breakthrough phase and the following steady state regime well relative to the measurements made (within 5% for load and 3% for temperature for cases shown in Figure 4-18 and Figure 4-19).

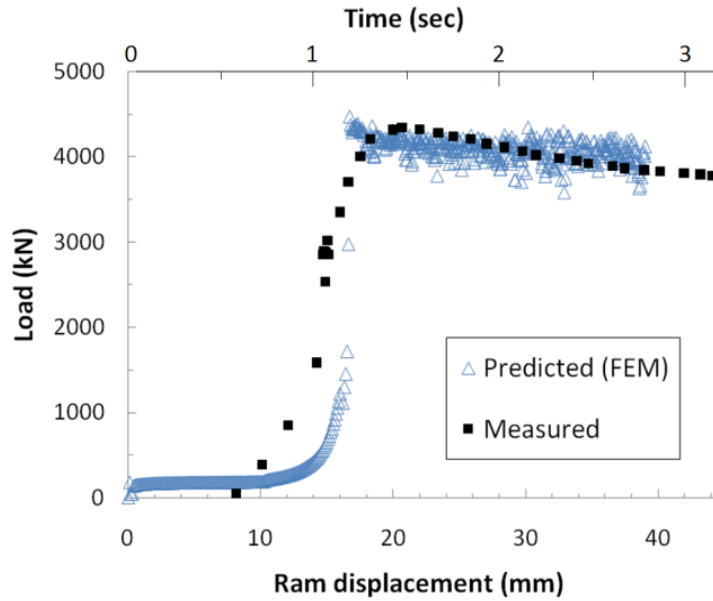


(a)

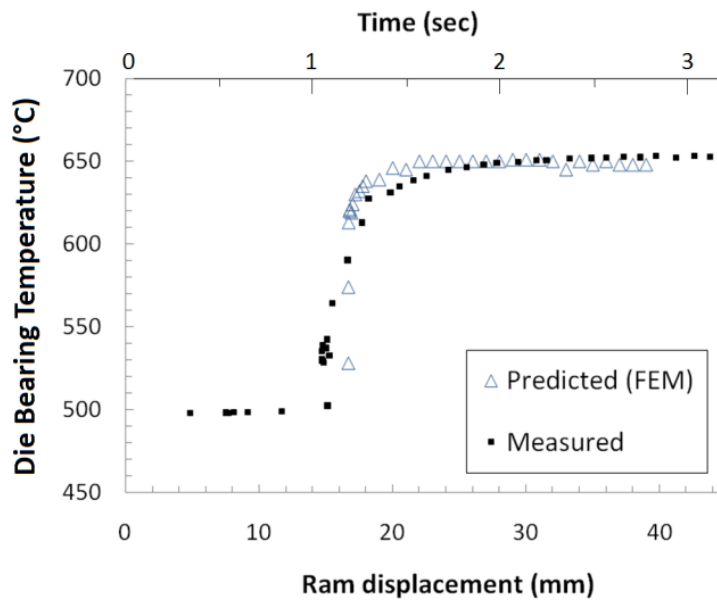


(b)

**Figure 4-18 Round bar extrusion (2D model) - comparison between model predictions (lines) and measurements (symbols) for extrusion load and temperature (a) billet temperature = 400°C and ram speed=2mm/s, (b) billet temperature = 500°C and ram speed=32mm/s, (for both cases extrusion ratio= 70, billets homogenized at 550°C for 8 hours and minimum mesh size=0.25mm.**



(a)



(b)

Figure 4-19 I-beam extrusion (3D model) - validation of simulation results for: (a) Extrusion load and (b) Temperature (Homogenization treatment prior to extrusion: 550°C for 8h, Extrusion temperature = 550°C).

The initial difference between the measured and predicted surface exit temperature arises due to the difference between the initial temperature used in the model (which is set to the billet preheat temperature) and the actual temperature of the die close to the position of the thermocouple at the beginning of the extrusion. As shown in the figure, during the steady state part of the extrusion, the predicted temperature is in good agreement with the measurements.



Due to the billet/container clearance, initially the billet has to be upset to fill the container before extrusion can commence. Assuming that the break-through (when the extrusion starts to exit the die) takes place when the billet fills in the die, the manually calculated ram stroke for break-through is 16.3 mm. Theoretically, the maximum load happens immediately after the break-through. The predicted stroke for maximum load shown in Figure 4-18 is 16.5 mm which is in good agreement with manual calculations.

Figure 4-20 shows the capability of the 2D FEM model to predict the extrusion load over the range of extrusion conditions outlined in Table 4-2 by comparing the predicted and measured loads at a ram position of 50% of the whole billet. As shown in the figure the difference of predicted load from measured values fall within +/-11% of the measured load, with the average difference of -1.4% and average absolute difference of 5.3%.

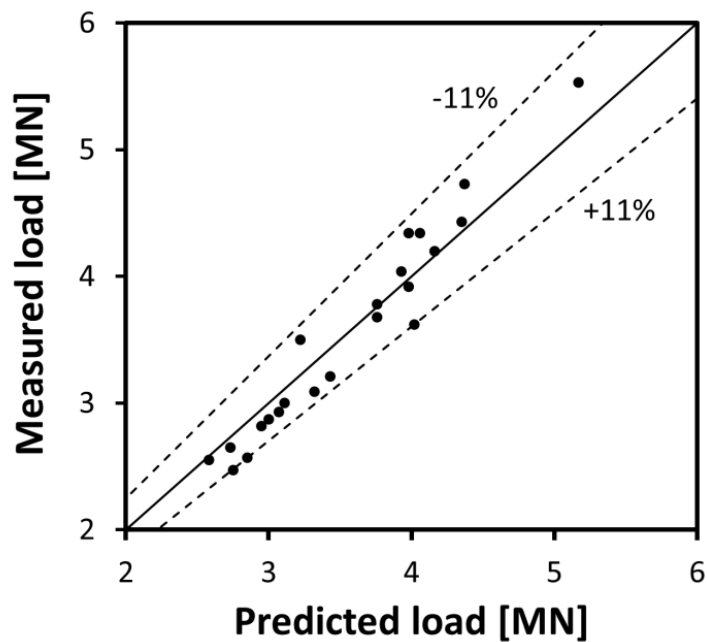


Figure 4-20 Graphical comparison of predicted and measured extrusion load for different conditions listed in Table 4-2, at a ram stroke where 50% of billet is extruded.

### 4.2.3 Post processing of FEM results

#### 4.2.3.1 Point tracking using DEFORM post-processor

The preliminary results from the FEM model were post-processed to get more interpretable data such as the flow pattern, temperature history and accumulated plastic strain. Techniques were also

developed to use the FEM model predictions in conjunction with an algorithm to predict changes to the grain shape and increases in the grain boundary area and how these varied spatially during extrusion. Post processing was also needed to extract the appropriate thermomechanical history data for use in the microstructure model equations. The first step in the post processing of the FEM results was tracking different points through the velocity field from the billet during extrusion and into the final extrudate. The spatial locations of the tracked points were selected so that the entire cross section of the extrudate was included and these were then back-tracked into the original billet. Back-tracking was done using the DEFORM post processor point tracking tool.

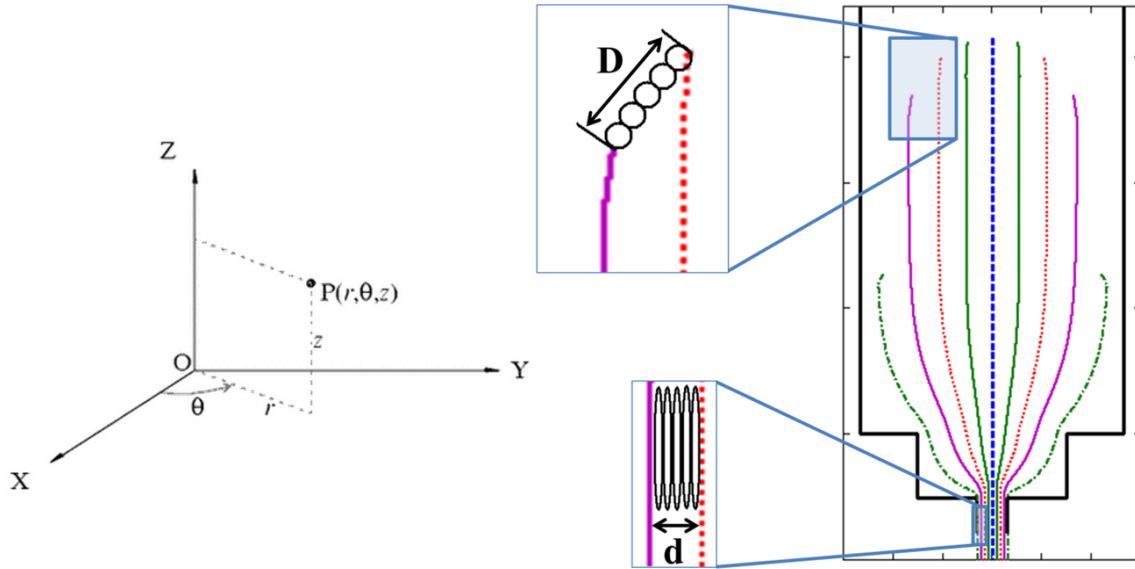
#### **4.2.3.2 Grain shape calculation**

Figure 4-21 shows the flow paths of different points in the round bar extrusion and also the schematic of the method used for calculation of grain thickness after the extrusion. It is assumed the original unreformed grains are spherical.

In this work a simple but effective method has been used to calculate the thickness of the grains after the deformation. In order to avoid complexity that arises from tracking of strain components, element rotation and the effect of remeshing, the thickness of the deformed grains are calculated based on the distance between two adjacent tracked points before and after deformation. As the number of grains between the two points remains unchanged during the deformation, an estimate of the final thickness of the deformed grains can be done using the Equation shown below:

$$\frac{\textit{Final grain thickness}}{\textit{Original grain size}} = \frac{d}{D} \quad 4-7$$

Where D is the distance between two adjacent tracked points before deformation and d is the distance between those points after the deformation (Figure 4-21). The original grain thickness was measured experimentally, so the only unknown parameter in the Equation 4-9 is the final grain thickness.



**Figure 4-21** Flow pattern for different points that all go to the same section in the extrudate and blow-ups showing the schematic of original shape and arrangement of initially spherical grains before and after the deformation.

During axisymmetric extrusion, the three principal strains are approximately in the direction of the cylindrical coordinate system axis ( $r$ ,  $\theta$ ,  $z$ ). Hence, the width and the length of deformed grains can be estimated as follows:

$$\frac{\text{Final grain width}}{\text{Original grain size}} = \frac{r_f}{r_0} \quad 4-8$$

Where  $r_f$  and  $r_0$  are final and original coordinates in the  $r$  direction. In addition, using volume constancy the final length of the grain is:

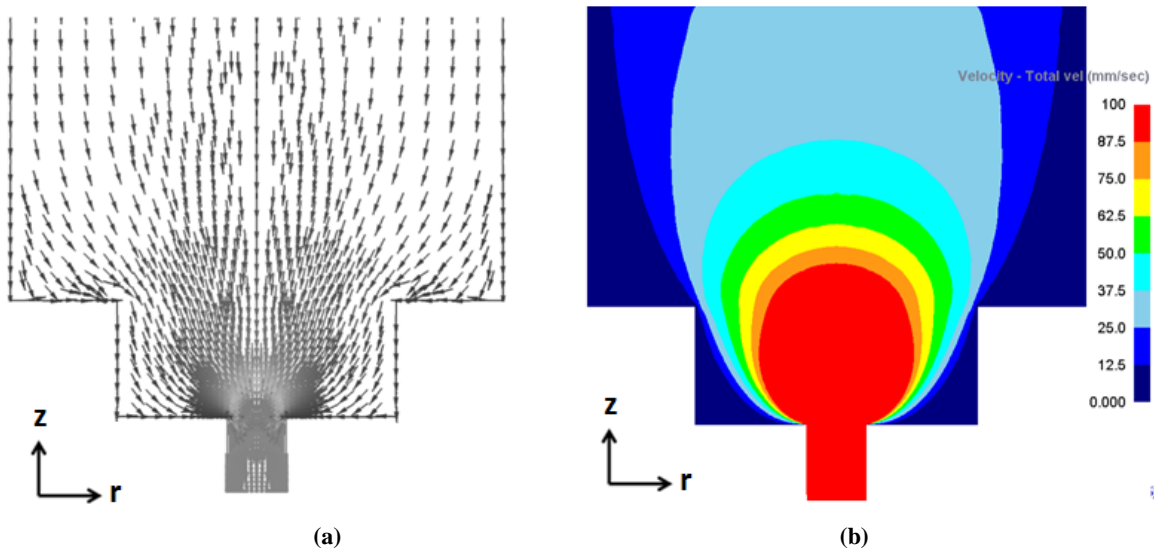
$$\frac{\text{Final grain length}}{\text{Original grain size}} = \left(\frac{d}{D}\right) \cdot \left(\frac{r_0}{r_f}\right) \quad 4-9$$

The same method was used to estimate the grain dimensions in 3D model (i.e. I-beam extrusion) after converting the Cartesian coordinates to Cylindrical coordinates using the Equations shown below:

$$r = \sqrt{X^2 + Y^2} \quad , \quad z = Z \quad 4-10$$

### 4.2.3.3 Transverse weld boundary calculation

Using MATLAB software, results for velocity flow fields from the FEM model were processed so that details of the flow pattern and transverse weld thickness could be determined. The first step in the post processing of the FEM results was tracking different points through the velocity field from the billet during extrusion and into the final extrudate. Figure 4-22 shows the direction and magnitude of velocity for each nodal point in the billet for an extrusion ratio of 70.



**Figure 4-22 FE model-predicted velocity field showing (a) the direction and (b) the magnitude of velocity through the deforming material (extrusion ratio = 70, arrows show the direction of velocity for each node).**

Predictions of the transverse weld shape and thickness were made by tracking the points of the boundary surface between the two billets. For this purpose, simulations were performed using a very fine mesh size ( $\sim 0.1$  mm at the die corner) and the simulation step after break-through was chosen to extract velocity fields for post-processing purposes. Figure 4-23 shows the distribution of element size at the die corner where the smallest mesh size was used. The spatial flow of the material through the die can be quantified by using the model-predicted velocity profiles at discrete locations to predict how the material will flow. This was done through a series of interpolation techniques using the model predicted data to ensure accuracy.

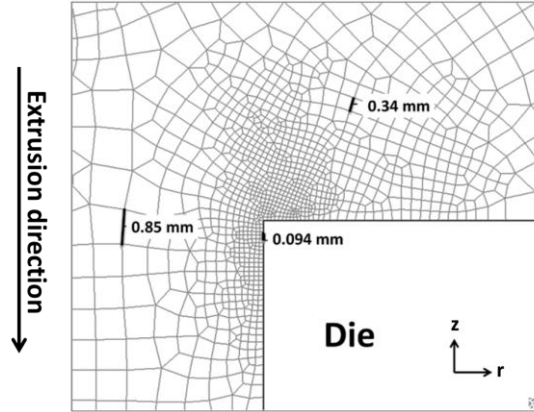


Figure 4-23 Finite element discretization of extruding material at the die corner showing the mesh size at different positions.

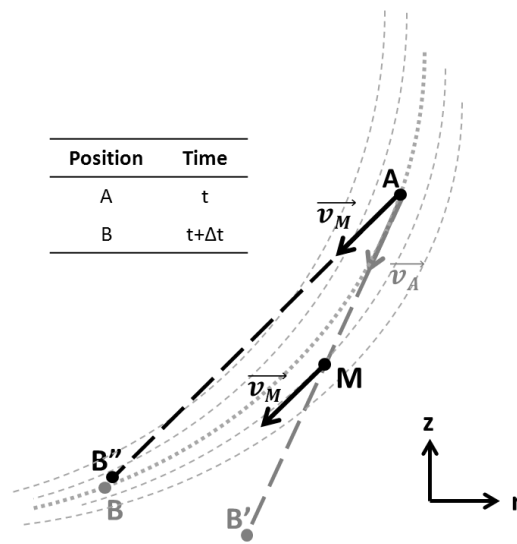
Extracted velocity fields consist of  $r$  and  $z$  components of velocity for nodal points scattered through the deforming body. The tracking procedure was performed using an interpolation technique embedded into the MATLAB software called the “TriScatteredInterp” function. Using this technique a surface of the form  $V_i = F(r,z)$  is produced that goes through all scattered data points so that by applying interpolant  $F$  on any query location  $(r,z)$  within the deforming body, the components of velocity,  $V_r$  and  $V_z$ , can be estimated. To get a continuous and smooth surface the “Natural neighbour” interpolation method [109] was used.

Figure 4-24 shows a schematic of the technique used to calculate the spatial material flow based on the FE predicted velocity field. Although DEFORM can predict the material flow using a point tracking technique, the spatial resolution of the material flow is limited by the mesh size. Using this technique, allows a fine mesh size (i.e. 0.1 mm or 100  $\mu\text{m}$  close to the die corner) to be used in DEFORM once steady state is achieved while not imposing limitations in terms of computational time required. In this technique, shown schematically in Figure 4-24, “A” is the position of a point at time  $t$ . In order to calculate the spatial position that point A will travel to in a given time increment  $\Delta t$  it is assumed that the average velocity of point “A” ( $v_{av}$ ) as it moves can be estimated using the starting velocity at point A ( $v_A$ ) (i.e.,  $\overline{v_{av}} \cong \overline{v_A}$ ). The estimation of the new position of point A at time  $t+\Delta t$  would be  $B' = A + \overline{v_A}\Delta t$ . Referring to Figure 4-24, in areas with high curvature of the flow lines, this method can result in a large numerical error in terms of the predicted position of point A ( $B'$ ) after a given time. In order to calculate a more accurate flow line, the velocity (magnitude and direction) at an intermediate point (M), half way between A and  $B'$ , is calculated and used as the starting velocity and direction for point A. The position of point M is determined using Equation 4-11. As shown in Figure 4-24, using this technique, a much more accurate spatial position

at the end of the time step, B'', can be calculated. This calculation is performed as shown in Equation 4-12. The length of the time step,  $\Delta t$ , was chosen so that the distance AB' is just a fraction of element size.

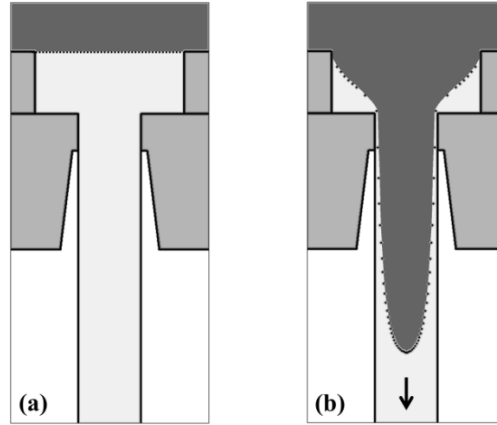
$$M = A + \frac{\vec{v}_A \Delta t}{2} \quad 4-11$$

$$B'' = A + \vec{v}_M \Delta t \quad 4-12$$



**Figure 4-24 Schematic showing the point tracking procedure during one time step (dotted lines represent the exact flow lines, B is the exact position of point A after time increment  $\Delta t$ , B' and B'' are numerically estimated position after time increment  $\Delta t$ ).**

Using this numerical technique, the material flow behaviour can be accurately extrapolated to longer times. Moreover, the position of each tracked point after it exits the die represents the boundary between the first and second billet or clad thickness layer, (Figure 4-25b). In the FE simulation, the material from the first and second billet were treated as the same material in terms of flow properties and the boundary or transverse weld that evolved between the two materials during extrusion was tracked. Figure 4-25 shows the points tracked from the billet to the extrudate before the ram started to move (Figure 4-25a) and after the breakthrough (Figure 4-25b).



**Figure 4-25 Determining the transverse weld shape using point tracking method for an extrusion ratio of 17, (a) position of points before extrusion starts, (b) position of tracked points right after the breakthrough.**

#### 4.2.3.4 Stored energy calculation

In this research, stored energy is assumed to come from two major sources: dislocations and grain boundaries. The stored dislocation energy was calculated using the Equations shown below [110]:

$$\rho = \left( \frac{\sigma_{avg}}{\alpha G b} \right)^2 \quad 4-13$$

$$E_{\perp} = C_1 \rho G b^2 \quad 4-14$$

Where  $E_{\perp}$  is stored energy from dislocations,  $\rho$  is dislocation density [ $m/m^3$ ],  $b$  is the burger's vector and  $G$  is the shear modulus.  $\alpha$  and  $C_1$  are material constants in order of 0.5,  $\sigma_{avg}$  is the average flow stress during the deformation and is calculated using the equation below:

$$\sigma_{avg} = \frac{\int_0^{\varepsilon} \sigma d\varepsilon}{\varepsilon} \quad 4-15$$

Where  $\sigma$  is the instantaneous flow stress and  $\varepsilon$  is the total plastic strain. The stored energy associated with the grain boundaries was calculated using Equation 4-16 as shown below:

$$E_{gb} = \gamma_{gb} A_{gb} \quad 4-16$$

Where  $\gamma_{gb}$  is grain boundary energy per unit area which is  $\sim 0.324 \text{ J/m}^2$  [21] and  $A_{gb}$  is the grain boundary area per unit volume. The total stored energy can be calculated using Equation 4-17:

$$E_{total} = E_{gb} + E_{\perp} \quad 4-17$$

When considering the driving pressure for recrystallization, the pinning pressure exerted by small particles on a moving grain boundary needs to be assessed. This pinning pressure is also known as “Zener Drag”. Equation 2-17 is used to calculate Zener drag. So that the driving pressure for recrystallization is:

$$P_D = 0.5\rho Gb^2 + \gamma_{gb} A_{gb} - \frac{3\gamma_{gb}F_V}{2r} \quad 4-18$$

In this work, the Zener drag is taken as the resultant of drag pressure from small particles (dispersoids) and large particles (constituent particles). Volume fraction and average size of dispersoids for AA3003 with different homogenization conditions were calculated by Du et al. [111] using mathematical models and those of constituent particles were measured experimentally by Geng [43] at UBC. Constants and tuning parameters used in this work are listed in Table 4-7.

**Table 4-7 Microstructure model constants and tuning parameters.**

Parameter	Value			Source
	8H500	8H550	24H600	
$F_v$ (Dispersoids)	0.014	0.014	---	Qiang Du [112]
$r$ (Dispersoids)	0.028 $\mu\text{m}$	0.054 $\mu\text{m}$	---	Qiang Du [112]
$F_v$ (Constituent)	0.028	0.035	0.039	Geng [43]
$r$ (Constituent)	0.9	1	1.2	Geng [43]
$G$ (room temperature)	$2.65 \times 10^4 \text{ MPa}$			Vatne et al. [62]
$b$ (room temperature)	$2.86 \times 10^{-10} \text{ m}$			Vatne et al. [62]



# Chapter 5

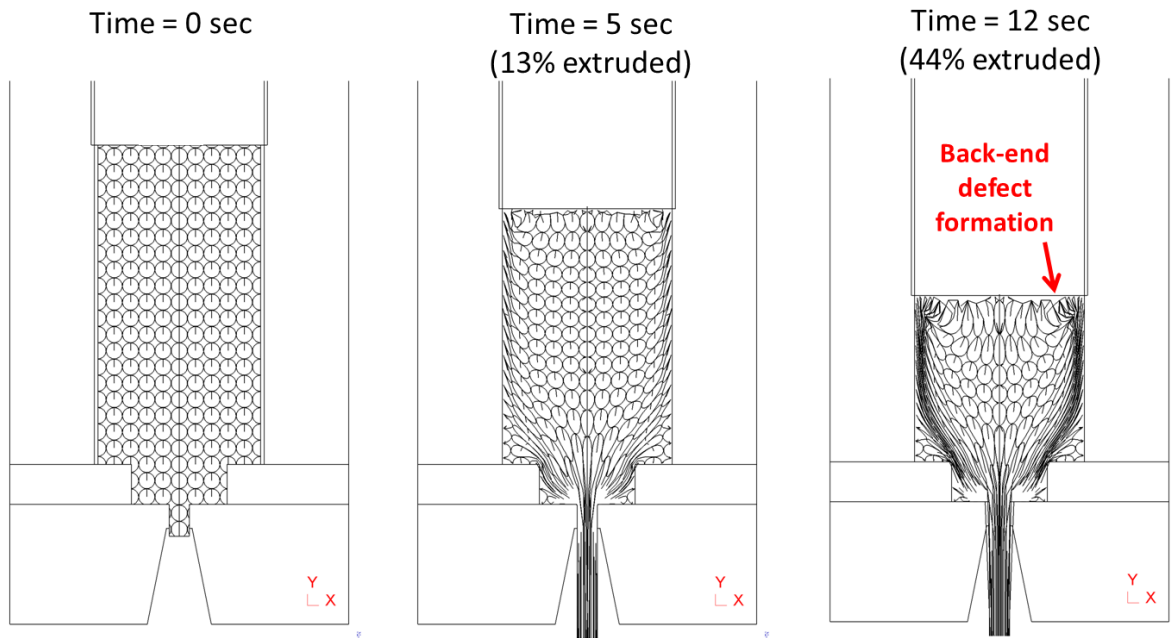
## Results and discussion

In this chapter model predictions for thermomechanical history and microstructure evolution are presented and discussed for the 2D and 3D models along with experimental studies that have been done for validation purposes. The majority of the model predictions are made for the mid-length section along the extrudate to be consistent with the position where the experimental measurements were made.

### 5.1 Round bar extrusion

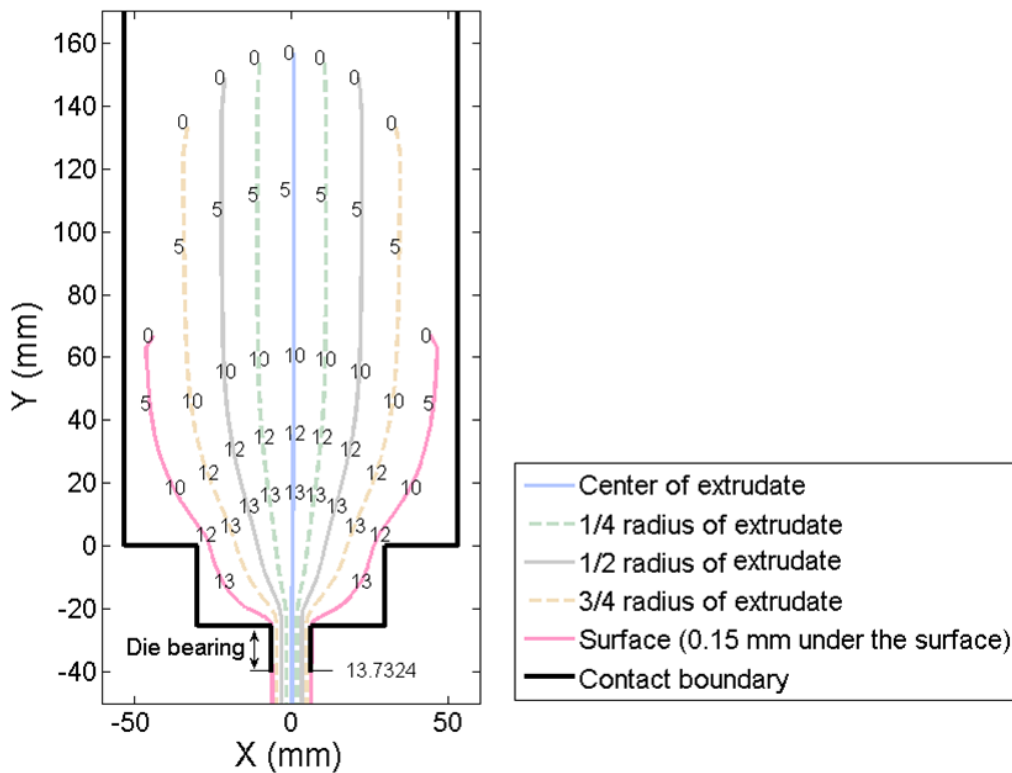
#### 5.1.1 Material flow

Figure 5-1 shows the model predicted deformation of an initial circular grid (diameter = 10 mm) in the billet during the extrusion process. Formation of shear zones, dead metal zones and the back-end defect (accumulation of material in front of the ram) can be observed.



**Figure 5-1 Model-predicted deformation of initial network of circular cells in the billet during the extrusion, (extrusion ratio = 70, billet temperature = 500°C and ram speed = 8 mm/sec).**

Figure 5-2 shows the predicted flow pattern during the extrusion in a different way using flow lines for similar extrusion conditions to that presented in Figure 5-1. In Figure 5-2 each line represents the path that a single point at the mid-length section of the extrudate travels during the extrusion process. The numbers on the line refer to the time in seconds to indicate how quickly the material flows and the spatial inhomogeneity of it. Referring to the original position of the points in the billet, a huge amount of deformation occurs in the outer quarter layer of the extrudate (between the lines  $\frac{3}{4}$  radius and surface of the extrudate).



**Figure 5-2 Model-predicted flow pattern through the rod thickness at the mid-length section of the extrudate (numbers on curves represent time after the extrusion starts in seconds, extrusion ratio = 70, billet temperature = 500°C and ram speed = 8 mm/sec).**

### 5.1.2 Thermomechanical history

Figure 5-3a shows a typical model-predicted thermal history from the start of extrusion to the end of quench and Figure 5-3b shows the temperature history for the same case magnified in the die region. The legend surface and center in Figure 5-3 refer to the center and 0.15 mm under the surface of the extrudate (Figure 5-2). At the start, both the center and surface are at the same temperature as the

preheated billet is just loaded into the container. Immediately after the ram touches the billet the center starts to cool down as it is closer to the ram which is the coldest part touching the billet (refer to Figure 5-2 for original positions of the extrudate center and surface in the billet). As expected there is a temperature rise when the material passes through the die (over time 13.5 s to 14 s) and the surface experiences a greater temperature rise than the center due to a higher amount of deformation as well as frictional heat. The time period that the material is passing through the die bearing is shown in Figure 5-3b which is about 25 ms for this case (the location of die bearing length is shown in Figure 5-2). Before the material enters the bearing length both center and the surface are experiencing the highest rate of temperature rise, since the majority of deformation occurs in this region. As shown in Figure 5-3b, in the die bearing zone the material at the surface is still gaining considerable heat. The heat sources in this region are the friction and deformation at the surface. In contrast, in the die bearing zone, the center is almost “dead” after it enters the bearing zone and its temperature rise is only a result of heat conduction from the surface towards the center. Immediately after the die exit (at the end of die bearing length) the surface and center temperatures equilibrate due to high thermal conductivity of aluminum and the large temperature gradient from center to the surface disappears. Then the extrudate cools during the air cool and water quench.

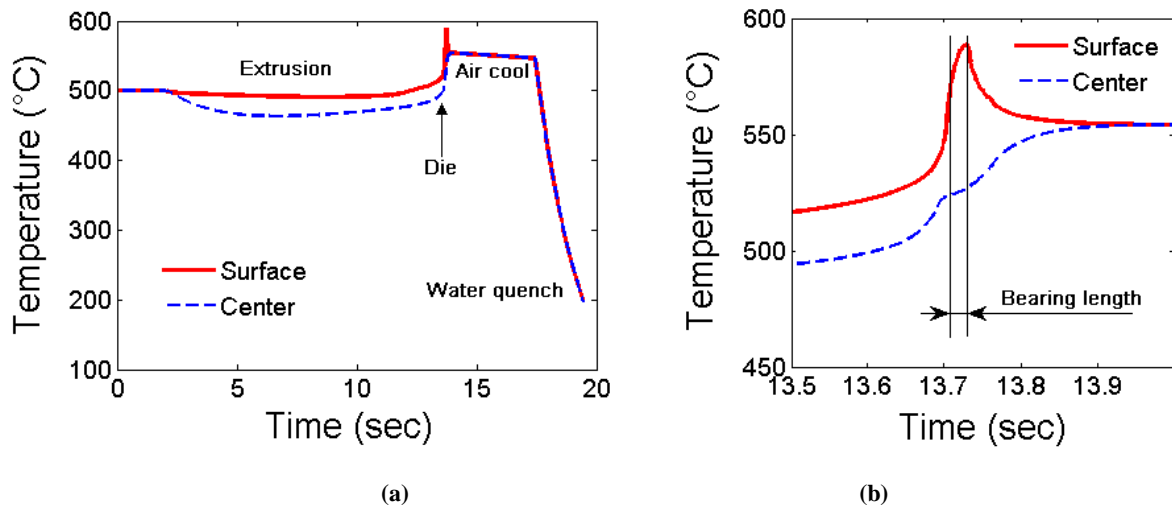


Figure 5-3 Temperature histories for center and surface of mid-length section of extrudate for: (a) whole extrusion cycle and (b) die region (ram speeds = 8 mm/sec, billet temperatures = 500°C and extrusion ratio = 70)

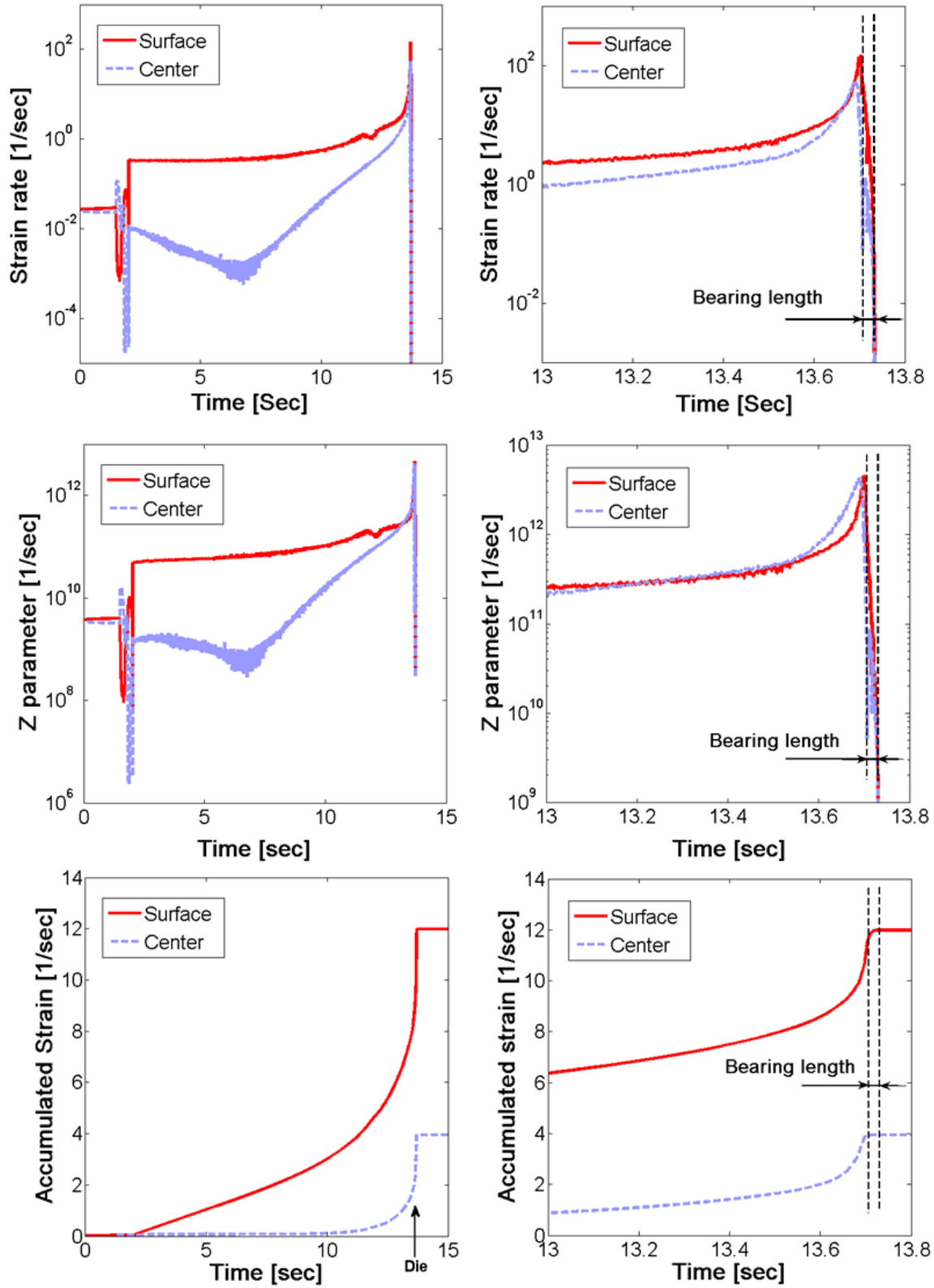
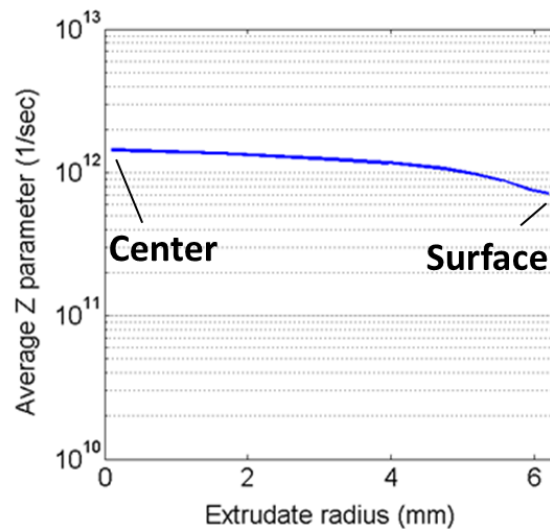


Figure 5-4 Histories of strain rate, Zener-Hollomon parameter and strain for center and surface of mid-length section of extrudate; (left) the whole extrusion cycle, (right) die region (ram speeds = 8 mm/sec, billet temperatures = 500°C and extrusion ratio = 70)

Figure 5-4 shows the histories of strain rate, the temperature compensated strain rate (Zener-Hollomon parameter, Z parameter) and accumulative plastic strain during the extrusion process. Due to the difference between the billet diameter and container inner diameter, which is the case in all extrusion processes, the extrusion starts with upsetting the billet until it completely fills the container. During this stage the billet is deforming with an even distribution of strain rate throughout its volume and at the end of this stage when the billet starts to touch and stick to the container, some rapid fluctuations occur at both the surface and center. After the billet completely fills the container, the surface that is in the shear zone deforms with a much higher strain rate relative to the center. Although the temperature at the center is less than that of surface, the Z parameter at the center is lower than that at the surface because of the higher strain rates experienced there.



**Figure 5-5 Average Zener-Hollomon parameter distribution from center to the surface of mid-length section of extrudate (ram speeds = 8 mm/sec, billet temperatures = 500°C and extrusion ratio = 70).**

Figure 5-5 shows the average Z parameter ( $Z_{avg} = \frac{\int_0^\epsilon Z d\epsilon}{\epsilon}$ ) experienced during the extrusion process from center to the surface of the material. As can be seen, the average Z parameter decreases from the center to the surface although the instantaneous Z parameter at the surface is higher than the Z parameter at the center during the majority of the deformation time (Figure 5-4). The reason is that during the last second of the deformation, the Z parameter at the center is higher than the surface and this happens exactly when the center material is accumulating the majority of its total strain (Figure 5-4). On the other hand, the surface material has gained a large portion of its strain during the low Z deformation but during this period the center has not accumulated considerable strain.

Figure 5-6 shows that the strain rate changes considerably with strain. As the majority of the strain takes place over a very short period of time in the die region, this Figure shows better detail of strain rate changes than Figure 5-4.

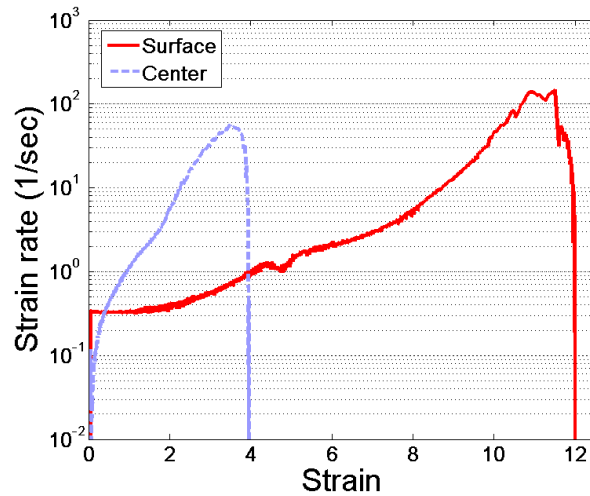


Figure 5-6 Strain rate changes versus accumulative plastic strain (ram speeds = 8 mm/sec, billet temperatures = 500°C and extrusion ratio = 70).

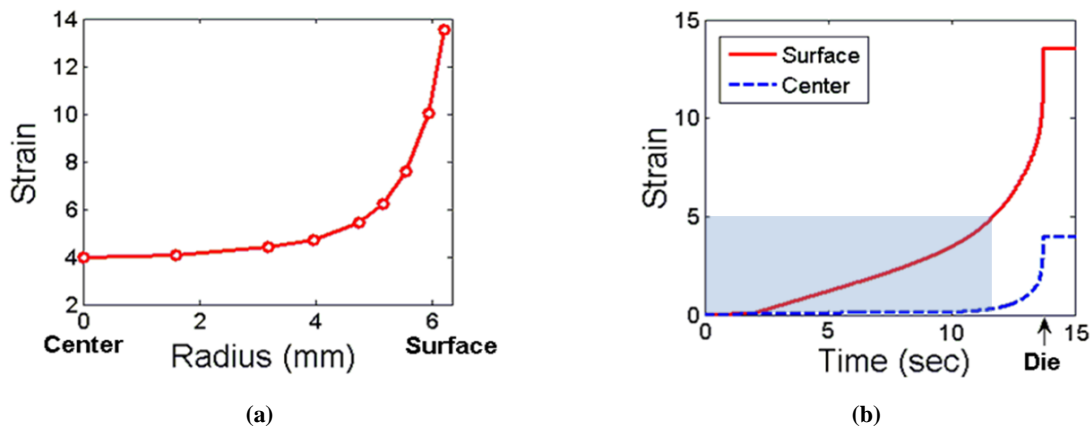


Figure 5-7 Model predicted (a) Spatial distribution of the accumulated effective plastic strain across the rod radius after extrusion, (b) strain history during the extrusion at the center and surface of the extrudate (for an extrusion ratio of 70, billet temperature of 500°C and ram speed of 8 mm/sec), the highlighted area represents the time period that the center is not gaining considerable strain.

Figure 5-7 shows the accumulated plastic strain from the center to the surface of the extrudate as well as the strain history at the center and surface of the extrudate. In Figure 5-7a high inhomogeneity

of the plastic strain distribution from center to the surface of the extrudate can be observed. In addition, referring to Figure 5-7b there is a large difference in the strain history experienced at the surface and center of the extrudate during the extrusion process.

The strain distribution curve (Figure 5-7a) shows that the severe strain inhomogeneity occurs over the last third of the radius and the slope of the curve increases towards the surface. The reason is that the surface passes through the shear zone or severe deformation zone (Figure 2-1). Figure 5-7b shows evidence of this, as it shows that before the billet material enters the die region (at the time ~12 sec) the surface has already accumulated an effective strain of 5.0, while the center at the same time has not experienced considerable strain.

### 5.1.2.1 Temperature history – Parametric study

Figure 5-8 shows the effect of extrusion conditions (including: extrusion ratio, ram speed and homogenization treatment) on the temperature of the extrudate center immediately after it exits the die (i.e. the time  $t = 14$  sec in Figure 5-3) when the center and surface temperatures equilibrate. So that, this temperature represents the temperature of the whole cross-section at die exit. According to temperature history shown in Figure 5-3 this is the highest temperature experienced at the center of the extrudate during the extrusion process.

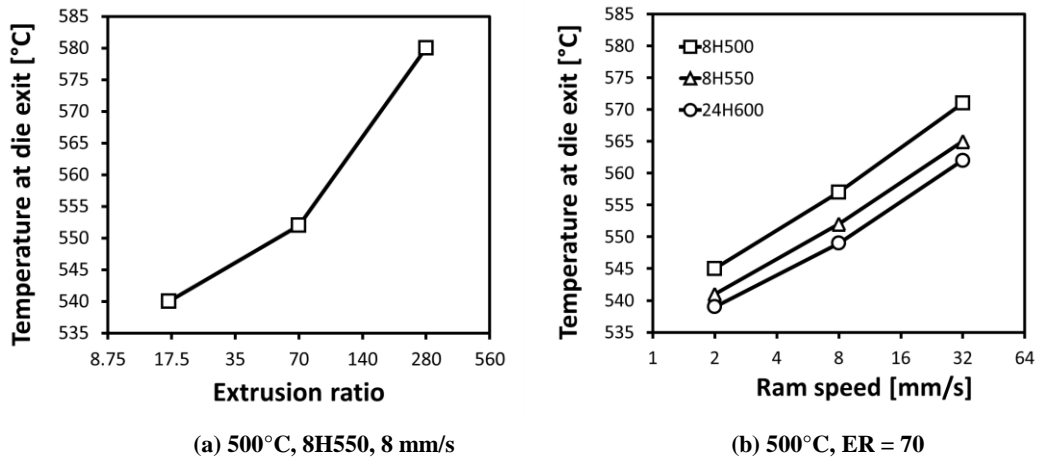


Figure 5-8 Model predictions for the effect of extrusion conditions on the temperature of the extrudate center at the mid-length section after it exits the die; (a) effect of extrusion ratio for ram speed of 8 mm/s, billet temperature of 500°C and homogenization of 8 hours at 550°C, (b) effect of ram speed for different homogenization conditions, billet temperature of 500°C, and extrusion ratio of 70.

Figure 5-9 shows the effect of ram speed on the predicted temperature histories at the center and surface of the extrudate for two different extrusion temperatures. At ram speeds of 2 and 8 mm/sec the material cools down to less than 250°C during the water quench but at a ram speed of 32 mm/sec the material remains at a high temperature even after the water quench. At a high ram speed of 32 mm/sec and extrusion ratio of 70 the extrudate moves with the speed of 2.24 m/sec and it spend only 0.625 sec in the quench bath which is not long enough to cool the material significantly. The effect of this on the microstructure evolution will be discussed later in this thesis.

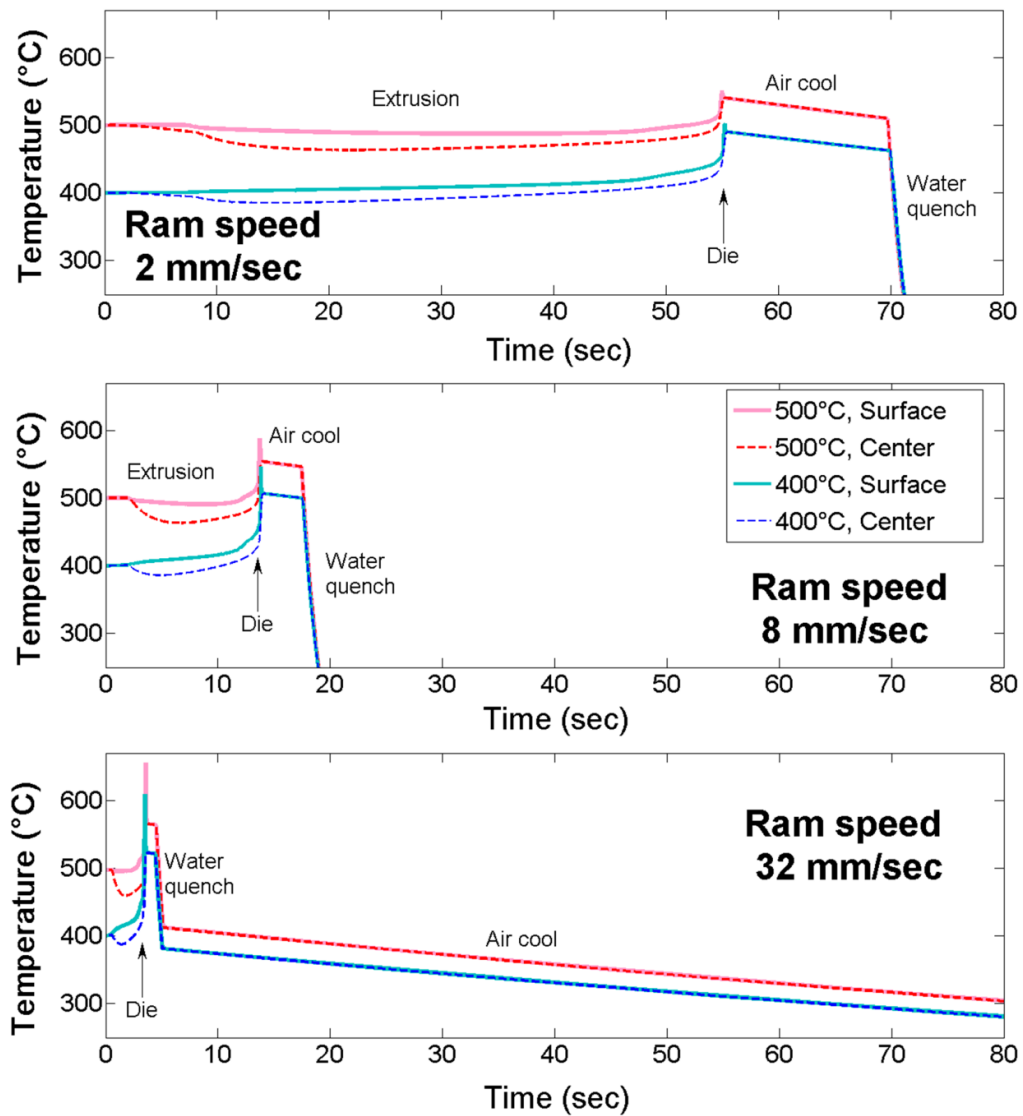


Figure 5-9 Model-predicted temperature histories for the center and surface of the mid-length section of extrudates for three different ram speeds; 2 mm/sec, 8 mm/sec and 32 mm/sec (homogenization = 8H550, extrusion ratio = 70 and billet temperature = 400°C and 500°C)



### **5.1.2.2 Summary**

Model predictions show a big difference between the center and surface of the extrudate in terms of thermomechanical history each experiences. This suggests that the microstructural evolution in the extrudate will be quite different.

Although the simulations show that the strain rate and temperature compensated strain rate (Zener-Hollomon parameter) at the surface are higher than the center most of the time during the extrusion, the average Zener-Hollomon parameter at the center is slightly higher than the surface.

Extrusion ratio, ram speed and pre-extrusion homogenization treatment have significant effect on temperature of the extrudate after it exits the die. Amongst these, the extrusion ratio has the largest and homogenization treatment has the least effect.

Simulations show that the ram speed has a large effect on the temperature history especially after the extrusion. Very high ram speeds (i.e. ~32 mm/sec) with a medium extrusion ratio (i.e. ER=70) can cause the extrudate to remain at high temperatures (>400°C) even after the quench bath.

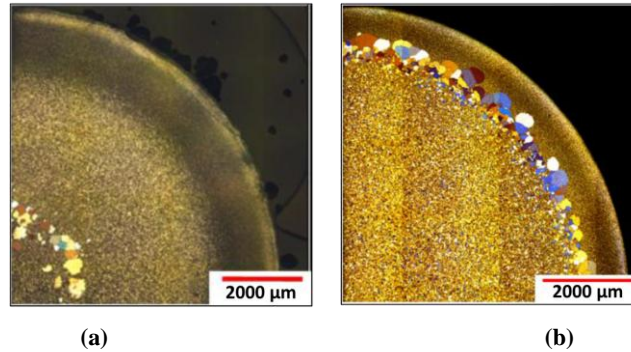
## **5.1.3 Microstructure evolution**

### **5.1.3.1 Microstructure characterization**

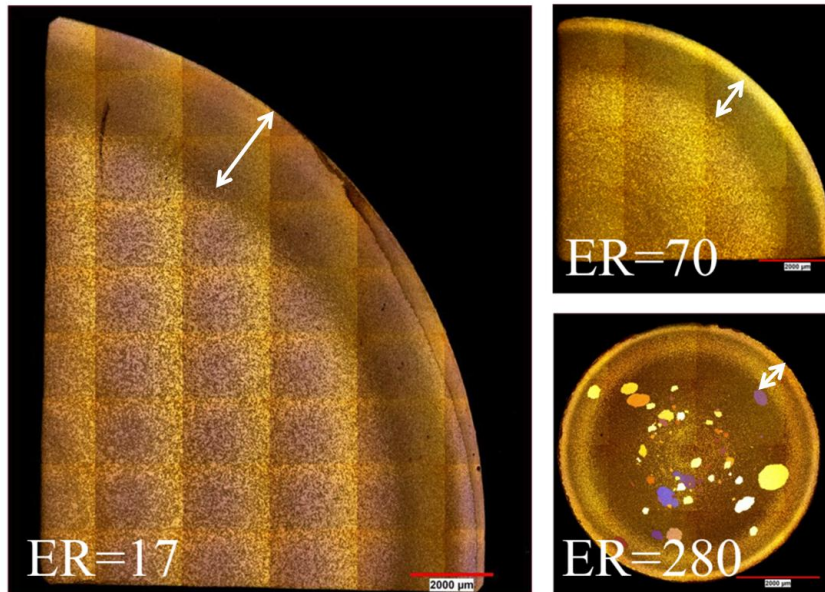
#### **5.1.3.1.1 Optical microscope observations**

Figure 5-10 shows the macrostructures in the as-extruded materials deformed under different extrusion conditions and for different homogenization treatments prior to extrusion. The macrographs shown in Figure 5-10 show the complexity and large variation of microstructure from the center to surface of the extrudates [17] as well as the strong effect homogenization practice can have on the as-extruded microstructures. For the sample shown in Figure 5-10a there are large recrystallized grains at the center of the extrudate while the rest of the transverse section appears to show unrecrystallized structure. One might expect that given the differences in thermomechanical history, the recrystallization would happen at the surface rather than the center due to large deformation at the surface of the extrudate. Figure 5-10b shows the fine recrystallized grains at the center parts and large recrystallized grains at subsurface of the extrudate. Optical micrographs for extrudates with other extrusion conditions and homogenization treatments are presented in Appendix B [17]. All the comments about grain structures in optical micrographs that is made in this thesis work has been confirmed by Grajales [17] who studied these structures with high magnification microscopy.

Figure 5-11 shows the cross-sectional macrostructure of extrudates with different extrusion ratios. In the three cases shown here, a relatively thick layer of a different colour is observed at the surface of the extrudate suggesting that a different structure at the surface and subsurface exists relative to the center of extrudate. As shown in Figure 5-11, the sample extruded with an extrusion ratio of 280 shows evidence of some large recrystallized grains spread across the section.

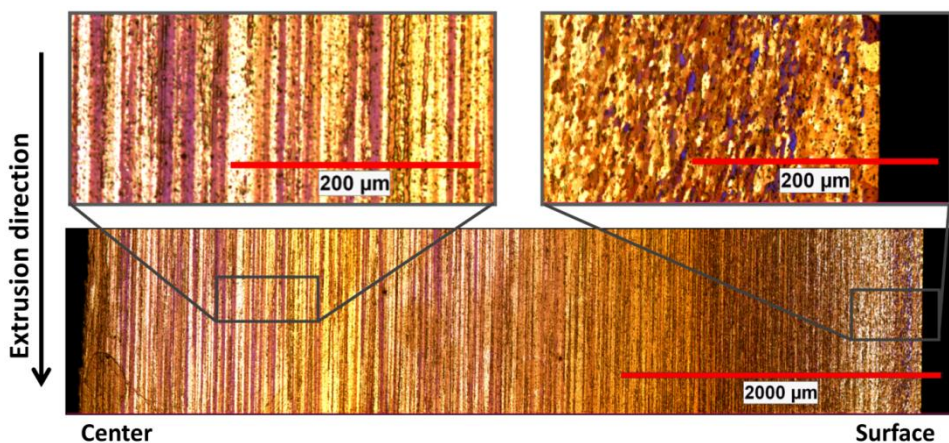


**Figure 5-10** Optical macrographs showing the quarter section of as-extruded macrostructure across the radius of extrudates with ER = 70; (a) homogenization of 8H500, billet temperature = 400°C, ram speed = 32 mm/sec, (b) homogenization of 24H600, billet temperature = 350°C, ram speed = 8 mm/sec (with permission from Grajales [17]).



**Figure 5-11** Optical macrographs showing the as-extruded transverse macrostructure across the radius of extrudates with three different extrusion ratios of 17, 70 and 280 (extrudate diameters of 1", ½" and ¼" or in millimeters; 25.4, 12.7 and 6.35 mm, respectively), for all three cases the billet temperature is 400°C and homogenization condition is 8 hours at 550°C. Ram speed for ER = 17 is 8 mm/sec and that of ER = 70 and 280 is 2 mm/sec, Macrographs reproduced with permission from Grajales [17].

Higher magnification micrographs were then prepared using longitudinal sections of the extrudates to investigate the grain structure through the radius of the extrudates (Figure 5-12). As observed in Figure 5-12, there is a fibrous structure of deformed grains at the center of the extrudate but at the surface no fibrous grains could be identified and the structure appeared to consist of granular fine grains. There are some possibilities for the mechanism of formation of this structure at the surface of the extrudate; discontinuous dynamic recrystallization (DDRX), continuous dynamic recrystallization (CDRX), geometric dynamic recrystallization (GDRX) or static recrystallization after extrusion (SRX). It is unlikely that static recrystallization has occurred as the material was immediately water quenched after the extrusion and a large number of dispersoids were introduced during the homogenization process creating substantial Zener drag (143 kPa for this case). On the other hand discontinuous dynamic recrystallization is less likely to happen in aluminum alloys due to high stacking fault energy [21] (refer to 2.1.2. for more explanation on the effect of SFE on microstructure evolution).



**Figure 5-12 Optical micrograph showing the longitudinal structure of extrudate from center to surface for an extrusion ratio of 70, homogenization treatment prior to extrusion: 550°C for 8h, billet with preheat of 400°C and ram speed of 2 mm/s, magnified graphs clearly show the fibrous structure at the center (upper left) and granular fine structure at the surface (upper right) [35].**

More investigations were performed using EBSD to quantify details of the extrudate structure, especially close to the surface since it appeared to be so different from that seen at the center.

### 5.1.3.1.2 EBSD microscopy

Figure 5-13 shows the measured EBSD maps from a longitudinal section of the extrudate at different locations. Based on optical microscope observations three locations from each sample were chosen for EBSD microscopy. Two 0.1x0.1 mm scans, one at the subsurface and one at the center, were performed to confirm the optical microscope observations about a fibrous center versus a granular surface. These scans were then also used for subgrain size measurements. The third scan with dimensions of 1x0.1 mm was taken from between center and surface to capture the transition from the fibrous to the granular grain structure. This long scan is also shown in Figure 5-14 with higher magnification. To better identify the grain structure the Euler colours are not shown and only HAGBs (bold black) and LAGBs (light gray) are presented in Figure 5-14. Long scans were performed to capture the transition location from a fibrous to a granular grain structure. Referring to Figure 5-14 the location of the transition for this sample falls in the limits of the scanned area.

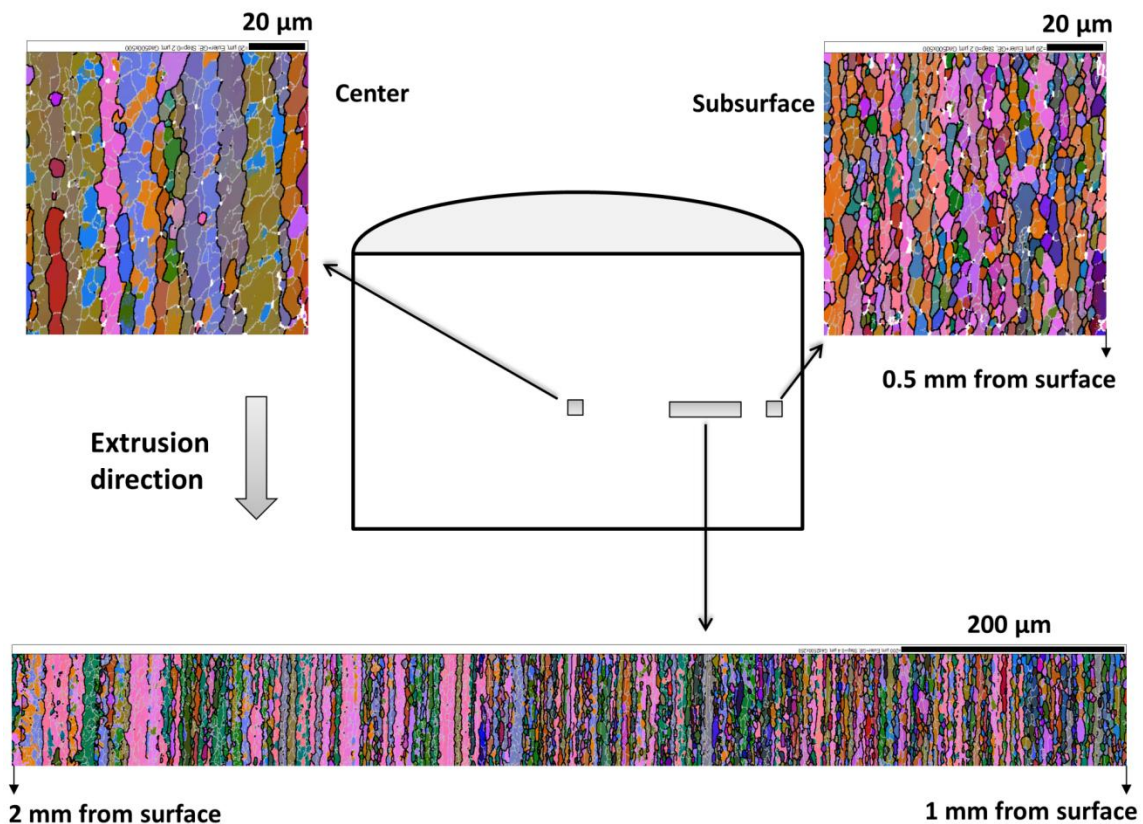


Figure 5-13 Locations on longitudinal section of extrusion sample chosen for EBSD analyses. The maps are for sample #4 in Table 4-4.

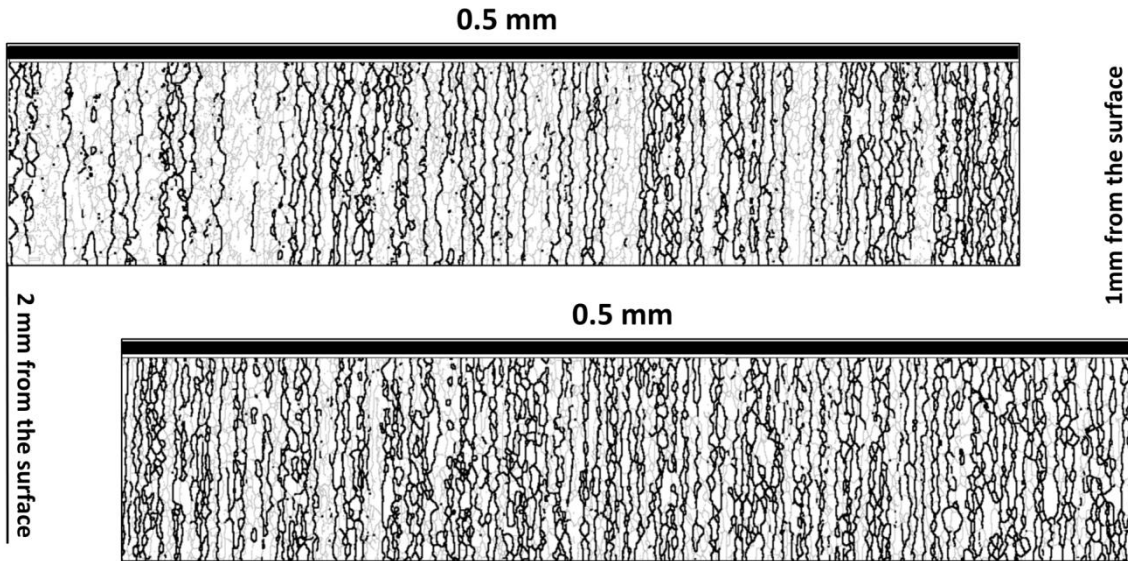
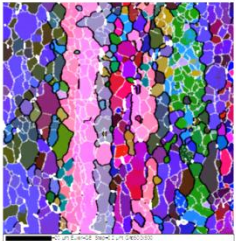
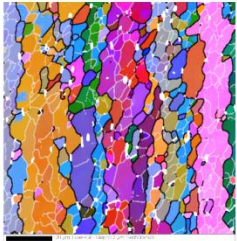
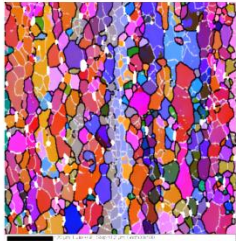
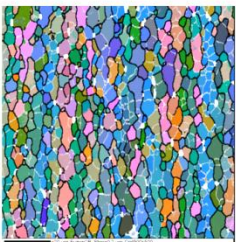




Figure 5-14 “1 mm long” EBSD map shown in Figure 5-13 split into two parts for magnification (sample #4 in Table 4-4).

The fibrous structure of heavily deformed grains is obvious at the center of the extrudate (Figure 5-13, top left) and the thickness of the grains are just a few times greater than the subgrain size. But at the surface (Figure 5-13, top right graph showing the surface structure) the majority of the grains have just one row of subgrains along their thickness and also the lengths of the grains are much more less than that at the center. These observations suggest the occurrence of grain splitting or fragmentation due to larger amount of deformation at the surface of extrudate. Referring to the 1 mm long scan taken from the subsurface (bottom EBSD map in Figure 5-13) it is observed that at the left side of the map which is closer to the center of the extrudate the fibrous structure is dominant and as we go closer to the surface the thickness of the fibers decreases and a more granular structure appears. The reason might be that the smaller grains start to pinch off when their thickness becomes equal to or less than the subgrain size. Moving from right to the left of the map more grains meet the criteria of pinching-off and a more granular structure has formed.

Figure 5-15 compares the center and surface structure for three different extrusion ratios. The homogenization condition and the billet temperatures are the same for all three conditions. The previous results are repeated for center and surface grain structure for all three extrusion ratios. All surfaces show the granular and more equiaxed structure and a fibrous structure is dominant at the center except for the largest extrusion ratio (ER = 280). In this case due to very large extrusion ratio some of grains at the center could fragment into smaller grains as well.

Sample	#1	#2	#3
Extrusion Ratio	17	70	280
Center			
Subsurface			

**Figure 5-15 EBSD maps from center and subsurface of extrusions with different extrusion ratios. Left sides of subsurface maps are at 0.8, 0.5 and 0.3 mm from the surface respectively for extrusion ratios of 17, 70 and 280 (for detailed extrusion conditions for each case refer to Table 4-4).**

In Figure 5-16 further analysis of the EBSD maps was done to characterize the nature and mis-orientation of neighbouring grains at the subsurface of the extrudate. The vectors in the extrusion direction and corresponding cumulative misorientation graphs (V1 and V2 in Figure 5-16a and V1 in Figure 5-16b) suggest that the vector lines are crossing original grains that have fragmented into smaller grains. For example for V1 in Figure 5-16a the majority of the line scan crosses small brown areas with mis-orientations of 10-18 degrees. The small range of mis-orientation for these separate grains ( $\sim 8^\circ$ ) suggests that they might have originally belonged to one single grain. Of course because the image is just showing a 2D section of the material the perforation mechanism for GDRX proposed by McQueen et al. [22] is also possible for these grains so that they might still be connected to each other (refer to Figure 2-2). In contrast to vertical vectors (in extrusion direction) the horizontal vectors are in transverse direction (along the radius of the extrudate) are crossing a number of thin areas with random misorientation changing from 0 to 62 degrees that suggests these lines are crossing a relatively large number of elongated grains that belonged to different original grains in the billet.

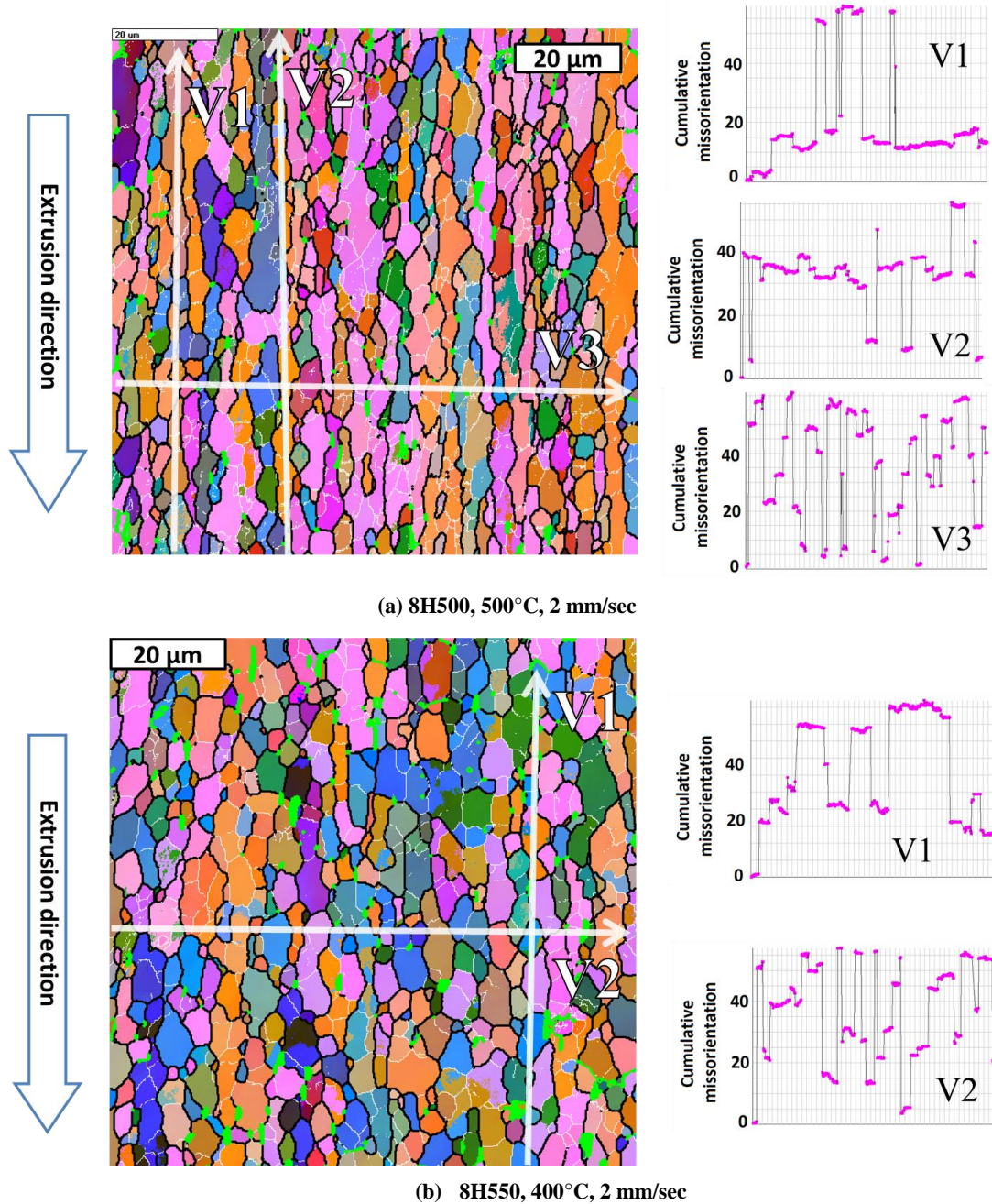
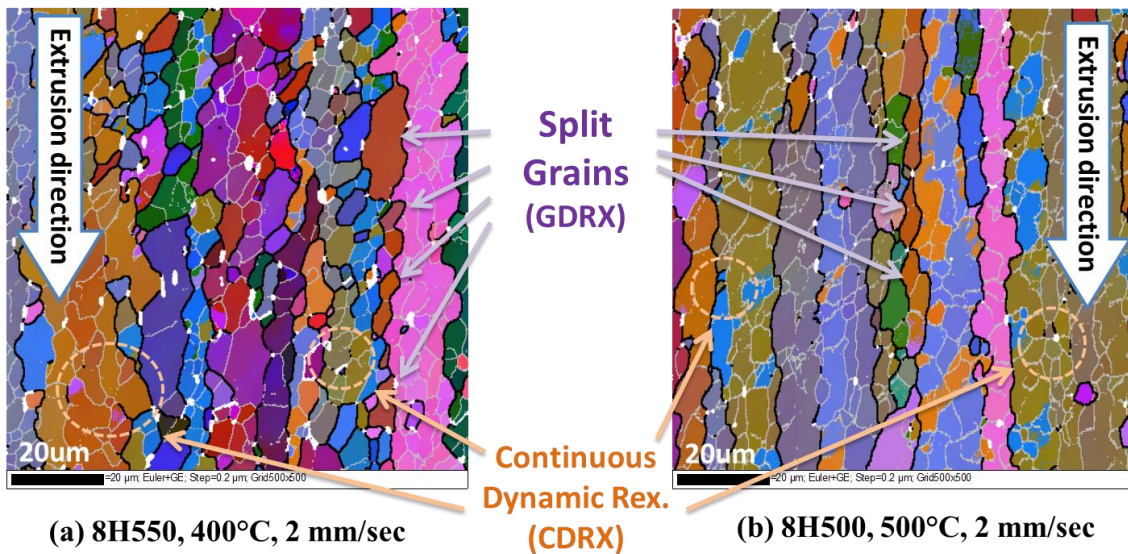


Figure 5-16 Cumulative misorientation line scans from selected locations at subsurface of extrudate showing the split grains in extrusion direction and random mis-orientation in the transverse direction (a) sample #4 and (b) sample #2 in Table 4-4.

Figure 5-17 shows suggested microstructural mechanisms responsible for some features observed in the EBSD maps taken from the center of the extrudates which were extruded at two different temperatures. In Figure 5-17a, grain boundary serrations are relatively coarse and irregular compared to Figure 5-17b in which they appear finer and more regular. The reason for this difference is not

identified and needs more experimental investigation. Apparently it could arise from the effect of homogenization (dispersoids) or deformation temperature. Dispersoids can pin the grain boundaries and the less the number of dispersoids is, the more mobile the grain boundaries are. The extrusion sample that was homogenized at 550°C before the extrusion has less number of dispersoids than the one homogenized at 500°C so that the grain boundaries can move faster and the serrations can take place easier. On the other hand deformation temperature has a large effect on the stored energy for subgrain growth as well as the mobility for boundary migration. At lower temperatures, higher stored energies can be achieved due to higher flow stresses but the mobility of boundaries decreases when the temperature decreases.



**Figure 5-17 EBSD maps from longitudinal section at the center of the extrudate, possible microstructural mechanisms for some features indicated on the figure, (a) sample #2 and (b) sample #4 in Table 4-4 (ER = 70).**

In case of larger serrations, grain boundaries could meet each other in smaller strains so that it may encourage the GDRX to happen sooner than finely serrated boundaries. Figure 5-18a and b show the “1 mm long” scans from a location close to the surface of the extrudate (right side of the maps are at 1 mm distance from the surface of the extrudate) for two extrusion shown in Figure 5-17a and b, respectively. More equiaxed small grains are observed in Figure 5-18a than Figure 5-18b and it seems the transition from fibrous to granular structure in Figure 5-18a is closer to the center of the extrudate than that of Figure 5-18b. It will be shown later that for both cases the grain deformation and subgrain



size are similar so it may be concluded that the difference in grain structure observed here could be due to serration effect discussed above.

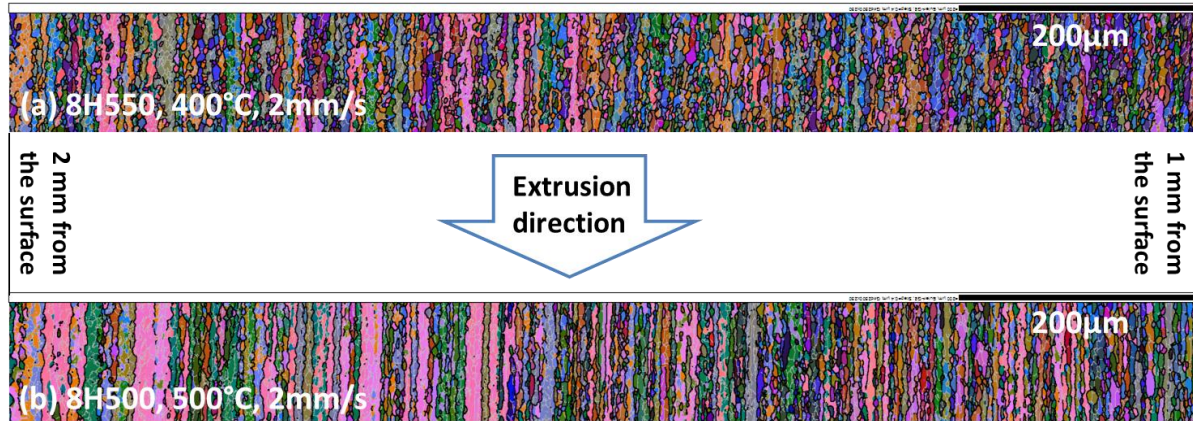


Figure 5-18 “1 mm long” EBSD maps from longitudinal sections at a location between the center and surface of the extrudates (refer to Figure 5-13 for exact location), (a) sample #2 and (b) sample #4 in Table 4-4.

### 5.1.3.2 Geometric Dynamic Recrystallization (GDRX)

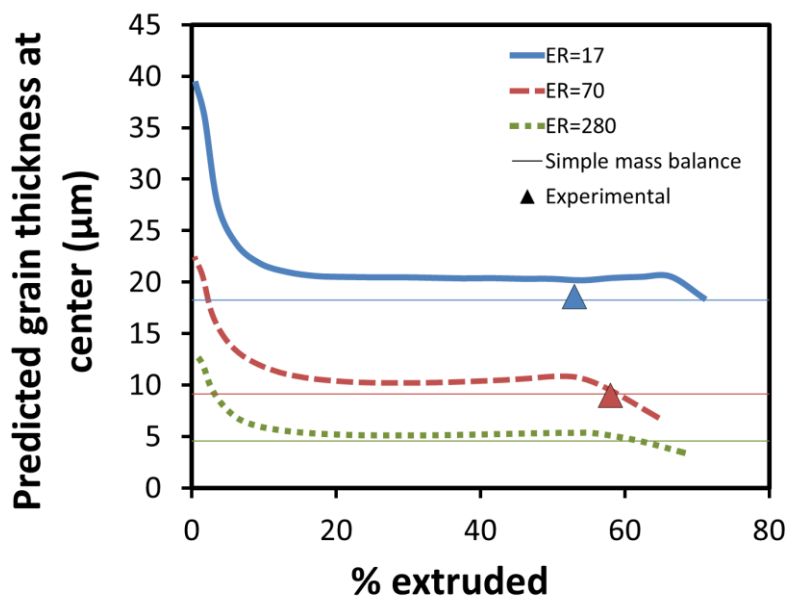
#### 5.1.3.2.1 Grain thickness during extrusion

Table 5-1 compares the model predicted grain thickness with the experimental measurements and a simple mass balance calculation at the center of the extrudate at a mid-length section. In the simple mass balance calculation the deformation is assumed to be homogenous such that the ratio of the final grain thickness to the initial grain thickness is equal to the ratio of the extrudate diameter to the billet diameter, i.e.,  $\frac{t}{t_0} = \frac{d_e}{d_b}$ , where the initial grain thickness is that measured in the billet ( $t_0 = 73 \mu m$ ) [17], the starting billet diameter is  $d_b = 101.6 mm$  and the extrudate diameter ( $d_e$ ) is 25.4, 12.67 and 6.35 mm for extrusion ratio 17, 70 and 280, respectively.

Table 5-1 Grain thickness comparison at the center of the extrudate (experimental results taken from [17])

ER	Position along the extrudate	Experimental measurement ( $\mu m$ )	Model prediction ( $\mu m$ )	Mass balance calculation ( $\mu m$ )	%Difference (model predictions to experimental measurement)
17	53%	18.6	20.1	18.4	+ 7.5%
70	58%	9.0	9.4	9.1	+ 4.4%
280	62%	---	4.6	4.6	---

Although the experimental measurements appear to match better against the simple mass balance calculations, the model predictions can show how the grain thickness at the center changes dramatically along the extrudate length based on details of the strain history. Figure 5-19 shows the model predicted grain thickness at the center line along the extrudate length for three extrusion ratios (17, 70 and 280). As observed, the predicted grain thickness at the center is greater than the mass balance prediction for most of the extrudate length. After 50% of the extrudate length, the model predicted grain thickness starts to decrease to less than mass balance. This decreasing trend seems to start sooner for extrusion ratios of 70 and 280 than the extrusion ratio of 17 but the reason is that the occurrence of this grain thickness decreasing trend is related to the “back-end” defect so that it is affected more by the distance of ram and die rather than the extrusion ratio. The length of the billet for extrusion ratio of 17 was 400 mm and for extrusion ratios of 70 and 280 it was 200 mm so that at the same percentage of extrusion the distance between the ram and die is less for shorter billets (ER = 70 and 280). On the other hand the grain thickness decreasing trend for extrusion ratio of 280 starts slightly later than extrusion ratio of 70 which confirms that the lower extrusion ratio is not the main reason for relative delay at extrusion ratio of 17.



**Figure 5-19 Comparison of model predicted (dashed lines) changes in the grain thickness along the length of the extrudate at the center-line relative to the mass balance approach (solid line) and experimental measurements (symbols for two different extrusion ratios of 17 and 70 (experimental results taken from [17])).**

Simulations show that for a billet length of 200 mm, the grain thickness reaches steady state value at the center-line during the first 20% of the extrusion and remains at this value until ~50% of the extrusion has occurred. Figure 5-20 shows the spatial change in the predicted grain thickness through the x-section of the extrudate at three different locations along the length of the extrudate (50%, 58% and 65% extruded). As shown in the figure, the grain thickness at the surface of the extrudate does not change considerably along the length of the extrudate.

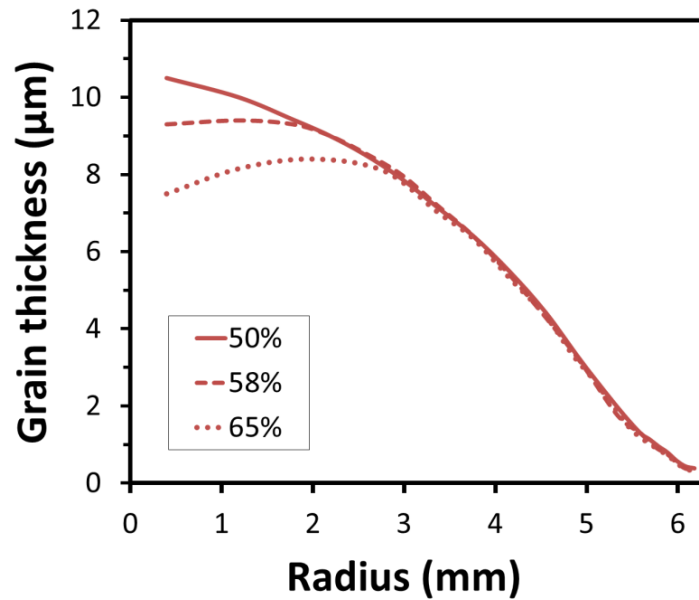


Figure 5-20 Model-predicted spatial grain thickness across the radius of the extrudate for three different locations along the extrudate using an extrusion ratio of 70, ram speed = 2 mm/sec and temperature = 500°C.

Figure 5-21 shows the model prediction for distribution of grain thickness across the radius of the extrudate for different extrusion conditions. Figure 5-21a depicts the effect of extrusion ratio on grain thickness and Figure 5-21b depicts the effect of temperature and ram speed. It can be concluded that compared to the effect of extrusion ratio, the effect of other extrusion conditions (extrusion temperature and ram speed) on the distribution of grain thickness across the extrudate is negligible.

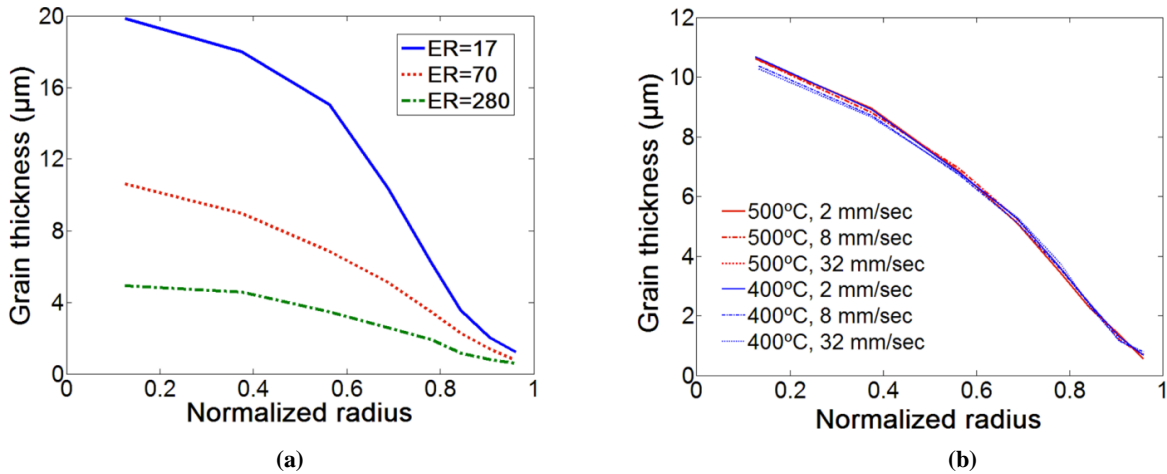


Figure 5-21 Grain thickness across the radius of extrudate at a mid-length section for (a) different extrusion ratios with extrusion temperature of 500°C and ram speed of 8 mm/s, (b) different temperatures and ram speeds with extrusion ratio of 70.

### 5.1.3.2.2 Mechanism for GDRX

As indicated in the literature GDRX has been shown in aluminum alloys that experience severe plastic strain to the point where the thickness of the grains approaches the size of the subgrains [21]. A simple GDRX mechanism is suggested here for a small grain between two large grains. Figure 5-22 shows the evolutions one single grain could undergo during a large scale deformation until pinch-off and GDRX. The grain thickness reduces with deformation until it reaches the subgrain size (Figure 5-22 a to d) and with more deformation the grain resists thinning, so that, finally to keep the continuity of the material (neighbouring grains) it pinches off to form smaller grains (Figure 5-22 d to e). This mechanism can then be extended to larger grains.

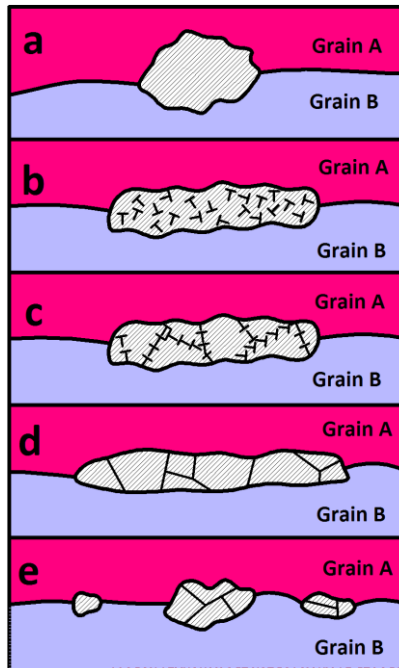
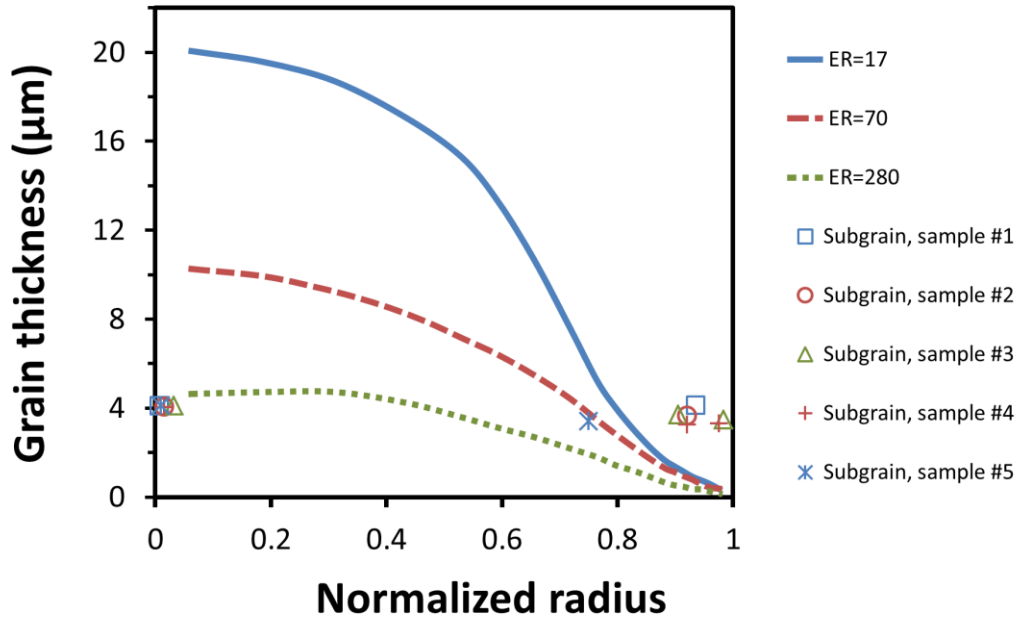


Figure 5-22 Schematic showing the stages that a grain undergoes during large strain deformation: (a) undeformed state, (b) dislocation jungle formation during the deformation, (c) dislocations reorder and develop cell structure or subgrains (DRV), (d) and (e) with more deformation the thickness of grain decreases until it reaches a critical value (i.e. subgrain size) under which the grain starts to split up to several grains.

Figure 5-23 compares the model predicted grain thickness with the measured subgrain size for extrusion samples listed in Table 4-4. As shown, the predicted grain thickness decreases rapidly from the center towards the surface of the extrudate and somewhere near the surface it reaches the measured subgrain size. From this point to the surface, the predicted thickness of grains is less than subgrain size but in theory the grain thickness cannot be less than subgrain size. So that grain pinch-off and Geometric Dynamic Recrystallization (GDRX) is suggested at the surface layer.



**Figure 5-23 Model-predicted grain thickness for different extrusion ratios across the diameter of the extrudate as well as measured subgrain size at different positions along the extrudate diameter for different extrudates listed in Table 4-4.**

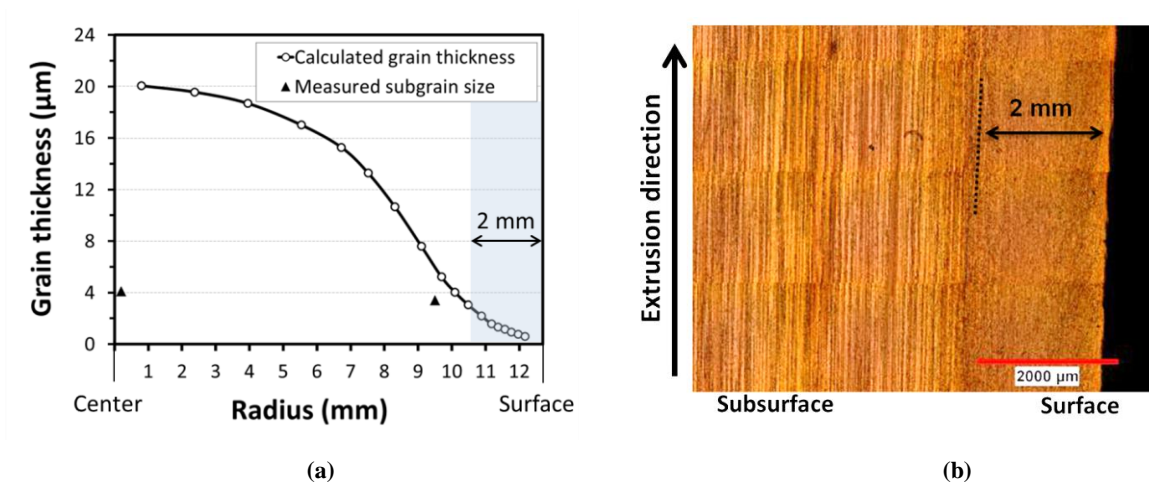
### 5.1.3.2.3 GDRX layer thickness

The FEM model was used to estimate the deformed grain thickness through the radius of the extrudate. The main input parameter of the model is the original grain size which was measured by optical microscopy technique. The measured average grain diameter in the billet is 73  $\mu\text{m}$  [17]. No considerable changes of grain size were found from center to the surface of the billet.

Figure 5-24a shows the calculated grain thickness from the center to the surface of the extrudate using the initial measured grain size of 73  $\mu\text{m}$ . As shown, the predicted grain thickness decreases rapidly from the center towards the surface of the extrudate and somewhere near the surface it reaches the measured subgrain size. Hereafter this point is called “critical radius”. Theoretically beyond critical radius the grains would split up to smaller grains and GDRX would occur. But in reality there is a distribution of grain size so that the grains that are smaller than average grain size would undergo GDRX sooner than the larger grains. So there might be partial GDRX for the small original grains within the critical radius as well as fibrous grains outside the critical radius for the large original grains.

Figure 5-24b shows a typical longitudinal microstructure observed at the surface of extrudates with an extrusion ratio of 17. As shown in Figure 5-24b, there is a relatively thick layer at the surface

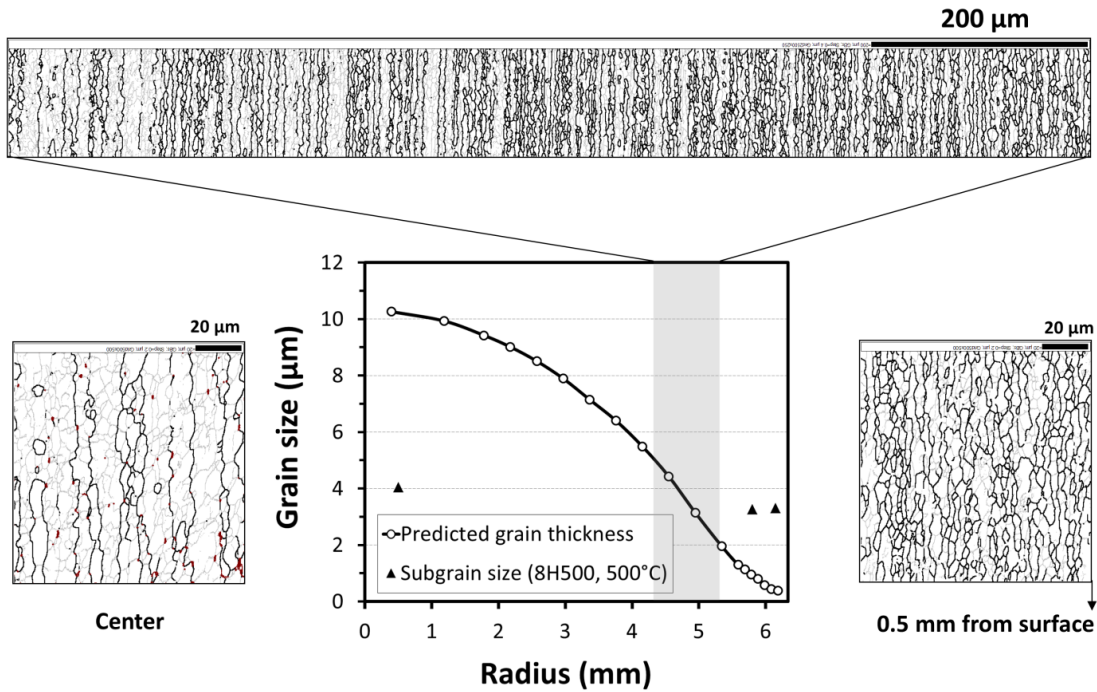
of the extrudate in which no fibrous structure can be recognized in the image. The thickness of this layer (2 mm) is in good agreement with the predicted thickness of GDRX on which the average thickness of deformed grains falls below the measured subgrain size.



**Figure 5-24 (a) Model predictions for grain thickness and subgrain size measured by EBSD, (b) Optical micrograph for the surface of the extrudate, (for both a and b: Extrusion ratio=17, Billet preheat temperature=500°C and ram speed = 8 mm/s, position along the extrudate = 53%) [35].**

Figure 5-25 shows the predicted average grain thickness from center to the surface of extrudate for extrusion ratio of 70 as well as measured subgrain size for center and surface. EBSD maps, showing HAGBs in bold black lines, are confirming the predictions for fibrous grains at the center (where the subgrain size is well below the grain thickness) and granular split grains at the surface (where the subgrain size is much larger than the grain thickness).

Looking at the “1 mm long” EBSD map shown in Figure 5-25 one may suggest that the transition from fibrous to granular grain structure (critical radius) falls between limits of this graph which is in agreement with model predicted results for grain thickness. As mentioned before the curve shows the average grain thickness so the larger and smaller grain would have different scenarios. Taking into account a distribution of grain size, experimental results are in good agreement with model predictions for estimation of the critical radius.



**Figure 5-25 Predicted grain thickness versus measured subgrain size for extrusion ratio of 70, ram speed of 2 mm/s, billet temperature of 500°C, homogenization of 8 hours at 500°C and the position of 52% along the extrudate (EBSD maps on sides of the graph correspond to locations of subgrain size measurements at center and surface and the “1 mm long” map corresponds to highlighted region on the graph).**

#### 5.1.3.2.4 Effect of extrusion ratio – model predictions

Figure 5-26 represents the method used for estimation of GDRX layer thickness at the surface of the extrudate. In this method GDRX is predicted for locations at which the grain thickness is less than average measured subgrain size. The thick gray bar shows the range of subgrain size measured for the extrudates with different extrusion conditions. As observed for the extrusion ratio of 280 the average grain thickness at the center is slightly above the range of measured subgrain size so that a considerable number of grains that were just smaller than the average grain size would undergo GDRX even at the center of the extrudate.



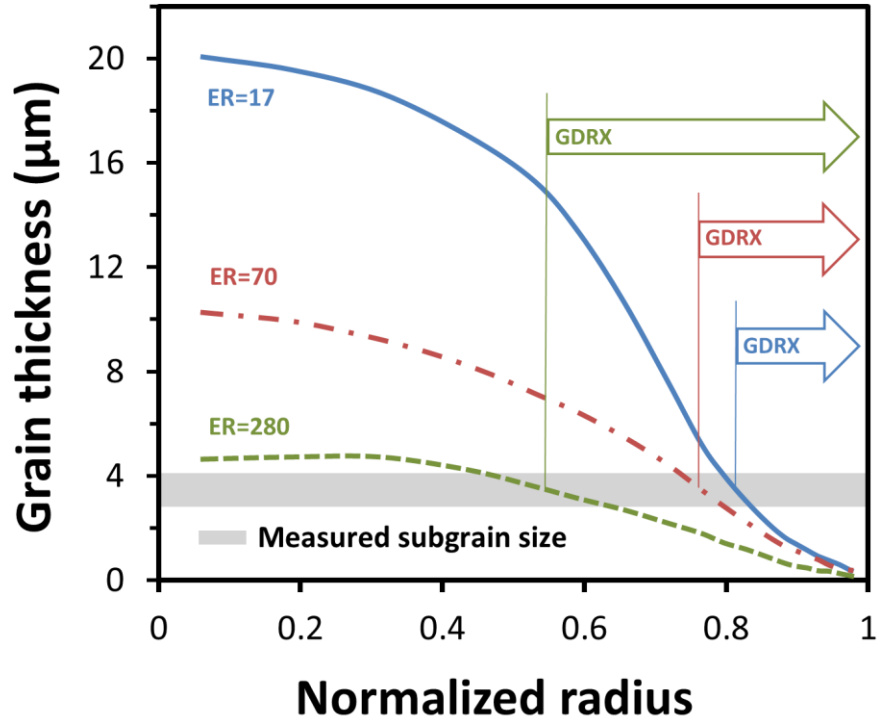


Figure 5-26 Estimation of GDRX layer thickness using the average subgrain size at the surface of the extrudate.

The model-predicted effect of the extrusion ratio on the thickness of GDRX layer from the surface in the extrudate is shown in Figure 5-27. Although the thickness of the GDRX decreases with the extrusion ratio (Figure 5-27a) the normalized thickness of GDRX at the surface is increasing (Figure 5-27b). Figure 5-27 show these model predictions graphically as a function of extrusion ratio. The error bars shows the range of estimated GDRX layer thickness based on the range of the measured subgrain size. Experimental measurements are the average surface layer thicknesses with different color visible on optical macrographs (i.e. Figure 5-10).

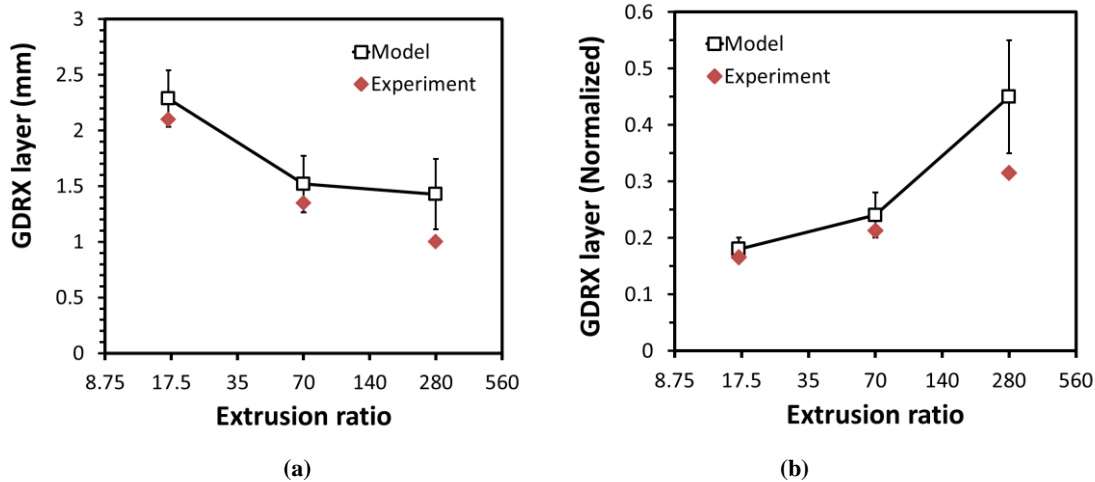


Figure 5-27 Effect of extrusion ratio on the thickness of the GDRX layer, (a) thickness in mm, (b) normalized based on extrudate diameter.

### 5.1.3.3 Stored energy and driving pressure for recrystallization

#### 5.1.3.3.1 Zener drag

Using Equation 2-17 the Zener drag for different homogenization conditions was calculated given the experimentally measured values for constituent particles [43] and simulation results for dispersoids [112]. In this work, the total drag pressure for recrystallization (Zener drag) was calculated by adding up the drag pressures from dispersoids and constituent particles. Table 5-2 shows the volume fraction and average radius of dispersoids and constituent particles as well as the calculated Zener drag for billets with different homogenization heat treatments. The effect of homogenization on the Zener drag is shown graphically in Figure 5-28 for three different homogenization treatments studied in this work.

Table 5-2 Constituent particle and dispersoid data for various homogenization treatments [43, 112] and calculated Zener drag.

Homogenization treatment	Constituent particles			Dispersoids			Total Zener drag (kPa)
	Volume fraction, $F_v$ (%)	Average radius, $r$ ( $\mu\text{m}$ )	Zener drag (kPa)	Volume fraction, $F_v$ (%)	Average radius, $r$ (nm)	Zener drag (kPa)	
8 h at 500°C	2.8	0.9	15	1.4	28	243	258
8 h at 550°C	3.5	1	17	1.4	54	126	143
24 h at 600°C	3.9	1.2	16	---	---	---	16

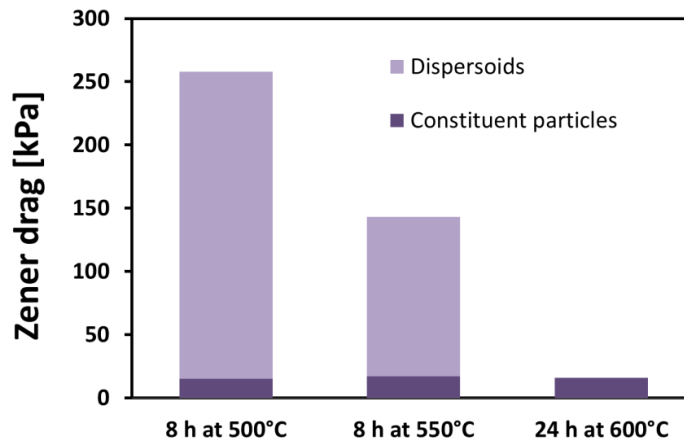
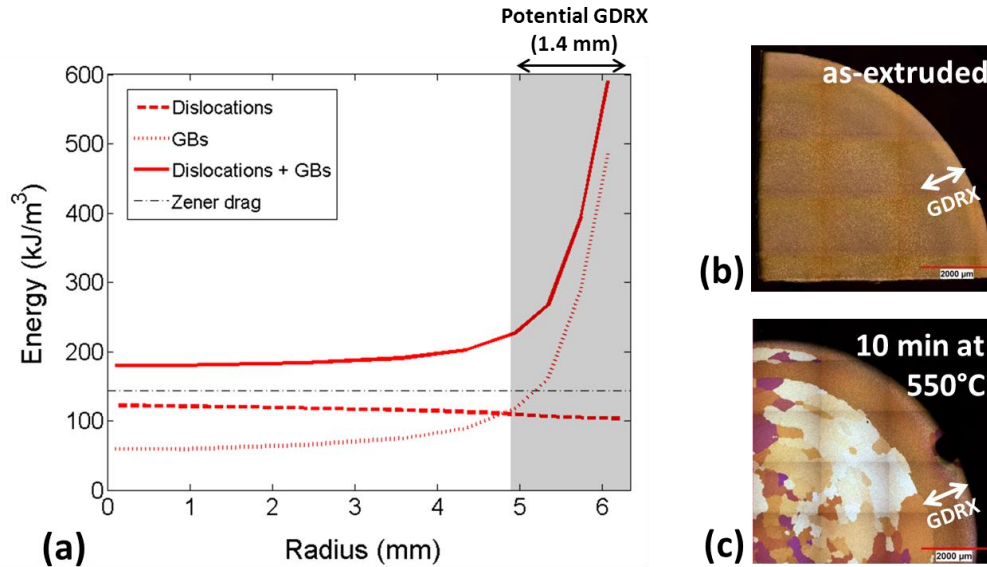


Figure 5-28 Predicted effect of homogenization on Zener drag.

#### 5.1.3.3.2 Stored energy – distribution across the radius

The calculated stored energy in dislocation structure and grain boundaries (GBs) is shown in Figure 5-29a from center to the surface for a selected extrusion trial. Figure 5-29 also includes two micrographs showing quarter section of the extrudate for as-extruded sample (Figure 5-29b) and a sample annealed for 10 minutes at 550°C. Compared to the homogenization condition of the original billet (8 hours at 550°C) the annealing at temperature of 550°C for 10 minutes does not considerably alter the precipitates size and distribution in the extrudate so that the Zener drag changes are not significant during the annealing treatment. Also, the annealing temperature is so close to the measured and model predicted die exit temperature of the extrudate, 548°C and 554°C respectively. No recrystallization in the as-extruded sample versus recrystallized structure in the annealed sample show that the extrudate did not have enough time for recrystallization before it reaches the quench bath (~3.5 sec in this case) but eventually due to positive driving pressure of recrystallization it will recrystallize when held at very high temperature. This observation is consistent with model predicted total stored energy that is higher than the Zener drag throughout the extrudate cross section. The highlighted region on the graph in Figure 5-29a shows the predicted GDRX layer at the surface which seems to overlap the unrecrystallized area in Figure 5-29c. These evidences may suggest that different microstructural mechanisms take place at the center compared to the surface of the extrudate.

Stored energy distribution for different extrusion conditions studied in this work is shown in Appendix A and micrographs for as-extruded samples and post-extrusion annealed samples can be found in Appendix B.



**Figure 5-29** Calculated stored energy and estimated Zener drag compared to microstructure at the same section for homogenization of 8 hours at 550°C, extrusion ratio of 70, ram speed of 8 mm/s and billet temperature of 500°C, (micrographs reproduced with permission from Grajales [113]).

Figure 5-29 along with figures and micrographs provided in Appendix A and Appendix B, indicate that including the grain boundary energy results in more realistic estimations of the total stored energy so that the driving pressure for recrystallization.

### 5.1.3.3.3 Effect of extrusion conditions

In Figure 5-30 the effect of extrusion ratio on the stored energy at the center of extrudate is shown for constant ram speed (8mm/s), temperature (500°C) and homogenization condition (8H550). The total stored energy increases considerably with the extrusion ratio. Stored energy from both grain boundaries and dislocations increases with extrusion ratio. The increase in grain boundary energy is obviously due to more elongation of grains so that more grain boundary area will be produced. The increase in dislocation energy is due to higher extrusion speed and strain rate when using larger extrusion ratio at the same ram speed. Corresponding microstructures for the three extrusions in Figure 5-30 are represented in Figure 5-31 that show a good agreement with stored energy predictions. For extrusion ratio of 17 the total stored energy is less than Zener drag so that there is no driving pressure for recrystallization. For this case no recrystallization is observed even after the annealing treatment (at 550°C for 10 minutes) [17]. For extrusion ratio of 70 as-extruded structure

shows no evidence of recrystallization but after the annealing treatment the center parts shows full recrystallization confirming the positive driving pressure for recrystallization. For extrusion ratio of 280 the driving pressure for recrystallization is so large that even as-extruded material is fully recrystallized.

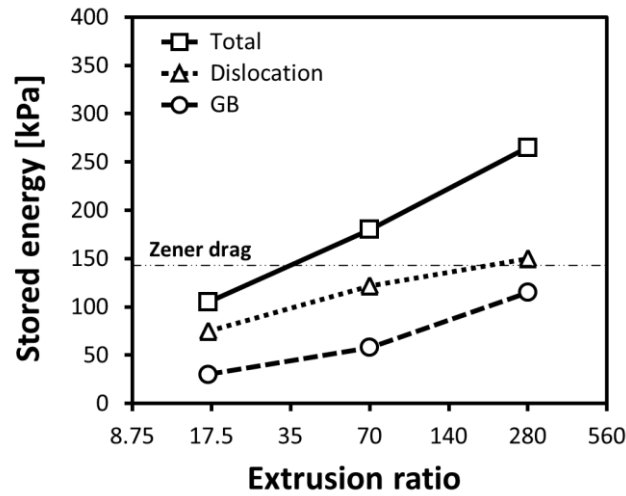


Figure 5-30 Model-predicted effect of extrusion ratio on stored energy at the center of mid-length section of the extrudate, extrusion temperature of 500°C, homogenization of 8 h at 550°C and ram speed 8 mm/s.

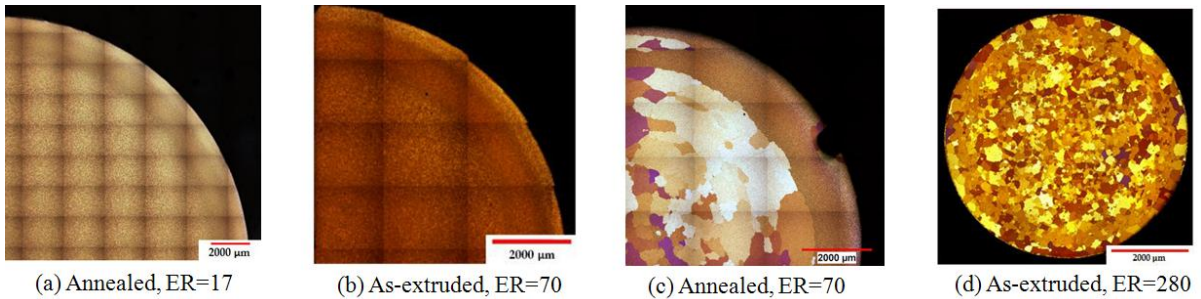
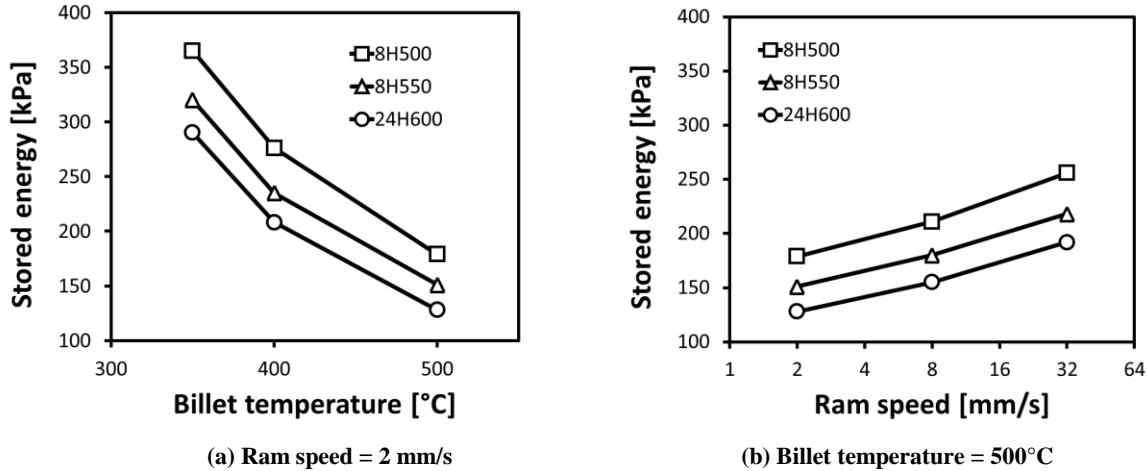


Figure 5-31 Macrographs from x-section of extrudates with the same conditions as extrudates in Figure 5-30, (Annealing treatment: 10 minutes at 550°C), Reproduced with the permission from Grajales [17].

It was shown, in previous section, that other than extrusion ratio, extrusion conditions do not considerably affect the extruded grain dimensions so that the stored energy from grain boundaries does not change considerably with temperature, ram speed or homogenization condition. Figure 5-32 shows the effect of temperature and ram speed on total stored energy in extrudate with three different homogenization treatments. Increasing the homogenization time and temperature would decrease the stored energy in the extrudate as it decreases the flow stress of the material. Gradient of stored energy

versus temperature is larger between 350°C and 400°C than between 400°C and 500°C, indicating that the effect of temperature on the stored energy decreases with increasing the temperature (Figure 5-32a). Figure 5-32b shows that the stored energy changes almost linearly with log(ram speed), indicating that in linear scale the effect of ram speed on stored energy would decrease with increasing the ram speed.



**Figure 5-32 Effect of temperature (a) and ram speed (b) on calculated total stored energy at the center of mid-length section of the extrudate with extrusion ratio of 70, (different homogenization treatments; 500°C for 8 hrs, 550°C for 8 hrs and 600°C for 24 hrs).**

The effect of extrusion temperature, ram speed and pre-extrusion homogenization treatment on total stored energy at the center of the extrudate is shown in Figure 5-33. As observed all three parameters studied here have considerable effect on the stored energy. Calculations show that temperature change from 400°C to 500°C has more effect on stored energy than homogenization and ram speed have while they are changing from one to another value used in this study.

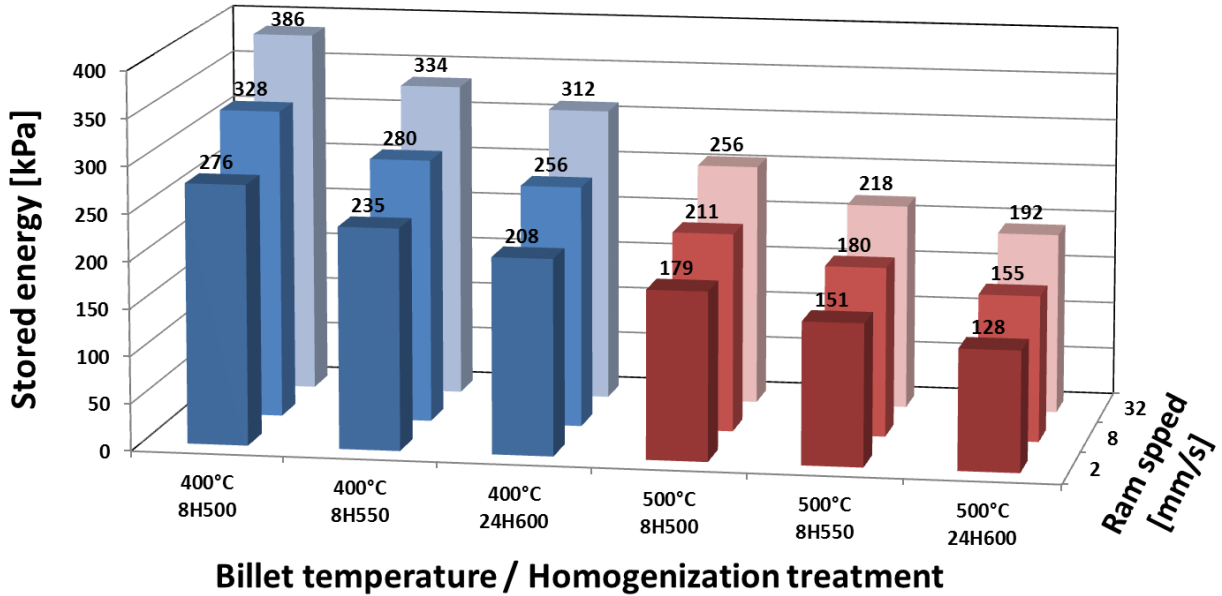


Figure 5-33 Effect of extrusion conditions and homogenization treatment on total stored energy at the center of mid-length section of the extrudate with an extrusion ratio of 70.

The driving pressure of recrystallization was calculated for different extrusion conditions to predict the ability of the material to recrystallization after extrusion. Figure 5-34 shows the driving pressure for recrystallization at the center of the extrudate for the cases shown in Figure 5-33. To obtain the value for driving pressure, the Zener drag was subtracted from the stored energy (4-18). As observed, the samples homogenized at 500°C for 8 hrs followed by extrusion at 500°C will not be able to recrystallize whereas all the others should be able to recrystallize. This shows the important role homogenization plays in the ability of the material to recrystallize after extrusion. These predictions are in agreement with optical microscope observations shown in Appendix B [17] for extruded and annealed structures.

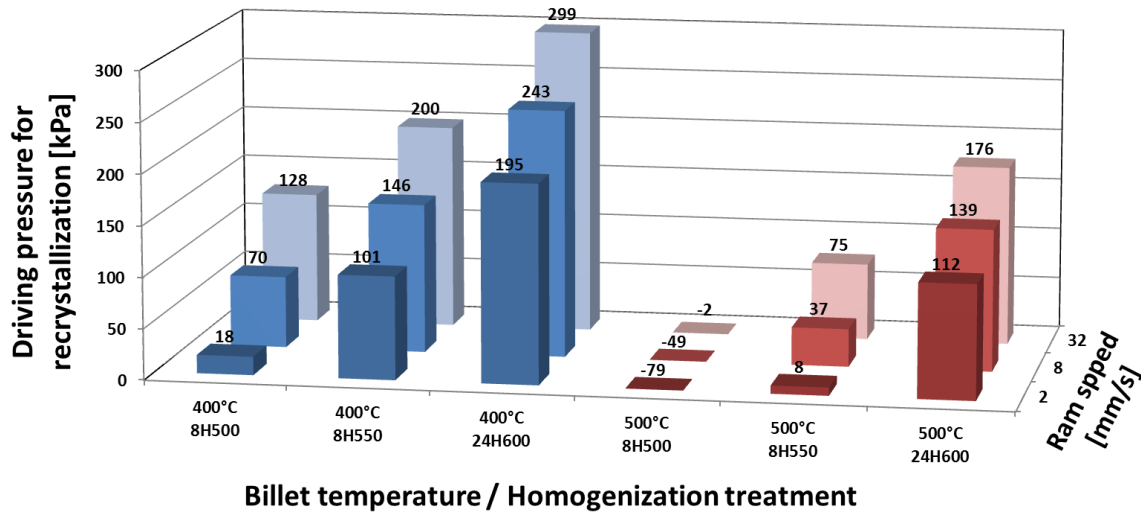


Figure 5-34 Effect of extrusion conditions and homogenization treatment on recrystallization driving pressure at the center of the extrudate with an extrusion ratio of 70.

Due to the quenching that took place immediately after the extrudate exits the die, the recrystallization was prohibited so that as-extruded structures observed with optical microscope [17] are not in agreement with calculated driving pressure. So that the calculated driving pressure was compared to micrographs taken from samples that were annealed after extrusion.

The changes of Zener drag during the extrusion process was ignored in this work due to very low changes in resistivity observed after the extrusion (Appendix C) suggesting that no significant amount of precipitates dissolve in the matrix during the extrusion and vice versa. On the other hand experimental measurements by Geng [43] showed that the constituent particles content and their shape remain unchanged after the extrusion suggesting the fracture of large particles is not likely to happen during the extrusion.

#### 5.1.3.4 Effect of ram speed on as-extruded microstructure

Figure 5-35 shows three micrographs taken from longitudinal section of extrudates with homogenization of 8 hours at 550°C, extruded at 400°C with different ram speeds of 2, 8 and 32 mm/sec. It is observed that for low ram speeds (2 and 8 mm/sec) the microstructure of extrudate consists of heavily deformed grains (fibrous structure) with no evidence of major recrystallization. But with increasing the ram speed to 32 mm/sec the extrudate becomes mostly recrystallized with taking into account the fact that all of extrudates were immediately quenched in water to retain as-extruded structure and to prohibit the recrystallization. Referring to Figure 5-34, all three cases in



Figure 5-35 have considerable driving pressure for recrystallization (101, 146 and 200 kPa respectively for ram speeds of 2, 8 and 32 mm/sec) so that all three cases are willing to recrystallization.

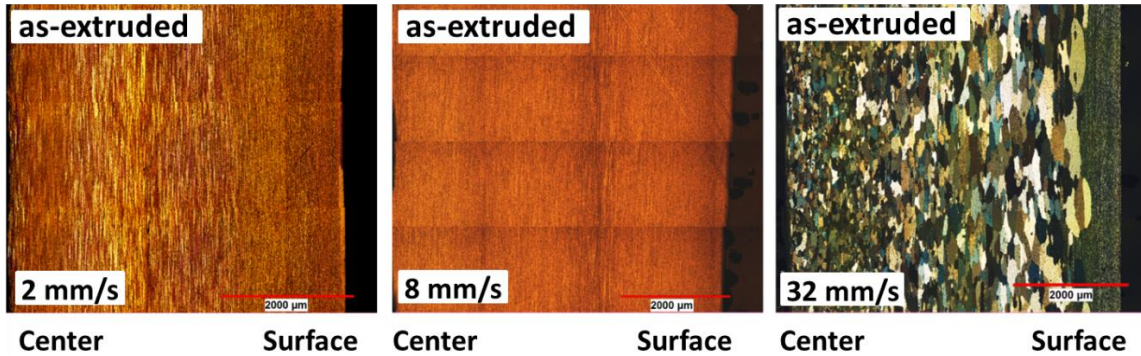


Figure 5-35 Micrographs of longitudinal section from center to the surface of as-extruded samples from extrudates with billet preheat temperature of 400°C, extrusion ratio of 70, homogenization of 8 hours at 550°C and different ram speeds of 2, 8 and 32 mm/sec (Reproduced with the permission from Grajales [17])

Figure 5-36 compares the as-extruded structure of the extrudate with billet preheat temperature of 400°C, extrusion ratio of 70, homogenization of 8 hours at 550°C, ram speed of 2 mm/sec with post-extrusion annealed samples. As observed in the figure, the samples annealed for 1 minute at 525°C and 10 minutes at 525°C show partially and fully recrystallized structures that is consistent with predicted driving pressure of recrystallization for this sample (refer to Figure 5-34).

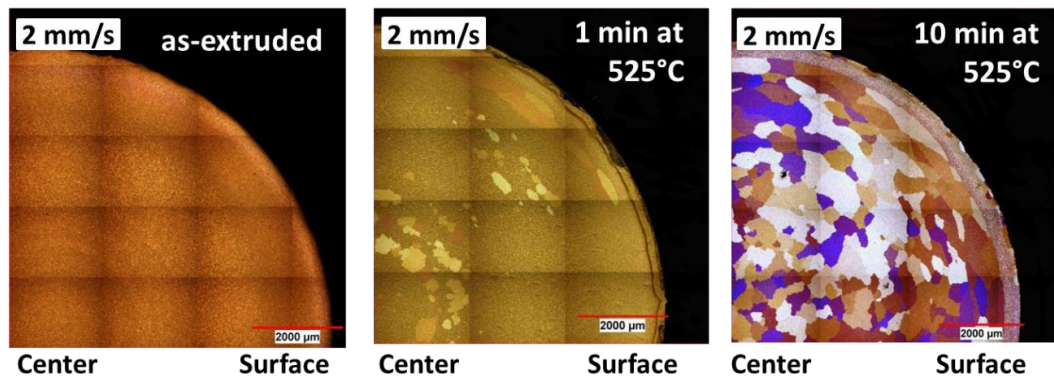
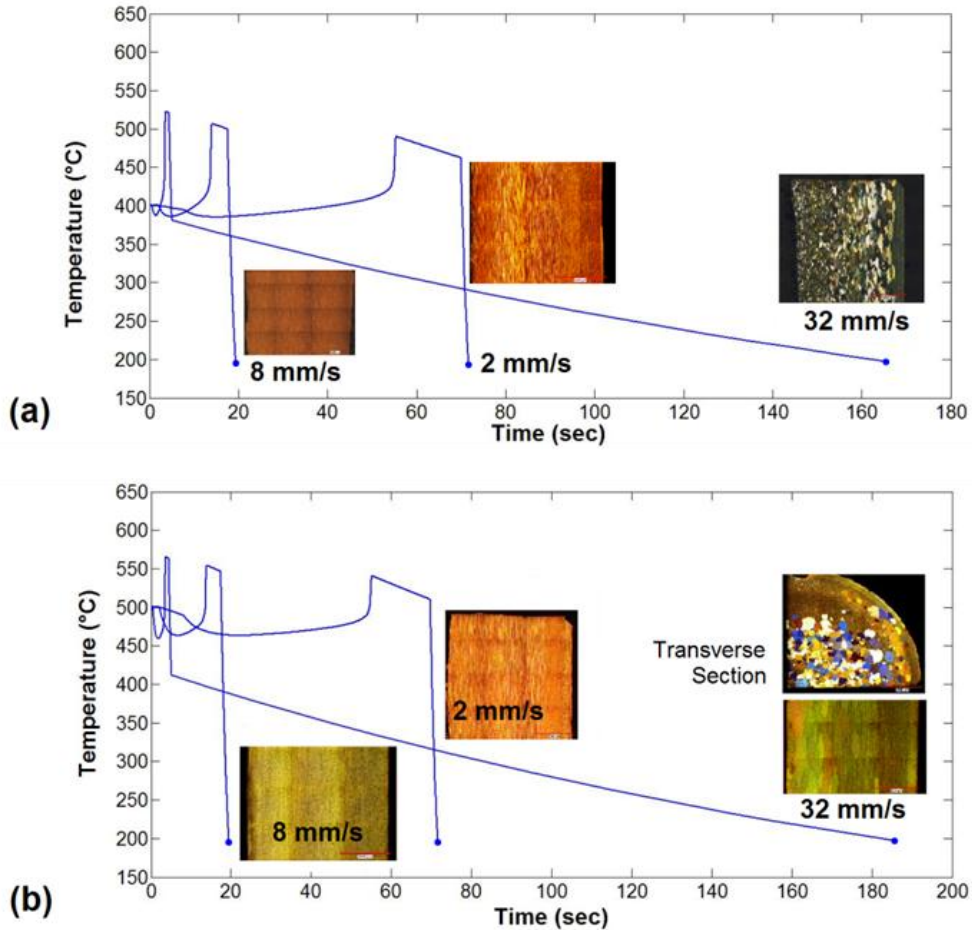


Figure 5-36 Micrographs of transverse section from center to the surface of the extrudate with billet preheat temperature of 400°C, extrusion ratio of 70, homogenization of 8 hours at 550°C, ram speed of 2 mm/sec and different post extrusion annealing conditions; as-extruded, 1minute at 525°C and 10 minutes at 525°C, (Reproduced with the permission from Grajales [17])

Experimental measurements shows that for very high ram speeds the temperature of extrudate after it exits the quench bath is not low enough to prevent microstructural changes (refer to Figure 5-9). The reason is that the length of quench bath is constant and with increasing the speed the period that the extrudate remains in the quench bath decreases so that the extrudate will lose less heat to water.

Figure 5-37 shows the thermal history for centerline during the extrusion and subsequent cooling for different extrusion conditions. The first rapid heat up in each curve is related to deformation heat generated in the material when passing through the die, after the die the extrudate cools down slowly in the air until it reaches the quench bath in which the temperature drops very quickly. The minimum temperature to which the thermal history is plotted is 200°C below which no significant microstructural evolution is expected to happen. As it is seen in the Figure 5-37 for both ram speeds of 2 and 8 mm/sec the model predictions show that during the water quench the temperature of extrudate drops below 200°C but for ram speed of 32 mm/sec the extrudate remains hot even after the quench and continues with low cooling rate in the air afterwards which allows the deformed hot material to rest in high temperature for relatively long time and the occurrence of significant recrystallization.



**Figure 5-37 Model predictions for effect of ram speed on temperature history at the center line during the extrusion and subsequent water quench and air cooling; (a) billet temperature = 400°C, (b) billet temperature = 500°C (micrographs shows the longitudinal section grain structure of extrudate for different conditions), Micrographs reproduced with the permission from Grajales [17].**

### 5.1.3.5 Summary

Numerically calculated grain thickness at the center of the extrudate shows a good agreement with experimentally measurements and simple mass balance calculations.

Simulations show a considerable change in grain thickness along the extrudate especially at the center of the extrudate. Steady state regime starts at the location of 15-20% extruded and lasts until 55-70% based on the length of the billet used.

The effect of the extrusion conditions on the distribution of grain thickness was studied using the model. It was concluded that the temperature and ram speed has ignorable effects on the grain thickness but as expected the extrusion ratio has considerable effect on the grain thickness through the cross section of the extrudate.

By comparing the model predicted grain thickness with the measured subgrain size, it was found that at the surface of the extrudate, the predicted grain thickness is much less than the subgrain size that suggests the occurrence of grain pinch-off and GDRX. Optical and EBSD microscope observations confirmed the existence and also the extent of the GDRX predicted by model.

Effect of extrusion ratio on the GDRX layer thickness was studied using the model. Although the GDRX layer thickness decreases with an increase in extrusion ratio but the fraction of the cross section area with GDRX increases.

Model predictions show that all extrusion conditions (extrusion ratio, temperature and speed) as well as homogenization treatment have considerable effect on stored energy in the material. The material extruded from more homogenized billets has larger driving pressure for recrystallization, although they have lower stored energy in them. Calculations for driving pressure of recrystallization are in very good agreement with experimental results for post-extrusion annealing.

Comparing the as-extruded structure with post-extrusion annealed structure for different ram speeds and referring to the effect of ram speed on temperature history of the extrudate, it was found that fully recrystallized as-extruded structure after very high ram speed could be a result of insufficient quench time rather than higher stored energy.

## 5.2 I-Beam extrusion

### 5.2.1 Material flow

Figure 5-38 shows the distribution of velocity during extrusion of the I-beam profile for two different billet temperatures of 400°C and 550°C. Due to sticking friction between the billet and the container, there is a layer of billet material with a very small velocity compared to the rest of the billet. Comparing the two cases shown in Figure 5-38, this layer is thicker for a billet temperature of 550°C compared to a billet temperature of 400°C. An explanation for this difference may be as follows: The container temperature and ram speed are the same for both cases ( $T_{\text{container}} = 450^{\circ}\text{C}$ ,  $V_{\text{ram}} = 14 \text{ mm/s}$ ). So that for the billet temperature of 400°C, the container is hotter than the billet but for a billet temperature of 550°C the container is colder than the billet. Due to this temperature difference between the container and the billet during extrusion, as shown in Figure 5-38, the container acts like a chill for the hotter billet ( $T_{\text{billet}} = 550^{\circ}\text{C}$ ) so that the flow stress of the surface layer of the billet that is in contact with the container would increase due to temperature drop to the container temperature. For the billet temperature of 400°C, the container heats up the surface of the billet and decreases the flow stress. As a result the material at the center of the 550°C billet moves faster than the 400°C billet to compensate for the higher flow stress at the surface.

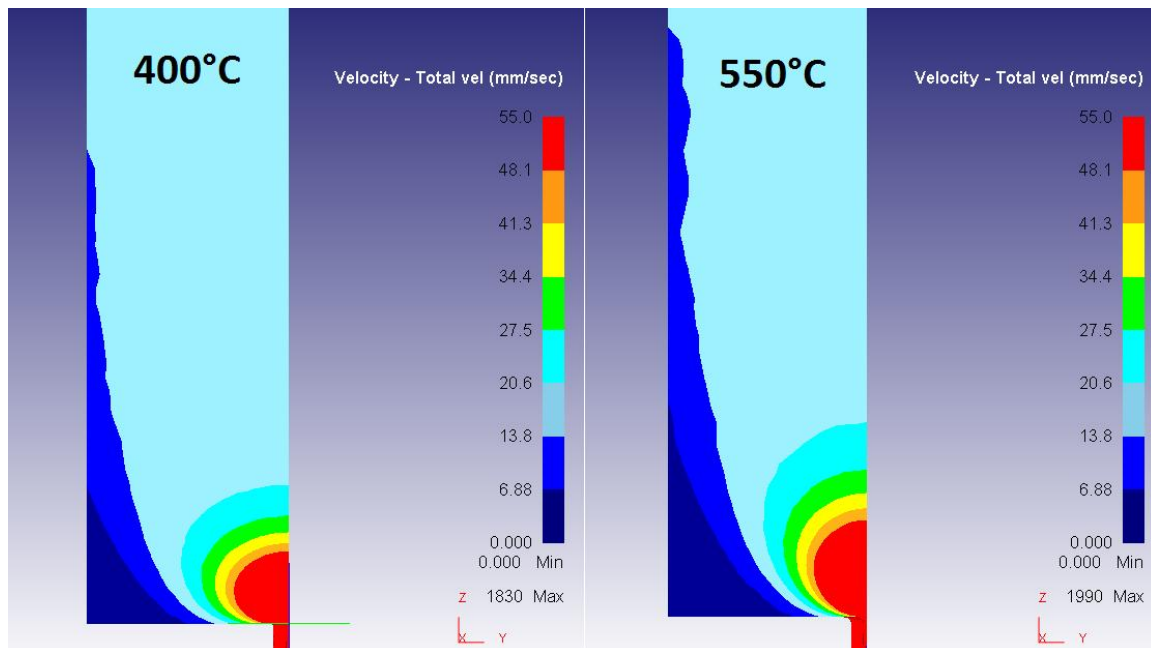


Figure 5-38 Model-predicted velocity distribution for material extruded at 400°C (left) and 550°C (right).

Figure 5-39 shows the flow pattern for different points through the thickness of the I-beam extrudate. As observed, there is a large difference between the two billet temperatures (400 and 550°C) and how the surface of the extrudate flows from the billet into the extrudate.

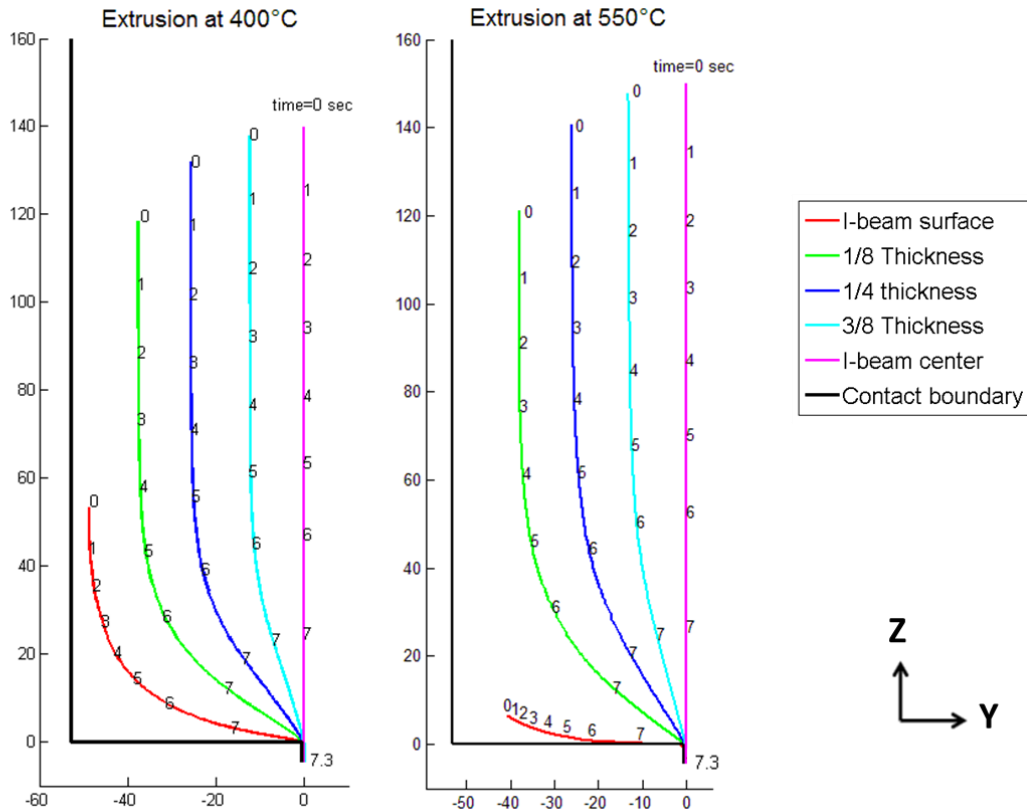
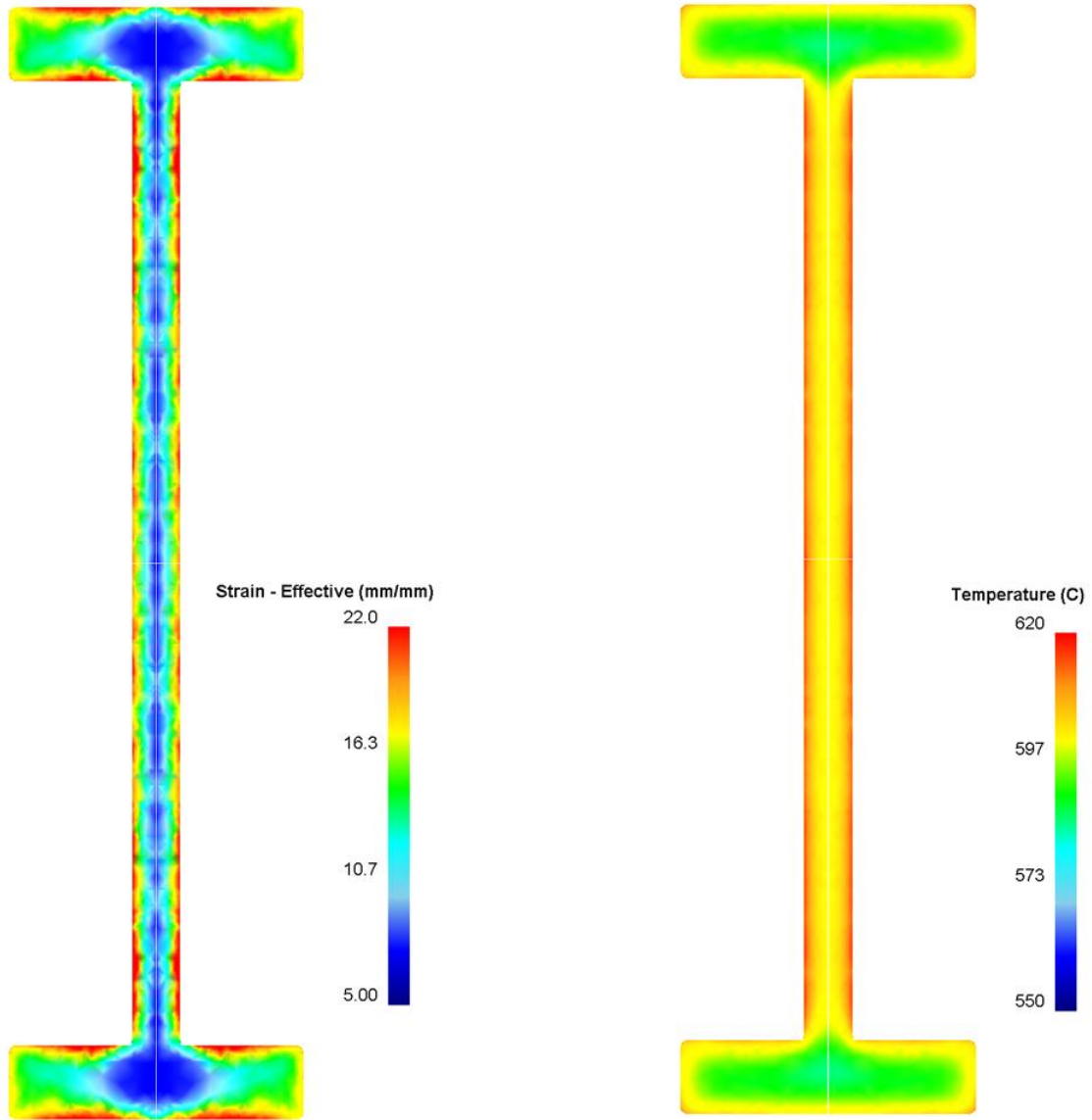


Figure 5-39 Model predicted flow pattern of different points through the half thickness of the mid-length section of I-beam extrudate at two different extrusion temperatures (from 'center' to the 'surface' shown in Figure 4-10).

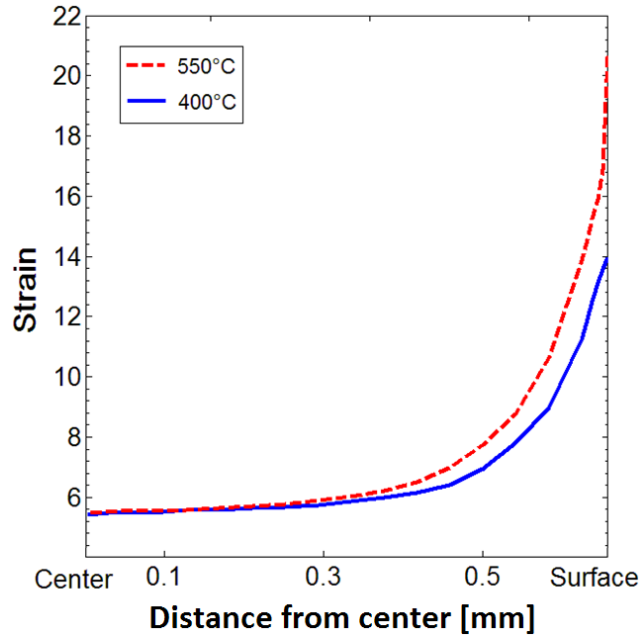
### 5.2.2 Thermomechanical history

The distribution of the effective strain and temperature across the mid-length section of the I-beam extrudate is shown in Figure 5-40 for a billet temperature of 550°C. The temperature distribution corresponds to the time when the extrudate is exiting the die.



**Figure 5-40 Model-predicted strain and temperature distribution through x-section at mid-length of the I-beam extrudate, (billet temperature = 550°C).**

Figure 5-41 shows the model-predicted strain distribution from the ‘center’ to the ‘surface’ (the ‘center’ to the ‘surface’ shown in Figure 4-10) of the mid-width of a section at the mid-length of the I-beam extrudate. The reason for the higher strain at the surface of the extrudate for the extrusion done with a billet temperature of 550°C is due to the container chilling effect at the surface of the billet as discussed earlier.



**Figure 5-41 Model-predicted strain distribution at the mid-length section through the thickness of the I-beam extrudate, ('center' and 'surface' refer to center and surface points mid-width across the I-beam as shown in Figure 4-10).**

Thermomechanical histories are shown for the 'center' and 'surface' of the I-beam extrudate for two billet temperatures of 400 and 550°C in Figure 5-42. The histories are shown for the last third of the time that the material spend in the container (from  $t = 5$  sec to  $t = 8.5$  sec). From time  $t = 0$  to 5 sec the trends in the thermomechanical histories (strain rate, temperature and strain) are similar to that of round bar extrusion (shown in the previous section). The effect of the constant container temperature for the different billet temperatures can be distinguished in the temperature histories for the 'center' and 'surface' in Figure 5-42, where the 'center' point for extrusion at 550°C is warmer than the 'surface' but due to the high deformation heat and large strains and friction experienced at the surface, this area is hotter than the centre when the material exits the die at  $t = 7.3$  sec. The Zener-Hollomon parameter for the billet material extruded at 550°C, follows the expected trends with the surface having a higher Z relative to the center during extrusion. For the billet at 400°C, the Z history is more complicated, with the surface having a higher Z for only a portion of the extrusion due to the heating of the surface by the container. Although the maximum strain rate at the surface of the 400°C extrusion is higher than the 550°C but the accumulated strain at the surface of 400°C extrusion is less than the 550°C extrusion. The strain rate and strain histories for the 'center' points are very similar for both billet temperatures.



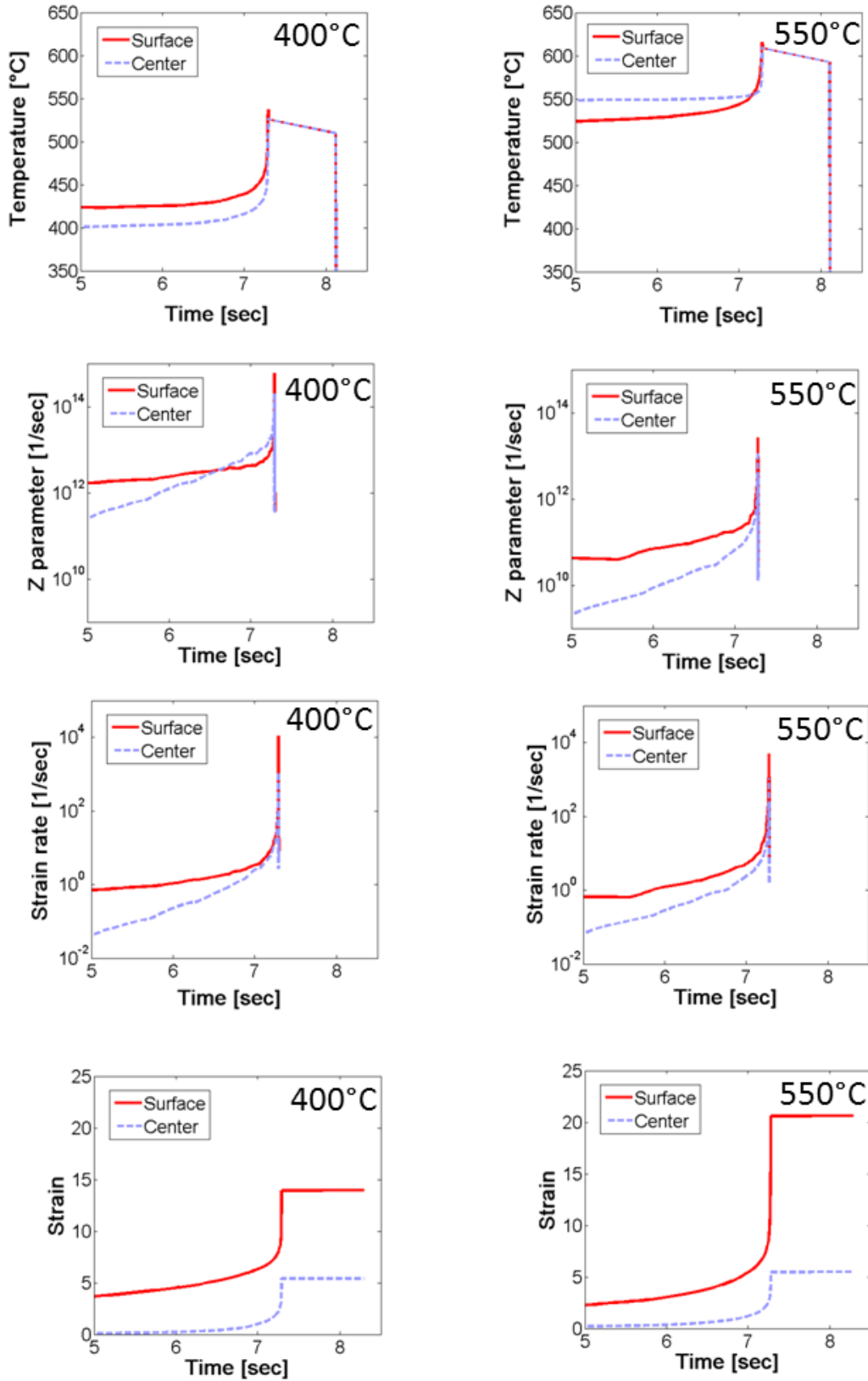


Figure 5-42 Thermomechanical history for 'center' and 'surface' on mid-width of I-beam mid-length section.

### 5.2.3 Microstructure evolution

Figure 5-43 shows the average Zener-Hollomon parameter during the extrusion from the ‘center’ to ‘surface’ of the extrudate for two different billet temperatures. Micrographs in Figure 5-43 show the recrystallized grain structure at four places through the thickness of the extrudate mid-width taken from tapered samples in the as-extruded condition. It has been found by researchers that the recrystallized grain size has an inverse relation with the Z parameter [114] which provides some indication of the stored energy during deformation. For the recrystallized structure shown in Figure 5-43 such a relation cannot be found between the recrystallized grain size and average Z parameter.

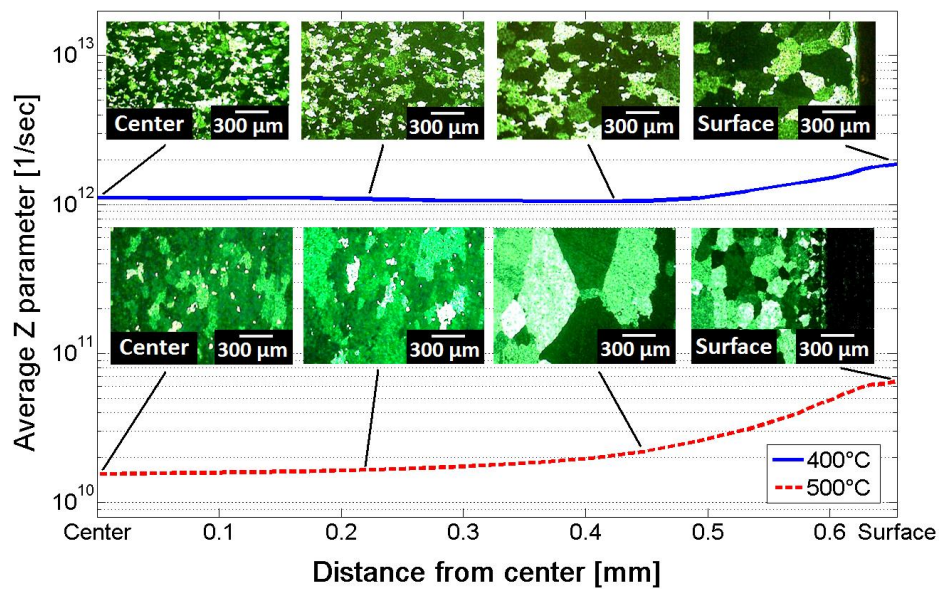


Figure 5-43 Average Zener-Hollomon parameter and micrographs of different areas of extrudate (Center and surface refer to center and surface points mid-width across the I-beam as shown in Figure 4-10, homogenization treatment before extrusion: 550°C for 8h) [12].

#### 5.2.3.1 Grain thickness

Model predicted grain thickness from the ‘center’ to ‘surface’ of the I-beam extrudate is shown in Figure 5-44 for two different billet temperatures. Figure 5-44 also shows the calculated subgrain size using the equation  $\delta^{-1} = A \ln Z + B$ , where A and B are material constants (for AA3003, A = 0.045  $\mu\text{m}^{-1}$  and B = 0.76  $\mu\text{m}^{-1}$  [115]). The predicted thickness even at the center part of the extrudate

(thickest grains at mid-width section) is less than  $1\mu\text{m}$  that is much less than the calculated subgrain size. Measured subgrain size for similar extrusion conditions in round bar extrusion is even higher than the calculated subgrain size ( $\sim 3\text{-}4\mu\text{m}$ ) confirming that GDRX is likely to happen through the whole thickness (from the ‘center’ to ‘surface’) of mid-width I-beam section. So that grain growth after GDRX might be responsible for the structures observed in Figure 5-43.

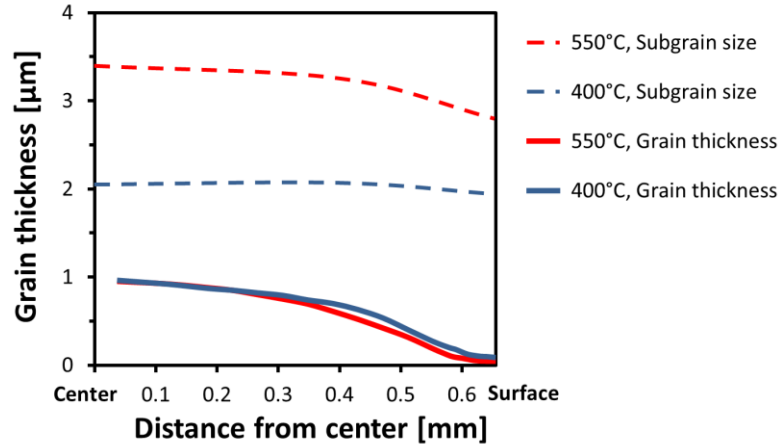


Figure 5-44 Model-predicted grain thickness and subgrain size from the ‘center’ to ‘surface’ at mid-length section of I-beam extrudate.

### 5.2.3.2 Stored energy

The distribution of the stored energy from dislocations and the distribution of total stored energy in the I-beam extrudate (from the ‘center’ to ‘surface’) are shown in Figure 5-45a and Figure 5-45b respectively. The distribution of dislocation energy looks consistent with the recrystallized grain size variations through the thickness of the extrudate (i.e. the lower driving pressure results in less number of recrystallization nuclei). For both extrusion temperatures of 400 and 550°C the total calculated stored energy is much higher than the calculated Zener drag resulting in a positive driving pressure for recrystallization.

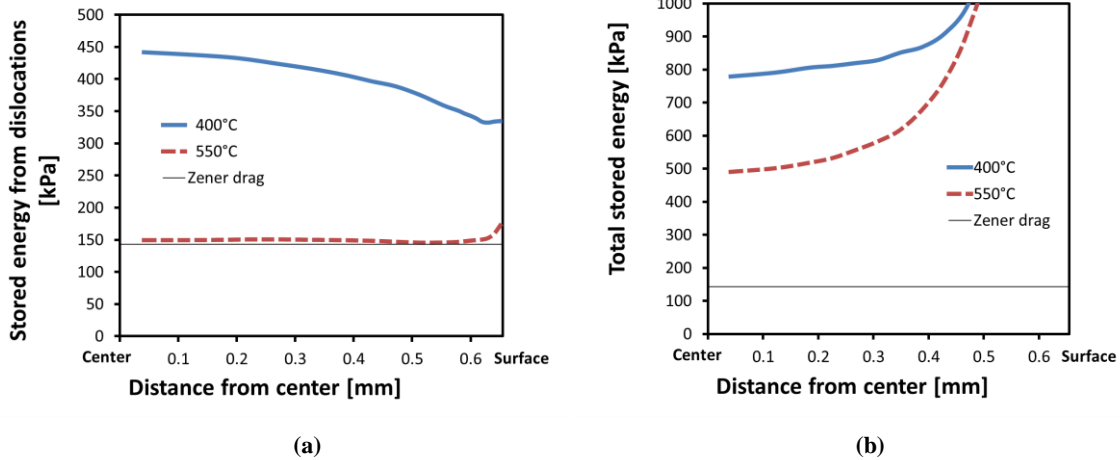


Figure 5-45 Calculated stored energy from the ‘center’ to ‘surface’ at mid-length section of I-beam extrudate; (a) stored energy from dislocations, (b) total stored energy (including energy from grain boundaries).

## 5.2.4 Summary

The relative temperature of container and the billet (whether the container is hotter or colder than the billet) during the extrusion has considerable effect on material flow and thermomechanical history and their distribution across the section of the extrudate.

The model-predicted grain thickness across the thickness of the I-beam very small ( $<1\mu\text{m}$ ) so that the GDRX is predicted over the whole thickness of I-beam.

Calculated stored energy is much higher than the Zener drag across the whole thickness which is in agreement with fully recrystallized structure observed in micrographs.

## Chapter 6

### Transverse weld formation

The validated 2-D extrusion model was applied to understand the formation of the transverse weld formation during billet-on-billet extrusion. This is a weld defect that occurs when billets are extruded sequentially and causes a clad layer (from the previous billet left in the feeder pocket) to weld itself onto the surface of the billet being extruded. Typically when billet-on-billet extrusion is done, a small portion of the length based on the volume of the feeder pocket (i.e. 10%) is removed from the front of the extrudate to ensure the transverse weld (TW) is removed. Quantitative information on the actual length of the transverse weld and how it is affected by the feeder geometry and extrusion parameters has not been examined. Figure 6-1 shows a schematic illustrating the formation of a transverse weld or clad surface layer between two consecutive billets being extruded. During the press stop (Figure 6-1c) when the butt is sheared and the next billet loads, a visible mark forms where the die bearing contacts the profile. This mark, known as the "stop mark", can be distinguished on the surface after extrusion.

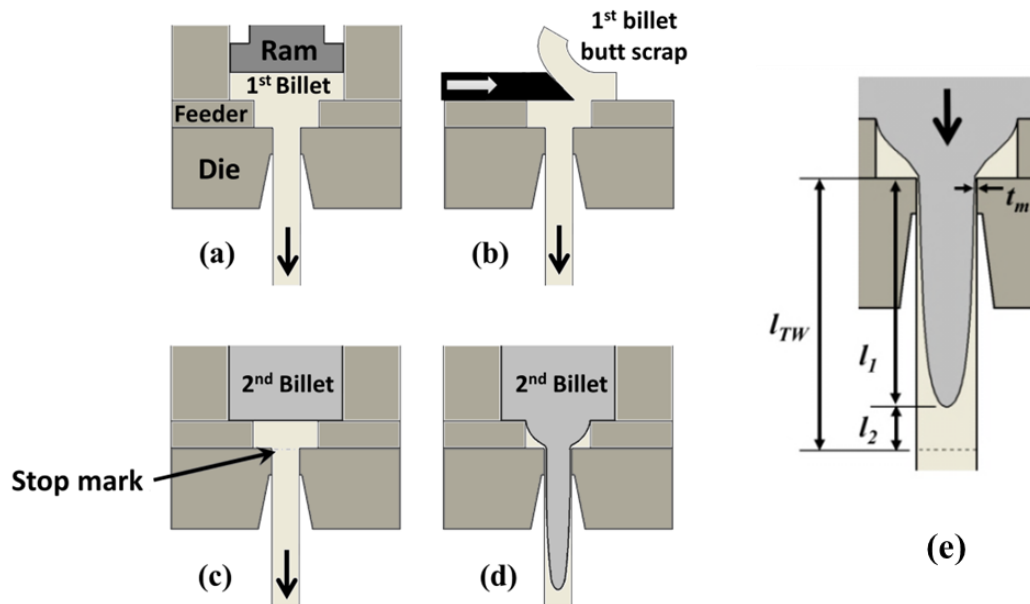


Figure 6-1 Schematic of transverse weld formation showing: (a) end of the extrusion of the first billet, (b) shearing the 10% billet butt off the first billet, (c) loading the second billet into the container, and (d) beginning extrusion of the second billet, showing the development of the transverse weld, (e) the length of the transverse weld ( $l_{TW}$ ) with minimum clad thickness of  $t_m$  divided into  $l_1$  and  $l_2$ .

Figure 6-2 shows x-section images of the transverse weld (black ring) at the start (a) and the middle of transverse weld (b) from an extrusion trial run at ARDC. As shown in Figure 2a, at a distance of 0.2 m from the stop mark, the thickness of the clad layer (TW) is 3.16 mm and at the distance of 1 m, Figure 2b, the clad layer thickness (TW) is 0.28 mm.

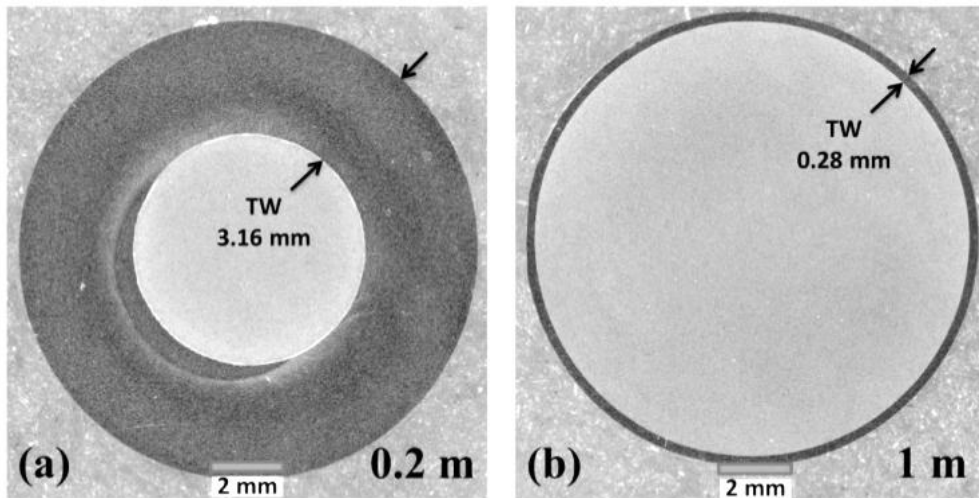


Figure 6-2 – Optical macrograph showing the cross section of transverse weld at 0.2 m (a) and 1 m (b) from stop mark for an extrusion ratio of 70 (first billet AA6063 and second billet AA3003) Trial #3 in Table 4-3, TW shown in the figure is the thickness of the transverse weld or clad layer, Macrographs reproduced with permission from Parson [116].

## 6.1 Dead metal zone

Due to the existence of a dead metal zone in the feeder pocket, there remains some amount of material from the previous billet inside the feeder at the end of the extrusion. Figure 6-3 shows a schematic of the model prediction of the boundary between the first and second billet at the end of extrusion and also the amount of material left from the previous billet in the dead metal zone inside the feeder. This dead metal zone is not completely static as there is always some movement of the material in this region towards the die (Figure 4-22) so that, even at the very end of the extrusion, theoretically the surface of the extrudate can be contaminated with material remaining in the feeder from the previous billet.

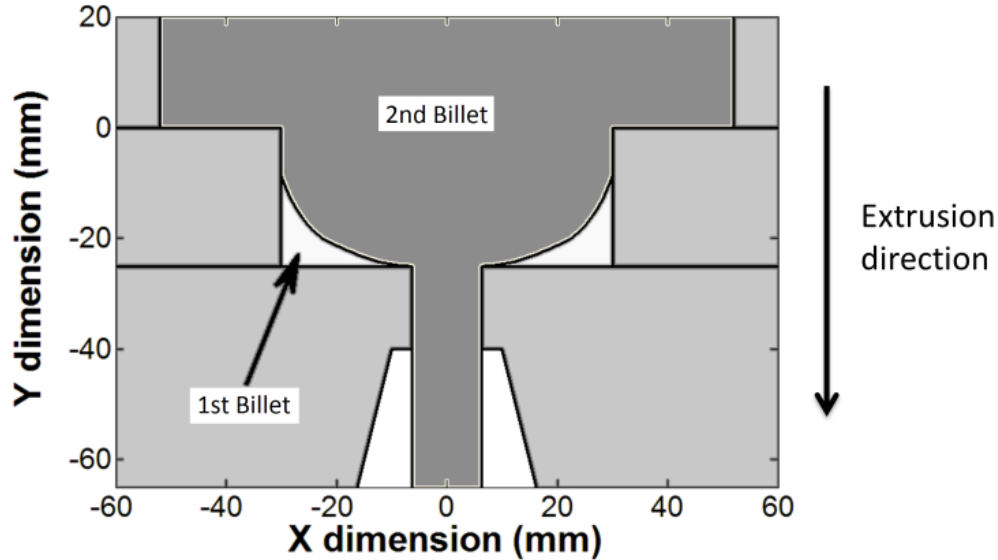


Figure 6-3 Model-predicted boundary between the first and second billet inside the feeder at the end of extrusion stroke (extrusion ratio = 70, billet temperature=500°C, ram speed = 2 mm/sec).

## 6.2 Evaluation of transverse weld thickness

Figure 6-4a shows the model prediction of the geometry of the transverse weld for the first 2 m of the extrusion for a 12.7mm bar extruded at a ratio of 70/1. To validate the model predictions, the thickness of the surface clad layer from the previous billet was measured at given positions (Figure 6-4b) and compared to model predictions. As shown in Figure 6-4, the model prediction of the thickness of this clad surface layer (155 $\mu\text{m}$ ) is in good agreement with experimental measurement (145 $\mu\text{m}$ ).

Table 6-1 and Figure 6-5 show a comparison between the model predictions and experimental measurements of the thickness of the transverse weld or clad layer at the surface of the extrudate at the front section of the sampling length (shown in Figure 4-7) for various extrusion conditions. As observed for the cases shown here, the difference between model predictions and experimental measurements is less than 25% under a range of extrusion conditions.

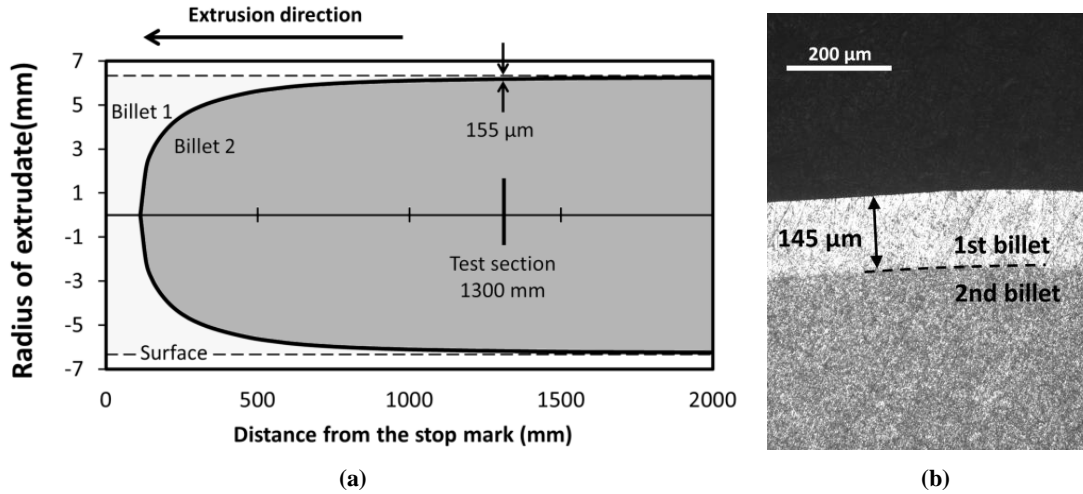


Figure 6-4 (a) Model predicted shape of the transverse weld between the first and second billet for the first 2m of the extrudate, (b) micrograph of extrudate x-section at 1300 mm from the stop mark showing the experimental measurement of the first billet layer clad onto the surface of the second billet (extrusion ratio = 70, billet temperature=500°C, ram speed = 2 mm/sec) first billet is AA6063 alloy and the second billet is AA3003.

Table 6-1 Thickness of surface weld layer (clad layer) for various extrusion conditions, regular feeder.

Test #	1	2	3	4	5	6
Extrusion ratio	17	17	70	70	70	280
Billet temperature (°C)	500	500	500	500	400	500
Ram speed (mm/sec)	8	8	2	2	2	2
Homogenization	8H550	8H550	8H500	8H500	8H500	8H550
Test section, distance from stop mark (% of total extrudate length)	10	12	10	10.5	10	10
Predicted surface clad thickness (μm)	110	85	155	135	135	55
Measured surface clad thickness (μm)	100	77	145	150	175	70
Error (%)	+10	+11	+7	-10	-21	-21



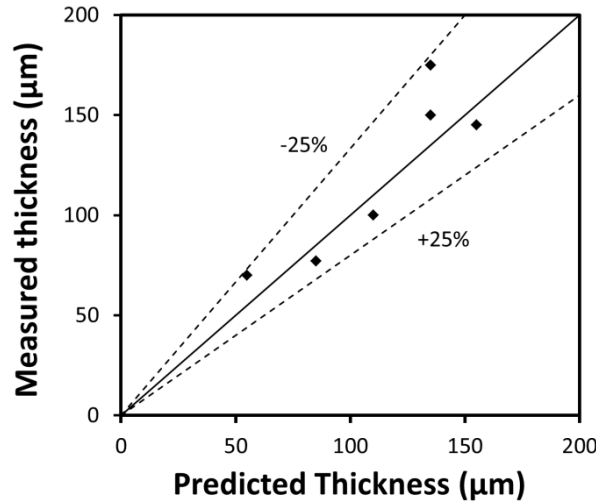


Figure 6-5 Graphical comparison of predicted and measured clad layer thickness on extrudate.

Figure 6-6 shows a comparison of model predictions of the clad layer against experimental measurements for the transverse weld thickness along the extrudate. For this feeder configuration and extrusion ratio, residual material from the previous billet was present along the entire length of the extruded profile. The model predictions of the clad layer thickness fit well with power law trend line with an exponent of about -1.5 which was earlier reported by Jowett et al. [102] for simple rectangular and shaped feeder plate geometries. As shown in Figure 6-6a, the model predictions are in good agreement with experimental measurements until the clad layer thickness is less than  $\sim 30 \mu\text{m}$ . This is probably due to the mesh size used near the surface ( $\sim 100 \mu\text{m}$ ); with a smaller mesh size the model predictions would most likely be more accurate to lower clad thicknesses. Figure 6-6b shows that extrapolating a trend line fit to the model predicted data above  $30 \mu\text{m}$  clad layer thicknesses fits well with experimental data over the entire length of the extrudate. This is true even at very low clad thicknesses i.e.  $< 10 \mu\text{m}$ .

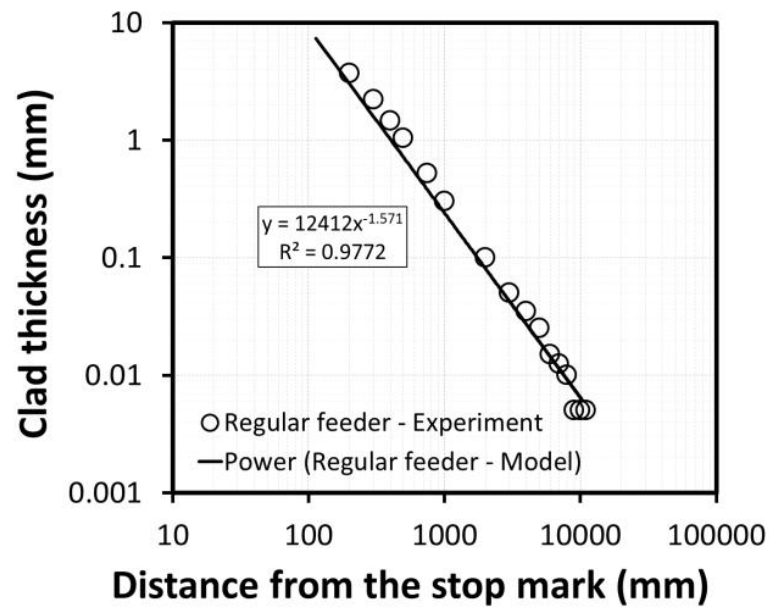
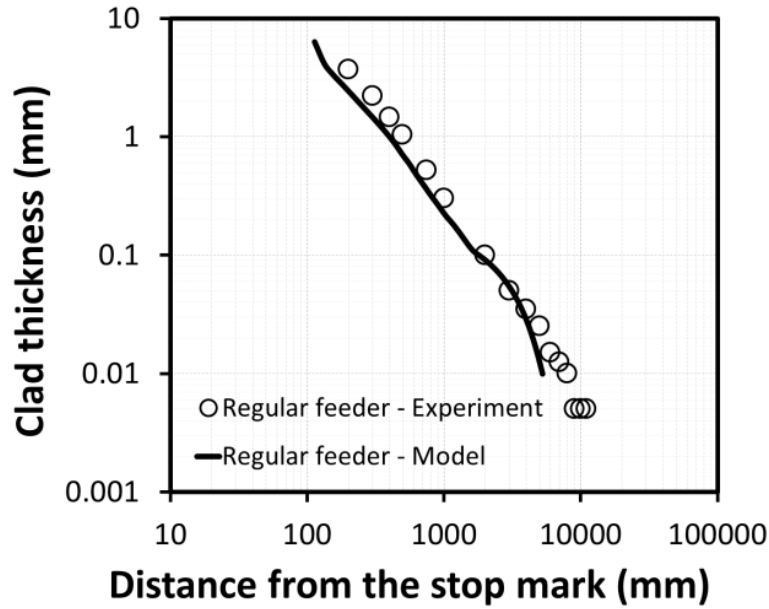


Figure 6-6 (a) Model predictions and experimental measurements for transverse weld thickness in logarithmic scale, (b) power law trendline fitted on model predictions, (first and second billet AA3003 with homogenization of 24H600 and 8H550, respectively), Experimental data from [116].

### 6.3 Effect of billet material [103]

The effect of different combinations of alloy types and homogenization practices on the transverse weld shape is shown in Figure 6-7. The effect of billet material on the formation and shape of the

transverse weld was negligible at least for the AA3XXX and AA6XXX alloys studied. Normally transverse scrap allowances are confirmed by macro-etching the profile cross section and determining the position at which the defect is no longer visible by the naked eye or using a low power microscope. In these tests the thickness of the residual material from the previous billet was measured by optical metallography on polished sections. When marker materials were used, the contrast between alternate billets was clear as shown in Figure 6-8a which allowed very thin layers  $<20\ \mu\text{m}$  in thickness to be identified along the entire profile length. In Figure 6-7 it is interesting to note that for AA6063 followed by AA6063 (large open squares) the metallographic examination only identified the transverse weld extending to 5m, i.e. half the extruded length. As shown in Figure 6-8b, even at the 1m position for AA6063 the contrast associated with the transverse weld was not clear compared with the marker material situation. As indicated by the trends in Figure 6-7 there is no reason why the weld length for AA6063 should be any shorter. In fact the original metallographic work only identified the transverse weld extending to 1000mm for AA6063 and based on the results for the marker materials, the samples were re-examined and traces of transverse weld were found at the 5m position. This result is not surprising as for the same material, observation of the transverse weld interface relies on resolution of the oxide film from the billet end surface which is progressively broken up as the weld progresses. For structural integrity the avoidance of the oxide layer is the main issue and normal practices usually ensure this is not incorporated in saleable product. However, this result does indicate that standard practices for determining scrap allowances typically underestimate the presence of residual material in surface layers  $<100\ \mu\text{m}$  in thickness. This suggests that most commercial products have a surface layer at least partially composed of the preceding billet which has implications for "streak" formation. Streak is a surface defect that appears on extrudate after anodizing, in form of narrow bands with different contrast from the surrounding [117]. The anodizing process is a chemical etching to produce a thick oxide layer on the surface of aluminum products.

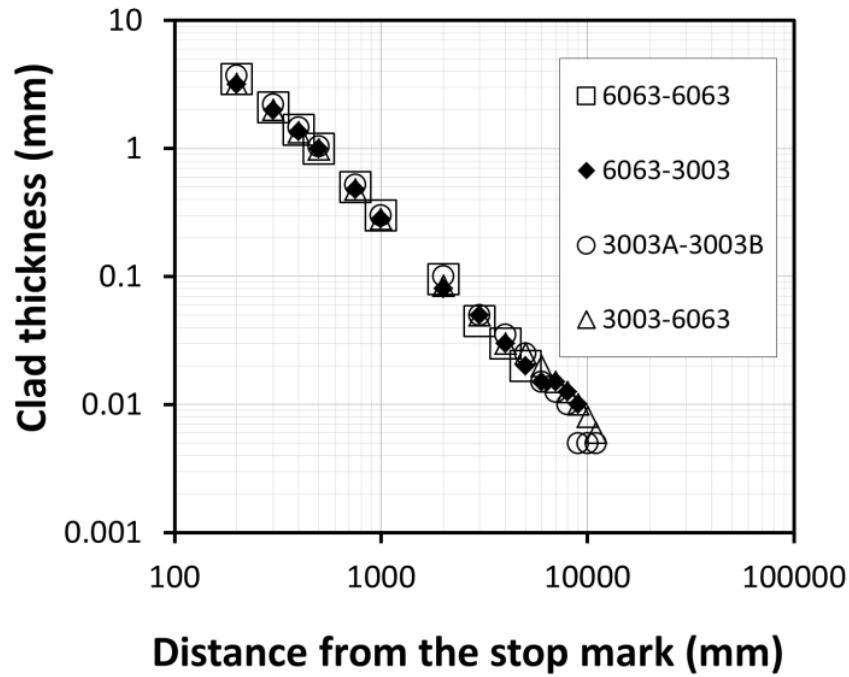


Figure 6-7 Effect of different billet material combination on the thickness of transverse weld along the extrudate (legends represent the codes for aluminum alloy used for first and second billets for each test, 3003A stand for 3003 aluminum alloy homogenized at 600°C for 24 hours and 3003B stands for the same alloy homogenized at 550°C for 8 hours), Experimental data from [116].

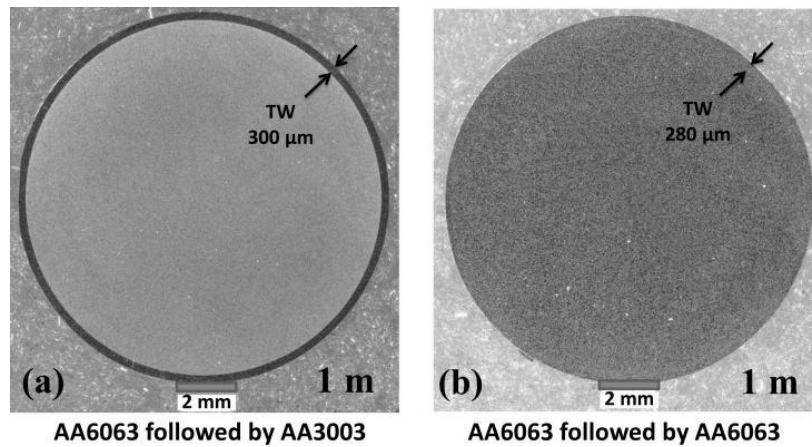


Figure 6-8 Comparison of transverse weld contrast for marker materials (a) and regular AA6063 (b) at 1000 mm position, Macrographs reproduced with permission from Parson [116].

## 6.4 Effect of feeder geometry

Figure 6-9 shows the model-predicted effect of feeder geometry on the shape of the transverse weld during the extrusion process for cylindrical and conical feeders. The first snapshot on the left is for a ram stroke of 16 mm at which the second billet completely fills the container and comes into intimate contact with the top of the feeder. At this point the billet starts to be pushed into the feeder. As the ram continues to move forward, the center region of the billet passes through the feeder and die much faster than the billet sides. For the tapered feeder configuration, the center of the billet passes through the die earlier than the regular feeder configuration. During the entire extrusion, the previous billet material left inside the regular feeder geometry is much larger in the case of the tapered feeder. This arises from both the lower initial volume of material remaining inside the tapered feeder from the first billet as well as the different metal flow pattern. At the end of the extrusion (ram stroke of 180 mm for this case), there is no prior billet material left in the tapered feeder but there is some prior billet material left inside the regular feeder.

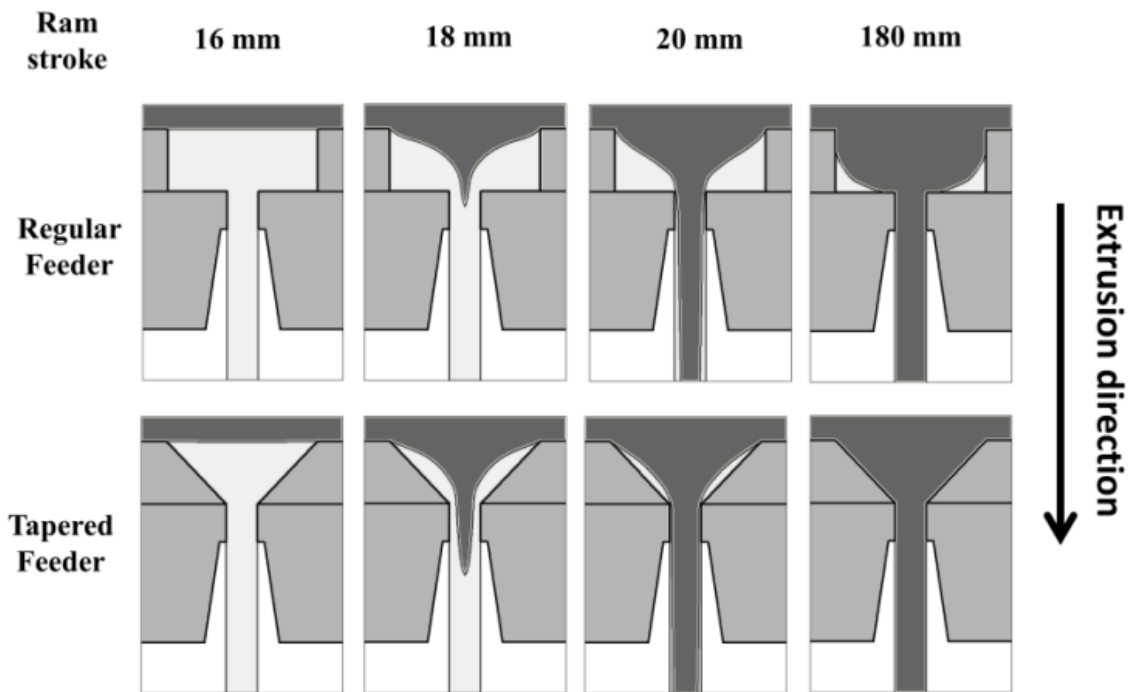


Figure 6-9 Model-predicted effect of feeder geometry on the shape of the transverse weld at different ram strokes, (Model predictions were done for an extrusion ratio of 70, billet temperature = 500°C, ram speed = 2 mm/sec).

Figure 6-10 shows the model predictions and measurements showing the effect of feeder geometry on the thickness and length of the transverse weld. It is observed that using a tapered feeder significantly decreases the length of product contaminated by the transverse weld defect and the clad thickness.

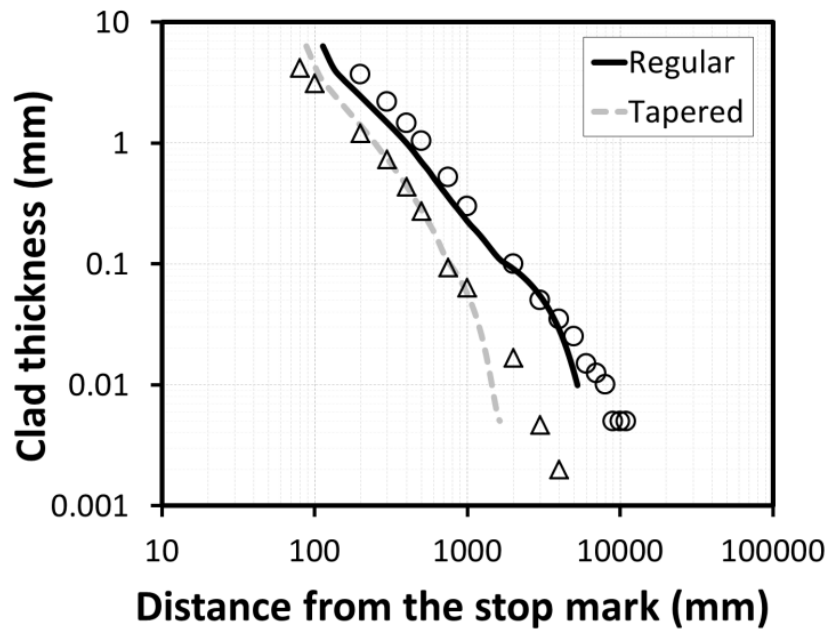
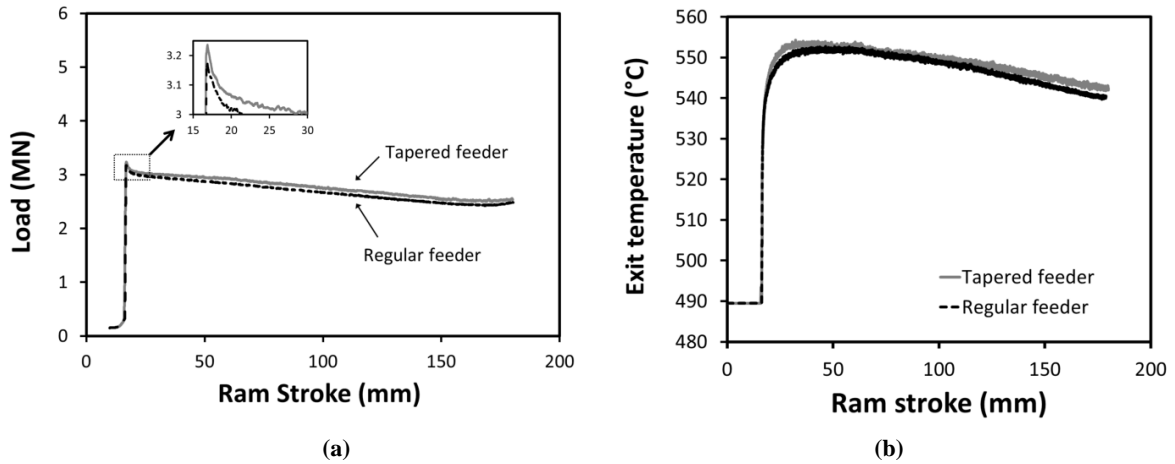


Figure 6-10 Comparison of model predictions (lines) to measurements (symbols) showing the effect of feeder shape on transverse weld geometry for extrusion ratio of 70, (model predictions for AA3003 billet with the homogenization of 8H550, extruded at 500°C and ram speed of 2 mm/sec, experimental data for trials #4 and #7 in Table 4-3), Experimental data from [116].

## 6.5 Effect of feeder geometry on extrusion load, temperature and accumulated strain – Model predictions

A potential increase in the extrusion load and surface temperature of the extrudate are two typical concerns when changing the die geometry. Figure 6-11a shows the predicted load-stroke curve for the extrusion produced using the two different types of feeder geometries. The predicted load for the extrusion with the tapered feeder is slightly larger than regular feeder. The peak load difference is not significant but the steady state load for the tapered feeder is about 4% higher than the regular feeder. The total calculated mechanical work (area under the Load-Stroke curve) for the extrusion with tapered feeder is about 3% larger than the regular feeder (460kJ for the tapered feeder versus 445 kJ

for the regular feeder). Figure 6-11b compares the effect of the die geometry on the predicted temperature of the extrudate surface at the die exit. Figure 6-11b shows that the temperature rise with using the tapered feeder is 2-3 degrees higher compared to the regular feeder plate.



**Figure 6-11 Model predictions for effect of feeder geometry on: (a) extrusion load, and (b) exit temperature at the surface of extrudate (extrusion ratio = 70, billet temperature = 500°C, ram speed = 2 mm/sec).**

Figure 6-12 shows the effect of feeder geometry on the material flow pattern and accumulative plastic strain in extrusion. As shown in Figure 6-12a, tapering the feeder has a negligible effect on the distribution of the accumulated strain in the extrudate, except at the surface where there is ~10% difference. However, the model-predicted flow lines in Figure 6-12b show there is almost no dead metal zone inside the tapered feeder relative to the regular feeder. The model prediction also shows that at the end of extrusion for the 2<sup>nd</sup> billet, there will be no material left inside the tapered feeder from the previous billet.

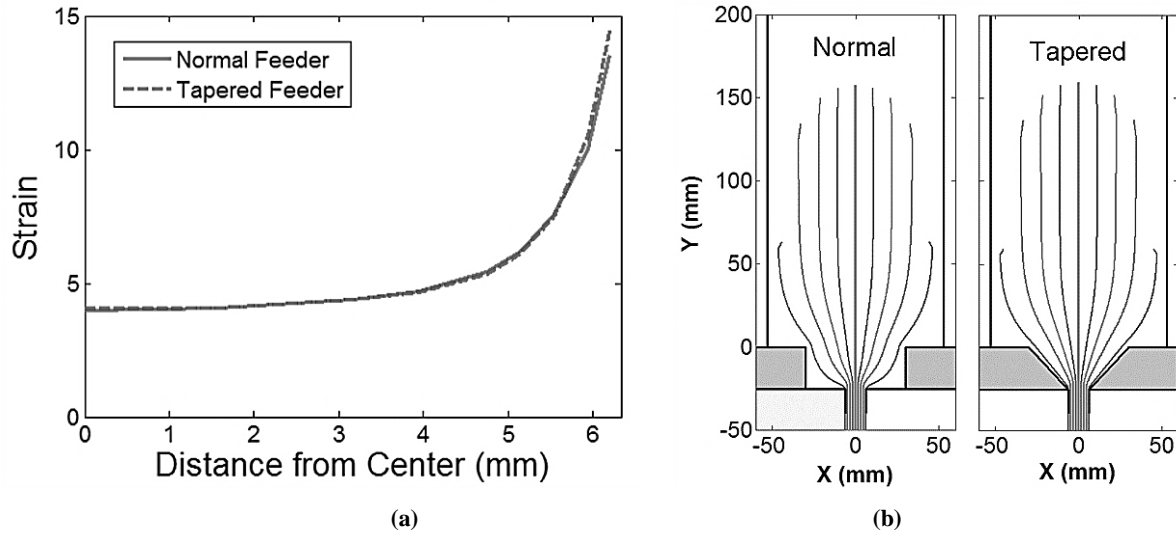


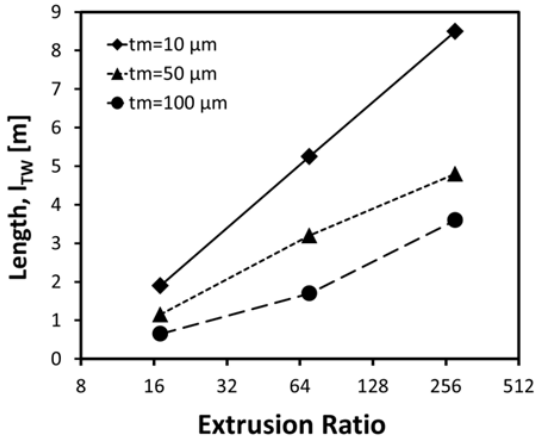
Figure 6-12 Model-predicted effect of feeder geometry on (a) effect of feeder geometry on accumulative plastic strain distribution along the extrudate x-section and (b) flow pattern in deformation zone (both figures are for mid-length x-section of extrudate).

## 6.6 Effect of extrusion ratio on transverse weld length – Model predictions for regular feeder

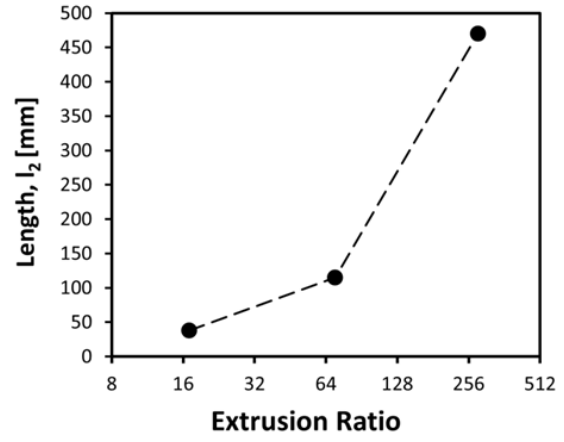
Figure 6-13a and c show the model-predicted effect of the extrusion ratio on the length ( $l_{TW}$  in Figure 6-1e) of the extrudate where the transverse weld maintains a minimum thickness ( $t_m$  in Figure 6-1e) of 10, 50 or 100  $\mu\text{m}$ . For Figure 6-13c and d, a normalized length was calculated by dividing the length of the transverse weld by the entire length of the extrudate to determine the percentage of the extrudate affected assuming different clad layer ( $t_m$ ) thicknesses.

As observed in Figure 6-13a, with increasing extrusion ratio the length of the transverse weld increases, but Figure 6-13c shows that the fraction of the extrudate affected by the transverse weld decreases. Normalized transverse weld length decreases significantly especially when considering a lower minimum clad thickness ( $t_m$ ) value. In other words a decreasing proportion of the billet weight has to be scrapped for the transverse weld at higher extrusion ratios. A similar trend is observed for the distance from the start of the weld to the visible stop mark on the surface of the extrudate,  $l_2$  in Figure 6-1e (Figure 6-13b and d). However, model predictions in Figure 6-13d show that the normalized value of  $l_2$  decreases from an extrusion ratio of 17 to 70 and remains almost constant as the extrusion ratio increases beyond this level.

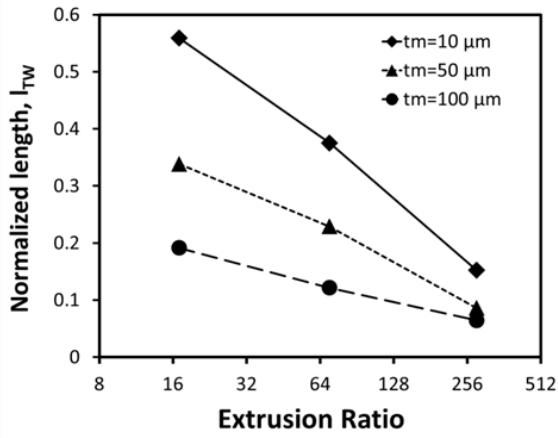




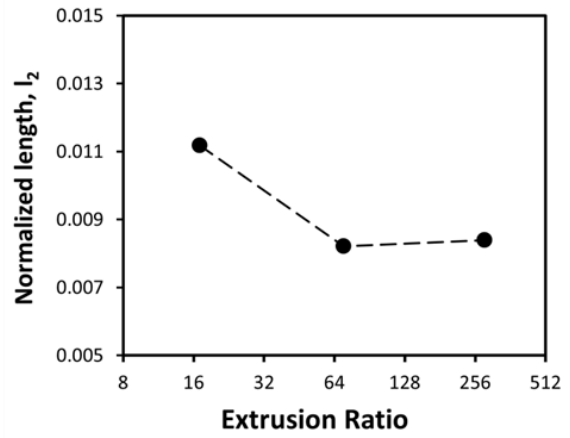
(a)



(b)



(c)



(d)

Figure 6-13 Predicted effect of extrusion ratio on transverse weld length for the regular feeder geometry (refer to Figure 6-1e for description of  $l_{TW}$ ,  $l_2$  and  $t_m$ ).

## 6.7 Summary

Using a simple but effective numerical technique in conjunction with FE model predictions, the thickness and length of transverse weld was accurately calculated for radically different feeder geometries giving good agreement with physical measurements.

For round bar extrusion using a simple cylindrical feeder, the simulations indicated that material from the preceding billet is still present in the dead zones of the pocket such that the surface of the product can be contaminated over the entire length. In the case of the tapered pocket, material from the preceding billet clears from the pocket during the push, significantly decreasing the transverse weld length. Moreover, the tapered feeder had little effect on the model-predicted load, temperature and strain distribution during extrusion relative to the regular feeder geometry.

Experimental measurements and model predictions indicate that the thickness of the clad layer as a function of extrudate position fits well with a power law with an exponent of -1.6.

The transverse weld length did not vary with the changes in billet material made in the study. However, using dissimilar materials did allow the depth of the surface layer to be tracked to  $<10\ \mu\text{m}$ , indicating that the normal methods industrially used to reveal the transverse weld disregard the presence of thin surface layers.

Simulations indicated that increasing extrusion ratio extended the physical transverse weld length. However, at higher ratios the normalized length or fraction of the billet weight associated with the weld scrap allowance decreased.

# Chapter 7

## Summary, conclusions and future work

### 7.1 Summary

The main objective in this research was to develop, validate and apply a quantitative model to study the effects of initial microstructure and process parameters on the microstructure evolution during and after the extrusion process for AA3XXX aluminum alloys. The modeling has been done using a commercial FEM code DEFORM in conjunction with calculations for the stored energy and grain shape evolution to predict the evolution of the microstructure of the deformed state during extrusion.

The validated model was also used to understand and quantitatively predict the formation of the transverse weld defect during billet-on-billet extrusion and how it is influenced by the extrusion conditions as well as die geometry.

The research has concentrated on AA3003 extrusions that are used for manufacturing of automobile radiator and heat exchangers. Two extrusion geometries were modeled and validated; round bar extrudate (2D) and an I-beam profile (3D). A wide range of process parameters were studied: extrusion temperature (350-550°C), ram speed (2-32 mm/s), extrusion ratio (17-280) and billet homogenization conditions (500°C for 8 hrs, 550°C for 8 hrs and 600°C for 24 hrs).

The experimental work consisted of conducting a series of extrusion trials using the fully instrumented extrusion press at Rio Tinto Alcan's Arvida facility in Jonquiere, Quebec and subsequent microscopic study on the extruded samples. The microscopic study includes both optical and EBSD observations.

Preliminary model validation included comparisons of the model predictions to measurements made for load and temperature during the extrusion trials. Secondary model validation included measurements of the material flow in terms of transverse weld formation and microscopic measurements of the grain thickness and subgrain size.

In terms of microstructural evolution, the stored energy or driving pressure for Static Recrystallization (SRX) and the occurrence of Geometric Dynamic Recrystallization (GDRX) were investigated. The driving pressure for SRX relates to a positive difference between the stored energy in the aluminum matrix and pinning force due to Zener Drag and that GDRX occurs when the predicted thickness of the deformed grains is less than the subgrain size.

## 7.2 Conclusions

In this research, well validated 2D and 3D thermomechanical models were developed and were successfully used for predicting the transverse weld formation and microstructure evolution during the extrusion of AA3003 aluminum alloy. The main contributions of this work to the state-of-the-art knowledge in this area are:

- The model could predict the dimensions of the transverse weld to thicknesses of 50  $\mu\text{m}$ .
- More conclusive experimentation has been made to investigate the occurrence of GDRX at the surface of the extrudate.
- The model could reasonably predict the thickness of the GDRX layer at the surface and the stored energy or driving pressure for SRX at the center of the extrudate.

The main conclusions that can be drawn from this research are listed below and have been separated into the three main areas namely: mathematical modelling and its effectiveness, microstructure evolution and effect of process parameters and transverse weld formation.

### 7.2.1 Mathematical modelling and its effectiveness:

- Comparisons indicated that model predictions of the load and temperature agree well with measured values during extrusion over a wide range of billet temperatures, ram speeds and extrusion ratios.
- The model is very sensitive to the mesh size at the die corner. At small mesh sizes ( $\sim 0.15\text{mm}$ ) a reasonable accuracy for predicted load can be achieved while the computational time increases dramatically with a decrease in mesh size that makes it unreasonable to use very small mesh sizes (i.e.  $< 0.1\text{ mm}$ ).
- Simulations show that the ram speed has a large effect on the temperature history especially after the extrusion. Very high ram speeds (i.e.  $\sim 32\text{ mm/sec}$ ) with a medium extrusion ratio (i.e.  $\text{ER}=70$ ) can cause the extrudate to remain at high temperatures ( $> 400^\circ\text{C}$ ) even after the quench bath.
- Numerically calculated grain thickness at the center of the extrudate shows good agreement with experimental measurements and simple mass balance calculations.
- Simulations show a considerable change in grain thickness along the length of the extrudate especially at the center of the extrudate. A steady state regime starts at a location of 15-20% extruded material and lasts until 55-70% based on the length of the billet used.

- The temperature and ram speed has very little effects on the grain thickness but as expected the extrusion ratio has considerable effect on the grain thickness through the cross section of the extrudate.
- Model predictions show a large difference between the center and surface of the extrudate in terms of thermomechanical history each experiences. This suggests that the microstructural evolution and microstructure mechanisms that occur in the extrudate at these different locations will be quite different.
- The relative temperature of container and the billet (whether the container is hotter or colder than the billet) during the extrusion has a considerable effect on material flow and thermomechanical history and their distribution across the section of the extrudate.

### **7.2.2 Microstructure evolution and effect of process parameters:**

- By comparing the model predicted grain thickness with the measured subgrain size, it was found that at the surface of the extrudate, the predicted grain thickness is much less than the subgrain size that suggests the occurrence of grain pinch-off and GDRX. Optical and EBSD microscope observations also suggested the existence of the GDRX predicted by the model while the thickness of the extrudate that experienced this form of recrystallization was in good agreement with experimental measurements. The GDRX layer thickness decreases with an increase in extrusion ratio but the fraction of the cross section area with GDRX increases.
- Model predictions show that all extrusion conditions (extrusion ratio, temperature and speed) as well as homogenization treatment have a considerable effect on the stored energy in the material. The materials extruded from billets that have received a longer homogenization treatment have larger driving pressure for recrystallization, although they have lower stored energy in them. Calculations for driving pressure of recrystallization are in very good agreement with experimental results for post-extrusion annealing.
- Due to huge deformation, the occurrence of GDRX seems to be inevitable at the surface of the extrudate, so that even for extrusions with high Zener drag where the post-extrusion recrystallization is prohibited (billet temperature of 500°C and homogenization of 8 hours at 500°C) the GDRX causes the inhomogeneity of microstructure through the cross-section of the extrudate. In this context, the homogenization at 600°C for 24 hours results in the most homogeneous structure (full recrystallization throughout the extrudate) especially at very

high ram speeds (ram speed = 32 mm/sec) where the as-extruded structure consists of relatively fine and equiaxed recrystallized grains through the cross-section of the extrudate.

- Amongst the extrusion conditions studied in this research, the temperature appears to have the largest effect on the microstructure of the extrudate which is expected based on the relative effect of temperature on stored energy compared to effect of ram speed and extrusion ratio.
- The model-predicted grain thickness across the thickness of the I-beam was very small ( $<1\mu\text{m}$ ) so that the GDRX is predicted over the whole thickness of I-beam.

### **7.2.3 Transverse weld formation:**

- Using a simple but effective numerical technique in conjunction with the FE model predictions, the thickness and length of transverse weld was accurately calculated for radically different feeder geometries giving good agreement with physical measurements.
- For round bar extrusion using a simple cylindrical feeder, the simulations indicated that material from the preceding billet is still present in the dead zones of the pocket such that the surface of the product can be contaminated over the entire length. In the case of the tapered pocket, material from the preceding billet clears from the pocket during the push, significantly decreasing the transverse weld length. Moreover, the tapered feeder had little effect on the model-predicted load, temperature and strain distribution during extrusion relative to the regular feeder geometry.
- Experimental measurements and model predictions indicate that the thickness of the clad layer as a function of extrudate position fits well with a power law with an exponent of -1.6.
- The transverse weld length did not vary with the changes in billet material made in the study. However, using dissimilar materials did allow the depth of the surface layer to be tracked to  $<10\mu\text{m}$ , indicating that the normal methods used to reveal the transverse weld in industry disregard the presence of thin surface layers.
- Simulations indicated that increasing extrusion ratio extended the physical transverse weld length. However, at higher ratios the normalized length or fraction of the billet weight associated with the weld scrap allowance decreased.

## **7.3 Future work**

### **7.3.1 Microstructure characterization**

- More EBSD microscope analysis on both longitudinal and transverse sections is needed to measure the grain and subgrain dimensions and their distribution and spatial variations for different extrusion conditions and homogenization treatments to better validate the model predictions for GDRX at the surface.
- Verifying the subgrain growth after the extrusion can be beneficial in better understanding the mechanism of microstructure evolutions during the extrusion. This can be done by measuring the subgrain size for extrusion samples annealed at different conditions.
- Development of experimental techniques to study the possibility of recrystallization in Dead Metal Zone and shear zone during the extrusion.

### **7.3.2 Modelling the microstructure evolution**

- Developing a simple equation or neural network model to calculate the stored energy of extrusion given the extrusion conditions and homogenization treatment. For this purpose a series of simulations must be performed over a range of extrusion conditions and homogenization treatments (like what has been done in this work), then using regression or neural network methods the calculated stored energy can be defined as a function of extrusion parameters. So that the stored energy for any other conditions can be estimated without time consuming simulations.
- Considering the grain and subgrain size distribution to calculate the GDRX, so that the fraction of pinched-off grains (or fraction of GDRX) can be calculated through the thickness.
- Developing microstructure models to predict the kinetics of recrystallization including nucleation, growth and abnormal grain growth.
- Developing physically based state variable microstructure models to study the interaction between dynamic evolutions during the extrusion such as precipitation, recovery and recrystallization.

### **7.3.3 Modelling the defect formation**

- Study the effect of feeder dimensions (i.e. feeder depth and width) on the extent and thickness of transverse weld defect.

- Modeling the formation of back-end defect and study the effect of process parameters and tooling geometry on its formation.



## Appendix A

### Stored energy for different extrusion conditions (round bar extrusion)

Figures C-1 and C2 show calculated stored energy across the mid-length section of round bar extrudate for different extrusion conditions studied in this work. Zener drag for different homogenization conditions are also shown in the figure.

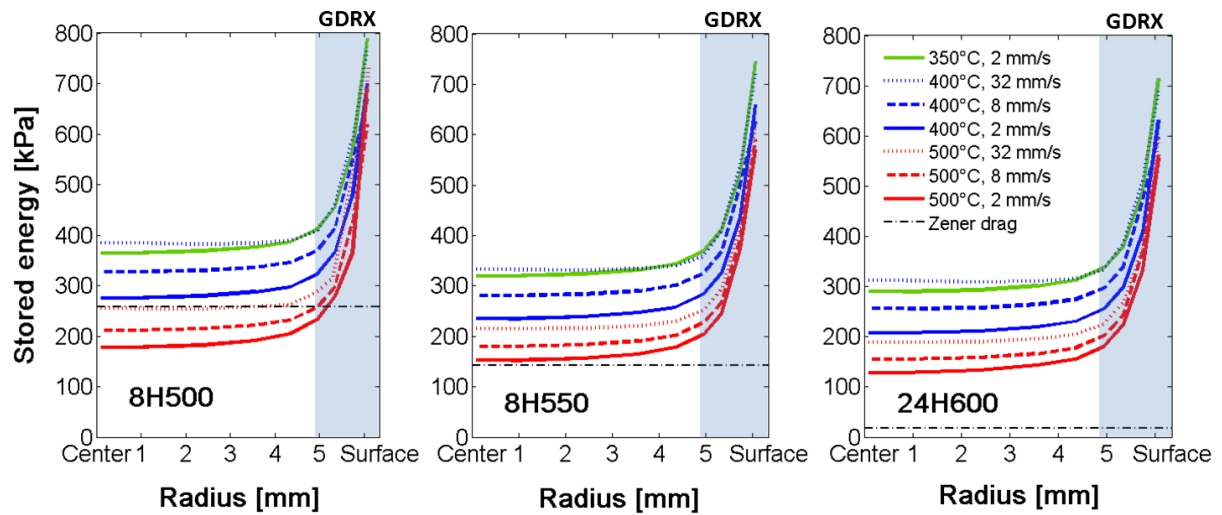
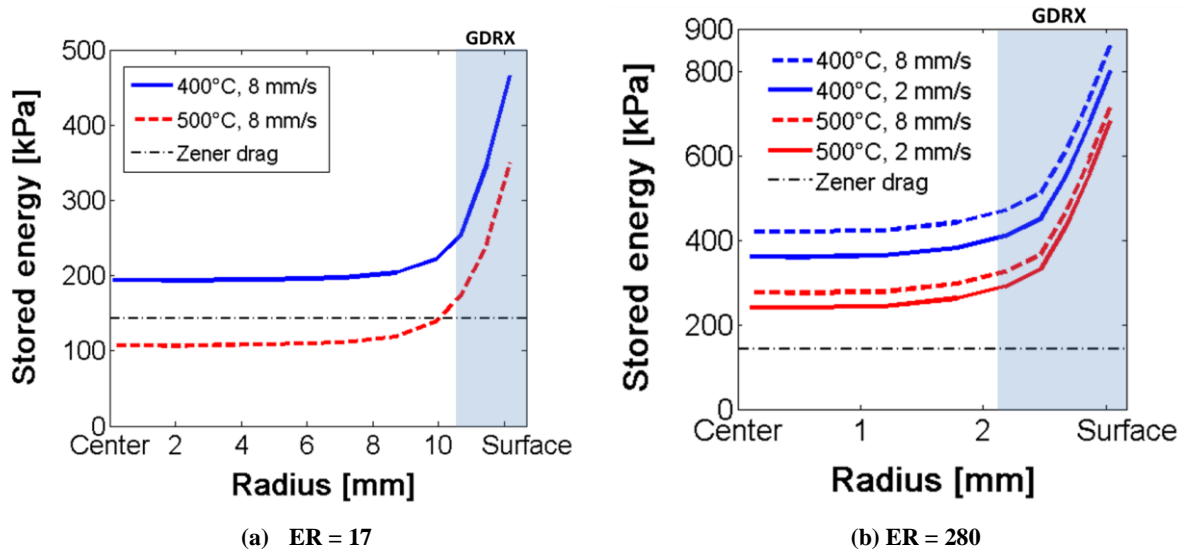


Figure C-1 Calculated stored energy across the radius from the center to surface of mid-length section of round bar extrudate with extrusion ratio of 70, different extrusion conditions and homogenization treatments.



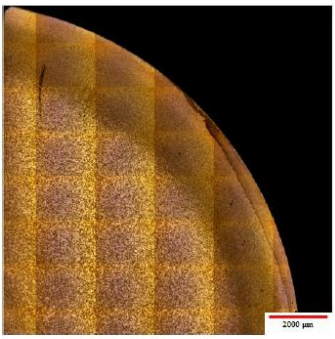
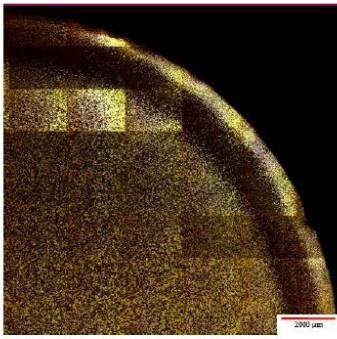


(b) Figure C-2 Calculated stored energy across the radius from the center to surface of the round bar extrudate with extrusion ratios of 17 (a) and 280 (b), homogenization treatment of 8 hours at 550°C.

## Appendix B

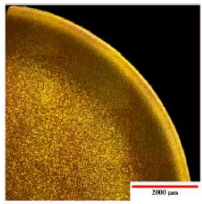
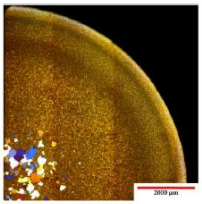
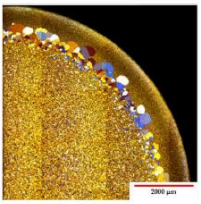

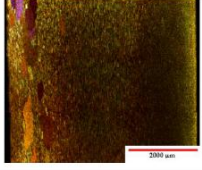
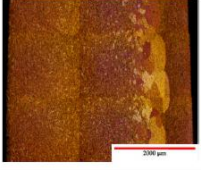



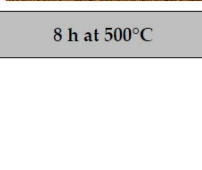
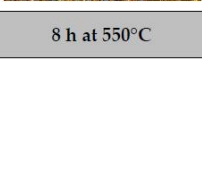
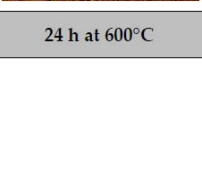
### Optical microscope observations after extrusion (round bar extrusion)

Optical micrographs taken from extrudate mid-length section showing microstructure of extrudate in as-extruded and annealed states are shown in following tables. The experiments were performed by coworkers in UBC [17, 113]. As extruded microstructure for different extrusion conditions and homogenization treatments are presented in Tables B-1 through B-5. Samples that showed no recrystallization or partial recrystallization were subject to annealing treatment. Table B-6 shows the microstructure of these samples after annealing for 10 minutes at 550°C.

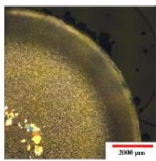
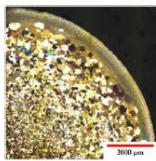
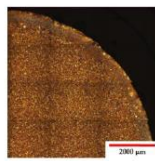
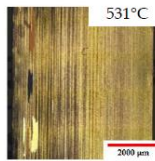
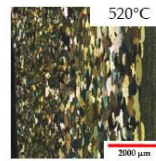
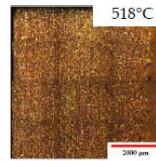
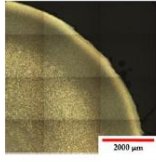
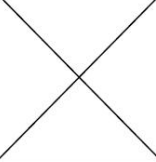
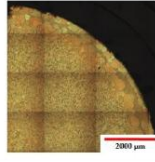
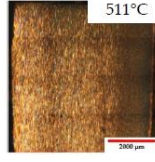
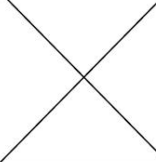
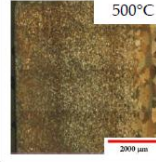
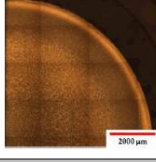
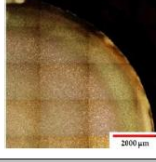
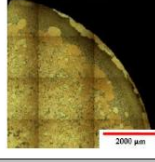
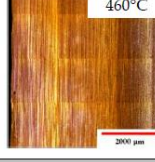
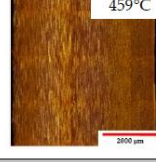
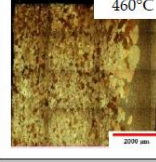
**Table B-1 As-extruded, ER = 17, Homogenization = 8H550, Ram speed = 8 mm/sec [17].**

Transverse		
Longitudinal		
T <sub>extrusion</sub>	400°C	500°C

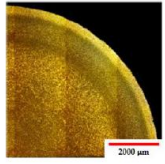
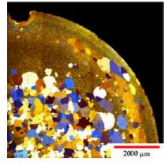
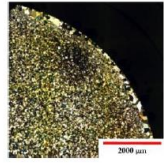
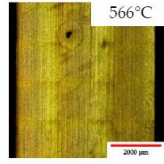
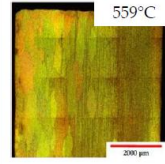
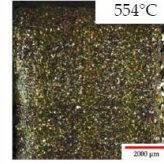
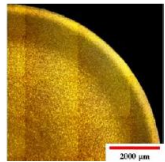
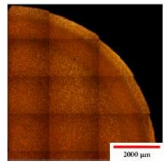
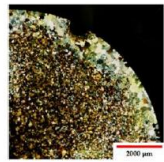
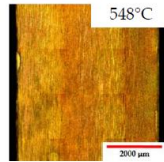
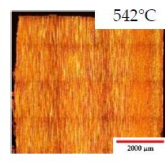
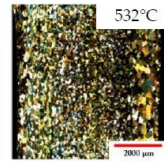
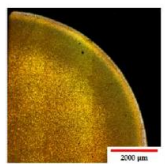
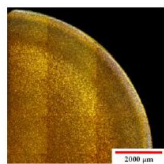
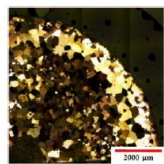
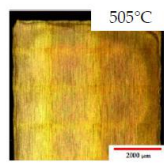
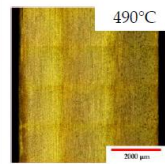
**Table B-2 As-extruded, ER = 17, Billet temperature = 350°C, Ram speed = 2 mm/sec [17].**

Transverse	Low mag. (50x)			
	High mag. (100x)			
Longitudinal	Low mag. (50x)			
	High mag. (100x)			
Homog.		8 h at 500°C	8 h at 550°C	24 h at 600°C

**Table B-3 As-extruded, ER = 70, Billet temperature = 400°C [17].**

Ram Speed (mm/s)	32						
	8						
	2						
Homog.		8 h at 500°C	8 h at 550°C	24 h at 600°C	8 h at 500°C	8 h at 550°C	24 h at 600°C
		Transverse			Longitudinal		

**Table B-4 As-extruded, ER = 70, Billet temperature = 500°C [17].**

Ram Speed (mm/s)	32							
		8						
			2					
	Homog.			8 h at 500°C	8 h at 550°C	24 h at 600°C	8 h at 500°C	8 h at 550°C
	Transverse				Longitudinal			

**Table B-5 As-extruded, ER = 280, Homogenization = 8H550 [17].**

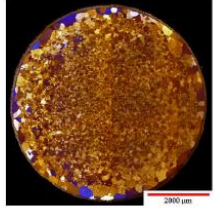
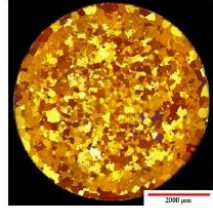
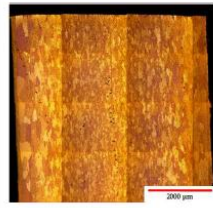
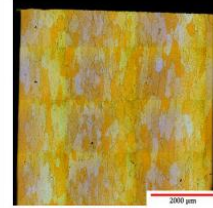
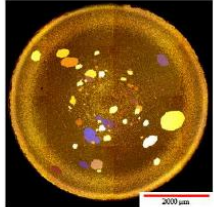
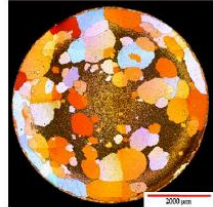
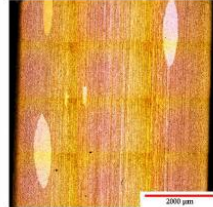
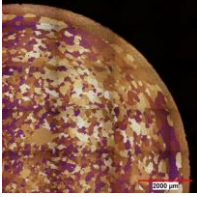


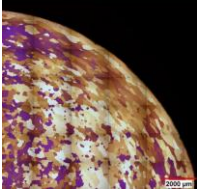
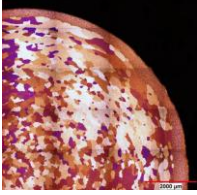
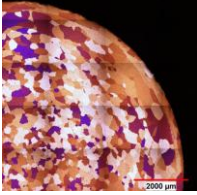
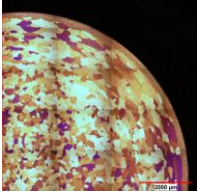
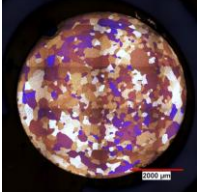
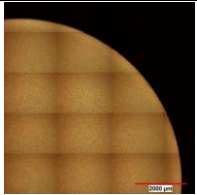
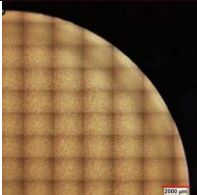
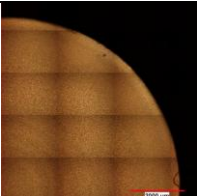
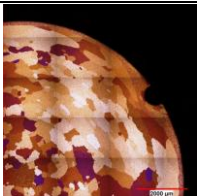
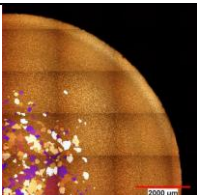
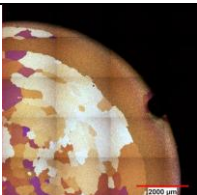
Ram Speed (mm/s)	8				
		2			
	T <sub>extrusion</sub>		400°C	500°C	400°C
	Transverse			Longitudinal	

Table B-6 Extruded at different conditions and annealed at 550°C for 10 minutes [113].

Billet temperature	Homogenization 8H500			Homogenization 8H550		
	ER	V <sub>ram</sub> [mm/s]	Annealed structure	ER	V <sub>ram</sub> [mm/s]	Annealed structure
350°C	70	2		70*	2*	
400°C	70	2		17	8	
	70	8		70	2	
	70	32		280*	2*	
500°C	70	2		17	8	
	70	8		70	2	
	70	32		70	8	

\* Annealing treatment: 525°C for 1 min

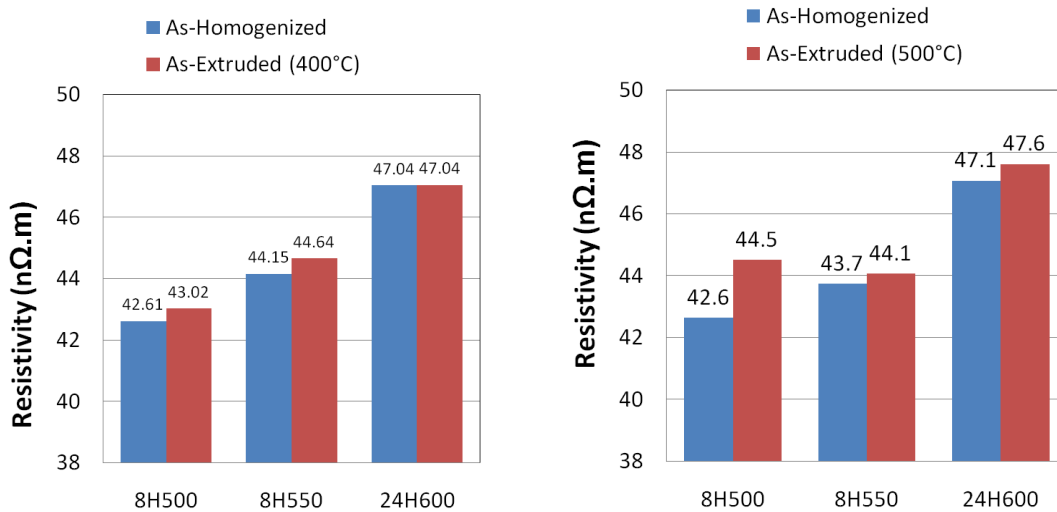
## Appendix C

### Resistivity changes after extrusion (round bar extrusion)

Conductivity measurements were performed on samples before and after extrusion and converted to resistivity. This was done to assess how much precipitation occurred during the extrusion process. Figure C-1 shows the resistivity before and after extrusion for different conditions. Only one case shows a relatively high increase in resistivity (8H500 extruded at 400°C) that means some alloying elements may have returned to solution during the extrusion. Using Lok's formula for resistivity (Equation C-1) [118] this change in resistivity corresponds to only 0.06% Mn to go back to solution. One may conclude that the changes in size and distribution of dispersoids during the extrusion for our conditions are not significant and this effect does not need to be included in the model.

$$\rho = 26.4 + 31.1W_{Mn} + 19.7W_{Fe} + 6.2W_{Si} \quad \text{C-1}$$

$\rho$  is resistivity in nΩ.m, and  $W_{Mn}$ ,  $W_{Fe}$  and  $W_{Si}$  are concentration of Mn, Fe and Si solute in the alloy matrix.



**Figure C-1 Measured electrical resistivity before and after extrusion for various homogenization conditions extruded at 400°C (Left) and extruded at 500°C (Right).**

## References

- [1] *2017 and Later Model Year Light-Duty Vehicle Greenhouse Gas Emissions and Corporate Average Fuel Economy Standards*, National Highway Traffic Safety Administration (NHTSA), 2012.
- [2] L. Cheah, J. Heywood and R. Kirchain, "Aluminum Stock and Flows in U.S. Passenger Vehicles and Implications for Energy Use," *Journal of Industrial Ecology*, vol. 13, no. 5, pp. 718-734, 2009.
- [3] J. Hirsch, "Aluminium in Innovative Light-Weight Car Design," *Materials Transactions*, vol. 52, no. 5, pp. 818-824, 2011.
- [4] "The Aluminum Association," The Aluminum Association Inc., [Online]. Available: <http://www.aluminum.org>. [Accessed 23 May 2013].
- [5] "World Aluminium," International Aluminium Institute, [Online]. Available: <http://www.world-aluminium.org>. [Accessed 23 May 2013].
- [6] "Canadian Aluminum Transformation Technology Roadmap - 2006 Edition," Réseau Trans-Al Inc., 2007.
- [7] ASM Handbook Vol.2, Properties and Selection: Nonferrous Alloys and Special-Purpose Materials, ASM International, 1990.
- [8] J. R. Davis, ASM Specialty Handbook: Aluminum and Aluminum Alloys, ASM International Handbook Committee, 1993.
- [9] P. K. Saha, Aluminum Extrusion Technology, ASM International, 2000.
- [10] H. Ekstrom, "Al-Mn Brazing sheet for heat exchangers," in *Virtual fabrication of aluminium products*, J. Hirsch, Ed., Weinheim, Wiley-VCH, 2006, p. 19.
- [11] A. Kubiak, "Effect of Homogenization on High Temperature Deformation behaviour of AA3XXX Aluminum Alloys," Master's Thesis, University of British Columbia, Vancouver, 2009.
- [12] Y. Mahmoodkhani, M. A. Wells, N. Parson, Y. Geng and W. J. Poole, "Mathematical Modelling of the Extrusion of AA3xxx Aluminum Alloys," *Proceedings of ICAA12*, pp. 566-571, 2010.
- [13] "Aluminum Extruders Council," [Online]. Available: <http://www.aec.org/designresources/>. [Accessed 28 May 2013].

- [14] T. Sheppard, *Extrusion of Aluminium Alloys*, Dordrecht: Kluwer Academic Publishers, 1999.
- [15] "fuzing.com," Fuzing, Inc., [Online]. Available: [www.fuzing.com](http://www.fuzing.com). [Accessed 5 May 2011].
- [16] N. Parson and R. Ramanan, "Optimising AA3003 for Extrudability and Grain Size Control," in *The Conference for Innovations in Aluminum Extrusion*, Orlando, Florida USA, 2008.
- [17] L. M. Grajales, "Effect of High Temperature Extrusion Conditions on the Microstructure of AA3003 Aluminum Alloy," Master's Thesis, The University of British Columbia, Vancouver, 2013.
- [18] M. Bauser, G. Sauer and K. Siegert, *Extrusion*, 2nd ed., ASM International, 2006.
- [19] A. Foydl, N. Ben Khalifa, A. Brosius and A. E. Tekkaya, "An assessment of the grain structure evolution during hot forward extrusion of aluminum alloy 7020," *Key Engineering Materials*, vol. 424, pp. 35-41, 2010.
- [20] Z. Peng and T. Sheppard, "A study on material flow in isothermal extrusion by FEM simulation," *Modelling and Simulation in Materials Science and Engineering*, pp. 745-763, 2004.
- [21] F. J. Humphreys and M. Harthely, *Recrystallization and related annealing phenomena*, 2nd ed., Elsevier, 2004.
- [22] H. J. McQueen, E. Evangelista and M. E. Kassner, "The classification and determination of restoration mechanisms in the hot working of Al alloys," *Zeitschrift fur Metallkunde*, vol. 82, no. 5, pp. 336-345, 1991.
- [23] S. Gourdet and F. Montheillet, "An experimental study of the recrystallization mechanism during hot deformation of aluminum," *Materials Science and Engineering*, vol. A283, p. 274-288, 2000.
- [24] C. Perdrix, M. Y. Perrin and F. Montheillet, "Mechanical Behavior and Structure Development of Aluminum During High Amplitude Hot Deformation," *Mémoires et études scientifiques de la Revue de métallurgie*, vol. 78, no. 6, pp. 309-320, 1981.
- [25] H. J. McQueen, O. Knustad, N. Ryum and J. K. Solberg, "Microstructure Evolution in Al Deformed to Strains of 60 at 400°C," *Scripta Metallurgica*, vol. 19, pp. 73-78, 1985.
- [26] J. K. Solberg, H. J. McQueen, N. Ryum and E. Nes, "Influence of ultra-high strains at elevated temperatures on the microstructure of aluminium. Part I," *Philosophical Magazine*, vol. 60, no. 4, pp. 447-471, 1989.
- [27] H. J. McQueen, "Micromechanisms of Dynamic Softening in Aluminum Alloys during Hot Working," *Hot Deformation of Aluminum Alloys Proc.*, pp. 31-54, 1991.
- [28] M. R. Drury and F. J. Humphreys, "The development of microstructure in Al-5% Mg during



- high temperature deformation," *Acta Metallurgica*, vol. 34, no. 11, p. 2259–2271, 1986.
- [29] H. Zhang, E. V. Konopleva and H. J. McQueen, "Effects of Mn dispersoid on hot working of Al–1Mn," *Materials Science and Engineering*, Vols. A319-321, p. 711–715, 2001.
- [30] W. Blum, Q. Zhu, R. Merkel and H. J. McQueen, "Geometric dynamic recrystallization in hot torsion of Al-5Mg-0.6Mn (AA5083)," *Materials Science and Engineering A*, vol. 205, pp. 23-30, 1996.
- [31] A. Gholinia, F. J. Humphreys and P. B. Prangnell, "Production of ultra-fine grain microstructures in Al–Mg alloys by conventional rolling," *Acta Materialia*, vol. 50, p. 4461–4476, 2002.
- [32] H. Jazaeri and F. J. Humphreys, "The transition from discontinuous to continuous recrystallization in some aluminum alloys I - the deformed state," *Acta Materialia*, vol. 52, p. 3239–3250, 2004.
- [33] C. Poletti, M. Rodriguez-Hortalá, M. Hauser and C. Sommitsch, "Microstructure development in hot deformed AA6082," *Materials Science and Engineering A*, vol. 528, p. 2423–2430, 2011.
- [34] W. H. Van Geertruyden, W. Z. Misiolek and P. T. Wang, "Surface grain structure development during indirect extrusion of 6xxx aluminum alloys," *Journal of Materials Science*, vol. 40, pp. 3861-3863, 2005.
- [35] Y. Mahmoodkhani, M. A. Wells, L. Grajales, W. J. Poole and N. Parson, "Modelling Grain Deformation during Extrusion of AA3003 using the Finite Element Method," in *ICAA13*, Pittsburgh, PA, USA, 2012.
- [36] F. Parvizian, A. Guzel, A. Jager, H. G. Lambers, B. Svendsen, A. E. Tekkaya and H. J. Maier, "Modeling of dynamic microstructure evolution of EN AW-6082 alloy during hot forward extrusion," *Computational Materials Science*, vol. 50, pp. 1520-1525, 2011.
- [37] A. Güzel, A. Jäger, F. Parvizian, H. G. Lambers, A. E. Tekkaya, B. Svendsen and H. J. Maier, "A new method for determining dynamic grain structure evolution during hot aluminum extrusion," *Journal of Materials Processing Technology*, vol. 212, p. 323– 330, 2012.
- [38] L. Donati, A. Segatori, M. El Mehtedi and L. Tomesani, "Grain evolution analysis and experimental validation in the extrusion of 6XXX alloy by use of a lagrangian FE code," *International Journal of Plasticity*, vol. 46, pp. 70-81, 2013.
- [39] A. Foyld, A. Segatori, N. Ben Khalifa, L. Donati, A. Brosius, L. Tomesani and A. E. Tekkaya, "Grain size evolution simulation in aluminium alloys AA 6082 and AA 7020 during hot forward extrusion process," *Materials Science and Technology*, vol. 29, no. 1, pp. 100-110, 2013.
- [40] Q. Du, W. J. Poole, M. A. Wells and N. Parson, "Microstructural Modeling of the

- Homogenization Heat Treatment for AA3XXX Alloys," *JOM*, vol. 63, no. 7, pp. 35-39, 2011.
- [41] Y. J. Li and L. Arnberg, "Evolution of eutectic intermetallic particles in DC-cast AA3003 alloy during heating and homogenization," *Materials Science and Engineering*, vol. A347, pp. 130-135, 2003.
- [42] Y. J. Li and L. Arnberg, "Quantitative study on the precipitation behavior of dispersoids in DC-cast AA3003 alloy during heating and homogenization," *Acta Materialia*, vol. 51, pp. 3415-3428, 2003.
- [43] Y. Geng, "Microstructure Evolution During Extrusion of AA3xxx Aluminum Alloys," Master's Thesis, The University of British Columbia, Vancouver, 2011.
- [44] J. D. Robson, "Microstructural evolution in aluminium alloy 7050 during processing," *Materials Science and Engineering A*, vol. 382, pp. 112-121, 2004.
- [45] E. Nes, N. Ryum and O. Hunderi, "On the Zener Drag," *Acta Metallurgica*, vol. 33, no. 1, pp. 11-22, 1985.
- [46] H. J. McQueen, "Effect of Solute and Precipitates on Hot Working Behavior of Al Alloys," *Hot Deformation of Aluminum Alloys Proc.*, pp. 105-120, 1991.
- [47] A. Miroux, Z. J. Lok, K. Marthinsen and S. van der Zwaag, "Solute and Second Phase Evolution During Industrial Processing of AA3103," *Materials Science Forum*, Vols. 539-543, pp. 281-286, 2007.
- [48] S. P. Chen, A. Miroux and S. ven der Zwaag, "Influence of concurrent precipitation on the nucleation kinetics during recrystallization in AA3003," *Materials Science Forum*, Vols. 519-521, pp. 16605-1610, 2006.
- [49] H. W. Huang, B. L. Ou and C. T. Tsai, "Effect of Homogenization on Recrystallization and Precipitation Behaviour of 3003 Alluminum Alloy," *Materials Transactions*, vol. 49, no. 2, pp. 250-259, 2008.
- [50] N. Parson, S. Barker, A. Shalanski and C. Jowett, "Control of Grain Structure in Al-Mg-Si Extrusions," *Proceedings of the 8th international aluminum extrusion technology seminar*, vol. 1, pp. 11-22, 2004.
- [51] L. De Peri Jr. and W. J. Misiolek, "Theoretical prediction and experimental verification of surface grain structure evolution for AA6061 during hot rolling," *Acta Materialia*, vol. 56, pp. 6174-6185, 2008.
- [52] W. Z. Misiolek and W. R. Van Geertruyden, "Combined numerical simulation and microstructure characterization for prediction of physical properties in extruded aluminum alloys," *Key Engineering Materials*, vol. 424, pp. 1-8, 2010.
- [53] W. H. Van Geertruyden, H. M. Brown, W. Z. Misiolek and P. T. Wang, "Evolution of Surface Recrystallization during Indirect Extrusion of 6xxx Aluminum Alloys," *Metallurgical and*

*Materials Transaction A*, vol. 36A, pp. 1049-56, April 2005.

- [54] A. R. Eivani, "Modeling of Microstructural Evolution during Homogenization and Simulation of Transient State Recrystallization leading to Peripheral Coarse Grain Structure in Extruded Al-4.5Zn-1Mg Alloy," PhD Thesis, Delft University of Technology, 2010.
- [55] Z. Peng and T. Sheppard, "Individual influence of forming parameters on surface recrystallization during aluminum extrusion," *Modelling Simul. Mater. Sci. Eng.*, vol. 12, pp. 43-57, 2004.
- [56] M. Jarrett and N. C. Parson, "Extrusion Method". UK Patent GB2285941, 1995.
- [57] X. Duan and T. Sheppard, "Simulation and control of microstructure evolution during hot extrusion of hard aluminium alloys," *Materials Science and Engineering*, vol. A351, pp. 282-292, 2003.
- [58] D. W. Suh, S. Y. Lee, K. H. Lee, S. K. Lim and K. H. Oh, "Microstructural evolution of Al-Zn-Mg-Cu-(Sc) alloy during hot extrusion and heat treatments," *Journal of Materials Processing Technology*, Vols. 155-156, pp. 1330-1336, 2004.
- [59] P. T. Wang, W. H. Van Geertruyden and W. Z. Misiolek, "Formation of Surface Recrystallization of Al-Mg-Si Alloy During Extrusion," in *Proceedings from 1st International Symposium on Metallurgical Modeling for Aluminum Alloys*, Pittsburgh PA, 2003.
- [60] A. Eivani, H. Ahmed, J. Zhou and J. Duszczuk, "The correlation between deformation conditions and peripheral coarse grain structure in extrusion of AA7020 aluminum alloy," in *Aluminum Alloys: Fabrication, Characterization and Applications - Proceedings of Symposia held during TMS 2008 Annual Meeting and Exhibition*, 2008.
- [61] H. R. Shercliff and A. M. Lovatt, "Modelling of microstructure evolution in hot deformation," *Philosophical Transactions of the Royal Society of London*, vol. 357, pp. 1621-1643, 1999.
- [62] H. E. Vatne, T. Furu, R. Orsund and E. Nes, "Modelling Recrystallization after Hot Deformation of Aluminum," *Acta Materialia*, vol. 44, pp. 4463-4473, 1996.
- [63] C. M. Sellars, "Modelling microstructural development during hot rolling," *Materials Science and Technology*, vol. 6, pp. 1072-1081, 1990.
- [64] A. J. McLaren and C. M. Sellars, "Modelling distribution of microstructure during hot rolling of stainless steel," *Materials Science and Technology*, vol. 8, pp. 1090-1094, 1992.
- [65] C. M. Sellars and Q. Zhu, "Microstructural modelling of aluminium alloys during thermomechanical processing," *Materials Science and Engineering*, vol. A280, pp. 1-7, 2000.
- [66] O. Grong and H. R. Shercliff, "Microstructural modelling in metals processing," *Progress in Materials Science*, vol. 47, pp. 163-282, 2002.

- [67] H. Ahmed, M. A. Wells, D. M. Maijer, B. J. Howes and M. R. van der Vinden, "Modelling of microstructure evolution during hot rolling of AA5083 using an internal state variable approach integrated into an FE model," *Materials Science and Engineering A*, vol. 390, pp. 278-290, 2005.
- [68] J. Talamantes-Silva, M. F. Abbod, E. S. Puchi Cabrera, I. C. Howard and J. H. Beynon, "Microstructure modelling of hot deformation of Al-1%Mg alloy," *Materials Science and Engineering A*, vol. 525, pp. 147-158, 2009.
- [69] X. Velay, "Prediction and control of subgrain size in the hot extrusion of aluminium alloys with feeder plates," *Journal of materials processing technology*, vol. 209, pp. 3610-3620, 2009.
- [70] P. S. Bate and W. B. Hutchinson, "Grain boundary area and deformation," *Scripta Materialia*, vol. 52, pp. 199-203, 2005.
- [71] J. Gil Sevillano, P. van Houtte and E. Aernoudt, "Large Strain Work Hardening and Textures," *Progress in Materials Science*, vol. 25, pp. 69-412, 1981.
- [72] S. B. Singh and H. K. D. H. Bhadeshia, "Topology of grain deformation," *Materials Science and Technology*, vol. 14, pp. 832-834, 1998.
- [73] I. Flitta and T. Sheppard, "Effect of pressure and temperature variations on FEM prediction of deformation during extrusion," *Materials Science and Technology*, vol. 21, pp. 339-346, 2005.
- [74] L. Li, J. Zhou and J. Duszczuk, "Prediction of temperature evolution during the extrusion of 7075 aluminium alloy at various ram speeds by means of 3D FEM simulation," *Journal of Materials Processing Technology*, vol. 147, pp. 360-370, 2004.
- [75] H. S. Valberg, *Applied Metal Forming including FEM Analysis*, Cambridge University Press, 2010.
- [76] Z. Peng and T. Sheppard, "Prediction of Static Recrystallization after Extrusion of shaped Aluminum Sections," *Materials Science Forum*, Vols. 467-470, pp. 407-420, 2004.
- [77] T. Ishikawa, H. Sano, Y. Yoshida, N. Yukawa, J. Sakamoto and Y. Tozawa, "Effect of Extrusion Conditions on Metal Flow and Microstructures of Aluminum Alloys," *Annals of the CIRP*, vol. 55, no. 1, 2006.
- [78] M. Schikorra, L. Donati, L. Tomesani and A. E. Tekkaya, "Microstructure analysis of aluminum extrusion: grain size distribution in AA6060, AA6082 and AA7075 alloys," *Journal of Mechanical Science and Technology*, vol. 21, pp. 1445-1451, 2007.
- [79] J. Zhou, L. Li and J. Duszczuk, "3D FEM simulation of the whole cycle of aluminium extrusion throughout the transient state and the steady state using the updated Lagrangian approach," *Journal of Materials Processing Technology*, pp. 383-397, 2003.
- [80] G. Li, J. Yang, J. Y. Oh, M. Foster, W. Wu, P. Tsai and W. Chang, "Advancements of Extrusion Simulation in DEFORM-3D," *Proceedings of The International Conference on*

*Extrusion and Benchmark*, 2009.

- [81] I. Flitta and T. Sheppard, "Nature of friction in extrusion process and its effect on material flow," *Materials Science and Technology*, vol. 19, pp. 837-845, 2003.
- [82] M. Arentoft, Z. Gronostajski, Z. Niechajowicz and T. Wanheim, "Physical and mathematical modelling of extrusion processes," *Journal of Materials Processing Technology*, vol. 106, pp. 2-7, 2000.
- [83] H. Sofuoglu and H. Gedikli, "Physical and numerical analysis of three dimensional extrusion process," *Computational Materials Science*, vol. 31, pp. 113-124, 2004.
- [84] M. Schikorra, L. Donati, L. Tomesani and M. Kleiner, "The role of friction in the extrusion of AA6060 aluminum alloy, process analysis and monitoring," *Journal of Materials Processing Technology*, vol. 191, pp. 288-292, 2007.
- [85] H. Valberg, "Metal flow in the direct axisymmetric extrusion of aluminium," *Journal of Materials Processing Technology*, vol. 31, pp. 39-55, 1992.
- [86] H. Valberg, "Extrusion welding in aluminium extrusion," *International Journal of Materials and Product Technology*, vol. 17, no. 7, pp. 497-556, 2002.
- [87] H. J. McQueen and N. D. Ryan, "Constitutive analysis in hot working," *Materials Science and Engineering*, vol. A322, pp. 43-63, 2002.
- [88] U. F. Kocks and S. R. Chen, "Constitutive laws for deformation and dynamic recrystallization in cubic metals," *Aspects of High Temperature Deformation and Fracture in Crystalline Materials*, pp. 593-600, 1993.
- [89] T. Sheppard, "Temperature changes occurring during extrusion of metals: comparison of balk, numerical, and integral profile predictions with experimental data," *Materials Science and Technology*, vol. 15, pp. 459-463, 1999.
- [90] X. Duan, X. Velay and T. Sheppard, "Application of finite element method in the hot extrusion of aluminum alloys," *Materials Science and Engineering*, vol. A369, pp. 66-75, 2004.
- [91] Z. Peng and T. Sheppard, "Simulation of multi-hole die extrusion," *Materials Science and Engineering*, vol. A367, pp. 329-342, 2004.
- [92] N. Boncheva, G. Petzof and L. Parashkevova, "Thermomechanical modelling of hot extrusion of Al-alloys, followed by cooling on the press," *Computational Material Science*, vol. 38, pp. 83-89, 2006.
- [93] G. Fang, J. Zhou and J. Duszczyk, "FEM simulation of aluminium extrusion through two-hole multi-step pocket dies," *Journal of Materials Processing Technology*, 2008.
- [94] F. Parvizian, T. Kayser, C. Hortig and B. Svendsen, "Thermomechanical modeling and simulation of aluminum alloy behavior during extrusion and cooling," *Journal of Materials*

- Processing Technology*, vol. 209, pp. 876-883, 2009.
- [95] M. Schikorra, L. Donati, L. Tomesani and A. E. Tekkaya, "Microstructure analysis of aluminum extrusion: Prediction of microstructure on AA6060 alloy," *journal of materials processing technology*, vol. 201, pp. 156-162, 2008.
- [96] T. Sheppard, "Prediction of structure during shaped extrusion and subsequent static recrystallisation during the solution soaking operation," *Journal of Materials Processing Technology*, vol. 177, pp. 26-35, 2006.
- [97] S. Kobayashi, S. OH and T. Altan, *Metal Forming and the Finite-Element Method*, New York: Oxford University Press, 1989.
- [98] L. Donati, L. Tomesani, M. Schikorra, N. Ben Khalifa and A. E. Takkaya, "Friction model selection in FEM simulations of aluminium extrusion," *International Journal of Surface Science and Engineering*, vol. 4, no. 1, pp. 27-41, 2010.
- [99] V. I. Johannes, C. W. Jowett and R. F. Dickson, "Transverse Weld Defects," in *Proceedings of the 6th International Seminar on Aluminum Extrusion Technology*, Chicago, IL, USA, 1996.
- [100] T. Hatzenbichler and B. Buchmayr, "Finite element method simulation of internal defects in billet-to-billet extrusion," *Journal of Engineering Manufacture*, vol. 224, pp. 1029-1042, 2010.
- [101] Q. Li, C. Harris and M. R. Jolly, "Finite element modelling simulation of transverse welding phenomenon in aluminium extrusion process," *Materials and Design*, vol. 24, p. 493-496, 2003.
- [102] C. Jowett, N. Parson, R. Guay, S. Fafard and A. Maltais, "The Dynamics of the Dead Zones in Hot Extrusion," in *Proceedings of the Tenth International Aluminum Extrusion Technology Seminar, ET'12*, Miami FL, USA, 2012.
- [103] Y. Mahmoodkhani, M. A. Wells, N. Parson, C. Jowett and W. J. Poole, "Modeling the formation of transverse weld during billet-on-billet extrusion," in *INALCO 2013*, Montreal, October 2013 (Accepted).
- [104] F. J. Humphreys, *VMAP is a suite of programmes developed for quantitative analysis of the EBSD data generated by the HKL Channel acquisition system*.
- [105] "SIGMATEST® 2.069 Device Sheet," [Online]. Available: <http://www.foerstergroup.com/>. [Accessed 31 May 2013].
- [106] J. Hodowany, G. Ravichandran, A. J. Rosakis and P. Rosakis, "Partition of Plastic Work into Heat and Stored Energy in Metals," *Experimental Mechanics*, pp. 113-123, 1999.
- [107] *DEFORM v10.0 Database*.
- [108] E. Sartori, "Convection coefficient equations for forced air flow over flat surfaces," *Solar*

*Energy*, vol. 80, no. 9, pp. 1063-1071, 2006.

- [109] P. F. Fisher, *Developments in Spatial Data Handling*, Verlag Berlin Heidelberg: Springer, 2005.
- [110] J. Go, W. J. Poole, M. Militzer and M. A. Wells, "Modelling recovery and recrystallisation during annealing of AA 5754 aluminium alloy," *Materials Science and Technology*, vol. 19, pp. 1361-1368, October 2003.
- [111] Q. DU, W. J. Poole, M. A. Wells and N. C. Parson, "Microstructure evolution during homogenization of Al–Mn–Fe–Si alloys: Modeling and experimental results," *Acta Materialia*, vol. 61, pp. 4961-4973, 2013.
- [112] Q. Du, Interviewee, *Dispersoid data for various homogenization treatments*. [Interview]. 8 April 2011.
- [113] L. M. Grajales, Interviewee, *Post-extrusion annealing*. [Interview]. October 2012.
- [114] M. A. Wells, D. J. Lloyd, I. V. Samarasekera, J. K. Brimacombe and E. B. Hawbolt, "Modeling the Microstructural Changes during Hot Tandem Rolling of AA5XXX Aluminum Alloys: Part I. Microstructural Evolution," *Metallurgical and Materilas Transaction B*, vol. 29B, pp. 611-620, 1998.
- [115] P. A. Hollinshead and T. Sheppard, "Substructure morphology in aluminium alloys AA3003 and AA3004," *Materials Science and Technology*, vol. 3, pp. 1019-1024, December 1987.
- [116] N. Parson, Interviewee, *Transverse weld depth*. [Interview]. 23 May 2013.
- [117] H. Zhu, M. J. Couper and A. KDahle, "Etching effects and the formation of Streaking Defects on Al Extrusions," *Aluminium International Today*, vol. Extrusion, no. May/June, 2011.
- [118] Z. J. Lok, "Microchemistry in Aluminium Sheet Production," PhD Thesis, Delft University of Technology, Delft, 2005.